Chemical Science

ROYAL SOCIETY OF CHEMISTRY

REVIEW

View Article Online
View Journal | View Issue

Check for updates

Cite this: *Chem. Sci.*, 2024, **15**, 4631

A molecular view of single-atom catalysis toward carbon dioxide conversion

Xin Shang,[ab] Xiaofeng Yang,[a] Guodong Liu,[a] Tianyu Zhang*[c] and Xiong Su*[a]

Carbon dioxide (CO_2) conversion has attracted much interest recently owing to its importance in both scientific research and practical applications, but still faces a bottleneck in selectivity control and mechanism understanding owing to diversified active sites. Single-atom catalysts (SACs) featuring isolated and well-defined active centers are proved to not only exhibit unparalleled performances in various processes of CO_2 conversion but also provide excellent research paradigms by circumventing the heterogeneity of active sites. Herein, we will not only critically review recent progress on the application of SACs in chemical CO_2 conversion based on previous comprehension of general thermodynamics and kinetics, but also try to offer a multi-level understanding of SACs from a molecular point of view in terms of the central atom, coordination environment, support effect and synergy with other active centers. Meanwhile, crucial scientific issues of research methods will be also identified and highlighted, followed by a future outlook that is expected to present potential aspects of further developments.

Received 21st December 2023
Accepted 6th February 2024

DOI: 10.1039/d3sc06863c

rsc.li/chemical-science

1. Introduction

The utilization of fossil fuels has greatly changed people's way of life and propelled the progress of human civilization. Now, however, it has become a double-edged sword damaging the climate and environment by the notorious greenhouse effect due to the substantial carbon dioxide (CO_2) emission.[1] The cumulative CO_2 emissions have caused global mean temperature changes for more than a century (Fig. 1a), implying an imperative need to impose restrictions on carbon emissions. Therefore, a growing consensus has been established that realizing 'carbon peak' and 'carbon neutrality' is of great significance in seeking a balance between efficiency and quality, further contributing to the desired sustainable development.[2,3] Besides applying renewable clean energy sources, such as solar, wind, wave, *etc.*, as substitutes for conventional fossil resources, carbon capture, utilization and storage (CCUS) is expected to provide supplementary solutions to meet the challenges of mitigating climate change by recycling the released CO_2 from

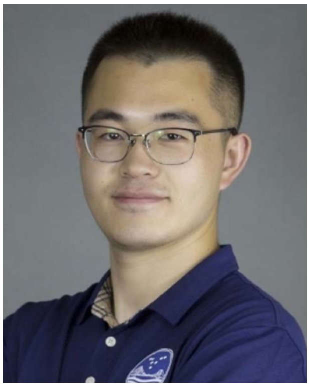

Xin Shang

Xin Shang received his B.S. degree from Tianjin University in 2016. Now, he is pursuing his PhD degree in the University of Chinese Academy of Sciences (UCAS), Dalian Institute of Chemical Physics, Chinese Academy of Sciences (DICP, CAS), supervised by Prof. Yan-qiang Huang. His research interests include C1 chemistry and synthesis and application of molecular sieves and nano-structured materials.

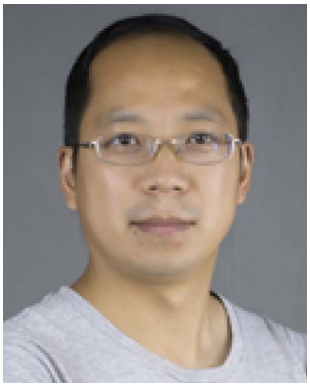

Xiaofeng Yang

Xiaofeng Yang received his B.S. from Nanjing University (2003) and PhD degree in 2010 from the Dalian Institute of Chemical Physics under the supervision of Prof. Tao Zhang. After 2 years of postdoctoral research in Prof. Jun Li's group at Tsinghua University on theoretical and computational catalysis, he joined the DICP again and was promoted to professor in 2019. His research interests include theoretical and computational catalysis and nano- and single-atom catalysis.

---

[a] *State Key Laboratory of Catalysis, Dalian Institute of Chemical Physics, Chinese Academy of Sciences, No. 457 Zhongshan Road, Dalian 116023, China. E-mail: suxiong@dicp.ac.cn*

[b] *University of Chinese Academy of Sciences, Beijing 100049, China*

[c] *College of Environmental Science and Engineering, Beijing Forestry University, Beijing 100083, China. E-mail: tzhang@bjfu.edu.cn*

the atmosphere.[4–7] Indeed, artificial transformation of CO_2, a nontoxic, widespread and renewable carbon source, into various value-added products might contribute to cleaner industrial production,[8–10] although there is still controversy regarding the economic efficiency of its scale development[11,12] (Fig. 1b), in which the high cost and low efficiency of practical processes are considered to be key barriers. In fact, not only the high energy input to break the C═O bonds (803 kJ mol^{-1}) but also the complicated reaction networks pose huge obstacles for the practical exploitation of CO_2 conversion for chemical synthesis. Feasible catalytic processes and advanced devices are thus in great demand, for which the fabrication of effective catalysts is one of the core issues.

Currently, catalysts play a vital role in most chemical syntheses by steering the reaction pathways towards lower activation energy barriers for the formation of specific intermediate species, thereby extensively increasing the rate of desired reactions. Homogeneous catalysts containing metal sites with well-defined coordination environments have been extensively used in CO_2 conversion for the synthesis of various organic compounds,[9,13–16] exhibiting a high turnover number (TON) and turnover frequency (TOF) due to the full contact between active centers and substrates in one phase. However, the difficulty of catalyst separation and inferior durability under harsh conditions still limit their practical application in large-scale industrial production. Heterogeneous catalysts, in contrast, are more easily separated and recycled,[17] but only a small fraction of surficial metal sites can efficiently participate in the catalytic cycles, since the chemical interactions always occur on specific interfaces.[18] Metal species with an uneven nature in traditional heterogeneous catalysts might even serve as troublemakers causing undesired side reactions or interfering in certain elementary steps, leading to deterioration of catalytic performance. Furthermore, the intrinsic complexity of CO_2 transformation regarding the multiple-branch reaction pathways and corresponding challenges in selectivity control lead to ambiguous structure–activity relationships and labyrinthine mechanism understanding owing to the diversity of active sites. And this makes the rational design of effective catalysts a difficult task because of the absence of systematic theories.

To overcome these problems and merge the merits of homogeneous and heterogeneous catalysts, a series of catalysts featuring atomically dispersed metal atoms on the interface as sustained active sites, *i.e.*, single-atom catalysts (SACs), have been proposed in recent decades[18–20] (Fig. 2), and were first introduced by Zhang and his co-workers in 2011.[21] And already before that, a few studies on catalysts with highly dispersed metal species have been conducted, disclosing that atoms in the isolated ionic or free state rather than ensembles might contribute to their major activity in various systems.[22–29] With continuous advances in high-resolution characterization techniques and computational chemistry, more unique properties of SACs have been unveiled and are expected to inject new vigor into a broader frame of catalytic science.[30–37]

Recently, fruitful academic achievements involving SAC materials have been springing up toward expanding application fields,[38–44] attracting worldwide interest for in-depth studies. In the meantime, the practical application of catalytic CO_2 conversion is also expected to benefit from the SAC materials,[45–48] demonstrating not only the boosted catalytic

Guodong Liu

Guodong Liu received his B.S degree in 1998 and PhD degree in 2019 from the Dalian University of Technology. He has been working in the Dalian Institute of Chemical Physics, Chinese Academy of Sciences (DICP, CAS), since 2019 and is in charge of developing heterogeneous catalysts on the industrial scale. His research interests include the synthesis of zeolite materials and their applications in aromatization of alkanes, alkylation of arenes, and epoxidation of alkenes.

Tianyu Zhang

Tianyu Zhang received his B.S. degree from the Dalian University of Technology and PhD degree from Southern Illinois University. He has been working in Beijing Forestry University as an assistant professor since 2021. His research interests include C1 molecular catalytic conversion and theoretical chemistry.

Xiong Su

Xiong Su received his B.S. degree from the Dalian University of Technology and PhD degree in industrial catalysis from the Dalian Institute of Chemical Physics (DICP), Chinese Academy of Sciences (CAS). He continued his academic career in the DICP as an assistant professor and was promoted to associate professor in 2017. His research interests include C1 chemistry and synthesis and application of molecular sieves and nanostructured materials.

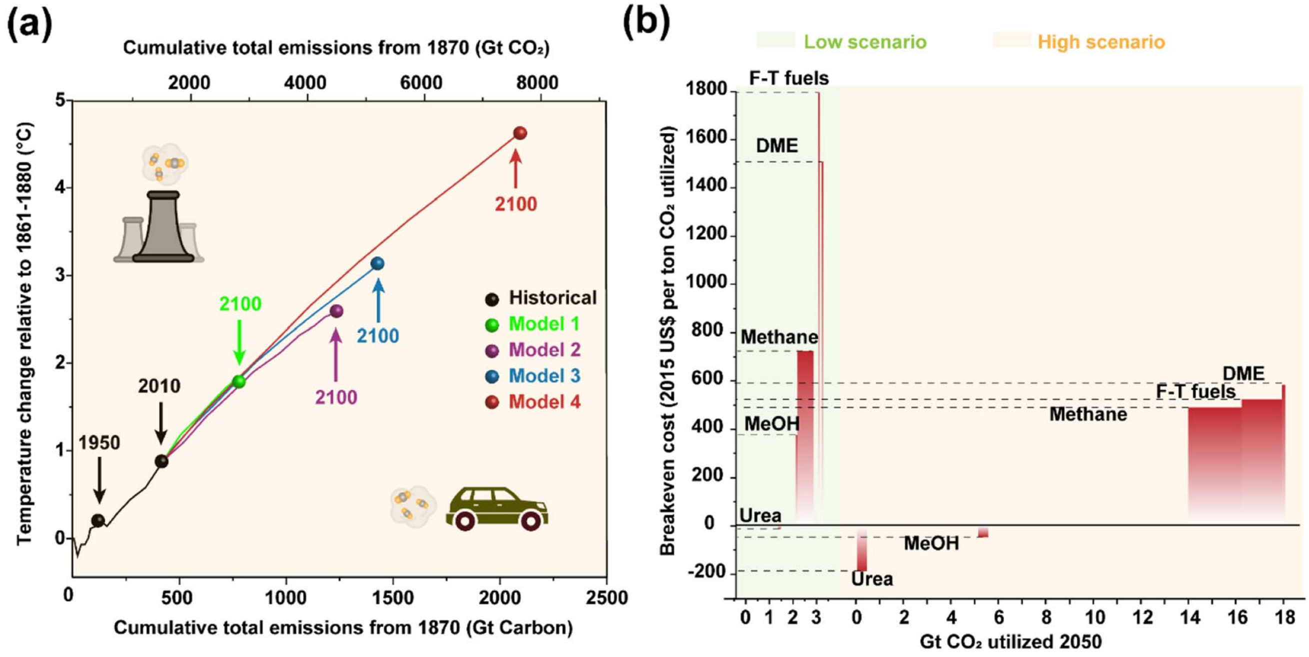

Fig. 1 (a) Simulated global mean surface temperature increase as a function of the cumulative total global CO_2 emissions as predicted by different models. Data are acquired from ref. 2 with permission from Springer Nature, copyright 2016. (b) Estimated CO_2 utilization potential and breakeven cost of different sub-pathways in low and high scenarios. Data are acquired from ref. 12 with permission from Springer Nature, copyright 2019.

activity propelled by complete exposure of metal sites with nearly 100% atom utilization, but also controllable selectivity stemming from the distinct geometric and electronic properties. Compared with the conventional heterogeneous metal catalysts based on nanoparticles (NPs) and nanoclusters (NCs), the viable regulation of chemical microenvironments on the atomic scale *via* modulating the coordination states, spatial distances as well as the synergy between metal sites and supports might lead to a great difference in electronic states, orbital hybridization and energy bands. Additionally, the incorporation of other types of active sites can make SACs adaptable for extensive applications without tarnishing the advantages of single atomic sites. These factors further promote the activation of CO_2 and stabilization of intermediate species with a corresponding match in energy and structure, offering an outstanding performance in multiple CO_2 conversion reactions.[49] More importantly, SACs with well-defined active sites, not only allow an exclusive selectivity, but also provide excellent paradigms for acquiring in-depth and comprehensive insights into catalysis. The studies on transformation of simple molecules such as CO_2 exemplify the modeling approach to gain deep insight into the intrinsic thermodynamics and kinetics of typical chemical reactions assisted by a combination of experimental and theoretical aspects, which might also inspire in-depth research studies of other more complex catalytic systems and rational design of more advanced catalytic materials from an atomic-scale perspective.

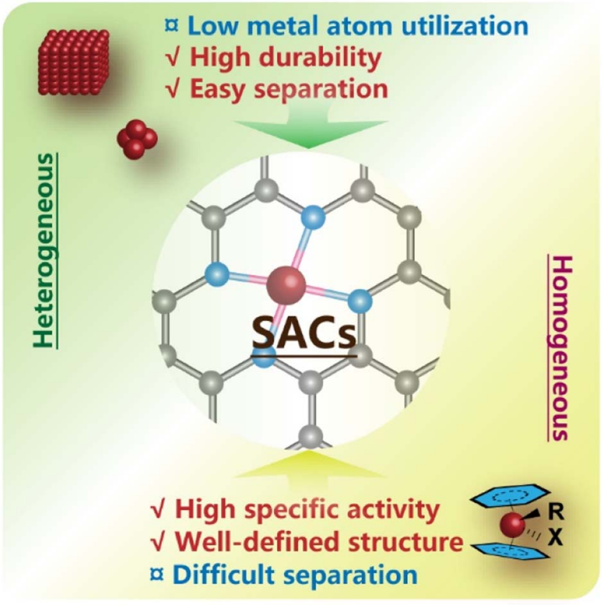

Fig. 2 Single-atom catalysts (SACs) incorporate the advantageous features of homogeneous and heterogeneous catalysts.

In this review, we will first introduce the general understanding of typical chemical CO_2 transformation. Then, we will concentrate on the recent progress on the application of SACs in chemical CO_2 conversion based on various reaction routes and products and attempt to provide a comprehensive understanding of catalyst design, process optimization and reaction mechanisms (Fig. 3). Thanks to their well-defined geometric and electronic structures, we could further offer a molecular understanding of SACs in CO_2 conversion with specific examples. The crucial scientific issues regarding SAC research and application will be also concluded and highlighted to gain in-

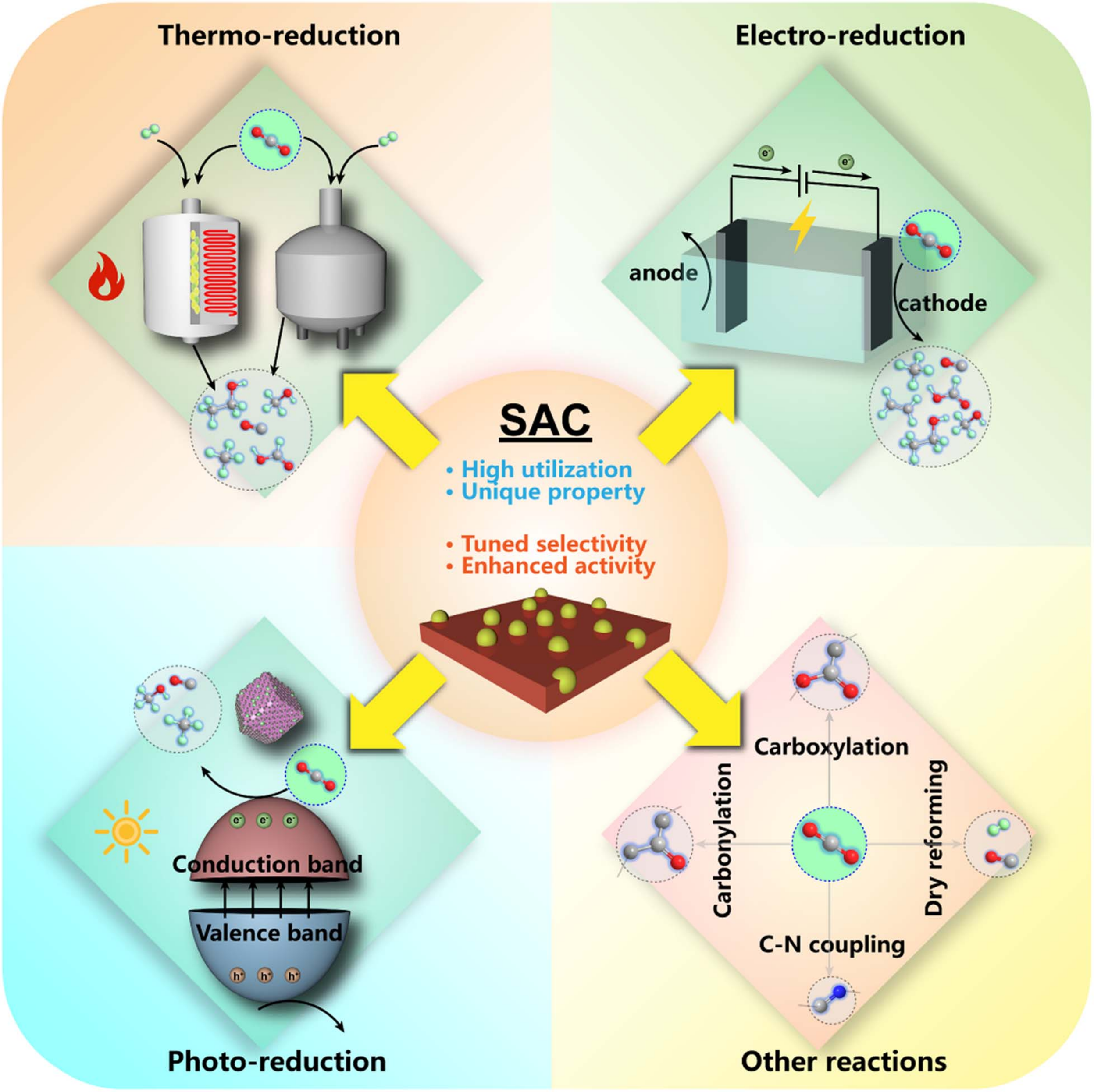

Fig. 3 An overview of SAC application in chemical CO_2 conversion displayed in this review.

depth insight. To inspire future research studies in such catalytic systems, we will also elucidate critical study methods and technological processes involving SACs for CO_2 conversion. An outlook for future research will be demonstrated eventually based on the analysis of the current research direction, expected to present a potential prospect for further development of SAC application in CO_2 conversion.

2. General understanding of CO_2 transformation

Before starting the discussion on the application of SACs in CO_2 transformation, the general understanding in terms of thermodynamics and kinetics should be briefly introduced in advance. The typical CO_2 transformation reactions involved not only the common reduction with hydrogen (H_2) and water (H_2O), but also other complicated synthesis processes with various heteroatomic and organic compounds, in which CO_2 could also be partially or completely reduced following distinct reaction routes. Therefore, understanding the reduction reactions will be the focus in the following discussion especially regarding thermodynamics, as other processes will also be discussed in brief.

2.1 Thermodynamics

Generally, the thermochemical reduction processes of CO_2 involve the co-transformation of CO_2 and H_2 molecules. Accordingly, we calculated the free Gibbs energy change and

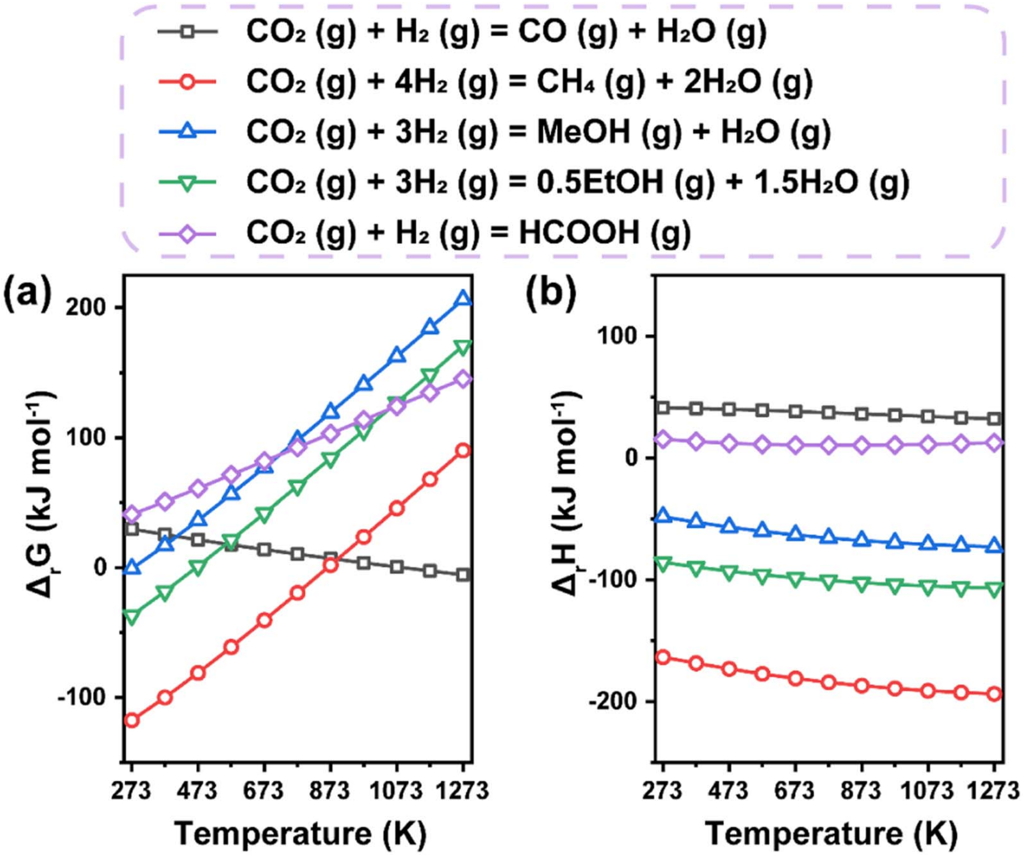

Fig. 4 Thermodynamic analysis of main thermochemical reduction routes to various products. (a) Free Gibbs energy change. (b) Enthalpy change. Data are based on HSC chemistry 6.0 software.

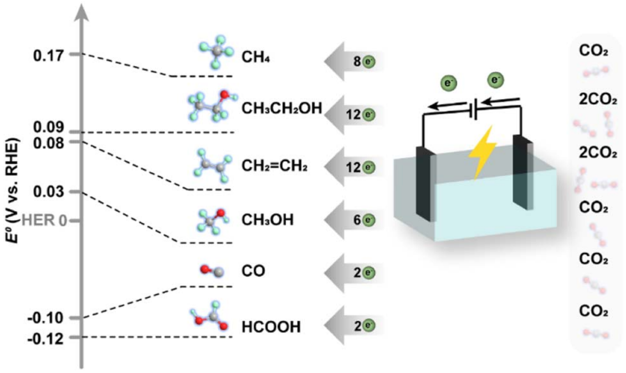

Fig. 5 Equilibrium reduction potentials and electron transfer numbers for various products from CO_2 reduction.

enthalpy change dependent on temperature in typical hydrogenation routes toward various products (Fig. 4). The increasing free Gibbs energy change with increasing temperature for most routes apart from the CO_2-to-CO reaction implies that lower temperature could be a more suitable condition for the synthesis of target products, which is also proved by the exothermic nature of most reactions. However, sufficiently higher operating temperature is always necessary in practical processes to ensure feasible efficiency, leading to inevitable side reactions due to their intersectional thermodynamic ranges. Therefore, the difficult selectivity control of CO_2 hydrogenation makes the design of efficient catalysts a great challenge.

On the other hand, the electrochemical reduction of CO_2 commonly involves the co-transformation of H_2O molecules and operation at ambient temperature and pressure, in which H_2O molecules provide protons and lose electrons to form O_2, as CO_2 molecules accept protons and electrons and are

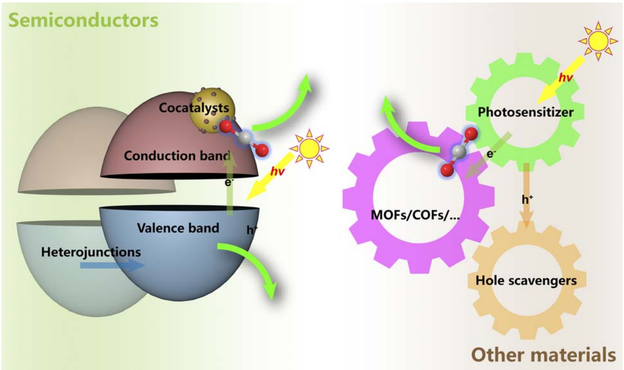

Fig. 6 Typical photocatalytic systems for CO_2 reduction.

transformed into various reduction products. There have been also reports on high-temperature electrolysis of CO_2 in solid-electrolyte cells for higher energy efficiency,[50] in which CO and O^{2-} are generated from CO_2 molecules, and then O^{2-} is transmitted to the anode surface through the electrolyte, losing electrons and forming O_2. For a more comprehensive understanding, the equilibrium reduction potentials of different electrochemical routes are demonstrated in Fig. 5, since the free Gibbs energy change could be well correlated with redox potentials according to the equation $\Delta G = -nFE$. Obviously, the redox potentials of most half reactions of electrochemical reduction processes are close to that of the hydrogen evolution reaction (HER, $2H^+ + 2e^- \rightarrow H_2$), making the HER a parallel reaction competing with CO_2 reduction by consuming the reactive electrons. Therefore, one of the core issues that the design of catalysts should take into account is to circumvent the influence of the thermodynamically inclined HER.

The photochemical reduction processes, much more complicatedly, are limited by not only the thermodynamic barriers lying on the CO_2 reaction pathways but also the energy transition for the light-to-electron procedures. Generally, the photoreduction of CO_2 encompasses three pivotal procedures, which are consecutive light adsorption, charge separation and migration, and catalytic transformation[45,51–54] (Fig. 6). For the facile formation and separation of photoexcited electron–hole pairs, semiconductor materials are commonly used as substrates due to their appropriate energy bandwidth. With the input of light in the specific wavelength range, electrons are excited from the valence band (VB) to the conduction band (CB), leaving the corresponding number of holes. Then, the electrons might participate in the reduction reactions, while the holes are responsible for the oxidation reactions. Quite similar to the cases in electrochemical processes, as the HER in the water photolysis process needs only two-electron transfer, CO_2 reduction always needs more electrons and involves more complex pathways in the whole reaction. This suggests that it should be more urgent to accelerate the photo-induced electron separation and migration rather than focusing on the CO_2 reduction kinetics. The challenges in both optoelectronic and catalytic processes still make the efficiency the Achilles' heel in limited practical application of the photocatalytic systems for CO_2 to valuable products.[45,51] Hence, so-called cocatalysts, certain kinds of modifiers and active components, have been introduced into the photocatalytic systems, playing a crucial role in enhancing charge separation and transfer and manipulating the activity and selectivity of CO_2 reduction towards specific products.[51,54]

The co-transformation of CO_2 with other molecules from simple C_1 hydrocarbon methane ($CO_2 + CH_4 \rightarrow 2CO + 2H_2$, $\Delta G = 170$ kJ mol^{-1}, $\Delta H = 243$ kJ mol^{-1}, 298 K) to various heteroatomic compounds and multiple-atom organics renders the systematic analysis of thermodynamics an impossible task due to the diversified conditions and products. In these cases, reaction kinetics is always much more important for its role in determining the specific activity and selectivity toward certain products.

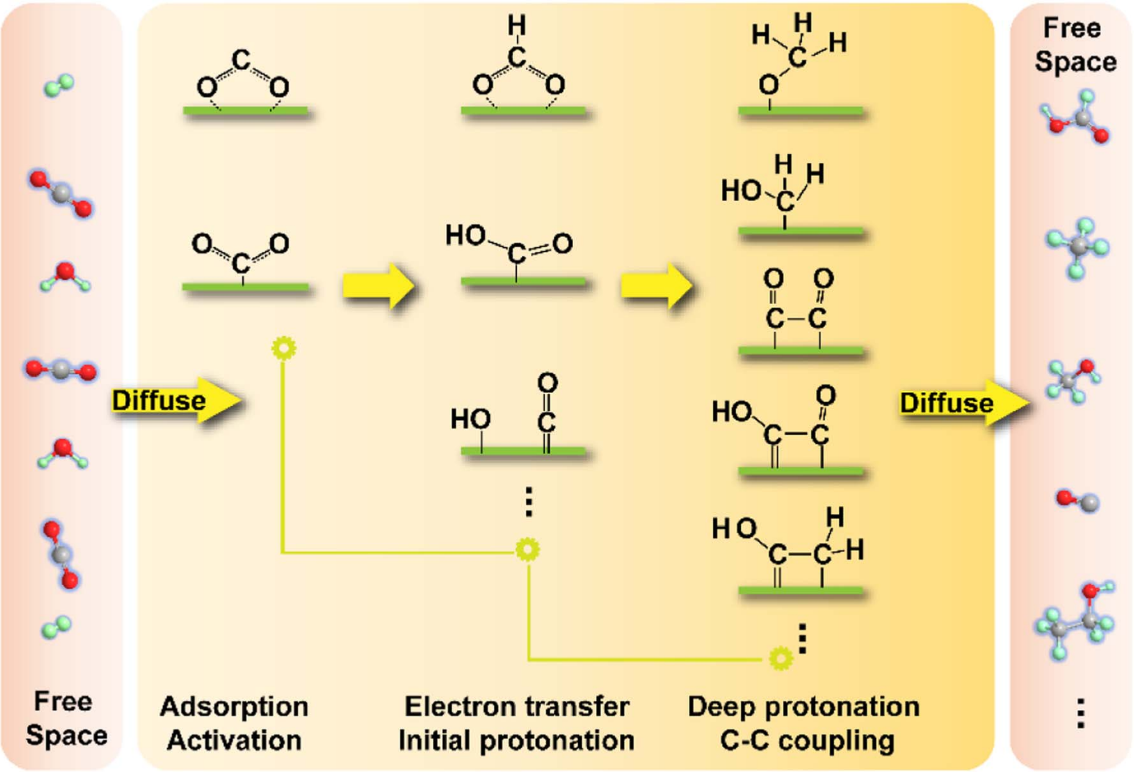

Fig. 7 Schematic illustration of specific important kinetic procedures in typical CO_2 reduction processes. In particular, we only list a part of the kinetic steps in this figure, and there could be other possible steps in various CO_2 transformation processes.

2.2 Kinetics

Prior to the chemical reactions, mass transfer, *i.e.*, the diffusion of CO_2 molecules and other reactants onto the reaction interface and the release of products from the active sites play a critical role in the kinetics of whole CO_2 transformation process. This is largely determined by the chemical interaction that can only function effectively in a limited range of distance, although potential long-range influences still exist. Reaction equilibrium and the regeneration of active centers would also partially depend on a sufficient diffusion rate rather than only the effect of chemical forces. In fact, diffusion processes in most heterogeneous catalytic systems cannot be ignored, and researchers endeavor to design catalysts with higher dispersion and smaller size and develop advanced reactors with enhanced capability of mass transfer to alleviate the negative influence of insufficient diffusivity. In this way, in-depth research into the intrinsic reaction kinetics of CO_2 transformation has a great significance. Herein, we will focus on the CO_2 reaction kinetics of reduction reactions in a hydrogen atmosphere or under aqueous conditions because of the universality of research studies and the great attention to them (Fig. 7). The other reactions involving CO_2 transformation kinetics would be discussed in conjunction with the introduction of specific catalysts.

The first stage of reaction kinetics is the initial adsorption and activation of CO_2 molecules, commonly involving the transfer of electrons between different reactants or the reactant and reactive interface. CO_2 is a typical linear nonpolar molecule comprising two σ bonds and two delocalized π bonds between one carbon and two oxygen atoms. The chemical bonds between carbon and oxygen fall in between a conventional double bond and triple bond, showing higher bonding energy and relative chemical sluggishness. The electron cloud in delocalized bonds is mainly bound to two oxygen atoms and the higher electronegativity of oxygen leads to lower reactivity of electron pairs in such bonding orbitals. In contrast, the lone electron pairs in the oxygen atom are believed to be able to be involved in the chemical transformation, making the CO_2 molecule an electron donor. On the other hand, the carbon atom in the CO_2 molecule has electron deficiency and could be an electron acceptor. Therefore, the typical activation routes of a CO_2 molecule include (i) input of electrons from catalysts to the carbon atom in the CO_2 molecule, (ii) the carbon atom in the CO_2 molecule takes away electrons from other electron-rich reactants, (iii) the CO_2 molecule donates lone electron pairs to catalysts and (iv) the CO_2 molecule donates lone electron pairs to certain electron-deficient reactants. Currently, most of the reduction processes follow the first two routes especially in the case of metal catalysis systems, while the latter two routes are more likely responsible for the initial activation of CO_2 in some oxide catalysis and coordination chemistry systems for certain organic syntheses. To enhance the adsorption and activation, researchers have devoted their efforts to delicate design of catalysts, mainly through modifying the energy bands and electronic orbitals to match the features of the CO_2 molecule for most thermochemical and electrochemical systems, and also through enhanced light-to-electron processes for photochemical systems.

After the initial activation, the transformation routes of CO_2 might go through certain protonation and C–C coupling processes and experience stepwise evolution of various intermediates and transition states, forming a labyrinthine reaction network. This brings one of the greatest challenges in the control of product selectivity, for which catalysts have to subtly steer the reaction pathway toward specific targets. Only eliminating the side reaction pathway can ensure the efficiency of the target reaction, just like trimming the hedge and removing the weeds from crops. The different intermediate routes are highly dependent on the electronic properties of reactive interfaces that are closely related to the chemical interaction between guest molecules and substrates, as the stability or the Gibbs free energy of transition states could be influenced by the interaction, thereby determining the activation energy barriers from the initial to the secondary stages. In some cases, the spatial location of active sites and specific geometric properties could also have an effect on the stabilization of intermediates especially for those needing the synergy of different active components in multiple-step synthesis or with distinctive steric structures. Decided by the nature of active sites, including but not limited to *COOH, HCOO* and *COHO (* represents the adsorption site) moieties could be the key intermediates in a typical reduction reaction toward C_1 products. They further go through protonation and electron transfer and are transformed into products with a higher H/C ratio. The kinetics of protonation steps in the thermochemical hydrogenation reaction and other multiple-molecule reactions (such as that with methane) might be also dependent on the supply of active H species stemming from activation and dissociation of H_2 and other H-rich molecules. A balance between the activation of different reactants therefore should also play a vital role in the reaction kinetics.

The situations are even more complex for the synthesis of C_{2+} products, as there might be more than one kinetically controlled step, including the bonding between diversified active intermediates. Uneven reactive interfaces and non-uniform active centers in conventional heterogeneous catalysts further aggravate these issues and interfere not only in in-depth research studies on the intrinsic mechanisms of catalytic processes but also in the rational design of catalysts for selective synthesis of specific products with higher efficiency. Fortunately, SACs have provided opportunities for disentangling the labyrinthine system.

3 Single-atom catalysis in typical CO_2 conversion routes

3.1 CO_2 conversion toward C_1 products

3.1.1 Thermochemical reduction. It has already been established that a frontier academic research hotspot focuses on CO_2 chemistry by applying CO_2 reduction with hydrogen to produce a variety of valuable chemicals with the input of thermal energy. Although the economy of large-scale

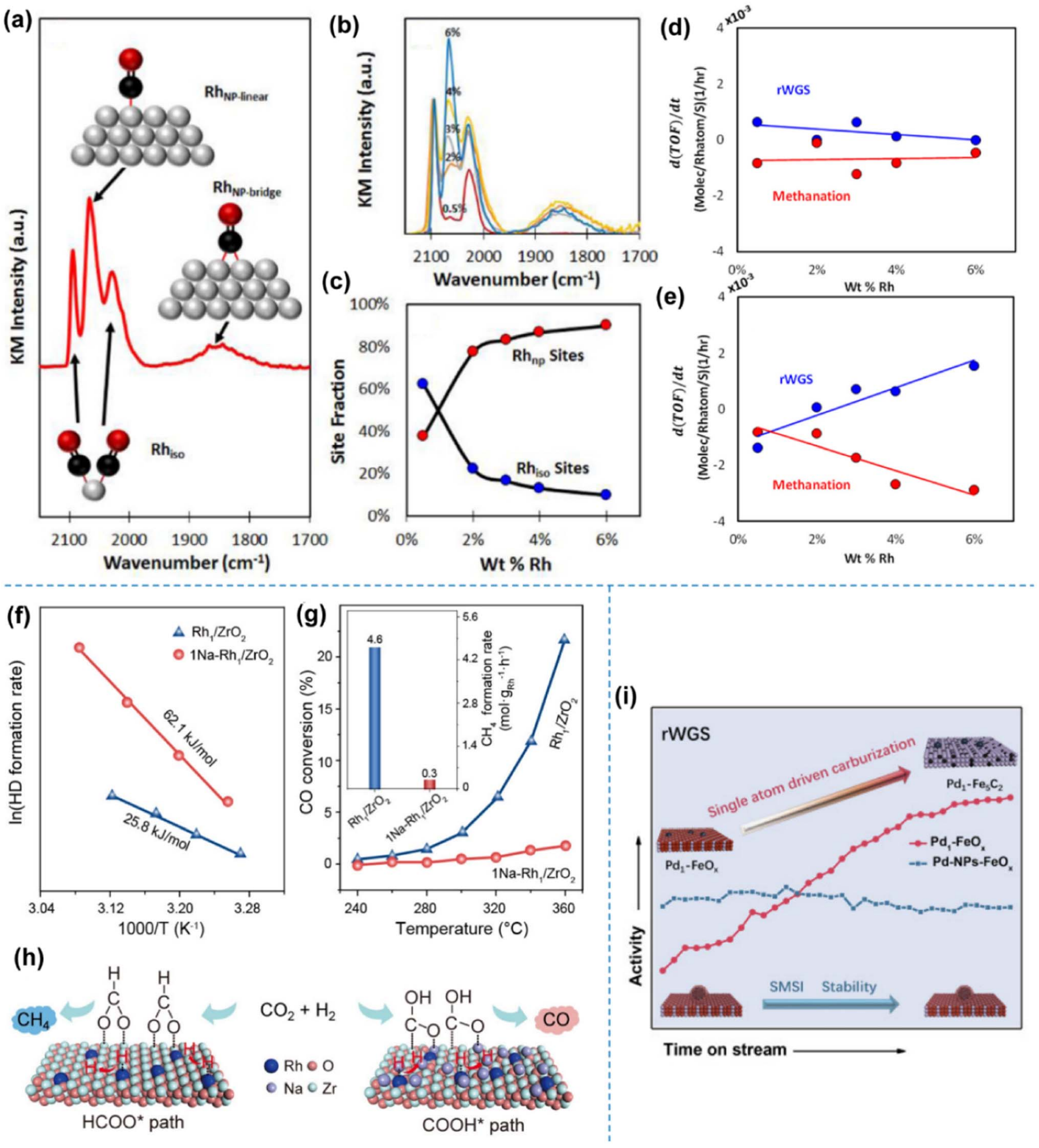

Fig. 8 (a) DRIFT spectrum obtained from a saturated layer of CO adsorbed at 300 K on 4% Rh/TiO_2. Insets show ball-and-stick models of the assigned vibrational modes. (b) DRIFT spectra of CO at all five weight loadings of Rh/TiO_2 catalysts. (c) Site fraction (%) of isolated (Rh_{iso}) and nanoparticle-based Rh sites (Rh_{NP}). Rate of TOF change (d(TOF)/d*t*) for both reaction pathways as a function of wt% Rh measured at 473 K and a feed ratio of (d) 0.25 $CO_2 : H_2$ and (e) 10 $CO_2 : H_2$.[79] (f) Arrhenius plots of Rh_1/ZrO_2 and $1Na–Rh_1/ZrO_2$ in the H_2-D_2 exchange reaction. (g) Catalytic performance of Rh_1/ZrO_2 and $1Na–Rh_1/ZrO_2$ in CO hydrogenation. (h) A schematic illustration of the regulation of $Rh_1–ZrO_2$ cooperativity by Na ions for selectivity tuning.[85] (i) Schematic of boosting CO_2 conversion to CO over $Pd_1–FeO_x$ *via* a SA driven carburization process.[86] Reproduced from ref. 79, 85 and 86 with permission from American Chemical Society, Wiley and Elsevier, copyright 2015, 2022, 2022.

deployment is still arguable due to the current insufficient efficiency of energy transformation and lack of a low-cost, massive, clean hydrogen supply (*e.g.*, from electrolysis and photolysis of water),[12] thermochemical routes are of great interest because of not only the more mature and solid industrial fundaments, but also their potential capability to directly synthesize different types of products especially involving complex C–C couplings.[7] There have been fruitful results for the production of valuable chemicals, *e.g.*, carbon monoxide (CO),[55,56] organic oxygenates,[57–64] and hydrocarbons[65–73] with the carbon number in a wide range of C_1–C_{11+} through processes of thermochemical CO_2 hydrogenation, several of which have even been advancing to the industrial stage,[72,74,75] suggesting a promising prospect of commercial application.[76] On the other hand, thermochemical CO_2 hydrogenation might also provide a feasible approach for the storage of hydrogen energy, in favor of the extended utilization of renewable resources.[8]

While conventional metal catalysts have realized plenty of catalytic processes at the expense of a harsh operating temperature and/or pressure as well as the high cost of precious metals, the utilization of SACs might become a powerful weapon to cope with the severe challenges in terms of energy cost and atom efficiency, and be expected to contribute to the higher selectivity of specific products due to their unique chemical properties. Herein, the thermochemical hydrogenation of CO_2 into valuable products including CO, CH_4, typical organic oxygenates, formic acid (HCOOH)/formate, methanol (MeOH) and ethanol (EtOH) by SACs will be discussed in the following section and critical scientific problems will be also summarized based on recent progress.

3.1.1.1 Carbon monoxide and methane. CO, an important platform chemical resource in industry for the production of a variety of valuable organic compounds, can be obtained *via* the well-known reverse water gas shift reaction (RWGS) from CO_2 and H_2. As a typical endothermic reaction (Fig. 4), RWGS would benefit from a relatively high operating temperature (usually above 673 K). Side reactions, especially methanation, however, might be also enhanced under such operating conditions, leading to a lowered CO yield and limited practical application. The competitive adsorption and activation of H_2 and CO_x molecules might play a vital role in the eventual selectivity of methane and CO, which could be adjusted by using the distinct properties of SACs.

Kwak *et al.* studied the activity of palladium and ruthenium-based SACs in CO_2 hydrogenation, taking support and particle size effects, respectively, into consideration.[77,78] As for Pd-based catalysts, the temperature programmed surface reaction (TPSR) and scanning transmission electron microscopy (STEM) experiments were used to show the disparate reactivity patterns of Pd on different supports (Al_2O_3 and carbon nanotubes) in an atomic dispersion and the morphology of traditional 3D clusters, respectively, under CO_2 hydrogenation. The morphology of Ru, on the other hand, was controlled by varying the loading on the same Al_2O_3 support, as also investigated by the STEM technique. In both studies, the shift of product distribution from CH_4 to CO was found in both systems when SA sites were dominant, although the feature of supports also played a critical role. Matsubu *et al.* applied diffuse reflectance infrared Fourier transform spectroscopy (DRIFTS) with CO as the probe molecule to quantify the fraction of isolated Rh sites (Rh_{iso}) and Rh sites (Rh_{NP}) on the surface of Rh NPs for a series of TiO_2 supported rhodium SACs.[79] Strong correlations were observed between the turnover frequency (TOF) of RWGS and the fraction of Rh_{iso}, and also between the TOF of methanation and the fraction of Rh_{NP} sites (Fig. 8a–e). The changing activity in a long-term operation could also be rationalized by a reaction condition-induced disintegration of Rh_{NP} into Rh_{iso}. This work provided a preliminary understanding of distinct catalytic behaviors between isolated atoms and nanoparticles for competing parallel reaction pathways. A similar dynamic change of SAC local structures in response to various redox conditions was also revealed by Tang *et al.* with more details through a combination of theoretical and experimental studies.[80] *Operando* studies showed that the single Rh atoms on TiO_2 could adapt their structures to the reaction atmosphere, and the first-principles modeling showed that the substitutional structure for the Rh atom over $Rh_1@TiO_{2-2x}$ was not catalytically active due to the strong adsorption energy of hydrogen on Rh that prevented CO_2 adsorption, indicating that the active site for Rh SAC on TiO_2 in the case of the RWGS reaction was the supported Rh_1/TiO_{2-x} site rather than the substitutional sites. This type of structural evolution could also be extended to various metals on supports for other redox reactions,[81–84] for which deeper insights have been gained with the advances in *operando* characterization techniques and modeling calculation. Li *et al.*, on the other hand, reported an alkali-promoted rhodium SAC for CO_2 hydrogenation.[85] The introduction of alkali ions (*e.g.*, Na) enables efficient switching of the reaction products from nearly 100% CH_4 to above 99% CO in a wide temperature range (513–713 K) with high activity and long-term stability at 573 K (Fig. 8f–h). The complete inhibition of deep hydrogenation of the CO intermediate products to CH_4 could be attributed to the significantly higher apparent activation energy and facilitated CO desorption over the Na-doped SAC by performing control experiments of H_2-D_2 exchange and CO hydrogenation reactions. Moreover, the intermediate change from formate to carboxy using alkali ions was the key to favorable CO formation, as unveiled by *in situ* spectroscopy and theoretical calculations. The improved stability also benefited from the addition of alkali ions due to the reinforced electronic interaction between isolated Rh sites and ZrO_2 supports. Notably, noble metal SAs could not only serve as active sites for the dissociation of CO_2 to CO, but could also surprisingly promote the dynamic evolution of the support, which in turn enhances the catalytic performance under specific reaction conditions. Du *et al.* observed such a dynamic evolution driven by Pd SAs over a Pd_1–FeO_x catalyst during the RWGS reaction[86] (Fig. 8i). The introduction of Pd atoms significantly changed the reduction and carburization behaviors of the FeO_x support *via* inducing the formation of oxygen vacancies. The atomically dispersed Pd species enabled continuous H_2 dissociation with a lower formation energy of oxygen vacancies, thereby endowing the FeO_x support with a deeper reduction state, facilitating further carburization with the CO product. In contrast, Pd NPs tended to exhibit a strong metal–support interaction (SMSI) with the FeO_x support as shown by the remarkable overlayers on the metal surface. Such a SMSI inhibited deep reduction and further carburization, resulting in an inferior activity compared with that of Pd_1–FeO_x, since iron carbide was believed to be a critical component for lowering the activation energy of CO_2 conversion to CO.

In addition, SACs based on non-noble metals have been also applied for tuning the activity and selectivity in RWGS. Millet *et al.* prepared a series of Ni SACs with MgO as the support by a solid solution approach.[87] Low-coordinated Ni sites on the surface of MgO predominated among the Ni species in the SACs, as predicted by hybrid-functional calculations. The isolated Ni atoms were active for the RWGS but were incapable of propelling deep hydrogenation, while Ni clusters might lead to the formation of CH_4 in contrast. The substitution of Mg atoms by Ni atoms on the surface of oxide was found to not only reduce the strength of CO binding at low-coordinated sites but also promote H_2 dissociation, so that the CO formation rates could show a positive correlation with the concentration of Ni on the surface. Liang *et al.* fabricated a cobalt-based SAC comprising isolated Co sites bonded to SBA-15 by the atomic layer deposition (ALD) technique, utilizing which 99% CO selectivity and near-equilibrium conversion of CO_2 were maintained for a 500-hour RWGS reaction at 873 K.[88] Co sites remained in a cationic state which was stabilized by strong Co–O–Si bonds, contributing to the H-assisted dissociation of CO_2 that was distinct from the commonly reported mechanisms. Moreover, it was found that the CO products were generated along with the shifting of Co sites between the tetrahedral field and the octahedral field, by which the whole catalytic cycle was driven. A similar result was reported in a recent study by Li *et al.*[89] The cobalt-based SAC synthesized by anchoring 4% Co atoms onto the nitrogen-doped carbon supports (Co–N–C) achieved nearly 100% CO selectivity and 52.4% CO_2 conversion at 773 K, while the 20%-Co-loading catalyst with mostly Co NPs favored the formation of CH_4. The H-assisted dissociation of CO_2 was also proposed to be responsible for the excellent performance over the Co SAC *via* the COOH* intermediate, whereas direct dissociation took place on Co NPs. However, it might be quite different in a case where other types of active sites were introduced. In a study by Dostagir *et al.*, the Co SA sites co-existed with oxygen vacancy sites over a ZrO_2-supported Co SAC, catalyzing CO_2 hydrogenation to produce CO with more than 95% selectivity.[90] *Operando* DRIFTS analysis showed that formate was the key intermediate, whose stabilization was achieved by the generation of oxygen vacancies derived from the synergy between Co and Zr. The subsequent decomposition of formate led to the formation of CO instead of methanol and methane by deep hydrogenation, since the adsorption of CO on active sites was less favorable than that of CO_2. Furthermore, Jiang *et al.* reported a molybdenum-based SAC for CO_2 hydrogenation to CO with a selectivity of almost 100%.[91] Single Mo atoms with a MoN_3 moiety supported by nitrogen-doped carbon enabled remarkable CO_2 adsorption and facile CO desorption on the basis of the calculated transition state energy. And the formation of CO was considered through a direct dissociation path rather than a H-assisted path as mentioned above.

Synthesis of CH_4 from thermochemical CO_2 hydrogenation, namely the CO_2 methanation (Sabatier) reaction, is another important pathway for CO_2 chemical conversion. In contrast to RWGS, methanation is a highly exothermic process, suggesting an advantageous operating range at lower temperature regarding thermodynamics (Fig. 4). In terms of kinetics, nevertheless, higher temperature is always needed to ensure significant reaction efficiency. In general, the methanation reaction can either go through a direct hydrogenation step in the absence of the CO intermediate, or undergo an indirect step with CO as 'bridge' species. Within a certain temperature, RWGS is believed to be a parallel reaction to the methanation reaction over a variety of catalytic systems just as mentioned above. Therefore, it might be a good angle to inhibit RWGS or enhance the deep hydrogenation of CO for higher yield of CH_4 from thermochemical CO_2 hydrogenation.[55,69,92] Indeed, the ostensibly different selectivities over various metal catalysts might be rationalized by the inherent kinetic differences, such as the activation and ad/de-sorption energy in each reaction pathway. With both theoretical and experimental insights, Chen *et al.* correlated the selectivity of CO_2 hydrogenation with the distinct activation energy between the dissociation barrier and the desorption of metal carbonyls over supported metal catalysts.[93] They concluded that decreasing the coordination number of metal sites to SA structures could contribute to the suppressed carbonyl dissociation with facile CO desorption, leading to increased CO formation, since the C–O bond scission of the main intermediates was considered as the rate-limiting step in CO_2 hydrogenation (Fig. 9). Correspondingly, the design of methanation catalysts could also be inspired by this descriptor regarding activation energy.

As reported by Kwak *et al.*, the tendency of methanation in CO_2 hydrogenation was enhanced with the increase in metal loading, in which the atomically dispersed metal centers were not the dominant species, suggesting that the SAC might not be suitable for methanation, although specific conditions would make some differences.[77,78] A similar view was held by Guo *et al.*,[418] as proposed in a study on low-temperature CO_2 methanation over a CeO_2-supported Ru SAC, nanoclusters (NCs), and NPs. The NCs with a size of 1.2 nm showed superior activity in comparison with the SAC and NPs, as well as 98–100% CH_4 selectivity at 463 K. *In situ* measurements demonstrated that CH_4 was formed dominantly *via* the CO route with metal carbonyls as the key intermediates, and Ce^{3+}–OH sites and Ru sites located at the metal–support interfaces were active for CO_2 dissociation and carbonyl hydrogenation, respectively. The strongest metal–support interaction and hydrogen spillover were present over the SAC and Ru NPs, respectively, leading to the corresponding suppression of metal carbonyl activation and the H_2O removal on the support surfaces. In contrast, there was a balance between the two effects over NCs, which might be the key parameter to optimize their catalytic performance.

Recently, on the other hand, research studies have confirmed that the preferential synthesis of CH_4 over SACs is also feasible in certain specific catalytic systems, breaking through the conventional understanding to some extent. In the work by Li *et al.*, Rh SAs supported on ZrO_2 without alkali promotor modification offered nearly 100% CH_4 selectivity in CO_2 hydrogenation.[85] The formation of CH_4 was through a HCOO* intermediate route, and facilitated by the uninhibited hydrogen activation with the help of Rh sites in the low valence

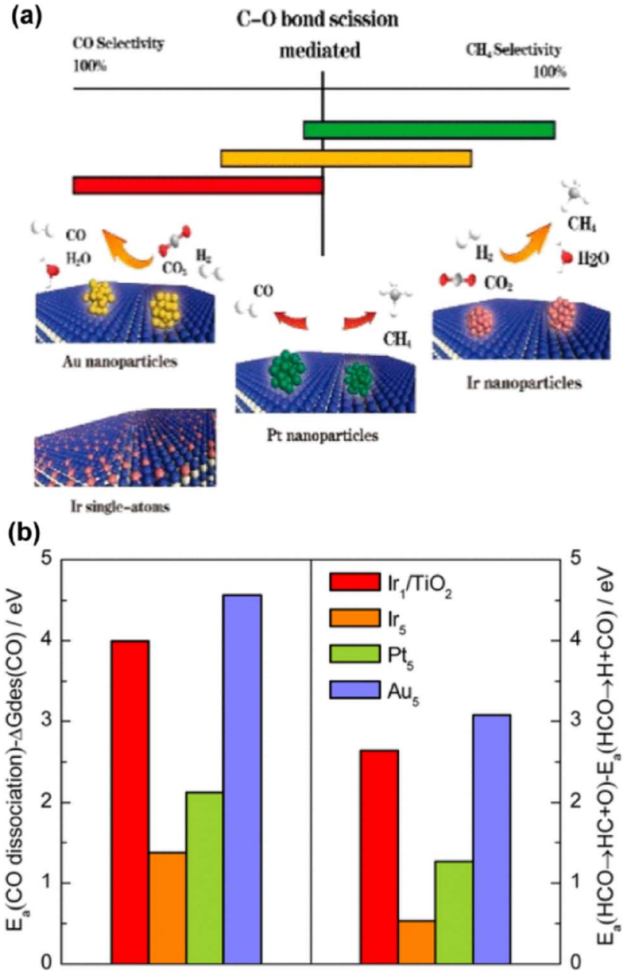

Fig. 9 (a) Correlation between the C–O bond scission and the selectivity of CO_2 hydrogenation. (b) (left) Difference between activation energies E_a for CO dissociation and desorption free energies of CO. (right) Difference in activation energies between HCO → HC + O and HCO → H + CO on PR1-Ir_1/TiO_2 (Ir_1/TiO_2) and stepped Ir (Ir_5), Pt (Pt_5), and Au (Au_5) surfaces.[93] Reproduced from ref. 93 with permission from American Chemical Society, copyright 2017.

state. This performance would be changed into a higher CO selectivity once alkali ions were introduced, since the Rh atomic sites were rendered into an electron deficient state with less H_2 activation capability and weakened CO adsorption. By regulating the electronic state of single metal atoms *via* tuning the interaction between metals and supports, the catalytic properties of SACs might be significantly changed and the corresponding performance would be quite different. Fan *et al.* used porous hexagonal boron nitride (pBN) to immobilize Ru in the atomic dispersion and obtained an enhanced catalytic activity of 1.86 mmol CO_2 per g_{cat} per s and CH_4 selectivity up to 93.5% for CO_2 methanation at 623 K and 1.0 MPa.[94] A vacuum filtration process allowed the Ru precursor to transform quickly into atomic Ru restricted onto the defects *via* B, N coordination. The Ru sites in a valence state reduced by interaction with B and N on the surface of supports remarkably lowered the maximum energy barrier from 1.56 to 1.07 eV of the consecutive hydrogenation process, contributing to the improved CH_4 production rate at an atomic scale (Fig. 10). Thus, it should be possible to extend the practical application of SACs into methanation for higher metal atom utilization efficiency, in case that further efforts are devoted for this research aspect.

Organic oxygenates such as formic acid (formate), methanol, ethanol and higher alcohols are a group of valuable compounds that are possible to be produced from CO_2 hydrogenation.[57,58,95,96] The controlled formation of organic oxygenates always needs an accurately regulated hydrogenation process to avoid either the generation of CO due to insufficient capability toward adsorption and hydrogenation of intermediates or the generation of CH_4 due to excessive hydrogenation. Complicated procedures involving adsorption, reaction and desorption of various reactants, intermediates and products make it a challenging task to develop catalysts with high efficiency for directional catalytic hydrogenation of CO_2 into organic oxygenates, in which SACs with specific structures could take advantage relying on their distinct advantages in not only high atom utilization but also their unique chemical properties.

3.1.1.2 *Formic acid and formate.* Formic acid is regarded as an important hydrogen storage medium, the synthesis of which might be of great significance in the promoted application of renewable and clean energy.[96–98] Fruitful results have been achieved for CO_2 hydrogenation to formic acid or formate *via* homogeneous metal complexes in basic media,[99] while the development of heterogeneous catalysts is more and more appealing due to the practicality in mass production. At this moment, SACs are expected to offer a unique opportunity for the transition from homogeneous to heterogeneous systems.[100] Shao *et al.* designed a porous organic polymer with aminopyridine functionalities to fabricate a stable Ir SAC for liquid-phase hydrogenation of CO_2 to formate with an extremely high turnover number of up to 25 135, comparable with that of homogeneous systems (Fig. 11).[101] The chemical structure of the Ir SA active site was identified to resemble that of a homogeneous mononuclear Ir pincer complex catalyst. Hence, the catalytic mechanism was supposed to be quite similar to that over a homogeneous Ir catalyst with this Ir-based SAC, *i.e.*, (i) Ir SA sites encountered the CO_2 reactant, (ii) the electron transfer from the metal hydride to CO_2 imposed a bend of 135° of the O–C–O unit and an elongation from 1.18 to 1.23 Å of the corresponding C–O bond, with an exothermic binding energy of 0.14 eV, (iii) then this intermediate was readily transferred to HCOO– by the rotation of its C–O bond to allow binding at the Ir site, with an exothermic energy as high as 0.70 eV and a barrier of only 0.07 eV, (iv) the amide-H near the other dangling O-end of the HCOO– intermediate assisted the preliminary formation of HCOOH– by bonding to the O atom, which was induced by the formation of a six-member ring involving an Ir atom in the AP-POP framework, and (v) this initial HCOOH– promoted further H_2 activation and dissociation on the site with the simultaneous transfer of H from the formic acid to the amide group (with a 1.00 eV barrier) to generate the final HCOOH product. The energy profile of the catalytic mechanism demonstrated the effectiveness of the Ir SAC and a quite similar catalytic mechanism that occurred during homogeneous

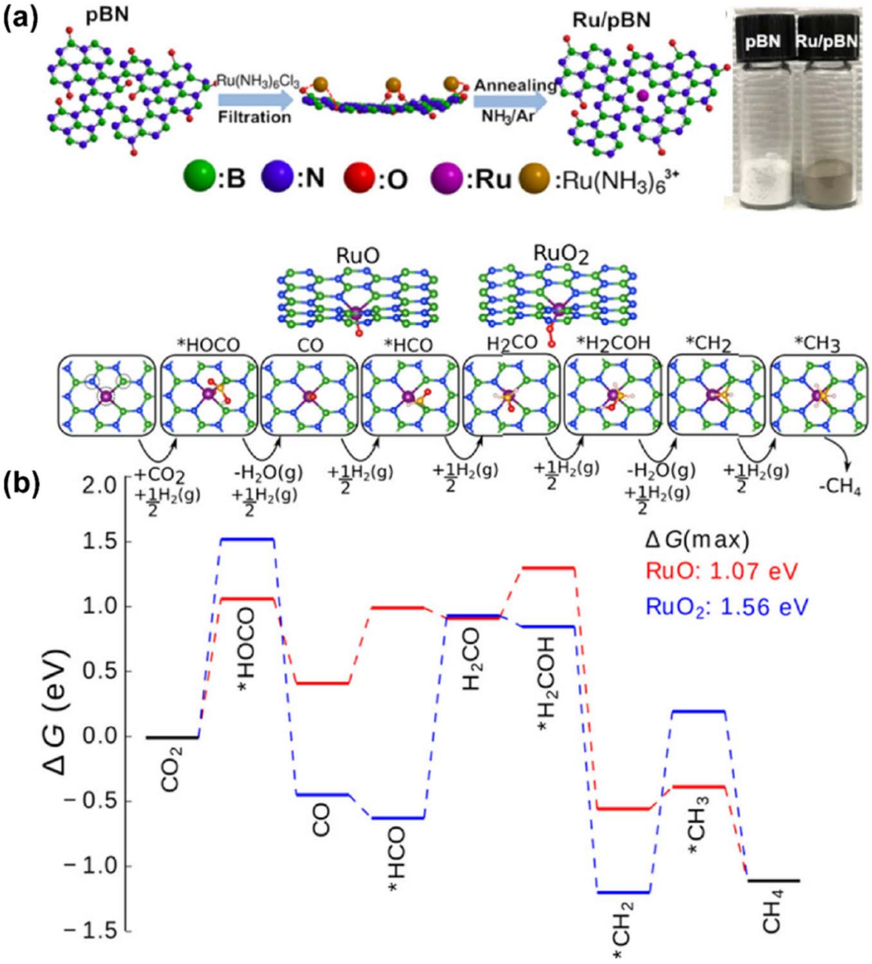

Fig. 10 (a) Schematic illustration for fabricating Ru/pBN-*x*F assisted by vacuum filtration drying. (b) Reaction free-energy diagram for CO_2 hydrogenation at 623 K.[94] Reproduced from ref. 94 with permission from American Chemical Society, copyright 2019.

catalysis, and thereby a concept of quasi-homogeneous catalysis was assigned to this system for the inherent associations between the homo- and hetero-catalytic processes. This result further suggested the great potential of SACs in CO_2 conversion to formate. Indeed, quite a few attempts have been made for the fabrication of heterogeneous catalysts by mimicking the previous homogeneous systems *via* introducing metal–organic complexes into a rigid framework, such as CTFs, MOFs and other organic polymers, in which electron-donating functional groups comprising N, O, and P moieties were commonly used as building blocks to enhance the electron density at metal SAs.[102–107] As a result, such SACs always delivered high TONs/TOFs, whereas the demand for enhancing the stability of metal SAs to overcome inferior recyclability is still urgent. For this, substantial efforts have been made on the structural engineering of the exquisitely designed catalysts. Moreover, there have been a few studies exploring the possibility of preparing materials without organic ligands. For instance, Mori *et al.* developed a stable and well-defined Ru SAC on the surface of a layered double hydroxide (LDH) for efficient selective hydrogenation of CO_2 to formic acid under mild reaction conditions (2.0 MPa, 373 K).[108] An active electron-rich Ru center was established by using triads of basic hydroxyl ligands at a particular location, with the electron-donating feature. A strong electronic metal–support interaction (EMSI) present between the Ru atoms and basic supports was evaluated by XPS spectroscopy and could be well correlated with the catalytic activity. By adjusting the type of metal ions and corresponding ratio in LDH, the CO_2 adsorption capacity in the vicinity of the Ru center could be also tuned. The catalytic performance would be also improved with higher CO_2 concentration on the surface. Wang *et al.* designed a solid micellar Ru SAC for efficient and stable water-free CO_2 hydrogenation to formate under mild reaction conditions,[109] directly obtaining concentrated formate solutions up to 4 mol L^{-1} in tertiary amines. The Ru SAC sites were stabilized by using the hexadecyl trimethyl ammonium (CTA^+) surfactant in the pores of the MCM-41 support, forming a solid micelle structure during preparation. By DFT modelling, the reaction was found to proceed *via* heterolytic hydrogen splitting, forming metal hydride species and subsequent hydride transfer over low-coordinated Ru(III).

In addition to the investigations into the design of various active SACs based on the vital metal–support interaction, the interaction between active metal species has also been taken into account especially in the case where metal loading is high enough to reduce the distance between separated sites to some extent. Indeed, the synergistic effect of active metal sites has been reported and proposed to play a critical role in CO_2 hydrogenation. Ren and co-workers reported their progress on the utilization of Pd SACs for CO_2 hydrogenation to formate.[110,111] One of their studies used a highly active dual single-Pd-atom catalyst with a microporous layered 2,6-pyridinedicarbonitrile-derived covalent triazine framework (2,6-DCP-CTF) as the support, efficiently converting CO_2 to formate

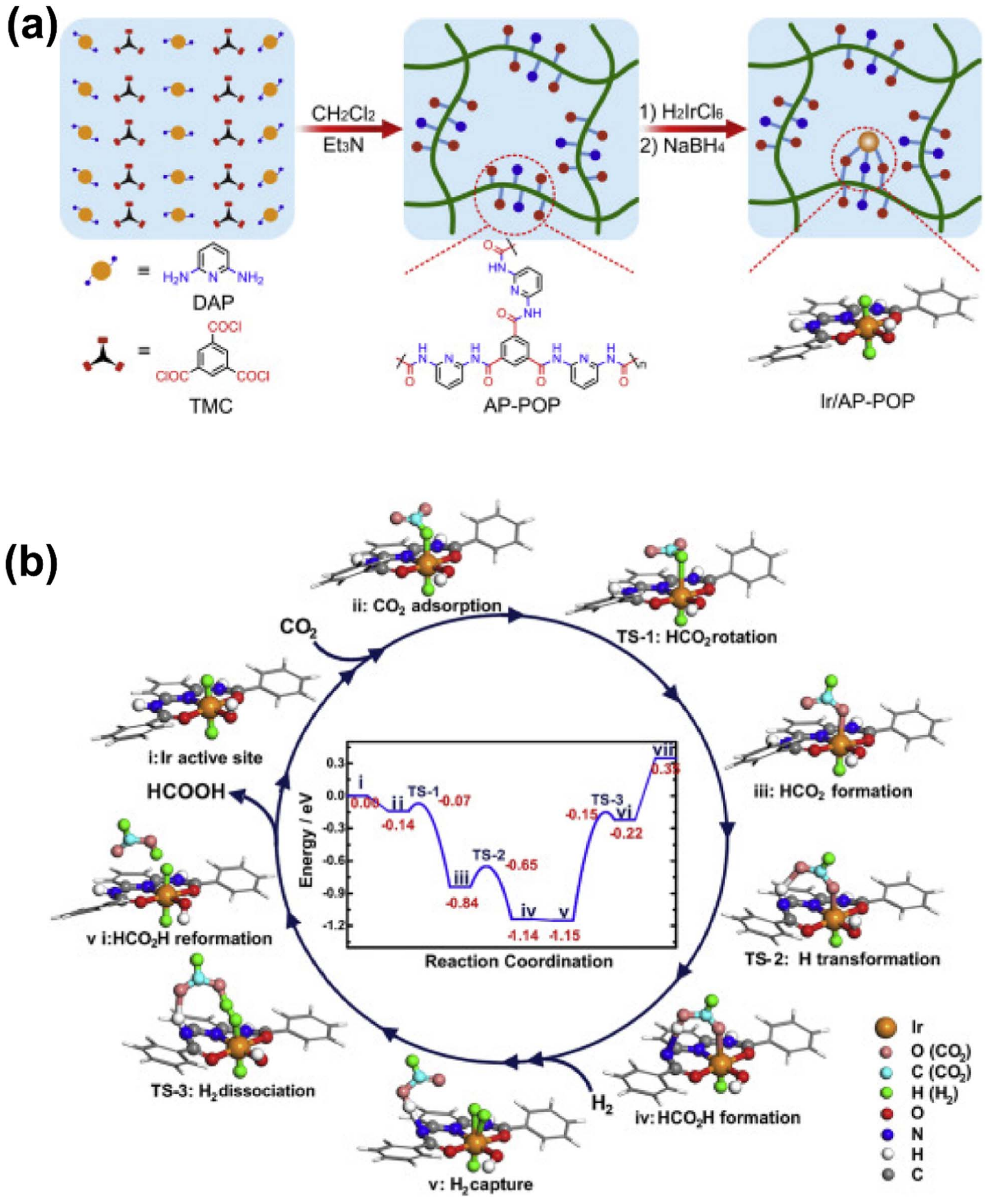

Fig. 11 (a) Schematic illustration of the synthesis of the Ir/AP-POP SAC. (b) The proposed reaction mechanism for CO_2 hydrogenation over the oppositely H bonded Ir SA active sites.[101] Reproduced from ref. 101 with permission from Elsevier, copyright 2019.

under ambient conditions with a turnover frequency (TOF) as high as 13.46 h^{-1}.[110] The microporous structures could enrich the concentration of reactants, while the dual Pd atoms within a nitrogen-rich environment exhibited a much lower barrier for this reaction than the Pd SA, and a rich nitrogen environment could further improve the intrinsic activity of Pd. A ternary

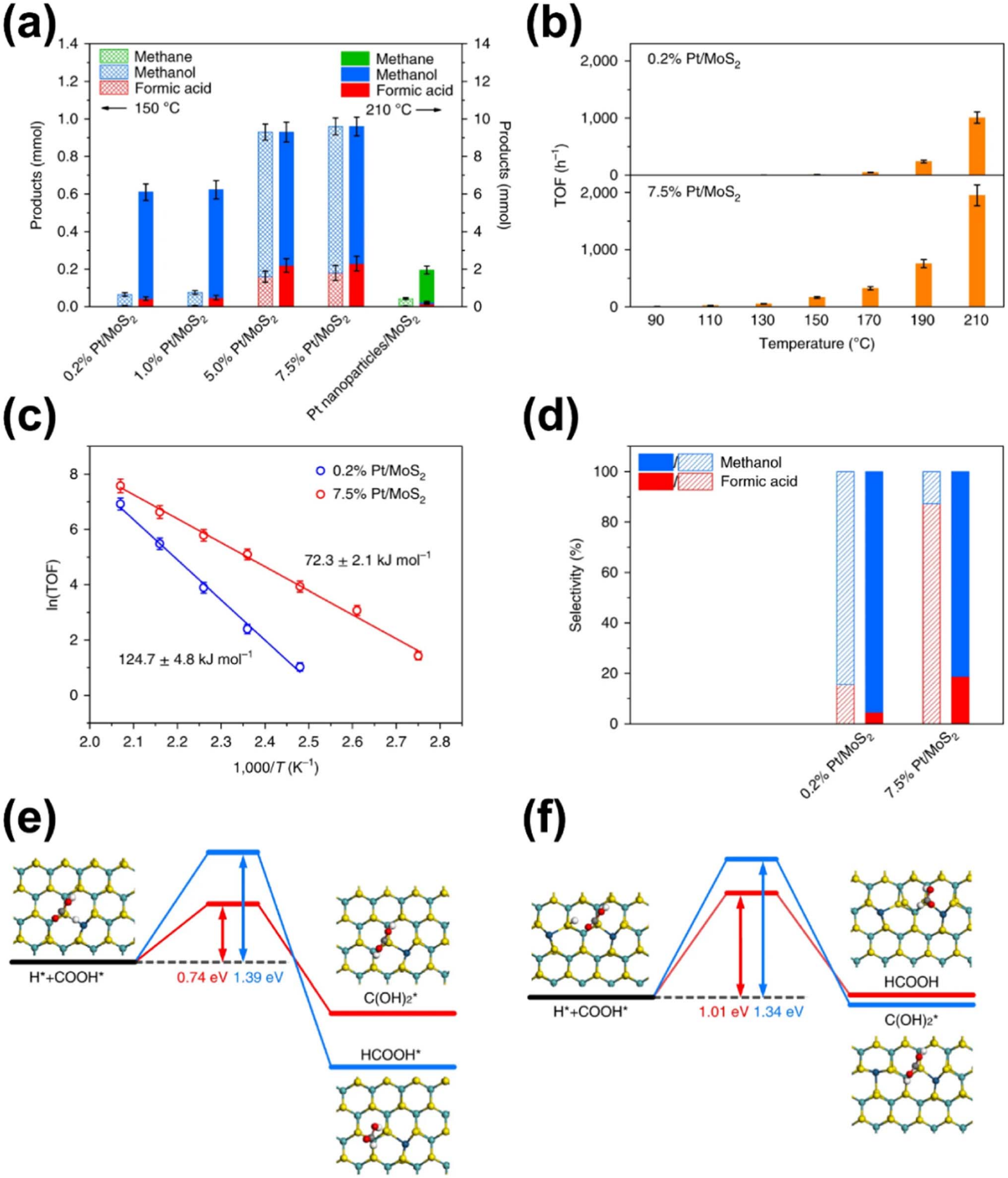

Fig. 12 (a) Comparison of products obtained by using atomically dispersed Pt/MoS_2 with different Pt loadings and Pt nanoparticles/MoS_2. (b) Comparison of TOFs with 0.2% Pt/MoS_2 and 7.5% Pt/MoS_2 as the catalyst at different temperatures. (c) The Arrhenius plots of 0.2% Pt/MoS_2 and 7.5% Pt/MoS_2. (d) Comparison of selectivity of products obtained by using 0.2% Pt/MoS_2 and 7.5% Pt/MoS_2 as catalysts at different ratios of CO_2 to H_2 after 3 h. Steps for the addition of a H atom to COOH* over (e) Pt_1/MoS_2 and (f) Pt_{2iii}/MoS_2, respectively.[112] Reproduced from ref. 112 with permission from Springer Nature, copyright 2018.

synergetic effect was shown to be responsible for the outstanding performance, as confirmed by modelling calculations. They also developed a synergistic structure with Pd SAs and NPs on 2,6-DCP-CTF as an efficient active site for CO_2 hydrogenation to formate.[111] The Pd SAs were believed to be in charge of CO_2 activation, while the Pd NPs were more likely to contribute to hydrogen dissociation based on theoretical calculations. Therefore, compared with the catalysts mainly comprising Pd SAs or NPs, this hybrid catalyst presented a better balance between the two key steps in CO_2 hydrogenation, leading to the improved catalytic activity. By further optimizing the ratio of Pd SAs to Pd NPs, a formate formation rate of 3.66 mol mol_{Pd}^{-1} h^{-1} could be obtained under ambient conditions (303 K, 0.1 MPa). Li *et al.* explored the activity of CO_2 hydrogenation dependent on the interaction between two neighboring Pt monomers over a Pt/MoS_2 SAC.[112] As indicated, the majority of Pt monomers were in the isolated state over the 0.2% loading SAC, while the neighboring Pt monomers predominated in the Pt species over SAC with a high Pt loading up to 7.5% in contrast. As for the catalytic performance, the SAC with neighboring Pt monomers demonstrated a significantly lower reaction barrier for CO_2 hydrogenation, and a stepwise reaction path *via* a formic acid intermediate rather than $C(OH)_2^*$ was demonstrated, leading to relatively high selectivity of formic acid. In contrast, the SAC with isolated Pt monomers favored a path with the absence of formic acid formation and higher activation energy (Fig. 12). These results clearly indicated the importance of the synergetic effect derived from the interaction between active metal sites.

3.1.1.3 Methanol. As one of the simplest liquid energy storage compounds and versatile C_1 building blocks, methanol has been appealing in both chemical and energy sectors over the past few decades, whose production from CO_2 hydrogenation has been considered to be a solution for excessive CO_2 emission and contribute to 'carbon neutrality'.[57,113–116] The initial studies on the methanol synthesis from CO_2 were originated from the conversion of syngas consisting of CO, CO_2 and H_2, which is mainly acquired through coal gasification, natural gas reforming and biomass transformation. The commercial production of methanol from CO_2 is generally realized with the utilization of copper-based catalysts, particularly those based on copper, zinc oxide and alumina ($Cu/ZnO/Al_2O_3$).[117,118] However, the efficiency of CO_2 conversion is still severely limited by thermodynamics (Fig. 4) under the specific operation conditions (503–573 K and 50–75 bar) applied with the standard $Cu/ZnO/Al_2O_3$. Thus, great efforts have been devoted for the modification of conventional Cu-based catalysts, as well as designing new catalysts containing entirely distinct compositions such as noble metals and reducible metal oxides.[57,63,119–121] Meanwhile, homogeneous hydrogenation of CO_2 into methanol undergoes a renaissance due to its high activity at low temperature,[122] which suggests the promising potential of SACs similar to that of homogeneous catalysts.

Recent studies have unveiled that SAs could play a critical role in Cu-based catalysts as either active components or promoters. Zhao *et al.* reported a Cu-based catalyst Cu/ZrO_2 with isolated active copper sites for methanol synthesis from CO_2 hydrogenation.[123] A strong dependence of CO_2 hydrogenation activity and selectivity on the nature of surface copper species was revealed. The undercoordinated cationic Cu_1–O_3 species, accumulating on the catalyst surface, were considered to form stable active sites and be in charge of high selectivity to MeOH (100%) during the catalysis process at 453 K. The pathway with HCOO* as the key intermediate was believed to be the most viable route for CO_2 hydrogenation on the isolated Cu_1–O_3 active sites, as the generation of HCOO* was achieved through the reaction between activated CO_2 and dissociative hydrogen formed over Cu SAs with the help of nearby oxygen atoms. In contrast, small copper NCs and NPs favored CO formation *via* RWGS, while larger particles exhibited little activity at low temperature (Fig. 13). Wu *et al.* used a Cu-based SAC (Cu/ZnO) to study the effect of introduced water content on the methanol synthesis from CO_2 hydrogenation.[124] They found that introduced water could act as a bridge between H atoms and CO_2 or intermediates, facilitating the transformation of COOH* and CH_2O*. The enhanced activity induced the generation of more water to react with CO *via* the water–gas shift reaction, resulting in an increase in methanol selectivity. With the introduction of optimal-content of water, a methanol selectivity of 99.1% could be obtained, while the CO_2 conversion exhibited a volcano-type curve with a peak value of 4.9%. Yang *et al.* developed a Cu-based catalyst with atomically dispersed Zn on a ZrO_2 support *via* a double-nozzle flame spray pyrolysis (DFSP) method.[60] Dynamic structural evolution of Zn species analyzed by *operando* XAS showed that atomic Zn sites were formed under specific reaction conditions *via* the strong interaction between the highly dispersed ZnO clusters and ZrO_2 support. The *operando* experiments as well as modeling calculations revealed that this unique Zn species promoted the selective formation of methoxy and subsequently methanol instead of decomposition to CO due to the stabilized formate intermediate and decreased hydrogen activation energy. As a result, a superior performance could be achieved over this SAC in comparison with that over the generally accepted active Cu–ZnO interface, while large and independent ZnO nanoparticles exhibited the poorest performance due to the absence of promotion of both hydrogen activation and intermediate stabilization. Furthermore, Wu *et al.* performed a systematic theoretical study on the mechanistic nature and catalytic pathways of Zn SAs and NCs on the surface of Zn/Cu alloy catalysts, in which surface oxidation was proved to make a great difference.[125] The Zn SAs were more active than the Zn NCs initially with more difficulty in subsequent surface oxidation under specific reaction conditions. After catalyst surface oxidation during CO_2 decomposition, more active species were switched to oxidized Zn NCs from Zn SAs. Further analyses show that this effect of surface oxidation could be attributed to not only the occupation of the strongest binding sites at the center of Zn NCs by O atoms, but also the higher positive charge and work function on the oxidized surface. The former made oxygenate intermediates adsorb on the Zn/Cu interface with moderate binding for further hydrogenation, while the latter directly promoted the hydrogenation of oxygenate intermediates.

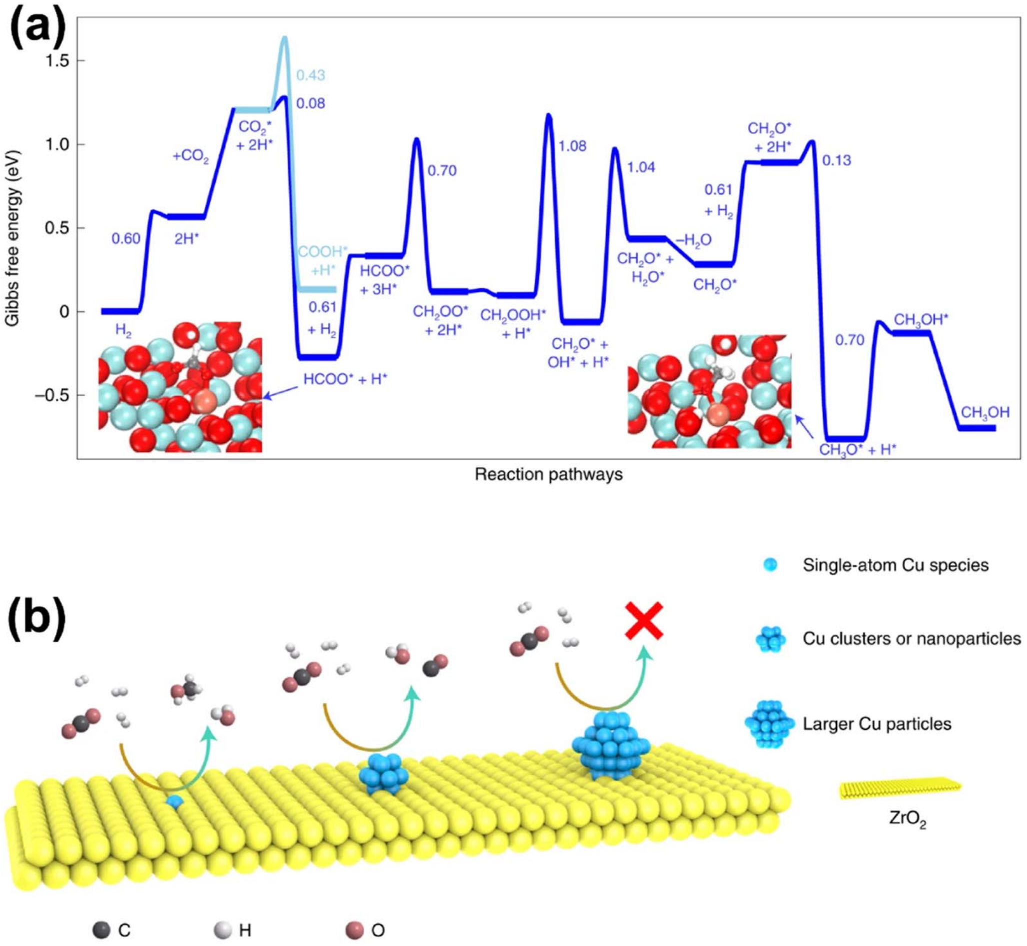

Fig. 13 (a) Gibbs free-energy profile of CO_2 hydrogenation to CH_3OH/CO. (b) Schematic diagram for the CO_2 hydrogenation reaction on different types of copper species.[123] Reproduced from ref. 123 with permission from Springer Nature, copyright 2022.

Apart from Cu-based catalysts, SACs based on noble metals for CO_2 hydrogenation to methanol have also attracted considerable attention due to their superior hydrogen activation capability at relatively lower temperature. Chen *et al.* reported a Pt-based SAC comprising an ensemble of Pt SAs coordinated with oxygen atoms in MIL-101 (Pt_1@MIL), with a turnover frequency (TOF) of 117 h^{-1} and a methanol selectivity of 90.3% in DMF at 3.2 MPa and 423 K for selective CO_2 hydrogenation to methanol, which were much higher than that of Pt_n@MIL with nanocrystals as the major Pt species.[126] In contrast to Pt_n@MIL with COOH* as the intermediate in CO_2 hydrogenation, Pt_1@MIL favored the pathway *via* HCOO* as the key intermediate, leading to a lower activation energy for the enhanced catalytic activity and corresponding higher selectivity toward methanol by suppressing the formation of CO. This research altered the reaction path with the help of a SAC to achieve enhanced performance, whereas some other studies reached similar goals by promoting the kinetics of the key reaction step during CO_2 hydrogenation. Dostagir *et al.* used an In_2O_3 catalyst promoted by single Rh atoms to obtain a high methanol productivity of 1.0 g_{MeOH} h^{-1} $g_{cat}{}^{-1}$ with intrinsic high selectivity over pure In_2O_3.[120] Rh species were atomically dispersed in the In_2O_3 matrix and were stabilized by charge transfer from neighboring In atoms under specific reaction conditions. Rh SAs promoted the dissociation of H_2 and consequent partial reduction of In_2O_3, leading to the formation of more oxygen vacancies on the catalyst surface, as the oxygen vacancies in In_2O_3 were considered to be the key active sites for the adsorption and activation of CO_2. The generation of formate species, a key intermediate in In_2O_3-catalyzed CO_2 hydrogenation, was also propelled by Rh SAs, as verified by DFT calculations regarding the activation barrier.

3.1.1.4 Summary. Despite suffering from relatively rigorous operation conditions, thermochemical hydrogenation processes still benefit from sophisticated equipment, high scalability and versatility. SACs with nearly 100% atomic utilization efficiency not only provide a promising prospect for wider application of noble metals in the effective conversion of CO_2, but also steer the reaction pathway towards exclusive synthesis of valuable products. The distinct electronic and geometric properties derived from specific coordination and interaction with neighboring atoms offer highly active interfaces for activation of CO_2 and stabilization of specific intermediates, thereby propelling the formation of C_1 products.

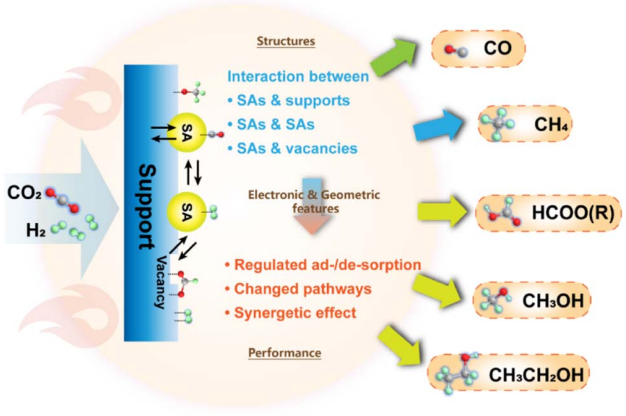

Fig. 14 A brief summary of SAC applications and key scientific problems in thermochemical CO_2 hydrogenation.

Furthermore, the studies on the production of C_{2+} products have also achieved inspiring results with the application of SACs, in which the specific features of SAs in combination with vacancy sites generated from defect engineering are incorporated for realizing C–C coupling in the systems. All these results indicate the potential of SACs in CO_2 thermochemical hydrogenation (Fig. 14).

3.1.2 **Electrochemical catalytic reduction.** Although the thermochemical route has provided certain opportunities for efficient CO_2 conversion, the economy of commercial application of the hydrogenation process is highly dependent on the cost of renewable hydrogen resources.[12] The feed hydrogen is supposed to be produced from water splitting, which could be driven by electrical energy from renewable sources, *e.g.*, wind and solar.[127] This would be also a promising solution for the storage of intermittent and fluctuating renewable energy. Thus, direct electrochemical reduction of CO_2 would demonstrate advantages compared to the thermal hydrogenation process, since it could not only merge electrochemical water splitting and the subsequent hydrogenation into one single process, but also enable the production of specific products in a more flexible way due to its common moderate operation conditions. In order to make it a profitable process for CO_2 electrochemical reduction, many aspects should be taken into account including intelligent electrode design, electrolyte tuning, equipment optimization and so on,[128,129] in which the design and massive production of highly active catalysts are some of the core subjects in both scientific and industrial fields and still challenging so far. With the rapid development of CO_2 electrochemical reduction research in recent years, various metal-based catalysts have been applied, thanks to their intrinsic high electro-conductivity facilitating electron transfer.[130] For further improving the specific activity of metal-based catalysts, SACs have been introduced into some systems due to their nearly 100% utilization of metals and distinct catalytic properties.[47,48,131–136] Herein, we will review the recent progress on the application of SACs in CO_2 electrochemical reduction for the synthesis of CO, CH_4, HCOOH and CH_3OH. The sophisticated design and preparation of SACs and their corresponding influence on the catalytic performance will be the focus for gaining deep insights.

3.1.2.1 Carbon monoxide. With the rapid development of electro-catalysis research over recent years, electrochemical CO_2 reduction has been considered a feasible alternative approach for the production of various chemicals, especially CO which is synthesized traditionally by RWGS *via* a thermal reduction process under harsh conditions.[129] As a reaction with a slightly negative equilibrium reduction potential of circa. −0.10 V *versus* the reversible hydrogen electrode (RHE) and involving two-electron transfer (Fig. 5), the production of CO might be one of the most fundamental and practical processes in electrochemical CO_2 reduction because of its possibly higher selectivity and larger current densities. Over a long period, substantial effort has been devoted to exploring efficient catalysts for reduction of CO_2 to CO. Noble metals like Au, Ag and Pd have been identified as useful catalysts with a high current efficiency and selectivity, but their high cost limits their practical application.[137] To further improve the efficiency of CO_2 reduction to CO and lower the cost to make it a more profitable process, ingenious catalyst design strategies have been developed. The application of SACs is one at the center of attention to overcome the existing complex problems regarding activity and selectivity compared to conventional bulk metal-based catalysts,[138] and this even provides non-noble metals with performance exceeding that of noble metals.[47,130,139]

Given that nickel (Ni) is a relatively low-cost metal commonly used in reduction reactions,[138,141] and inspired by the previous research studies that unveiled the potential of Ni-based molecular catalysts in CO_2 transformation,[142–144] plenty of studies have been devoted for the application of Ni-based SACs in electrochemical CO_2 reduction. Yang and his co-workers (Fig. 15) fabricated a Ni-based SAC containing isolated, high-density, low-valent Ni anchored on a N-doped graphene matrix for CO_2 reduction.[140] Through the combination of *operando* X-ray absorption spectroscopy (XAS) and X-ray photoelectron spectroscopy (XPS) techniques, Ni(I) was identified as the active center, for which the structure evolution during the CO_2 reduction was further illustrated. The active sites had an effect by the delocalization of the unpaired electron in the Ni $3d_{x^2-y^2}$ orbital, and a $CO_2^{\delta-}$ species was formed *via* spontaneous charge transfer from Ni(I) to the carbon 2p orbital in CO_2. In this way, the energy barrier for electrochemical CO_2 reduction was remarkably reduced, leading to a specific current of 350 A g_{cat}^{-1} and turnover frequency of 14 800 h^{-1} at a mild overpotential of 0.61 V with 97% faradaic efficiency (FE) for CO formation. Generally, the preparation methods of SACs have a great effect on the fine structure of active sites, which further determines the catalytic performance. Since the carbon-based supports are always essential for maintaining sufficient electron transfer capability, the kernel task for the fabrication of SACs is embedding the metal SAs into the carbon matrix, for which substantial efforts have been made. One of the recently proposed strategies is using metal organic framework (MOF) materials as precursors.[145,146] The metal atoms with high density can be fixed into the MOF crystals preliminarily by the strong

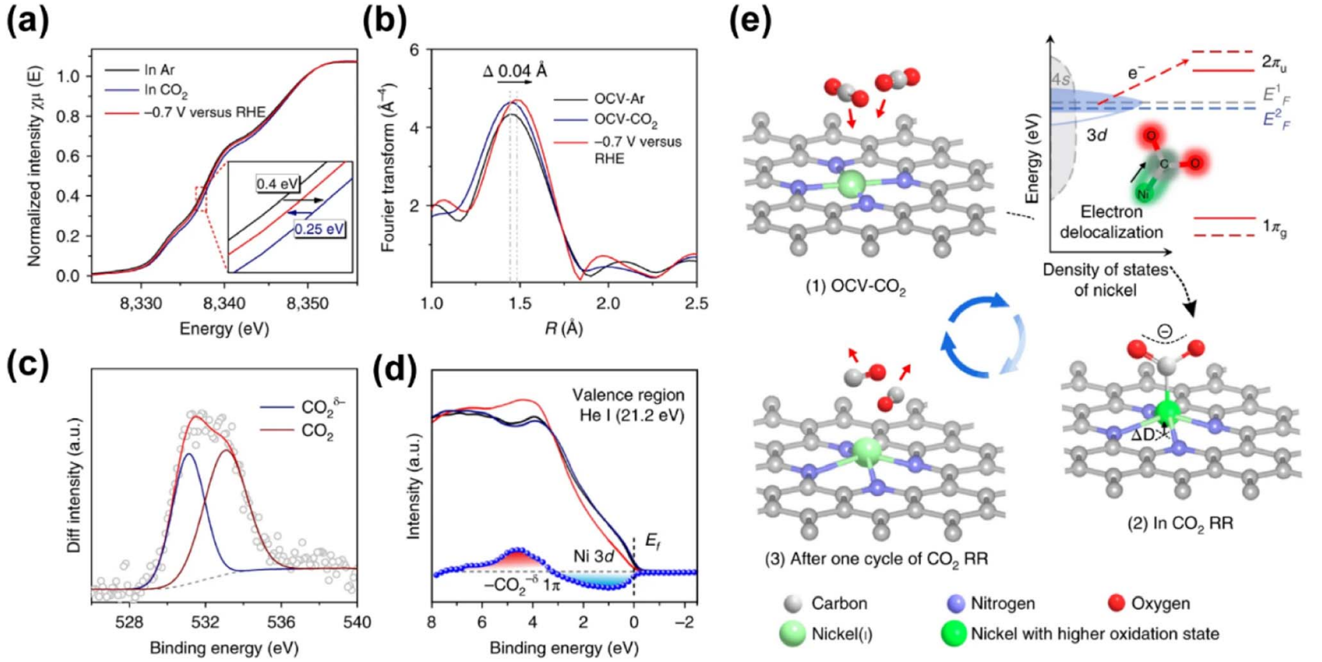

Fig. 15 (a) Normalized *operando* Ni K-edge XANES spectra for A-Ni-NG at various biases (*versus* RHE) in 0.5 M $KHCO_3$ aqueous solution at room temperature and 1 atm of Ar or CO_2. The inset shows the enlarged Ni K-edge XANES spectra. (b) Fourier transform magnitudes of EXAFS spectra (without phase correction) of A-Ni-NG under open-circuit voltage bias in Ar (OCV-Ar) and CO_2 (OCV-CO_2), and at −0.7 V (*versus* RHE), in which an expanded Ni–N bond was detected. (c) Change in the XPS O 1s intensity induced by CO_2 adsorption for A-Ni-NG. (d) Valence band spectra of A-Ni-NG before (black line) and after (red line) CO_2 gas exposure, and after desorption of CO_2 by thermal treatment at 773 K for 20 min in a vacuum (dark blue line). The blue line shows the variation in the valence band spectra of A-Ni-NG induced by CO_2 adsorption. (e) Structural evolution of the active site in electrochemical CO_2 reduction.[140] Reproduced from ref. 140 with permission from Springer Nature, copyright 2018.

bonding between metals and the moiety of ligands. Then ligands should be partially removed in an appropriate way, so that the low coordination SAs can be well exposed to the reactant phase in a stable form. Another strategy is introducing specific dopants (*e.g.*, nitrogen) in the preparation process or post-treatment to as-obtained carbon supports, since the lone pair electrons in doping elements provide an enhanced capability for chemical bonding to the metal atoms.[147–149] Since the coordination of SAs on carbon supports with high loading always needs excess dopants, the formation of miscellaneous structures is always inevitable with non-uniform introduction of dopants onto the catalysts, resulting in some adverse effects on catalytic performance. Hence, Xi *et al.* synthesized carbon-supported Ni SACs *via* a joule heating strategy, ensuring the coordination of 80% of N dopants with metal atoms.[150] It was plausible that the exclusion of the ineffective N species led to the superior performance of optimized Ni SACs in electrocatalytic CO_2 reduction with a high FE above 92% for CO formation in the potential range of −0.7 to −1.9 V *versus* RHE, while the competing hydrogen evolution reaction (HER) was suppressed. Such a preparation strategy could be also facilely extended to the synthesis of various metal-based SACs. Moreover, not only do the metal atom sites have great influence on the eventual catalytic performance of SACs catalyst, but the features of the support could play an important role in many systems for CO_2 electroreduction.[132] He *et al.* constructed a Ni-based SAC comprising a porous carbon membrane with interconnected nanofibers and hierarchical pores, supporting abundant Ni SAs for CO_2 reduction to CO.[151] This membrane with high mechanical strength and well-dispersed Ni SAs combined gas-diffusion and catalyst layers into one configuration, which could establish a stable three-phase interface for CO_2 electroreduction. Eventually, CO could be produced *via* a *COOH intermediated route with a 308.4 mA cm^{-2} partial current density and 88% FE over a 120-hour test. Moreover, the defects of certain supports could also exhibit a significant effect on the catalytic performance.[152] In the work by Boppella *et al.*,[152] the synergy between Ni–N_4 and metal free defect sites over the N-doped carbon support was revealed in CO_2 reduction. They investigated and compared the kinetic and thermodynamic behaviors of four possible active sites during CO_2 transformation, which were Ni–N_4-defects (defects as active centers), Ni–N_4–C (C near pyrrolic N as active centers), Ni–N_4–Ni (Ni as active centers) and Ni–N_4–N (pyrrolic N as active centers), according to the free energy diagrams determined by DFT calculations. As a result, Ni–N_4–N sites coupled with metal-free C near pyrrolic N sites were supposed to provide not only a lower energy barrier for the formation of COOH* intermediate species leading to promoted CO_2 activation, but also an optimum CO* binding energy facilitating CO desorption, resulting in a higher intrinsic catalytic activity (CO FE of 94% at −0.6 V and CO partial current density of 59.6 mA cm^{-2} at −1 V). To gain a comprehensive understanding of reaction mechanisms regarding the structure of active sites and possible reaction

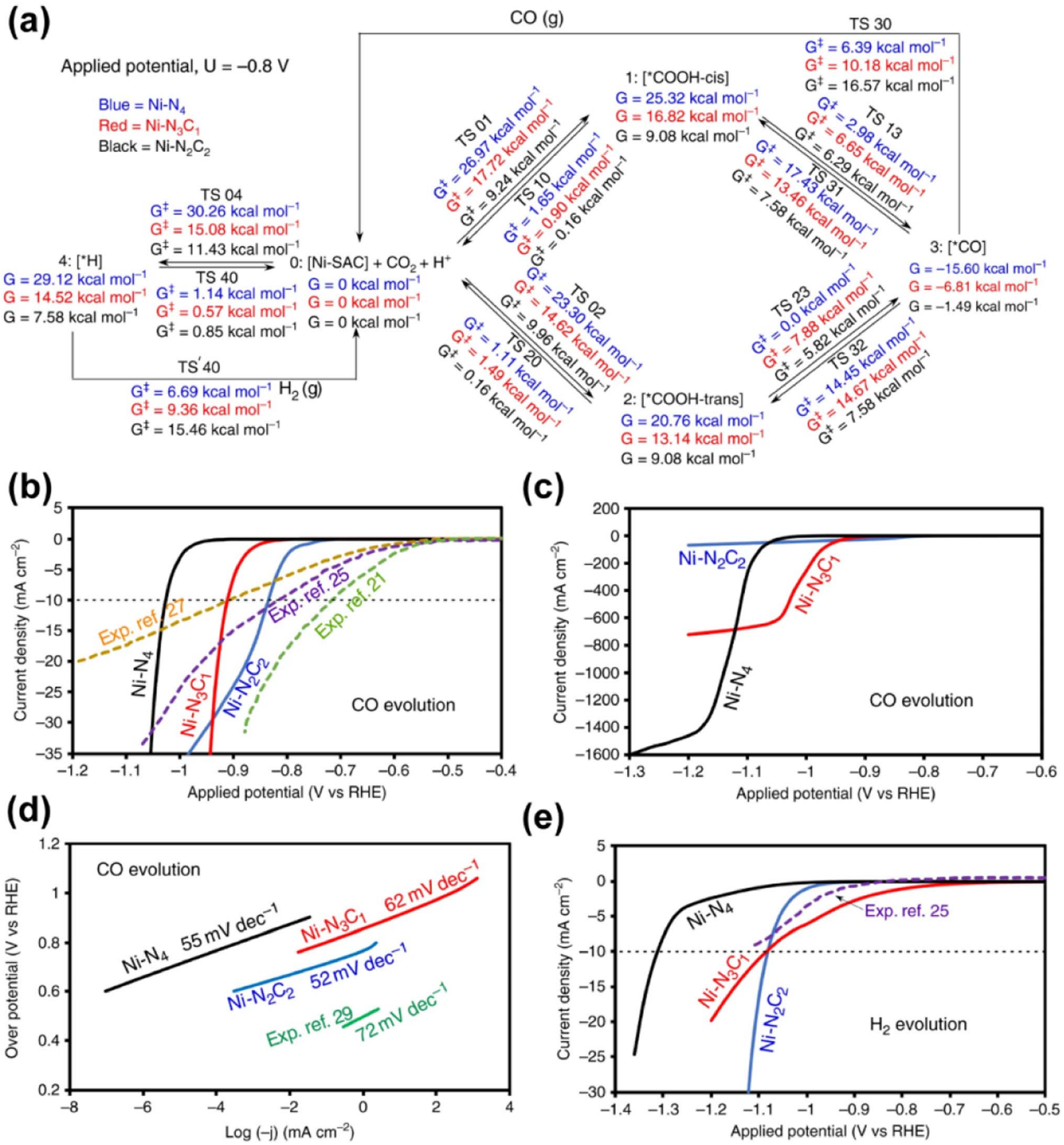

Fig. 16 (a) Schematic representation of free energies at 298 K and pH 7 for −0.8 V applied potential. This summarizes all reaction intermediates (0–4) and transition state (TS) free energies involved in the reduction of CO_2 on a nickel single site at −0.8 V constant applied potential. (b) Calculated partial current densities for CO evolution during CO_2 reduction on Ni–N_2C_2, Ni–N_3C_1 and Ni–N_4 along with experimental data for comparison (equivalent number of nickel atoms). (c) Large partial current densities for CO evolution during CO_2 reduction on Ni–N_2C_2, Ni–N_3C_1 and Ni–N_4. (d) Tafel slopes calculated from the I–V curves for CO evolution on Ni–N_2C_2, Ni–N_3C_1 and Ni–N_4 during CO_2 reduction, showing good agreement with the Tafel slope from the experiment. (e) Calculated partial H_2 current densities as a function of applied potential during CO_2 reduction on Ni–N_2C_2, Ni–N_3C_1 and Ni–N_4 along with experimental data for comparison (equivalent number of nickel atoms), at pH 7 and 298 K.[153] Reproduced from ref. 153 with permission from Springer Nature, copyright 2020.

kinetics over Ni-based SACs, advanced computational chemistry tools have been also used besides the great efforts made in experimental research. Hossain *et al.* used a new grand canonical potential kinetics (GCP-K) formulation, which could describe the electron transfer with proton or hydrogen transfer as a continuous process.[153] Since the commonly accepted reaction route of electrochemical CO_2 reduction to CO involves four consecutive steps: (a) linear CO_2 binding to the catalyst surface (*), forming bent $*CO_2^-$ *via* electron transfer; (b) hydrogen transfer from water which converts adsorbed $*CO_2^-$ into the adsorbed *COOH intermediate; (c) a second hydrogen transfer from water which converts the adsorbed *COOH intermediate into bound *CO; and (d) bound *CO desorption from the catalyst surface as gaseous CO, leaving the surface empty (*) for another reaction cycle, the possible sites over Ni-SACs including Ni–N_2C_2, Ni–N_3C_1, and Ni–N_4 were evaluated based on these procedures (Fig. 16). Distinct kinetics was exhibited over each kind of site, and the best overall performance was predicted to be present on Ni–N_4 with a CO FE of nearly 100% and current density of 40 mA cm^{-2} at a potential of −1.05 V, while the other sites showed slightly inferior performance. Meanwhile, the XPS N, C 1s and Ni 2p binding energy (BE) shift and the CO vibrational frequencies for various sites were also predicted for helping in the identification of the active sites, and all these predicted values showed surprising agreement with the experimental results. This work further suggests that it should be a good modeling material for SAC to associate the theoretical analysis and experimental research. More recently, Li *et al.* studied the effect of acidic microenvironments on a Ni–N–C SAC for CO_2 electrolysis in a membrane electrode assembly (MEA) electrolyzer.[154] To overcome the frequent severe carbon loss in common alkaline and neutral electrolytes, the authors developed an acidic membrane electrode assembly electrolyzer with a tailored local concentration ratio of H^+ and K^+. They found that the addition of both H^+ and K^+ favored the adsorption of CO_2 and desorption of CO species energetically, despite simultaneously enhancing the adsorption of H* (competitive adsorption with CO_2). As a result, they achieved an energy efficiency of 45% for CO production at pH 0.5 with CO_2 loss reduced by 86% at 300 mA cm^{-2}, as compared to that under alkaline conditions. Notably, they also realized a CO_2–CO–C_{2+} process with 99% FE of C_{2+} products (46% FE of ethene) *via* a two-step CO_2 electrolysis process by the tandem combination of such an acidic MEA electrolyzer and an alkaline MEA electrolyzer.

In addition to Ni-based SACs, SACs comprising iron species have been also used in electrochemical CO_2 reduction. For example, Gu *et al.* reported an iron-based SAC that produced CO from CO_2 reduction at an overpotential as low as 80 mV, and the partial current density could reach 94 mA cm^{-2} at an overpotential of 340 mV.[139] Discrete Fe^{3+} ions, coordinated to pyrrolic N atoms of the N-doped carbon support, were identified as active sites by the *operando* XAS technique. During the electrocatalysis process, the active centers could maintain a +3 oxidation state through a possible electronic coupling to the conductive carbon support, driving faster CO_2 adsorption and weaker CO absorption in comparison with conventional Fe^{2+} species. In this way, a comparable performance to that of noble metal catalysts was obtained. In order to further improve the activity of the Fe SAC, phosphorous SAs were introduced into N-doped carbon supported Fe SAs (Fe-SAC/NPC) for CO_2 electroreduction to CO in an aqueous solution, as reported by Sun *et al.*[155] Experimental analysis combined with DFT calculations suggested that P SAs mainly in the form of P–C bonds were located in high coordination shells, particularly the third coordination shell of the Fe center, leading to enhanced electronic localization of Fe. Thus, the Fe center could contribute more electrons to bond with the key *COOH intermediate, enabling the facile formation and stabilization of this intermediate on Fe with a decreased energy barrier. As a result, this SAC exhibited a CO FE of nearly 97% at an overpotential of 320 mV, comparable to state-of-the-art gold catalysts. Taking mass transfer into consideration, Zhang *et al.* prepared a hierarchical carbon foam confining Fe-based SAC with the assistance of a SiO_2 template.[156] The Fe SAs coordinated with four nitrogen atoms (FeN_4) confined in a carbon matrix at the atomic-scale served as the active sites for electrocatalytic CO_2 reduction to CO with an optimized CO FE of up to 94.9% at a moderate potential of −0.5 V *vs.* RHE. With the utilization of the special carbon support, the pore-enriched effect at the macro-scale favored the diffusion of substrate molecules, while the graphene nanosheets at the nano-scale enhanced charge transfer. ^{57}Fe Mössbauer spectroscopy, involving the resonant and recoil-free emission and absorption of γ-rays by atomic nuclei, is useful to probe tiny changes in the energy levels of the atoms. Li *et al.* exploited this technique for *operando* monitoring of the dynamic behaviors of Fe SA moieties under specific reaction conditions (Fig. 17).[157] By means of *operando* XAS and a quantum-chemical study, the *in situ*-generated four pyrrolic nitrogen atom-coordinated low-spin (LS) Fe(I) (LS $Fe^{I}N_4$), featuring monovalent Fe(I, d^7) with an unpaired electron in the d_{z^2} orbital of a pseudo-D_{4h} ligand field, had been identified as the reactive center for the conversion of CO_2 to CO. The optimal binding strength of CO_2 to the LS $Fe^{I}N_4$ site, with strong orbital interactions between the singly occupied d_{z^2} orbital of the Fe(I) site and the singly occupied π* orbital of the [COOH] fragment, was considered as the key factor for the excellent performance.

Copper-based catalysts have been widely used in electrochemical reduction of CO_2 to valuable chemicals, especially involving the C–C coupling process.[158–164] When the size of Cu species is downsized to the atomic scale, distinct catalytic performances have been found, which makes the selective production of CO possible.[165–167] In a pioneering research study by Li and his co-workers,[166] a catalyst featuring two adjacent copper atoms, namely the 'atom pair', was reported to carry out the critical bimolecular step in CO_2 reduction. With stable Cu_1^0–Cu_1^{x+} pair structures, this catalyst could readily adsorb H_2O and CO_2 over neighboring Cu_1^{x+} and Cu_1^0 sites, respectively. This adsorption configuration was verified by a combination of experiments and modeling calculations. It significantly reduced the activation energy of CO_2, so that the performance could be promoted with a FE_{CO} of above 92% at relatively low potentials. Another strategy was proposed by Chen *et al.* *via* introducing other active component dispersed Cu clusters (Cu_x) into a Cu SA co-coordinated with a N and S anchored carbon matrix (Cu–S_1N_3) to develop a tandem catalyst (Cu–S_1N_3/Cu_x) for CO_2 reduction to CO.[167] In a typical reaction process, the Cu–S_1N_3 atomic interface offered an optimized binding energy for the key intermediate *COOH, while the adjacent Cu_x accelerated the protonation of $*CO_2^-$ by enhancing the water dissociation

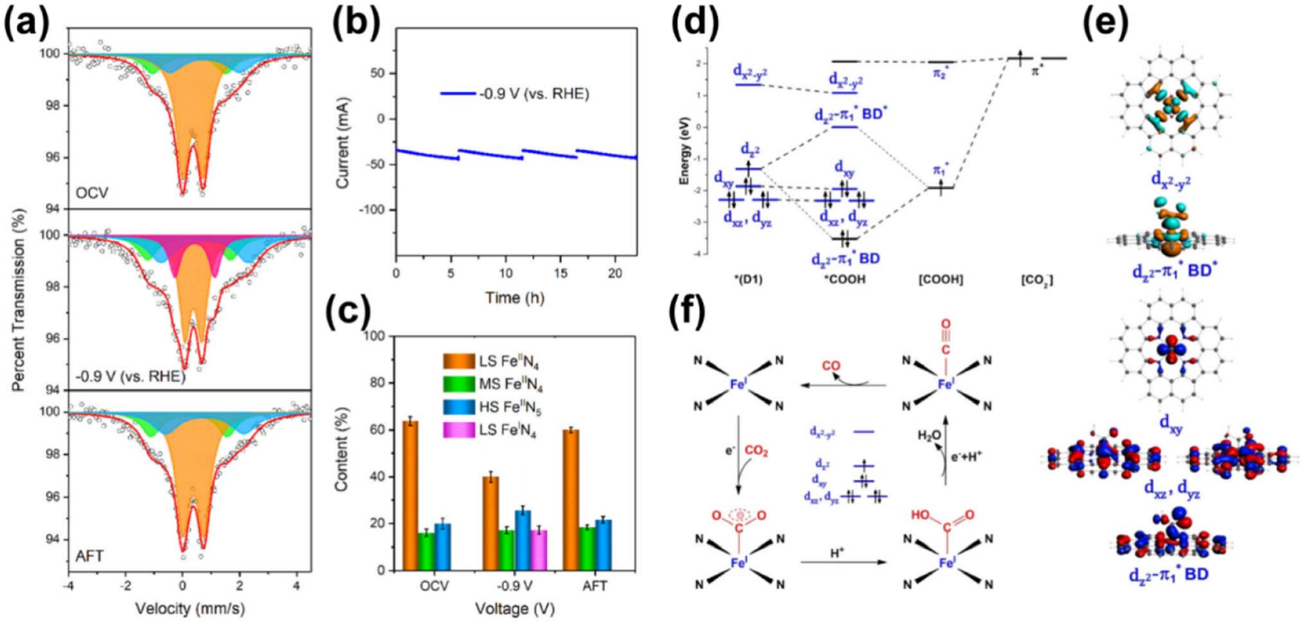

Fig. 17 (a) *Operando* ^{57}Fe Mössbauer spectra of ^{57}Fe-enriched Fe-NC-S recorded at OCV, −0.9 V (*vs.* RHE), and after the CRR. The orange, green, blue, and purple doublets could be assigned to LS Fe^{2+} in $Fe^{II}N_4$, MS Fe^{2+} in $Fe^{II}N_4$, HS Fe^{2+} in $N{-}Fe^{II}N_4$, and LS Fe^{2+} in $Fe^{I}N_4$, respectively. (b) Current–time response of ^{57}Fe-enriched Fe-NC-S for the CRR. (c) Content of different Fe moieties and reactive intermediates obtained from operando ^{57}Fe Mössbauer measurements. (d) Schematic Kohn–Sham molecular orbital (MO) energy-level correlation diagram between CO_2 and the active Fe site of D1 for the CO_2 activation step. (e) Selected contour plots of MOs for the *COOH intermediate with the D1 model. (f) Proposed reaction pathway of the CRR over D1. The acronym CRR refers to the CO_2 reduction reaction conducted in CO_2-saturated 0.5 M $KHCO_3$ solution.[157] Reproduced from ref. 157 with permission from American Chemical Society, copyright 2021.

and *H transfer to the $Cu{-}S_1N_3$ sites. In this way, the tandem catalyst exhibited much higher FE_{CO} (above 90%) compared with the catalysts with a single component (50–70%).

Zinc, as an earth-abundant metal, has shown some promising properties as an active component in CO_2 electrochemical reduction.[168] Recently, there have been also some achievements in terms of Zn-based SACs for the production of CO from CO_2 reduction.[169–171] Li *et al.* fabricated a nitrogen-stabilized SAC featuring low-valence zinc atoms ($Zn^{\delta+}$–NC).[169] Saturated four-coordinate ($Zn{-}N_4$) and unsaturated three-coordinate ($Zn{-}N_3$) sites coexisted, and the latter was in charge of Zn species at the low-valence state, as speculated from XPS, XAS, electron paramagnetic resonance (EPR), and DFT. Further calculations suggested that the unsaturated $Zn{-}N_3$ could remarkably reduce the energy barrier for the formation and stabilization of the key COOH* intermediate thanks to the electron-rich environment of Zn (Fig. 18), leading to a high FE_{CO} of up to 95% at a current density of 1 A cm^{-2} in a flow cell. Furthermore, the preparation and corresponding properties of supports were also considered as key factors that made a great difference in some Zn-based SACs.[170–172] Hao *et al.*[170] succeeded in loading Zn SAs on the N-doped carbon nano-onions (ZnN/CNO) for CO_2 electroreduction to CO. A FE of CO up to 97% at −0.47 V (*vs.* RHE) could be obtained, beyond that of Zn SAs on a two-dimensional planar and porous graphene substrate with larger surface area. Systematical characterization studies and DFT calculations indicated that the superior performance of the CNO support could be attributed to the increased curvature, which could tune the surface charge and subsequent adsorption energies of key intermediates, and thereby improve the selectivity for CO generation. Coincidentally, Fang *et al.*[171] also unveiled the effect of curvature on Zn SAs supported on curved N-doped carbon nanofibers (Zn SAs/N–C) by a facile noncovalent self-assembly approach. In this SAC, Zn atoms in $Zn{-}N_4$ sites were identified as the actual active sites, while adjacent pyridine-N could synergistically decrease the free energy barrier for intermediate *COOH formation. In particular, the curvature of the catalyst made Zn 3d electrons in the Zn–N bonds return to the Zn atom, leading to an increase in electron density of Zn and accelerating CO_2 electroreduction to CO. In addition to commonly reported Zn-based SACs with $Zn{-}N_x$ sites as the sole active component, Zheng *et al.* develop a SAC with an isolated zinc site embedded in nitrogen, sulfur co-doped hierarchically porous carbon (Zn–NS–C) to realize CO_2 electrochemical reduction to CO.[173] Combined structural characterization and electrochemical experiments as well as theoretical calculations revealed the synergistic effects of auxiliary S and isolated $Zn{-}N_4$ sites. The bicarbonate adsorption and dissociation were promoted by the adjacent S atoms, resulting in an increased proton transfer rate and boosted reaction kinetics of $*CO_2$ protonation to form *COOH. In this way, this SAC provided enhanced activity of CO_2 reduction with a high CO FE of 99% at an industrial-level current density of 200 mA cm^{-2} and a corresponding turnover frequency of 11 419 h^{-1}. More recently, Hu *et al.* reported a so-called 'synergistic near- and long-range regulation' strategy with the help of a modified Zn SAC.[174] They embedded ZnN_4 sites in hollow carbon supports with co-decorated sulfur and phosphorus in the first coordination shell and surrounding carbon matrix, respectively (ZnN_4S_1/P-HC). According to theoretical calculations, the S atom present in the axial position significantly distorted the planar coordination structure of the Zn SA site, thereby increasing the charge density of the active center, which could be further elevated by the redistribution of electrons stemming from the introduction of P atoms in the second coordination layer. Such a remarkable change in electronic state provided varied interactions between Zn SA sites and specific reaction intermediates, especially *COOH. An enhanced adsorption strength of *COOH was observed due to the increased overlap of Zn (3d) and *COOH (2p) orbitals, thus promoting the formation of *COOH with a lower energy barrier, then leading to the production of CO.

The application of SACs in CO_2 electroreduction can be further extended to cobalt.[175–178] Pan *et al.* developed a robust Co-based SAC with an atomically dispersed Co–N_5 site anchored on polymer-derived hollow N-doped porous carbon spheres for CO_2 electroreduction to CO.[176] The hollow structure of the SAC was fabricated by a combination of pyrolysis and etching procedures with SiO_2 as the template. Meanwhile, the metal atoms were embedded by coordination with N. On the basis of various experiments and modeling calculations, Co–N_5 sites were disclosed to be the main active center for CO_2 activation, the formation of the key intermediate COOH* and the desorption of the CO product. As a result, a high FE of CO of above 90% could be achieved over a wide potential range from −0.57 to −0.88 V with remarkable stability. Lin *et al.* constructed a Co-based catalyst based on covalent organic frameworks (COFs) comprising cobalt porphyrins for the aqueous electrochemical reduction of CO_2 to CO.[177] XAS data revealed that the chemical environment offered by the COF plays an important role in the electronic structure of the catalytic cobalt centers, thereby contributing to the high activity of catalysts and FE to CO. Han *et al.* established a Co-based catalyst featuring atomically

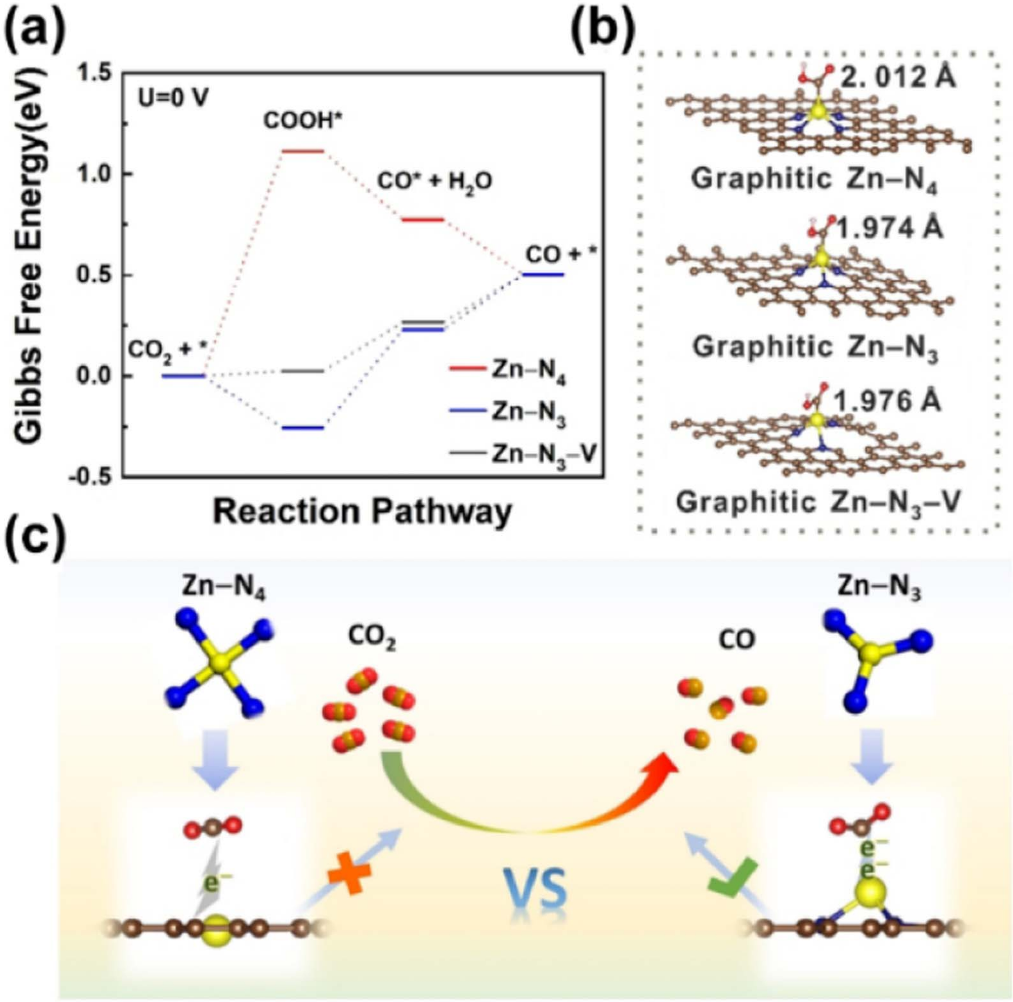

Fig. 18 (a) Calculated Gibbs free energy diagram for CO_2-to-CO conversion using graphitic Zn–N_4, Zn–N_3 and Zn–N_3–V models at $U = 0$ V and pH = 0. (b) DFT calculated geometry of graphitic Zn–N_4, Zn–N_3 and Zn–N_3–V sites with key intermediate COOH*-adsorbed species. (c) Comparison of the active site of electron-rich Zn–N_3 with that of Zn–N_4.[169] Reproduced from ref. 169 with permission from Wiley, copyright 2021.

dispersed active centers for electrocatalytic CO_2 reduction,[178] which was synthesized *via* an axial coordination assembly using tetra(4-pyridyl) porphyrin cobalt(II) as building blocks, resulting in an ultra-thin morphology. The well-defined structure enabled the precise identification of the active sites for d-orbital energy engineering. The promoted activity of this catalyst for electrocatalytic CO_2 reduction originated from the elevated energy level of d_{z^2} in Co 3d orbitals, leading to a remarkable FE of 96% to CO at an overpotential of 500 mV. A similar strategy was also reported by Shen *et al.*,[179] in which an organic molecule porphyrin was used as the ligand to coordinate the Co atoms, and a performance dependent on the pH value was exhibited when the SAC was used in electrocatalytic CO_2 reduction.

Apart from the metals mentioned above, other kinds of transition metals have been also explored regarding the design of SACs and their application in electrochemical CO_2 reduction to CO. For instance, a cadmium (Cd)-based SAC was prepared by a unique gas-migration, trapping, and emitting strategy for CO_2 reduction to CO.[180] A Cd loading amount as high as 30.3 wt% could be achieved through the gas-migration and trapping processes, while the emitting process could readily modulate it from 30.3 to 1.4 wt%. At an optimum loading amount of 18.4 wt%, the maximum FE of 91.4% for CO was obtained at −0.728 V, following the proton-decoupled electron-transfer mechanism. The Cd–N_4 structure was revealed to be the main active site for the reduction of the Gibbs free energy barrier in the rate-determining hydrogenation step of the key intermediate *COOH. Manganese (Mn) as the third transition metal after iron and titanium among all transition elements in natural abundance, has also been applied in the construction of SACs for electrochemical CO_2 reduction to CO.[181,182] Through a halogen and nitrogen dual-coordination strategy, a Mn-based SAC was successfully fabricated with graphene as the support for effective CO_2 reduction to CO.[182] The dual coordination involving chlorine, bromine and iodine all achieved enhanced performance by modifying the electronic structure of active Mn sites, and thus the free energy barrier for the rate-determining step of the formation of the intermediate was reduced. In contrast, the enhanced effect on Fe and Co SACs with the same dual coordination was not as significant as that on Mn, indicating a strong correlation with the nature of metal. Wang *et al.* also applied a Mn-based SAC supported on a carbon substrate for CO_2 electrochemical reduction to CO.[181] The difference was that oxygen instead of halogens was co-doped with N into the SAC. Isolated Mn–N_4 moieties were considered to be the main active sites for CO_2 reduction, while the epoxy groups in the second coordination spheres adjusted the electronic structure of the catalyst with reduced reaction energy barriers. The catalytic performance was enhanced accordingly, achieving a high CO FE of 94.5% with a CO current density of 13.7 mA cm^{-2}, as well as a low overpotential of 0.44 V in an aqueous environment. In addition, a silver-based SAC was also prepared by thermal transformation of silver (Ag) NPs over a non-carbon substrate MnO_2, as Zhang *et al.* reported.[183] With simultaneous MnO_2 reconstruction from the MnO_2 (211) to (310) lattice plane, the Ag NPs drove the formation of Ag SAs confined firmly on the surface. Compared with the Ag NPs, the Ag SAC exhibited a much lower formation energy of the *COOH intermediate at −0.7 V, as well as a higher electronic density close to the Fermi level, leading to strong interactions between Ag SA sites and the *COOH intermediate. This difference contributed to the excellent performance of the Ag SAC with a CO FE of 95.7%, in contrast to that of the Ag NPs of less than 60%. Moreover, SACs based on rare earth metals such as yttrium (Y) and scandium (Sc) have been synthesized successfully on a carbon support (Y_1/NC and Sc_1/NC) and exhibited excellent catalytic activities for carbon dioxide reduction.[184] Compared with common SACs featuring atomic transition metals supported on N-doped carbon supports in a N-coordinated form (M–N_x), the reported Y_1/NC and Sc_1/NC contained metal atoms with a large radius, which tended to be anchored to the large-sized carbon defects through six coordination bonds of N and C. This coordination further modulated the local electronic structure of Y/Sc sites, and surprisingly endowed the generally inactive Y- and Sc-based nanomaterials with considerable activity for room-temperature electrochemical reaction, suggesting the distinctive effect of SACs on catalytic performance.

On the basis of the well-known d band center theory, transition metals with a narrow d band have been widely used as active components in various catalysis systems, whereas main group metals had always been thought to be nearly inactive due to a broadened single resonance derived from the interaction of valence orbitals of adsorbates with the delocalized s/p-bands.[185–189] However, there have been quite a few studies concentrating on the catalytic application of main group metals over recent years,[190] where SACs also distinguish themselves for electrochemical CO_2 reduction. For instance, Wang *et al.* reported an s-block magnesium-based SAC with atomically dispersed magnesium atoms embedded in graphitized C_3N_4 (Mg–C_3N_4) for electroreduction of CO_2 to CO.[191] Since the formation of the *COOH intermediate is assumed to be the rate determining step of the whole reaction process with transition metals as active sites, the desorption of *CO is always ignored although it has a higher energy barrier according to some modeling calculations. Indeed, the strong hybridization between localized d orbitals and CO would lead to limited CO desorption and further reaction cycles. In this case, the Mg SAs with a delocalized s orbital would provide a solution by weakening the CO adsorption (Fig. 19a). As a result, Mg–C_3N_4 demonstrated a high TOF of 18 000 h^{-1} at a a CO FE above 90%, while the flow cell fabricated with Mg–C_3N_4 offered a large current density of −300 mA cm^{-2}. More recently, Wang *et al.* developed an O doping strategy to localize electrons on p orbitals of a calcium SAC with active sites in asymmetric coordination (Ca–N_3O, one O and three N coordinated atoms with one Ca).[192] The asymmetric coordination of Ca–N_3O improves *COOH formation, thereby enhancing the CO_2 activation, in addition to the intrinsic virtue of the ability of main group metals to inhibit the competitive HER and CO poisoning induced by strong adsorption of CO species, leading to an excellent TOF of ∼15 000 per hour in an H-cell and a large current density of −400 mA cm^{-2} with a CO FE of no less than 90% in a flow cell. Moreover, Zhang *et al.* inventively fabricated main group element gallium-based (Ga) SACs with a nitrogen,

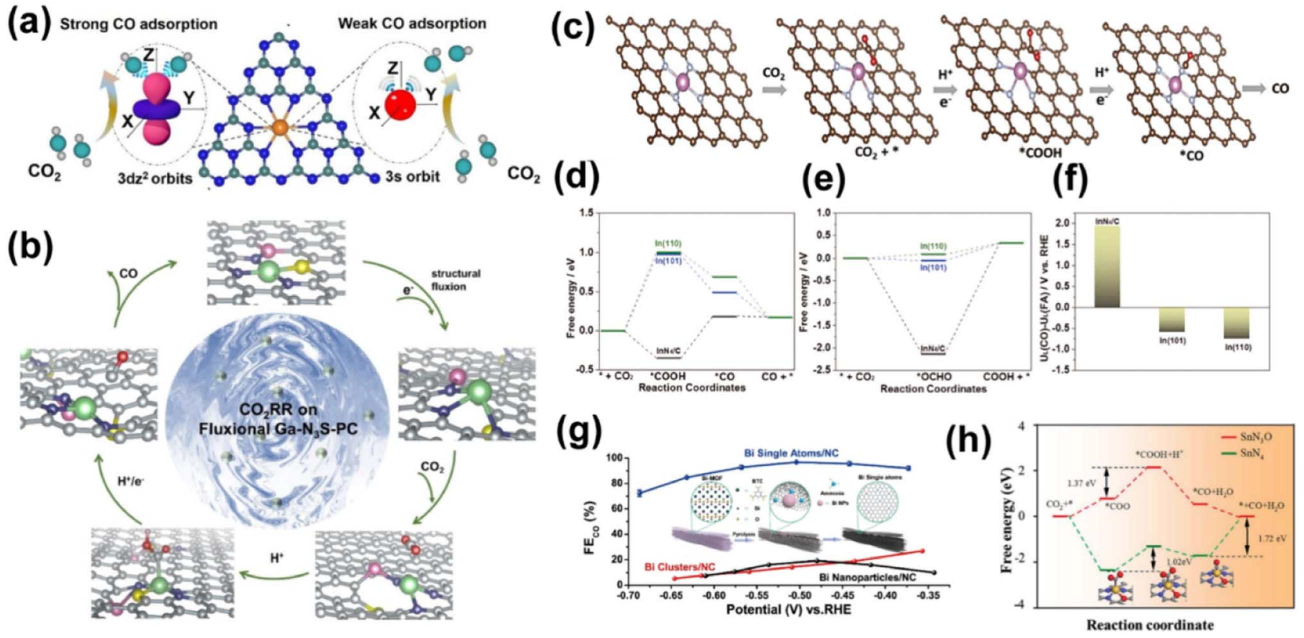

Fig. 19 (a) Mechanism of CO production on Mg–C_3N_4.[191] (b) Schematic diagram of the CO_2RR catalytic process on the fluxional Ga-N_3S-PC catalyst.[193] (c) The catalytic pathway on InN_4/C based on the COOH* and CO* adsorption intermediates after optimization.[194] Gibbs free-energy diagrams of (d) CO_2-to-CO and (e) CO_2-to-formate over different simulated models.[194] (f) Difference in limiting potentials for CO_2 reduction to CO and formate over different simulated models.[194] (g) Performance of the Bi SA compared with NCs and NPs.[196] (h) The calculated Gibbs free energy diagrams for CO_2-to-CO over SnN_3O_1 and SnN_4.[198] Reproduced from ref. 191, 193, 194, 196 and 198 with permission from Wiley and American Chemical Society, copyright 2019, 2021, 2022.

phosphorous and sulfur atomic coordination environment for electrochemical CO_2 reduction.[193] The Ga-N_3S-PC structure in this SAC that was constructed *via* a polymer pyrolysis strategy surprisingly displayed specific fluxional properties in contrast to a typical Ga–N_4–C structure with a rigid skeleton. Theoretical simulations further revealed the adaptive dynamic transition of Ga derived from a flexible three-dimensional structure, optimized the adsorption energy of the *COOH intermediate and renewed the active sites on time, leading to a CO FE of ∼92% at −0.3 V *vs.* RHE (Fig. 19b). Moreover, indium (In) that is from the same group as gallium, has been also applied in SAC-catalyzed electrochemical CO_2 reduction to CO by Guo *et al.*[194] They synthesized an atomic In-anchored N-doped carbon catalyst through pyrolysis of In-bearing MOFs, in which the In species in oxidized state predominated and coordinated with N. This SAC exhibited higher double-layer capacitance, larger CO_2 adsorption capacity, and lower interfacial charge transfer resistance thanks to the highly dispersed active sites, resulting in a FE of CO of up to 97.2% and total current density of 39.4 mA cm^{-2} as well as a turnover frequency (TOF) of ∼40 000 h^{-1}. The specific In–N sites also contributed to CO selectivity by suppressing the formation of formate owing to the changed energy barrier, as revealed by theoretical calculations (Fig. 19c–f). Bismuth (Bi) and antimony (Sb) from the same main group have been also used to construct SACs for electrochemical CO_2 reduction to CO.[195–197] Zhang *et al.* prepared a Bi–N_4 dominated catalyst by thermal decomposition of a Bi-based metal–organic framework (Bi-MOF) and dicyandiamide (DCD).[196] *In situ* environmental transmission electron microscopy (ETEM) analysis offered an opportunity to directly observe the reduction of a Bi-MOF into Bi NPs and subsequent redispersion of NPs into atomic species with the help of NH_3 released from DCD decomposition. The obtained Bi SAC exhibited much higher FE of CO (97%) than that over Bi NP or NC dominated catalysts (Fig. 19g), to which the Bi–N_4 sites made great contributions by accelerating the formation of the key intermediate COOH* with a lower free energy barrier. Wang *et al.*, on the other hand, developed an atomically dispersed N, S co-coordinated bismuth SAC (Bi-SAs-NS/C) *via* a cation and anion simultaneous diffusion strategy for electrocatalytic CO_2 reduction.[197] The bonded Bi cation and S anion could be synchronously diffused into the N-doped carbon layer as a Bi_2S_3 compound. Bi and S were captured by the abundant N-rich vacancies and carbons on the support, respectively, at high temperature, leading to the formation of co-coordinated Bi sites (Bi–N_3S/C). The replacement of one coordinated-N with less electronegative S in the Bi–N_4C center was proved to be highly effective in reducing the energy barrier of intermediate formation in the rate-limiting step and enhancing the reaction kinetics. Thus, a high FE of CO of over 88% in a wide potential range with a maximum value of 98.3% at −0.8 V *vs.* RHE and a current density of 10.24 mA cm^{-2} could be achieved. Recently, Sb has also been exploited for electrochemical CO_2 reduction to CO, in which the single atom Sb sites exhibited superior performance compared with bulk Sb or Sb_2O_3, even surpassing other reported SACs.[195] In addition, SACs based on tin (Sn) were reported as well for efficient electrochemical CO_2 reduction.[198] Guo *et al.*[198] prepared Sn SACs comprising atomically dispersed SnN_3O_1 active sites supported on a N-rich carbon matrix (Sn–NOC). The atomic arrangement of SnN_3O_1 reduced the activation energy for *COO and *COOH formation and significantly increased the energy barrier for HCOO* formation. Sn–NOC gave CO as the exclusive product, whereas HCOOH and H_2 were the predominant products for the classic Sn–N_4 configuration (Fig. 19h).

Apart from these SACs with only single atom active sites mentioned above, there have been also a few reports on catalysts involving dual atom sites or synergy between single atom sites and other types of active sites. Since these catalysts are also inspired by the theories of SACs, we include them in the following discussion for more a comprehensive understanding. For instance, Ni dual-atom sites and Pd dual-atom sites have been constructed and reported for electrocatalytic CO_2 reduction to CO.[199,200] In the former case, Ni dual-atom sites were revealed to be key to induce the adsorption of hydroxyl and the formation of electron-rich active centers, providing a moderate reaction kinetic barrier of *COOH formation and *CO desorption.[199] As for the latter case, Pd dual-atom sites showed advantages in CO production owing to the moderate adsorption strength of CO* derived from the electron transfer between Pd atoms.[200] Hetero-diatomic catalysts such as Ni–Fe, Ni–Cu and Ni–Zn have been also applied in electrocatalytic CO_2 reduction to CO.[201–203] For Ni–Cu[202] (Fig. 20g–k) and Ni–Zn[201] (Fig. 20a–c), heteronuclear coordination was considered to modify the d-states of the metal atoms, narrowing the gap between the d-band center of the Ni orbitals and the Fermi energy level to strengthen the electronic interaction at the reaction interface, resulting in a lower free energy barrier and a reduced activation energy for the formation of the key intermediate. The excellent performance of Ni–Fe,[203] on the other hand, was attributed to the orbital coupling between the catalytic iron center and the adjacent nickel atom, resulting in an alteration in the orbital energy level, unique electronic states and a higher oxidation state of iron (Fig. 20d–f). The binding strength to *CO was weakened over Ni–Fe compared with Fe-SAC, playing a vital role in the enhanced efficiency for CO production. Furthermore, catalysts featuring the synergy between SAs and other active species have been studied for the electrocatalytic CO_2 reduction to CO. Wang *et al.* applied a novel solid-state atomic replacement transformation strategy for constructing a catalyst containing both PtZn nanocrystals and Ni SA sites.[204] Through the exchange between the Ni in the PtNi nanoalloy and the Zn in ZIF-8-derived Zn_1 on nitrogen-doped carbon (Zn_1–CN) at high temperature, $(PtZn)_n/Ni_1$–CN was obtained. This fabricated catalyst showed a synergistic effect combining PtZn nanocrystals and Ni SA sites on the CO_2 reduction reaction with a lower energy barrier for CO_2 protonation and CO desorption. The application of this unique strategy could be extended to other metal alloys such as PtPd. Li *et al.* tuned the CO selectivity of Cu by alloying a second metal Sb into Cu, forming an antimony-copper single-atom alloy catalyst (Sb_1Cu) with

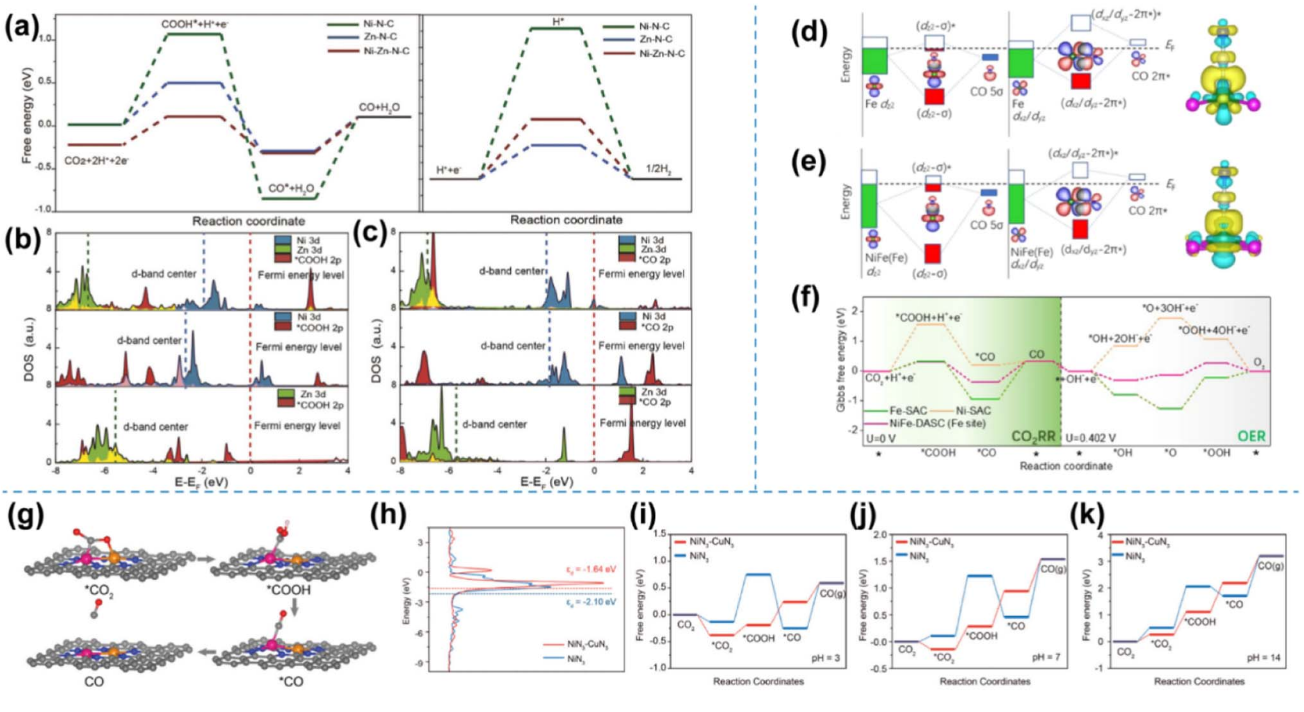

Fig. 20 (a) The free energy of each intermediate state on the metal atom sites in Zn–N_4–C, Ni–N_4–C, and ZnNi–N_6–C. Projected DOS (PDOS) for Zn/Ni 3d orbitals and oxide 2p orbitals including COOH (b) and CO (c).[201] Schematic illustration of orbital interactions between adsorbed CO (5σ and 2π*) and the 3d orbital (d_{z^2}, d_{xz}/d_{yz}) of the Fe site in the (d) Fe-SAC and (e) NiFe-DASC. (f) Calculated free energy diagrams for CO_2RR and OER processes.[203] (g) The catalytic pathway on NiN_3–CuN_3 based on the *COOH and *CO adsorption intermediates after optimization. (h) The density of states of Ni d-orbitals in NiN_3–CuN_3 and NiN_3. (i–k) Gibbs free energy diagrams of CO_2 conversion to CO over NiN_3–CuN_3 and NiN_3 with free energy correction at pH = 3, 7, and 14.[202] Reproduced from ref. 201–203 with permission from Wiley and Springer Nature, copyright 2021, 2023.

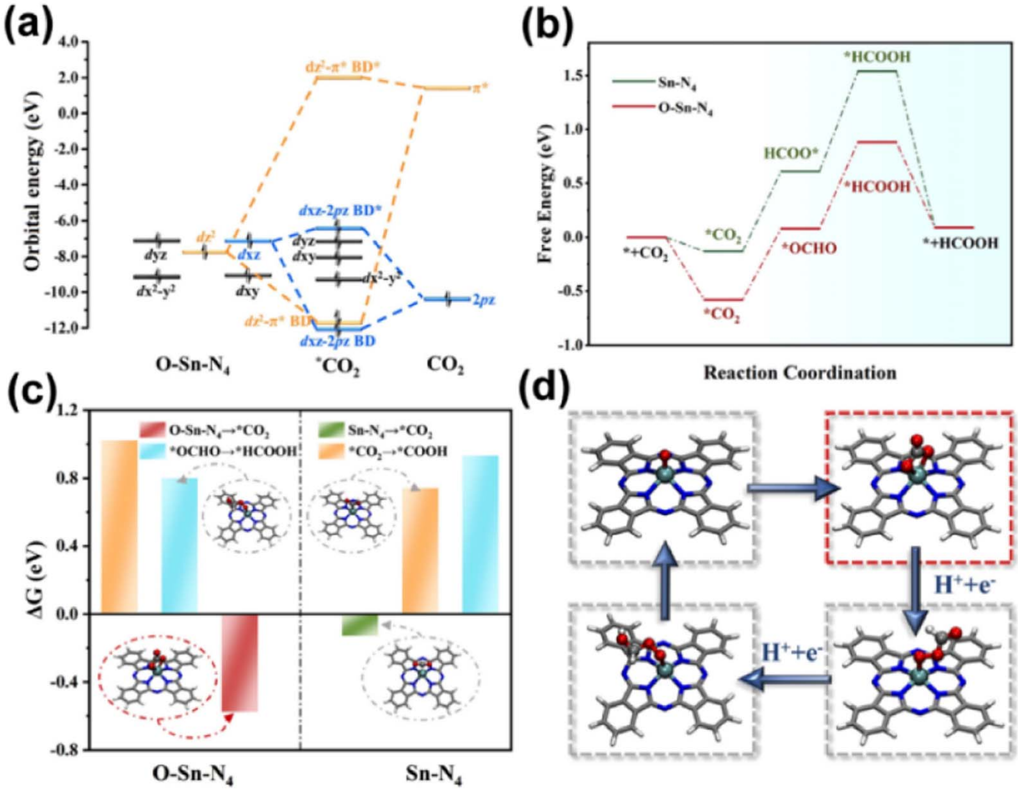

Fig. 21 (a) Schematic Kohn–Sham molecular orbital (MO) energy-level correlation diagram between CO_2 and the O–Sn–N_4 site during the CO_2 capture step (* + CO_2 → *CO_2). (b) Calculated Gibbs free energy diagrams for CO_2 reduction to HCOOH over O–Sn–N_4 and Sn–N_4 sites. (c) Calculated ΔG for HCOOH and CO production over O–Sn–N_4 and Sn–N_4 sites. (d) Proposed reaction pathway for CO_2 reduction over the O–Sn–N_4 site.[210] Reproduced from ref. 210 with permission from American Chemical Society, copyright 2023.

isolated Sb–Cu interfaces.[205] The atomic Sb–Cu interface promoted CO_2 adsorption/activation and weakened the binding strength of CO*, suppressing the facile C–C coupling reactions over conventional Cu crystals, leading to enhanced CO selectivity with a FE of over 95%.

3.1.2.2 *Formic acid and formate.* To synthesize formic acid and formate *via* an electrochemical route is another appealing subject in CO_2 reduction due to the versatility of formic acid or formate in chemical production and energy industries. The process of CO_2 conversion to HCOOH features two-electron transfer, identical to that of CO_2 conversion to CO, with a slight lower reduction potential of −0.12 V *versus* RHE (Fig. 5). This indicates that the production of HCOOH might be another fundamental process involving the most preliminary procedures in CO_2 conversion. However, practical application of CO_2 reduction is still limited by the sluggish kinetics and significant side reactions such as the HER.[190] Owing to the challenges in both increasing the reaction rate and steering reaction selectivity, it is urgent to develop catalysts with high efficiency and reliability. In addition to modifying the conventional nanostructure catalysts, SACs have been exemplified as an affordable solution to the above problems. For instance, Shang *et al.* designed an In SAC with $In^{\delta+}$–N_4 atomic interface active sites for electroreduction of CO_2 to formate to overcome the low FE and poor durability over common In-based catalysts.[206] Compared with the reference sample with dominant NPs, the SAC exhibited a lower free energy barrier for the formation of the HCOO* intermediate leading to higher activity, while the superior selectivity of formate could be rationalized based on the more positive difference between limiting potentials for CO_2 reduction and H_2 evolution. This strategy could further be extended to other main group elements, such as Sb.[207] The positively charged $Sb^{\delta+}$–N_4 ($0 < \delta < 3$) active sites could endow the Sb SAC with a formate FE of 94.0% at −0.8 V *versus* RHE in a similar way as $In^{\delta+}$–N_4 did, transcending the performance over the catalyst with NPs. On the other hand, Xie and co-workers fabricated Mo and Sn SACs with N-doped graphene as a support, both of which demonstrated excellent performance for formate production.[208,209] The reduction of CO_2 to formate could not only benefit from the Mo SAs anchored on the N-doped graphene, which provided the substrate with a higher current density at relatively lower overpotential,[208] but could also be favored by the positively charged Sn SA sites, which promoted CO_2 activation and protonation *via* stabilizing CO_2^{-}* and $HCOO^{-}$*.[209] The N doping in graphene also facilitated the reaction by expediting the desorption of formate products *via* lowering the desorption energy and increasing the length of the bond between the metal and $HCOO^{-}$* intermediate.[209] Notably, to gain an in-depth understanding of CO_2 electrochemical reduction reactions, Deng *et al.* developed a series of model Sn SACs with well-defined structures and employed a combination of *operando* characterization techniques for monitoring the variation in both SAC structures and surface key intermediate species.[210] Particularly, ^{119}Sn Mössbauer spectra were collected for more accurate analysis of chemical state evolution of the Sn moiety due to the specialty of Mössbauer with regard to the Sn element. Surprisingly, Sn(IV) was exclusively formed in the case where SAs were immobilized on a functionalized carbon nanotube (CNT–OH), while Sn(II) of different concentrations coexisted in other reference samples. Assisted by DFT simulations, the authors proposed a reasonable SA structure featuring Sn(IV)–N_4 moieties axially coordinated with oxygen (O–Sn–N_4) and correlated it with CO_2 reduction performance. They further confirmed that surface-bound bidentate Sn carbonate species were formed from O–Sn–N_4 sites in an initial stage and changed the electronic distribution for favorable formation and protonation of *OCHO species, thereby propelling the CO_2 conversion into HCOOH (Fig. 21).

Moreover, given that the applications of Cu-based catalysts are always limited by their poor selectivity towards specific products, Zheng *et al.* found an opportunity to inhibit the side reactions with the assistance of lead (Pb) SAs.[211] Although the identification of true active sites was still ambiguous, it was plausible that exclusive formate production was promoted by the Cu sites of Pb_1Cu *via* guiding the first protonation step towards a HCOO* path instead of a COOH* path. Such a promotion effect was also reported over a SnO_2-based catalyst, in which the abundant oxygen vacancies (O_v) were triggered by the doping of Cu/Bi/Pt single atoms. These O_v held the key to stabilizing the oxidation state of Sn species and promoting the adsorption of the *OCHO reaction intermediate, resulting in a high formate FE of >80% and a cell energy efficiency of about 50–60% in a wide range of current densities up to 500 mA cm^{-2} in a commercial flow cell.[212]

3.1.2.3 Methane. CH_4 is also an important light hydrocarbon resource, whose production from electrochemical CO_2 reduction is attracting worldwide attention in both scientific research and practical industry. Nevertheless, the process of CO_2 reduction to CH_4 involves reaction paths of transferring as much as eight electrons and eight protons, indicating a much more complicated pathway with more possible parallel reactions in comparison with that of CO and HCOOH formation. Indeed, comprehensive understanding of the reaction pathways toward CH_4 is still equivocal and highly dependent on the different catalytic systems. Copper (Cu) is known for its good performance in multi-electron transfer. SACs based on Cu have been designed for CO_2 electrochemical reduction to CH_4 correspondingly, whereas reasonable regulation of active sites is indispensable for remarkable efficiency. By anchoring Cu SAs on the unique platform graphdiyne, Shi *et al.* achieved a considerable CH_4 FE of 81% *via* CO_2 reduction.[213] The authors believed that the platform graphdiyne not only stabilized Cu SAs against aggregation, but also favored the formation of Cu–C bonds, which was confirmed to play a vital role in the generation of the *OCHO intermediate rather than *COOH (Fig. 22). This shift of intermediate significantly inhibited the formation

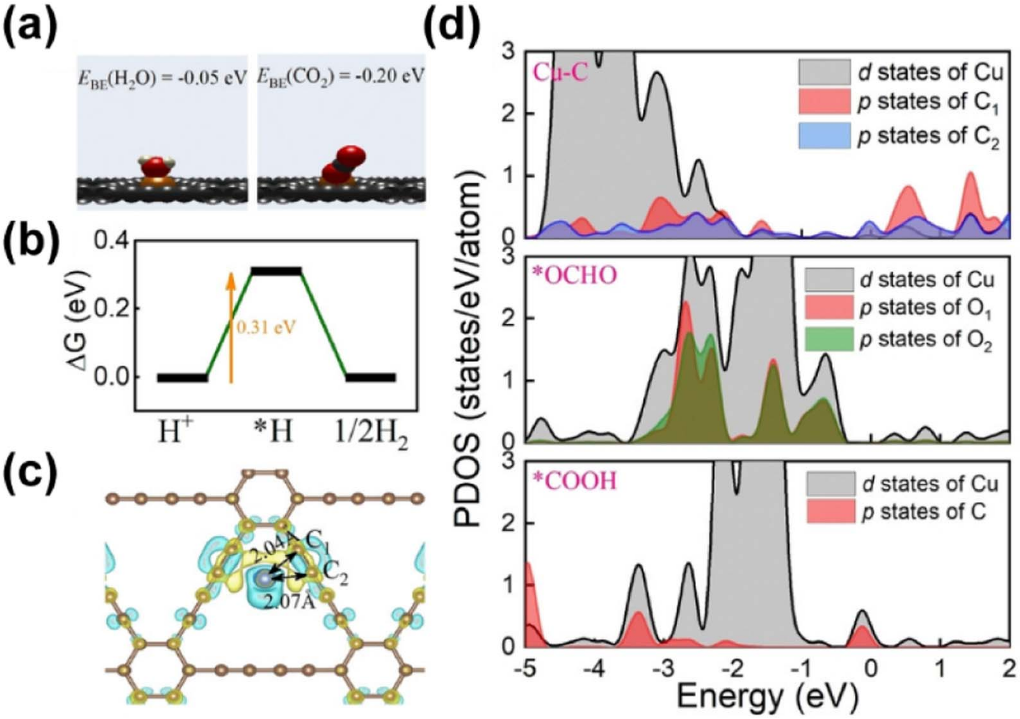

Fig. 22 (a) The binding energy of CO_2 and H_2O on Cu SAs/GDY. Insers show the calculation models of adsorbed CO_2 and H_2O, respectively. (b) Free energy diagram for the HER. (c) The charge density difference (CDD) before and after the bonding of the Cu atom and GDY. (d) Projected density of states (PDOS) of the interface Cu–C atoms in Cu SAs/GDY, and the intermediates *OCHO and *COOH.[213] Reproduced from ref. 213 with permission from Wiley, copyright 2022.

of CO and other side products by efficiently modulating the reaction pathway, leading to the preferential production of CH_4. Further tailoring the structure of normal graphdiyne with specific electron-withdrawing/-donating groups, on the other hand, offered another good opportunity for the regulation of Cu SA sites.[214] It was found that subtly introduced functional groups –F (fluorine) had a great effect on decreasing the pK_a of the adsorbed water molecule, then forming a more acidic local environment that promoted the protonation of CO_2 reduction intermediates for CH_4 production. In contrast, other groups such as –H and –OMe (methoxy) exhibited inferior performance. This difference arose from the discrepancy of the Cu valence in various chemical environments, while a more positive charge state stemming from the electron-withdrawing effect provided an excellent CH_4 FE of 72% from CO_2 reduction. Furthermore, for the cases in the absence of carbon supports, other strategies have also been proposed to modify the Cu SA sites.[215,216] Loading Cu SAs onto the metal oxide substrates with abundant Lewis acid sites was considered as an effective strategy to improve the activity of CO_2 reduction to CH_4.[216] It was speculated that strong Lewis acid sites in the form of a metal center with positive charge could facilitate the activation of CO_2 into *COOH and HCOO* intermediates with a lower energy barrier, while the selectivity was determined by using the formation energy in different pathways. This rationalized the superior performance of the Cu/Al_2O_3 SAC with substantial strong Lewis acid sites compared to that of the Cu/Cr_2O_3 SAC with weak acid sites. The effect of O_v was also highlighted in a Cu/CeO_2 SAC for CO_2 reduction to CH_4,[215] in which Cu SAs in the most stable structure with a low coordination number of 5 were well dispersed on CeO_2 nanorods. With the assistance of O_v, the adsorption and activation of carbon dioxide molecules were both enhanced. An inhibited C–C coupling was also achieved, thanks to the isolated state of active Cu SA sites, leading to enhanced formation of CH_4.

Metals other than Cu have been also studied for CO_2 electrochemical reduction to CH_4. For instance, Han *et al.* developed a SAC with Zn SAs dispersed on microporous N-doped carbon.[217] Zn–N_4 was identified as the dominant active sites which preferred to bond to the O atoms of intermediates rather than C atoms. As a result, *OCHO was formed during the reduction process, suppressing the generation of CO and enhancing the production of CH_4 accordingly. Ren *et al.* constructed a series of SACs with Fe SAs coordinated with boron (B) and C for promoting multi-electron reduction to CH_4.[218] By extensive theoretical calculations, the authors found that the introduction of B changed the adsorption strength of reaction intermediates by forming various FeB_xC_y structures, among which FeB_2C exhibited the best performance. The adsorption energy of the O atom played a crucial role in the regulated pathway with the weakened binding strength of *OCHO and enhanced binding strength of *HCOOH on the surface, which reduced the energy barrier of *OCHO to *HCOOH and accelerated the reaction kinetics. This change in adsorption energy of the O atom was confirmed to be associated with the more negative d-band center and the optimal Fe atomic magnetic moment of FeB_2C.

In addition, theoretical calculations further suggested some distinctive SACs that might take advantages in CO_2 reduction to CH_4.[219] By using DFT calculations, Back *et al.*[219] investigated the catalytic properties of TiC, TiN, and the corresponding single-atom catalysts for CO_2 electrochemical reduction. Among various SACs with single transition-metal atoms inserted into the surface defect sites of TiC, iridium-doped TiC (Ir@d-TiC) was found to exhibit a remarkably low overpotential of −0.09 V, which is the lowest value among that of any catalyst reported in the literature used to selectively produce CH_4 (−0.3–−1.0 V). This superior performance originated from a lacked sigma-type bonding interaction between *CO and Ir SA as compared to the cases of bare TiC or Ir(111), resulting in weakened *CO binding and the corresponding easier reduction in the limiting potential.

3.1.2.4 *Methanol.* Due to the wide applications of methanol in both chemical and energy industries, direct synthesis of methanol from electrochemical CO_2 reduction has raised considerable concern, although it is still a great challenge to achieve such a process encompassing six-electron and six-proton transfer. Given that Cu is still the only metal that exhibits appreciable efficiency in CO_2 reduction involving multiple electron transfer currently,[158,220] pioneering studies on SACs for methanol production have been focused on retrofitting Cu-based catalysts. Yang *et al.* developed an effective strategy for massive production of SACs with Cu SAs decorated through-hole carbon nanofibers, denoted as Cu SAs/TCNFs, for utilization as a cathode for CO_2 reduction.[221] Benefitting from the specific structure of the carbon membrane and highly dispersed Cu–N_4 sites, more active Cu SAs could effectively participate in the reaction. As such, the reduction process was promoted dynamically, resulting in a high current density of up to −93 mA cm^{-2}. As for the selectivity, DFT calculations indicated that Cu–N_4 sites possessed a relatively higher binding energy for the *CO intermediate, so that further reduction into methanol could become feasible rather than forming a gaseous CO product. As a result, nearly pure methanol in the liquid phase with 44% FE could be achieved over this Cu SAC. Inspired by the observation of the clearly different selectivities of methanol produced from CO_2 reduction in aqueous and non-aqueous solutions, Kong *et al.* designed a cuprous cyanamide (Cu_2NCN) crystal featuring isolated Cu(I) ions strongly conjugated with NCN^{2-} (Fig. 23).[222] They compared the dissociation enthalpy of O–C and Cu–O over typical Cu/Cu_2O sites and Cu_2NCN sites, respectively. It was found that $\Delta H_{Cu-O} > \Delta H_{C-O}$ in the former sites which propelled the formation of CH_4 without a C–O bond, whereas $\Delta H_{Cu-O} < \Delta H_{C-O}$ in the latter case, offering a chance to retain the C–O bond for methanol formation. They rationalized this conclusion by using a modern hard–soft acid–base (HSAB) theory, where weakened bonding was always formed between softer acidic sites (delocalized sites) and hard bases such as *O and *OR (R = H or alkyl). By introducing suitable delocalized electron states into isolated ionic Cu species, their soft acidic nature might be enhanced with reduced Cu–O bond strength. Based on this strategy, the formation of methane was suppressed and 70% FE towards methanol was reached with a methanol partial current density of −92.3 mA cm^{-2} and a production rate of 0.160 μmol

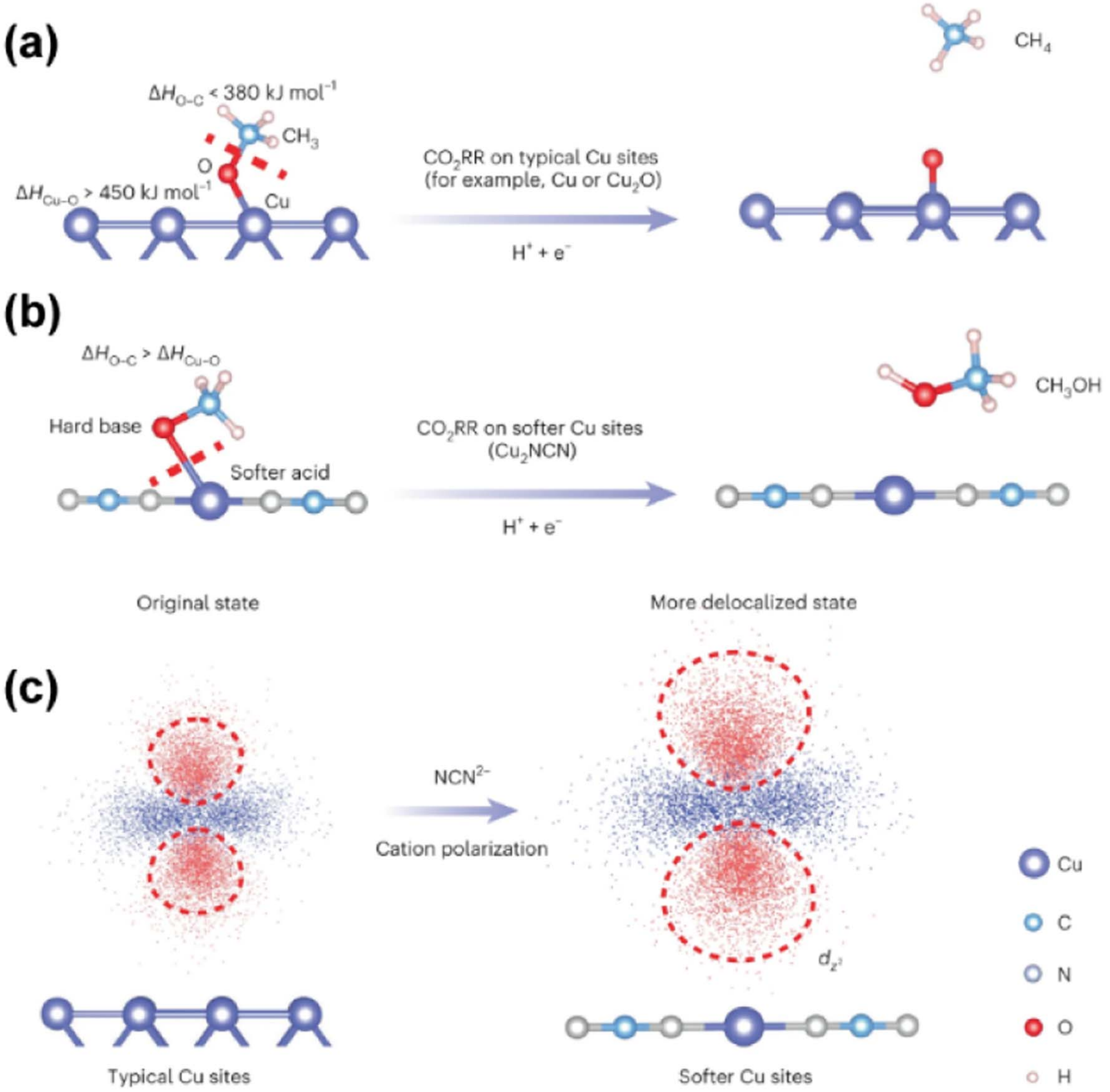

Fig. 23 (a) Typical Cu catalytic sites (for example, Cu or Cu_2O) display a relatively strong Cu–O bond (that is, the bond dissociation enthalpy, $\Delta H_{Cu-O} > 450$ kJ mol^{-1}) compared with the O–C bond (ΔH_{O-C} in OCH_3 is <380 kJ mol^{-1}), thus leading to cleavage of the O–C bond to release $^*CH_3$ and then form CH_4. (b) ΔH_{Cu-O} can be tuned to a lower value than ΔH_{O-C} at a softer acid site (for example, Cu_2NCN), enhancing the CO_2-to-CH_3OH selectivity. (c) Schematic illustration of the delocalized d-electron cloud induced by NCN^{2-} in Cu_2NCN.[222] Reproduced from ref. 222 with permission from Wiley, copyright 2022.

s^{-1} cm^{-2} in MEA-based cells. Furthermore, based on the investigations into the binding energy of *CO, Wu *et al.* developed a non-copper SAC with cobalt phthalocyanine immobilized on carbon nanotubes (CoPc/CNT), which could catalyze the CO_2 reduction to methanol *via* a so-called domino process *via* CO as the intermediate.[223] They found that Co–N_4 possessed a similar binding energy to that of Cu, compared with too strong binding over Fe–N_4 and too weak binding over Ni–N_4. Intuitively, Co–N_4 with a moderate binding energy mimicking Cu was expected to achieve a deep reduction just like that in the case of Cu. Indeed, individual CoPc dispersed by CNTs exhibited an appreciable methanol FE of up to 40%.

3.1.2.5 *Summary.* The direct electric energy input endows CO_2 reduction with feasible operation under mild conditions. The application of SACs in CO_2 electrochemical reduction not only pushes forward the practical utilization of noble metals, but also renders non-noble metals a suitable choice for preferential synthesis of specific products. Through modifying the chemical microenvironment of SACs *via* regulating parameters such as coordination (with heteroatoms like N, S, and O) and spatial distance (with other SA sites), appreciable performance regarding production of C_1 chemicals is demonstrated. Notably, the common well-defined active sites of SACs make theoretical calculations always take advantage in the investigation of the structure and mechanisms, as the theoretical calculations would in turn contribute to the reasonable prediction and good design of advanced SACs.[224]

3.1.3 Photochemical reduction. Given that thermal and electric energy are typical secondary energy sources, whose acquisition is always accompanied by perceptible loss during the processes of transformation and transfer inevitably, directly utilizing primary energy other than fossil resources in practical industry has been of great interest for a long time. Sunlight is just one of such generous primary energy sources. Inspired by the natural photosynthesis process that transforms CO_2 into carbohydrates with the energy supplied by sunlight, researchers have been pursuing bionic approaches to manufacture various chemicals from CO_2 through photochemical routes like the green plants are doing, endowing industrial production with renewable and clean features.[225] For making such "green plants" emerge and grow on land, great efforts have been devoted for studies on fundamental theories, design of novel materials and establishment of effective processes, in which the exploration of advanced photocatalysts is one of the focus points to break through the bottleneck of efficiency and economy.[45,51] In recent years, owing to the unique geometric and electronic structures of single atoms and inspired by the significant progress in thermo- and electro-catalysis, SACs have also been used in photoreduction of CO_2 for altering the energy bands of semiconductor materials, promoting the separation of photoexcited electron–hole pairs, propelling charge transfer and consumption, as well as modulating the adsorption and activation of CO_2 and the corresponding intermediates during the reaction processes.[45,226–228] Herein, significant progress on the application of SACs in photochemical CO_2 reduction will be demonstrated, encompassing the design of catalysts, optimization of processes and insights into mechanisms.[229]

C_1 products such as CO, HCOOH, CH_3OH and CH_4 are versatile platform chemicals in industry, whose production from photochemical CO_2 reduction is expected to confront the current excessive emission issues. Given the fairly long history of studies on conventional non-carbon-based semiconductors, researchers have achieved fruitful results on enhancing the selective synthesis of C_1 products by establishing SACs on the basis of previous studies. For instance, by adsorbing isolated Bi ions onto the surface of TiO_2 2D nanosheets, electron transfer from Bi ions to the TiO_2 substrate was presented by analyzing the density of states and corresponding charge density difference.[230] Such a transfer induced a built-in electric field from the surface of TiO_2 to the interior, and propelled the separation of electrons from photoexcited charge carriers and subsequent migration towards the surficial reaction region, thereby facilitating the reduction of CO_2 to CH_4 with an evolution rate of 4.1 μmol g^{-1} h^{-1}, 5.6 times larger than that for blank TiO_2. Embedding Cu SAs into anatase TiO_2, on the other hand, took effect in a distinct way, which results in CH_4 production with a 66-fold enhancement with respect to that of pristine TiO_2.[231] The introduction of Cu SAs first induced the formation of O_v by fortifying the surface reducibility of TiO_2 with an exposed mid-gap O state above the Fermi level in Cu_1/TiO_2. The combination of Cu SAs and vacancies contributed to the stabilization of intermediates on the TiO_2 surface. In contrast to Cu_2/TiO_2 with neighboring Cu atoms rather than the isolated state, in which electron localization was disturbed, Cu_1/TiO_2 with electron localization to the active Cu centers possessed strong Lewis basicity. This could further promote the electron transfer to the oxygen p state of CO_2, breaking the symmetry of CO_2 into two p states of each terminal oxygen atom and bending the C–O–C

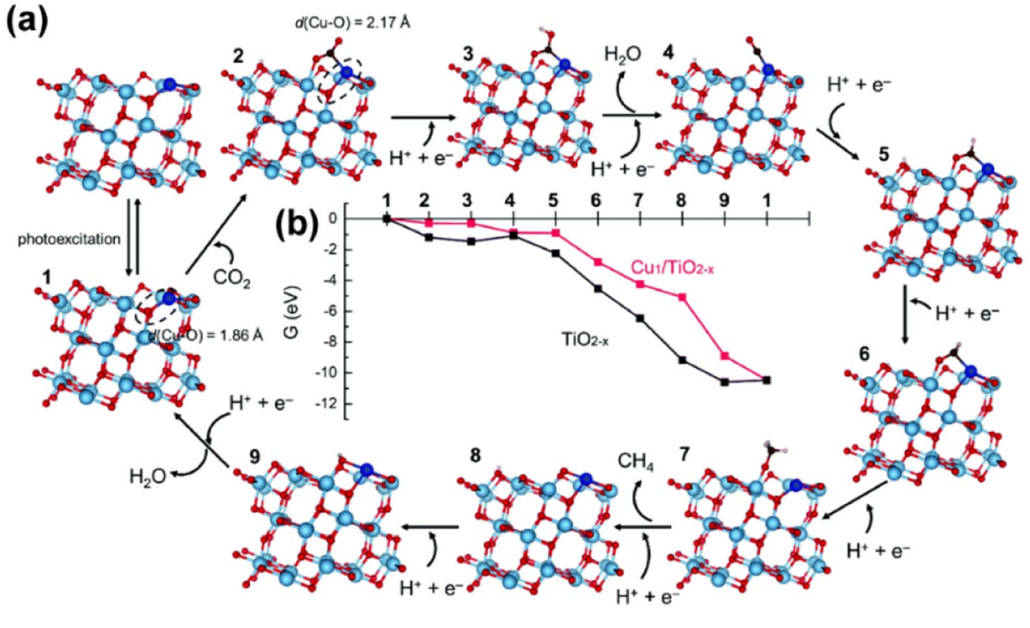

Fig. 24 Photocatalytic CO_2 reduction at Cu_1/TiO_2 with an oxygen vacancy. (a) CO_2 reduction mechanism at Cu_1/TiO_{2-x} and (b) DFT energetics of CO_2 reduction at Cu_1/TiO_{2-x} and TiO_{2-x}. During the reduction process, the photoexcited electron is assumed to be transferred from the conduction band minimum of TiO_2 (−0.25 V *versus* RHE).[231] Reproduced from ref. 231 with permission from Royal Society of Chemistry, copyright 2022.

bond angle, favoring the chemisorption of CO_2 molecules (Fig. 24). The effect of the Cu valence state might also play an important role in the performance of Cu/TiO_2 SACs and has drawn attention in some other reports. Jiang *et al.* thought that Cu^0 served as the active sites for CO_2 reduction to CO over the Cu/TiO_2 SAC, which could be formed through reduction of Cu^{2+} by photogenerated CB electrons of TiO_2 under solar irradiation.[232] However, Cu^0 active sites suffered from gradual oxidation into Cu^{q+} by the generated O_2, providing the Cu/TiO_2 SAC with slowly decreasing activity, since Cu^{q+} was difficult to be reduced under the reaction conditions thermodynamically. In this case, the activity could be restored by opening the reactor for exposure to air or oxygen leading to complete oxidation to Cu^{2+}. Then, the reactor should be resealed for the reduction of Cu^{2+} to Cu^0 and the next reaction cycle. A similar dynamic evolution of Cu species over a Cu SAC with atomically dispersed Cu on mesoporous TiO_2 was also observed by an *in situ* XAS technique.[233] The difference was that the Cu^0/Cu^+ mixture was proposed to be more efficient for CH_4 production based on a synergy with the meso-structure and enhanced charge carrier transfer. Further introducing other types of active components into the Cu/TiO_2 SAC provided opportunities for boosted CO_2 reduction. By using such a strategy, Yu *et al.* constructed an excellent photocatalyst where Cu SAs and Au–Cu alloy NPs coexisted on TiO_2, achieving a record-high formation rate of 3578.9 $\mu mol\ g^{-1}\ h^{-1}$ for CH_4 and appreciable production of C_2H_4.[234] It was found that there was a synergistic effect between Cu SAs and Au–Cu alloy NPs. Such an effect could enhance the adsorption and activation of CO_2 and H_2O and lower the overall activation energy barrier, particularly that of the rate-determining steps for CH_4 and C_2H_4 formation.

Apart from TiO_2, SACs based on other non-carbon-based substrates have been also extensively reported. One of them was based on a combination of Ni SAs and defect-rich zirconia.[235] The Ni SAs were considered to have an effect on the kinetics of CO_2 conversion to CO by lowering the energy barrier in a *COOH intermediated pathway. Besides, the H_2 desorption as a competitive reaction consuming photogenerated electrons was also suppressed to a certain extent with the assistance of Ni SAs. Ding *et al.* compared the performances of a photocatalyst with Ag SAs supported on manganese oxide (Ag-HMO) and its counterpart with Ag NPs (Ag/HMO) for photocatalytic CO_2 reduction.[236] As a result, the Ag SAC exhibited a higher activity of CH_4 production of up to 0.61 mol mol^{-1}, which was 1.53 times as high as that of Ag NPs. This difference was rationalized by the promoted electron transfer from Ag to HMO, adsorption of visible light and the activation of CO_2 over the SAC. A similar contrast was presented over the Pt–V_2O_5 SAC derived from vanadium-based polyoxometalates and Pt NPs supported on V_2O_5.[237] Separated groups containing Pt–V and V in the precursor were converted into mono-dispersed Pt centers and surrounding vanadium oxide, respectively. The Pt SA sites were in the positive oxidation state, and tetra-coordination geometry assisted by four surface oxygen atoms of V_2O_5 favored the formation of the *COOH intermediate *via* a proton-coupled electron transfer process, followed by hydrogenation into *CO. The Pt SA site further stabilized *CO for its deep hydrogenation into CH_4. The distinctive properties of Pt–O and tremendously enhanced atom utilization contributed to excellent activity that was 25 times higher than that of Pt-NP-V_2O_5. In some cases, significant dependence of activity on the distinct vacancies was shown on SACs with the same metal SAs. This correlation was unveiled over a CdS supported Au SAC by selectively creating Cd or S vacancies before anchoring Au atoms (Fig. 25).[238] As for S vacancy dominated CdS, electrons tended to be localized at Au SA sites based on DFT calculations. In contrast, electrons were more likely to accumulate at the vacancy sites over CdS with abundant Cd vacancies. This difference in electron spatial arrangement made the adsorption type of CO_2 change from physical adsorption to chemical

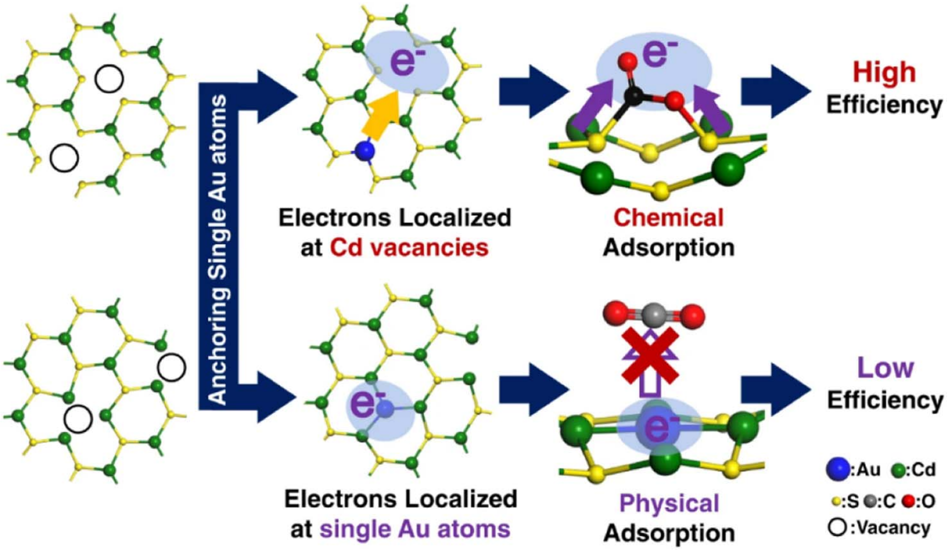

Fig. 25 Schematic illustration of single Au atoms in CdS to promote CO_2 photoreduction.[238] Reproduced from ref. 238 with permission from Springer Nature, copyright 2021.

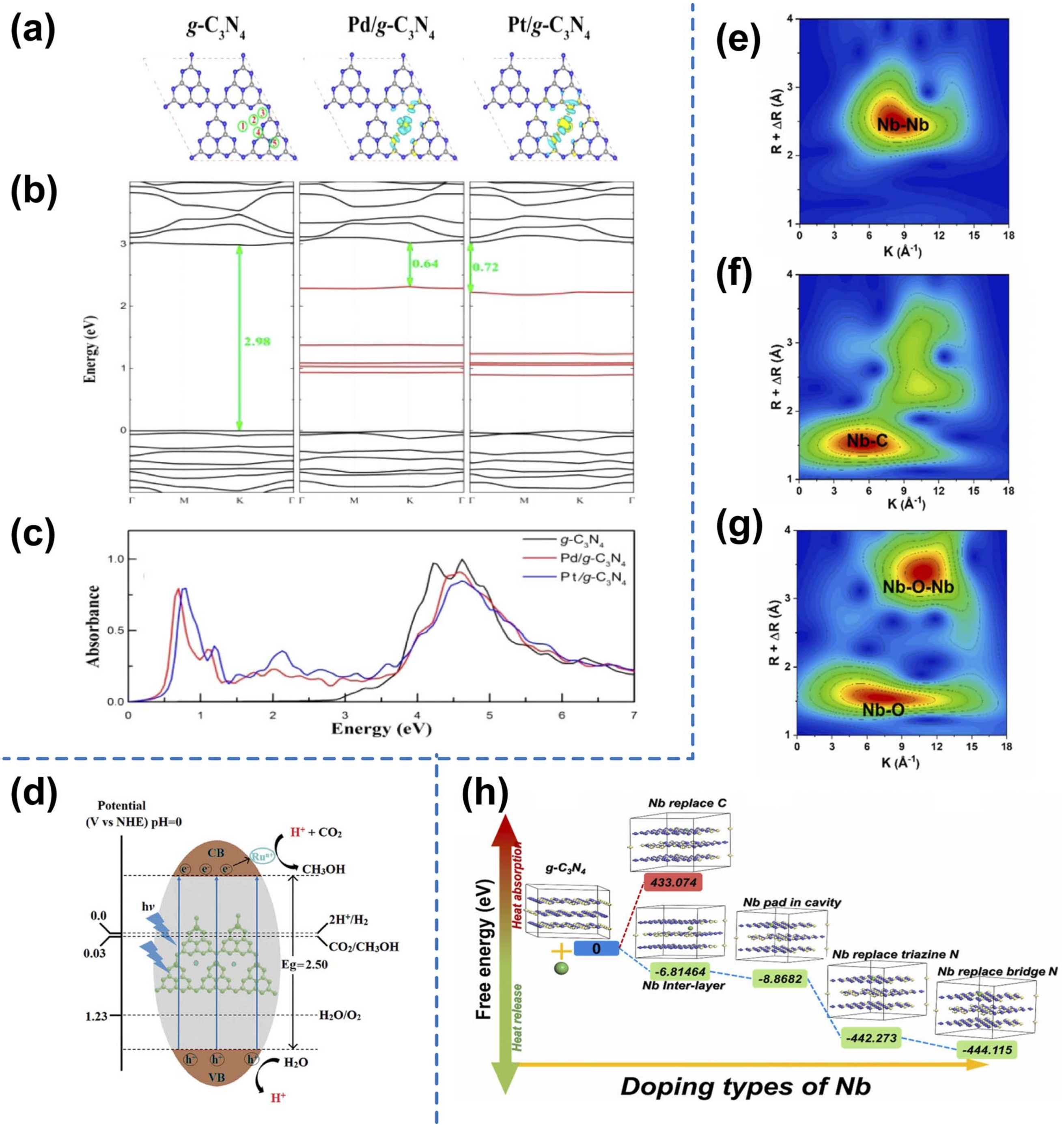

Fig. 26 (a) Optimized structure and plots of 3D differential charge densities, (b) band structures, and (c) optical absorption spectra of g-C_3N_4, Pd/g-C_3N_4, and Pt g^{-1}-C_3N_4.[252] (d) Possible schematic representation of the photocatalytic mechanism over the RuSA-mC_3N_4 surface under visible light irradiation.[250] The WT-EXAFS plots of Nb-foil (e), CNNb0.06 (f), and Nb_2O_5 (g), respectively; free energy (h) of various possible modes of single-atom Nb using DFT calculations.[243] Reproduced from ref. 240, 243, 250 and 252 with permission from American Chemical Society, Wiley and Elsevier, copyright 2016, 2020, 2023.

adsorption. In contrast to catalysts without Au or with NCs, the strong hybridization of Au 5d and S 2p orbitals for the SA sites endowed CdS with superior efficiency of photo-electron transfer on the surface and a corresponding lower energy barrier for the formation of key intermediates during CO_2 reduction. More recently, a silicon-based Co SAC was reported for the production of syngas with a highly tunable H/C ratio.[239] A solid-state epitaxy method was used for the construction of such a SAC with Co SAs well dispersed on crystalline silicon, through a multistep variable-temperature annealing including the preliminary incorporation of Co atoms in the Si lattice and the following decomposition of the $CoSi_2$ domain. With the addition of a particular photosensitizer and sacrificial agent, CO and H_2 yields of 4.7 mol $g_{(Co)}^{-1}$ and 4.4 mol $g_{(Co)}^{-1}$ were achieved through visible-light-driven CO_2 reduction, in which the H/C ratio could be tuned from 0.8 to 2 by modulating the Co loading amount.

Owing to their distinctive electronic energy band structures and fairly controllable physical properties such as porous structure and electrical and thermal conductivity, carbon-based semiconductors including various pure or heteroatomic carbon materials have been also widely studied and applied in photocatalysis.[51,240,241] More importantly, carbon materials are considered as a renewable resource that is promising for sustainable utilization. Thus, there have been quite a few reports on SACs with carbon-based semiconductors as substrates. Graphitic carbon nitride (g-C_3N_4), as one of the most advanced carbon-based materials with excellent photochemical properties,[242] has exhibited superior performance in CO_2 reduction in collaboration with various metal SAs.[243–256] Generally, SACs based on noble metals such as Pd, Pt, Au, and Ru played a crucial role in two aspects: the first is functioning as active sites for CO_2 adsorption and activation as well as the stabilization of various intermediates; the second is manipulating the band structure of g-C_3N_4 for enhanced visible-light absorption (Fig. 26a–d).[250–252] The former feature also offered chances for the modulation of the product selectivity by controlling the kinetic pathways involving the formation and transformation of key intermediates with varied free energy barriers, *e.g.*, the dominant product was shifted from HCOOH over Pd SAs to CH_4 over Pt SAs,[252] while a higher yield of methanol was exhibited over Ru SAs.[250] The latter feature, on the other hand, could afford higher efficiency of energy utilization in a practical process. In addition, non-noble metals such as Co, Ni, and Cu have also demonstrated outstanding performance in the SA state on a g-C_3N_4 substrate.[245,253–255] In the above cases, the effect of N coordination in charge of the stabilization of SAs and local electron density of metal sites was mentioned more than one time. This effect was mainly derived from the interaction between the lone-pair electrons in the adjacent N atoms and d orbitals of metal SAs, imposing a positive oxidation state on SA sites in g-C_3N_4 that was slightly lower than that in oxides.[252] This was an intuitive result according to the differences in electronegativity of N and O. SAs in the lower positive oxidation state were considered to be in favor of the adsorption and activation of reactants in some cases. However, in a niobium (Nb) SAC, carbon atoms were believed to coordinate with metal SAs exclusively in g-C_3N_4 with abundant N vacancies (Fig. 26e–h).[243] In this case, polarized Nb–C bonds provided a high-speed channel for the directional transfer of photogenerated electrons and accordingly restrained the recombination, while the N vacancies were more likely to be responsible for the enhanced formation of charge carriers. Recently, it has been reported that SACs, particularly those that were based on rare earth metals such as lanthanum (La), dysprosium (Dy), and erbium (Er), could serve as a so-called electron bridge to assist charge transfer especially in heterojunction photocatalysts with a Z-scheme structure.[244,247,248,257] To clarify, the Z-scheme structure was proposed for describing the photosynthesis process in natural bionts initially, and the concept was introduced into artificial photocatalysis systems for establishing excellent heterojunction photocatalysts with both enhanced electron transfer and sufficient redox potential for surface reactions.[258–260] As a heterojunction was constructed to solve the dilemma of stronger light absorption (need a narrow gap between the CB and VB) or higher potential (need a wide gap between the CB and VB), a heterojunction with a Z-scheme structure featured a staggered band configuration with a medium for electron transfer from the lower CB in the oxidation semiconductor to the higher VB in the reduction semiconductor. In this way, both enhanced charge-separation efficiency and retained redox ability can be simultaneously achieved. Coincidentally, SAs of some rare earth metals with 4f levels between the VB of a certain semiconductor and CB of g-C_3N_4 were supposed to act as such a medium, as reported in recent studies.[244,247,257] Specific rare earth metal SAs could also function as key active centers for CO_2 activation, intermediate formation and products, *e.g.*, CO desorption.[248] In contrast, other transition metal SAs, like cobalt, were also claimed to have an effect on the prolonged lifetime besides engaging in the reduction reaction over Z-scheme heterojunctions.[261]

The SAs could further be introduced into other functional carbon-based materials, such as N-doped CNTs,[262] N-doped oxidized graphene,[263] and N-doped carbon.[264,265] Different supports provided not only distinct porous structures for mass transfer which imposed an enrichment or evacuation effect, but also specific chemical environments for the stabilization of SAs that were also endowed with regulated electronic properties. Notably, in some cases, N-doped carbon supports did not possess the attributes of a semiconductor with insufficient capability to harvest light; photosensitive reagents such as $[Ru(bpy)_3]Cl_2 \cdot 6H_2O$ (bpy = 2,2′-bipyridine) should be added into reactors for the generation of photo-excited electrons, and a sacrificial hole scavenger such as triethanolamine (TEOA) should be also involved in the systems for the removal of holes. This suggested that carbon supports in contact with both SAs and photosensitive reagents also functioned as a bridge for electron transfer.[263–265]

Apart from widely used semiconductors, reticular materials represented by metal organic frameworks (MOFs) and covalent organic frameworks (COFs) featuring high specific area and an abundant porous structure, have been also exploited as photocatalysts for CO_2 reduction recently.[226,266–270] Thanks to the tunable structural and chemical properties, MOFs and COFs are also ideal choices for bearing metal SAs to further modify the catalytic performance. Resembling the circumstances in N-doped carbon substrates, most MOF and COF materials need auxiliary reagents to assist in light harvesting and hole scavenging as well. SAs embedded in MOFs and COFs are more likely to serve as active sites for CO_2 activation, and thereby the reticular materials show advantages as they are endowed with a large active interface.[266] Besides these general scenarios, some other factors might be equally important for optimizing the performance. Zhong *et al.* fabricated a 2,2′-bipyridine-based COF bearing single Ni sites (Ni-TpBpy) for exclusive selective production of CO from CO_2 photoreduction.[267] Under visible

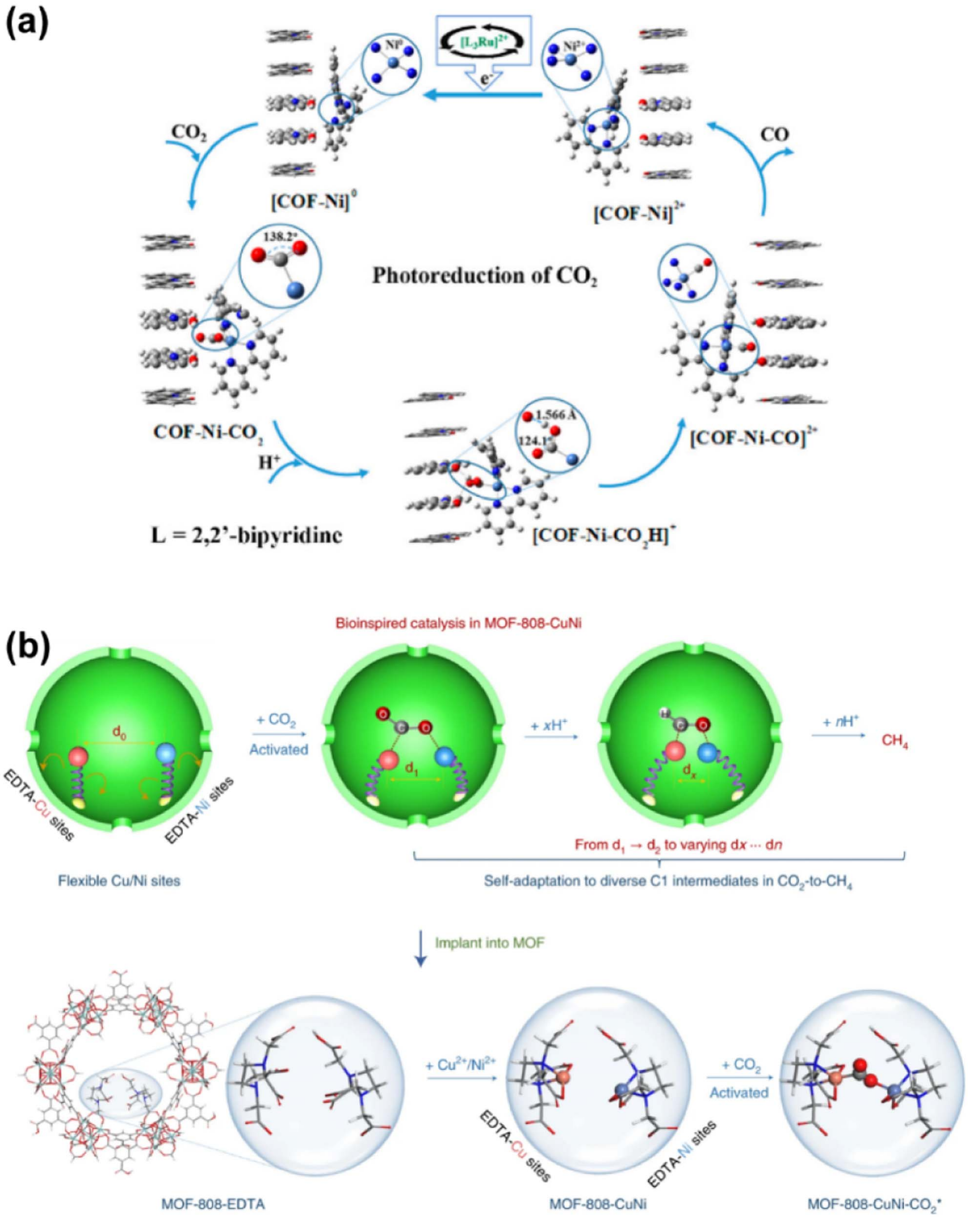

Fig. 27 (a) Proposed reaction mechanism for the photoconversion of CO_2 into CO on Ni-TpBpy.[267] (b) Implanting flexible and self-adaptive Cu/Ni DMSPs into MOF-808 for highly selective CO_2 photoreduction to CH_4.[268] Reproduced from ref. 267 and 268 with permission from American Chemical Society and Springer Nature, copyright 2019, 2021.

light irradiation, $Ru(bpy)_3^{2+}$ was excited and transferred electrons for the subsequent reduction of coordinated CO_2 molecules on Ni-TpBpy. H_2 evolution could be well inhibited due to the higher affinity of CO_2 species than that of H^+. As CO_2 was activated by Ni SAs, verified by the bent configuration of coordinated CO_2 molecules, the significantly decreased free energy of the COF–Ni–CO_2H intermediate could be ascribed to the formation of hydrogen bonds between COOH and the keto group of the TpBpy moiety (Fig. 27a). Thus, TpBpy not only functioned as a host for CO_2 molecules and Ni SAs but also played a vital role in the enhanced activity and selectivity of the reduction of CO_2 to CO. Given that the activation of reactants and transformation of intermediates always involve complex variations in chemical bonding between C–O, C–H and C–C during the whole process of CO_2 reduction, the capability to adapt such variations might be the key to stabilize the intermediates for a lower energy barrier in a specific reaction pathway. Hence, inspired by the mechanisms of enzymes in organisms, Li *et al.* demonstrated a photocatalyst with flexible Cu–Ni dual-metal-site pairs (DMSPs) featuring dynamic self-adaptive behavior to match mutative C_1 intermediates for CO_2 photoreduction to CH_4.[268] The DMSPs were incorporated into a MOF to afford their respective SA forms in a flexible microenvironment. Based on DFT calculations, it was proposed that the distance between Cu and Ni SA pairs ($d_{Cu–Ni}$) with an original value of 4.312 Å, was adjusted to 4.454 Å to match the COOH* intermediate after one proton-coupled electron transfer process, followed by a further change to 4.356 Å after COOH* was converted into HCOOH*. Such accommodations provided key intermediates with a strong binding, thereby suppressing desorption, and leading to facilitated deep protonation to CH_4 (Fig. 27b). Similar dependences of SA sites and intermediate species have been also reported in other systems, *e.g.*, Cu SAs in a MOF (Cu/UiO-66-NH_2) exhibited lower formation energy of COOH* and CHO* and capability for subsequent coupling between them, resulting in appreciable selectivity to methanol and ethanol;[271] Mo SAs in a COF (Mo-TpBpy) favored CO adsorption, thereby enhancing the synthesis of CH_4 and C_2H_4.[269] Such dependences are also associated with distinct ligands, *e.g.*, Co–O_4 atomic sites in Co-2,3-DHTA-COF exhibited superior performance for CO production from CO_2 photoreduction due to the lower energy barrier in the ligand exchange process between Co-2,3-DHTA-COF and CO_2, compared with that of its counterpart with different ligands (Co-TP-COF).[270]

Recently, MXenes, a family of two-dimensional (2D) transition metal carbides, nitrides, and carbonitrides, have attracted burgeoning research interest for their application in photocatalysis due to their outstanding structural and electronic properties. However, the scarcity of active sites limits the exploitation of MXene-based photocatalysts, and therefore metal SAs have been incorporated into certain MXenes, providing a high-efficiency reaction interface for CO_2 reduction.[272] Co SAs immobilized on a $Ti_3C_2T_x$ MXene by bonding with C and O atoms, were found to facilitate the formation of the *COOH intermediate with lower free energy in comparison with that of a blank MXene support, while the MXene support not only served to host the isolated Co sites, but also accepted electrons from the light absorber $[Ru(bpy)_3]^{3+}$ and transferred them to Co sites toward CO_2 conversion.

3.1.3.1 *Summary.*

Light-drive CO_2 reduction might be a truly sustainable process which is expected to realize a net CO_2 emission of nearly zero due to the utilization of a completely renewable energy source. SACs function not only as co-catalysts with incorporation into existing semiconductor materials but also as the sole catalyst in the presence of photosensitizers and sacrificial agents. In the former cases, SACs play a crucial role in both the activation of reactants and generation/transfer of photoexcited electrons *via* modulating the energy band of semiconductors. In the latter cases, MOFs and COFs with high specific area and abundant porous systems serve as common substrates for anchoring metal SAs, providing larger interfaces for the contact between photosensitizers and active sites, thereby enhancing the electron transfer and reaction kinetics.

3.1.4 Dry reforming.

The dry reforming process provides a promising prospect for the burgeoning global cyclic economy with not only a syngas output that serves as a building block for the synthesis of various chemicals, but also the consumption of CO_2 and CH_4 that are both culprits of the greenhouse effect. Although having been studied for decades, the large-scale adoption of the dry reforming reaction in industry has not seen the light of dawn due to the high energy demands and commonly occurring catalyst deactivation under rigorous conditions, particularly for that based on non-noble metals.[274] The tough operation parameters determined by the thermodynamic natures also limits practical efficiency of the dry reforming process.[275] All these problems lead to a great requirement for advanced catalysts, among which SACs provide a glimmer of hope for the solutions. The strong affinity for carbon atoms renders metallic nickel a highly active component in dry reforming reactions to break C–H of methane. In contrast, too strong binding of carbon atoms on Ni NPs might bring about the excessive pyrolysis of methane, resulting in the formation of an inert carbon layer covering the active sites and eventual deactivation. To fight against the pervasive deactivation over Ni-based catalysts, Qiao *et al.* fabricated a SAC with atomically dispersed Ni SAs, well-stabilized by interaction with Ce-doped hydroxyapatite.[276] The isolated Ni atoms could function as intrinsically coke-resistant sites thanks to their unique ability to only activate the first C–H bond in CH_4, thereby circumventing the deep decomposition of CH_4 into deposited carbon, further contributing to its excellent activity and stability in a 100 h dry reforming reaction. Tang *et al.* designed a SAC comprising CeO_2 nanorods and two sets of SA sites, Ni and Ru.[273] The SAC with two sets of SAs exhibited a much lower apparent activation energy and higher turnover rate for the production of H_2 and CO compared with the SAC with only one set of SAs (Fig. 28). These results were rationalized by a synergy effect between Ni SAs and Ru SAs. The Ni SA sites were responsible for the progressive CH_4 oxidation towards CO and H, while the Ru SA sites were in charge of activation of CO_2 into CO and O with the collaboration of neighboring oxygen vacancies (O_v) over CeO_2. The generated H atoms over Ni SA sites were considered to be coupled over Ru SA sites rather than Ni, since this process was favorable in both thermodynamics and

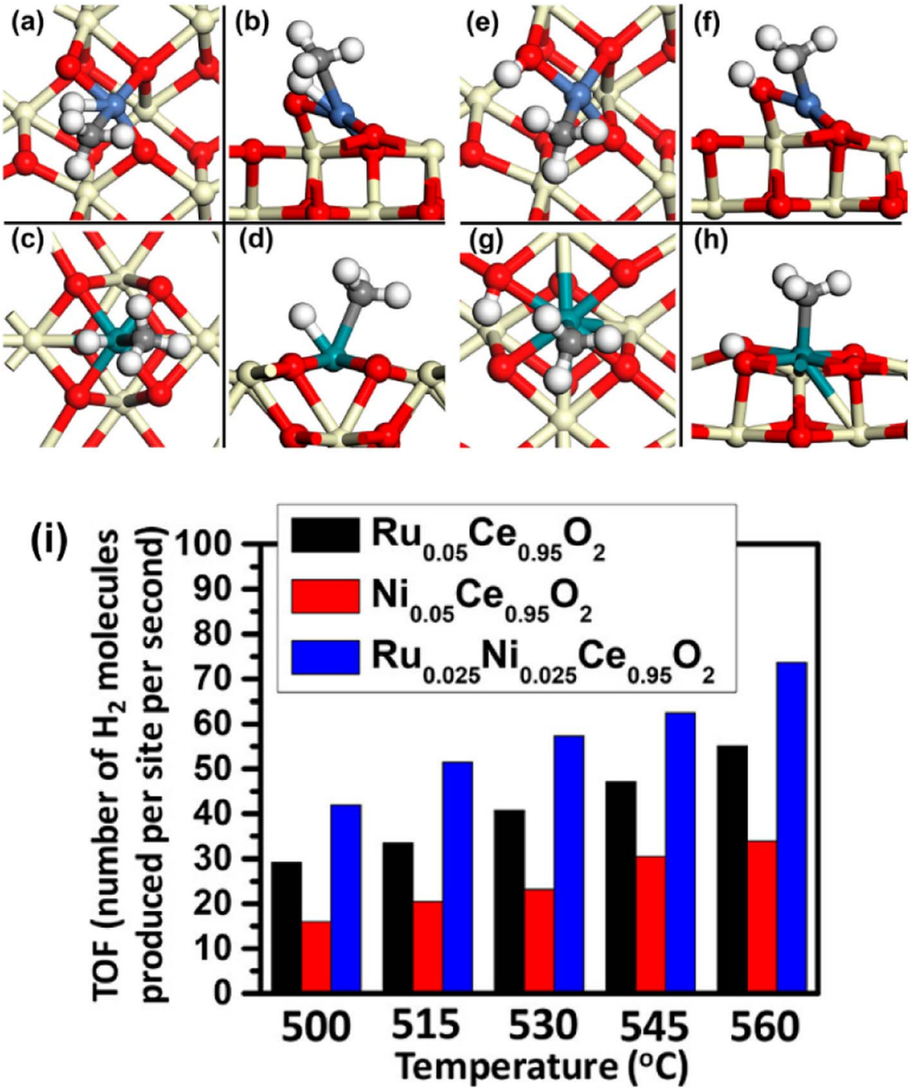

Fig. 28 Top views and side views of transition-state geometries of CH_4 activation and intermediate structures of the formed CH_3 and H on Ni_1 and Ru_1 sites on CeO_2. Top and side views of transition-state geometries of CH_4 activation on Ni_1 (a and b) and Ru_1 (c and d) and intermediate geometries of CH_3 and H formed on the Ni_1 site (e and f) and Ru_1 site (g and h). (i) Turnover frequency (TOF) of reforming CH_4 with CO_2 in terms of hydrogen production per Ni_1 site of $Ce_{0.95}Ni_{0.05}O_2$, per Ru_1 site of $Ce_{0.95}$ $Ru_{0.05}O_2$, and per Ni_1 or Ru_1 site for $Ce_{0.95}Ni_{0.025}Ru_{0.025}O_2$ at 773–833 K. In the calculation of TOFs, the number of catalytic sites for $Ce_{0.95}Ni_{0.025}Ru_{0.025}O_2$ is the total number of Ni and Ru atoms of the topmost surface layer of $Ce_{0.95}Ni_{0.025}Ru_{0.025}O_2$.[273] Reproduced from ref. 273 with permission from American Chemical Society, copyright 2019.

kinetics as unveiled by DFT calculations. Notably, the O_v in the CeO_2 support played a vital role in not only the activation of CO_2 but also the stabilization of metal SAs. By manipulating the O_v, the performance of SACs in dry reforming reactions could be further modified, as reported by Wu *et al.*[277] They constructed a series of Ni/CeO_2 SACs with various concentrations of O_v by introducing different metal cations to partially replace Ce^{4+} on the surface of supports. On the premise of equally active Ni SAs for efficient C–H activation, the dependence of activity and durability on concentration of O_v was supposed to be attributed to the promoted adsorption and activation of CO_2 molecules, as well as the much easier removal of surface coke assisted by active O species adsorbed on O_v. The prompt elimination of coke plus the stabilization effect of O_v on Ni SAs assuaged the deactivation to some extent and guaranteed excellent performance during a long-term test. In the cases where noble metals were used, the regulation of O_v could also take effect in a similar way. For instance, by doping Pt SAs onto CeO_2 rods, the formation of surface O_v could be also enhanced.[278] The Pt SA and bonded lattice O atoms showed a synergy effect on the activation of methane *via* an O-assisted dissociation, while the activation of CO_2 was largely propelled by the surface O_v. Moreover, the noble metals in the form of SAs could also facilitate resistance to carbon deposition by improving the reducibility of active components without inducing the oligomerization of C–H species due to the isolated spatial distribution.[279] Apart from the above conventional thermo-catalytic dry reforming process, a light-driven process has been proposed

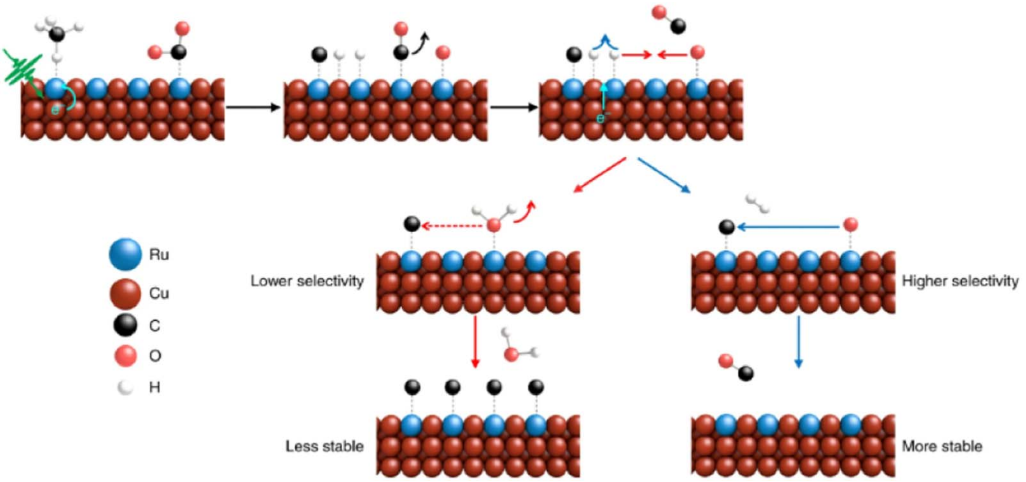

Fig. 29 Schematics of enhanced selectivity and stability in photocatalysis *via* the electronic transition mechanism. The green pulse indicates light excitation. e^- represents the hot carrier and the cyan arrow indicates transfer and surface excitation by hot carriers. Blue and red arrows indicate the reaction path of photocatalysis and thermocatalysis, respectively. The dashed arrow indicates a less probable reaction path.[280] Reproduced from ref. 280 with permission from Springer Nature, copyright 2020.

and performed with a photocatalyst featuring a Cu NP 'antenna' with Ru SA 'reactor' sites on the NP surface.[280] The introduction of Ru SAs was found to be able to not only lower the activation barrier of CH_4 dehydrogenation steps relative to pristine Cu NPs for enhanced activity, but also inhibit the RWGS reaction and coke formation for excellent durability, which would be reversed once the aggregation of Ru SAs occurred. Given that completely different performances were demonstrated in a photo-synthesis system and a thermo-synthesis system, a hot-carrier mechanism was speculated to also be responsible for the acceleration of C–H activation and of H_2 desorption, which enabled kinetic matching of CO and H_2 formation, leading to minimized RWGS and coking reactions (Fig. 29).

3.2 CO_2 conversion toward C_{2+} products

3.2.1 Thermochemical reduction. Ethanol, as a renewable resource, features lower toxicity than and comparable versatility to methanol in both the energy industry and chemical production.[281] Although in comparison with methanol, the ethanol synthesis from CO_2 hydrogenation is more thermodynamically favorable (Fig. 4), it is still a great challenge to design catalysts with high efficiency, since the generation of ethanol involves not only the stepwise hydrogenation procedures, but also the controllable formation of C–C bonds. Hence, most of the studies on highly selective synthesis of ethanol *via* direct CO_2 hydrogenation are in their infant stage currently, in which the application of SACs has provided some inspiration for future research studies.

A group of Pd-based SACs fabricated by Caparrós *et al.* with various supports, were applied in gas phase hydrogenation of CO_2 into ethanol.[282] A catalytic performance dependent on the specific interaction between Pd SAs and different inorganic oxide supports was found, which was attributed to the particular architecture established for C–C coupling. NP species were confirmed to be inactive for the formation of ethanol by increasing the reaction temperature to create a NP-dominated catalyst. It was an inspiring result that a SAC could work in a complicate hydrogenation process leading to the formation of ethanol. However, ethanol yield was limited by severe RWGS over this Pd SAC, and deep insights into the relevant reaction mechanism were still absent. Ye *et al.* studied the whole process of CO_2 hydrogenation into ethanol in depth over an Ir-based SAC.[59] They designed a bifunctional SAC (Ir_1–In_2O_3) by anchoring monoatomic Ir onto the In_2O_3 carrier with abundant vacancy sites. On the one hand, a part of the feed CO_2 was activated by a Lewis acid–base pair formed by the coupling between the isolated Ir atom and the adjacent oxygen vacancy on the surface of In_2O_3, followed by the generation of intermediate species of carbonyl (CO*) adsorbed on the Ir atom ($Ir^{\delta+}$–CO*). On the other hand, another part of the feed CO_2 was activated and transformed into methoxide species by oxygen vacancies (CH_3O^*–O_v). Cohesive corporation between the two types of active sites offered great opportunities for an effective C–C coupling reaction, resulting in a high selectivity for ethanol (>99%) with an excellent initial turnover frequency (481 h^{-1}) for the hydrogenation of CO_2 in the liquid phase (Fig. 30). In a subsequent study by the same group, 1D Mo_2C nanowires with dominant (101) crystal surfaces were modified by the deposition of atomic Rh and K for CO_2 hydrogenation to ethanol.[283] In comparison with unmodified β-Mo_2C that only converted CO_2 to methanol, $K_{0.2}Rh_{0.2}$/β-Mo_2C demonstrated an ethanol selectivity of 72.1% at 423 K. As the active carrier β-Mo_2C was in charge of the formation of CH_3O^* intermediates, Rh SAs served as the active sites for activation of CO_2 and stabilization of CO adsorbed species (CO*) in an electron-deficient state, favoring the subsequent CO* insertion. As such, the synergistic effect between these two functionalities led to highly specific controlled C–C coupling. The introduction of K had an effect by promoting the adsorption and activation of CO_2, as well as regulating the activation of hydrogen, resulting in a more

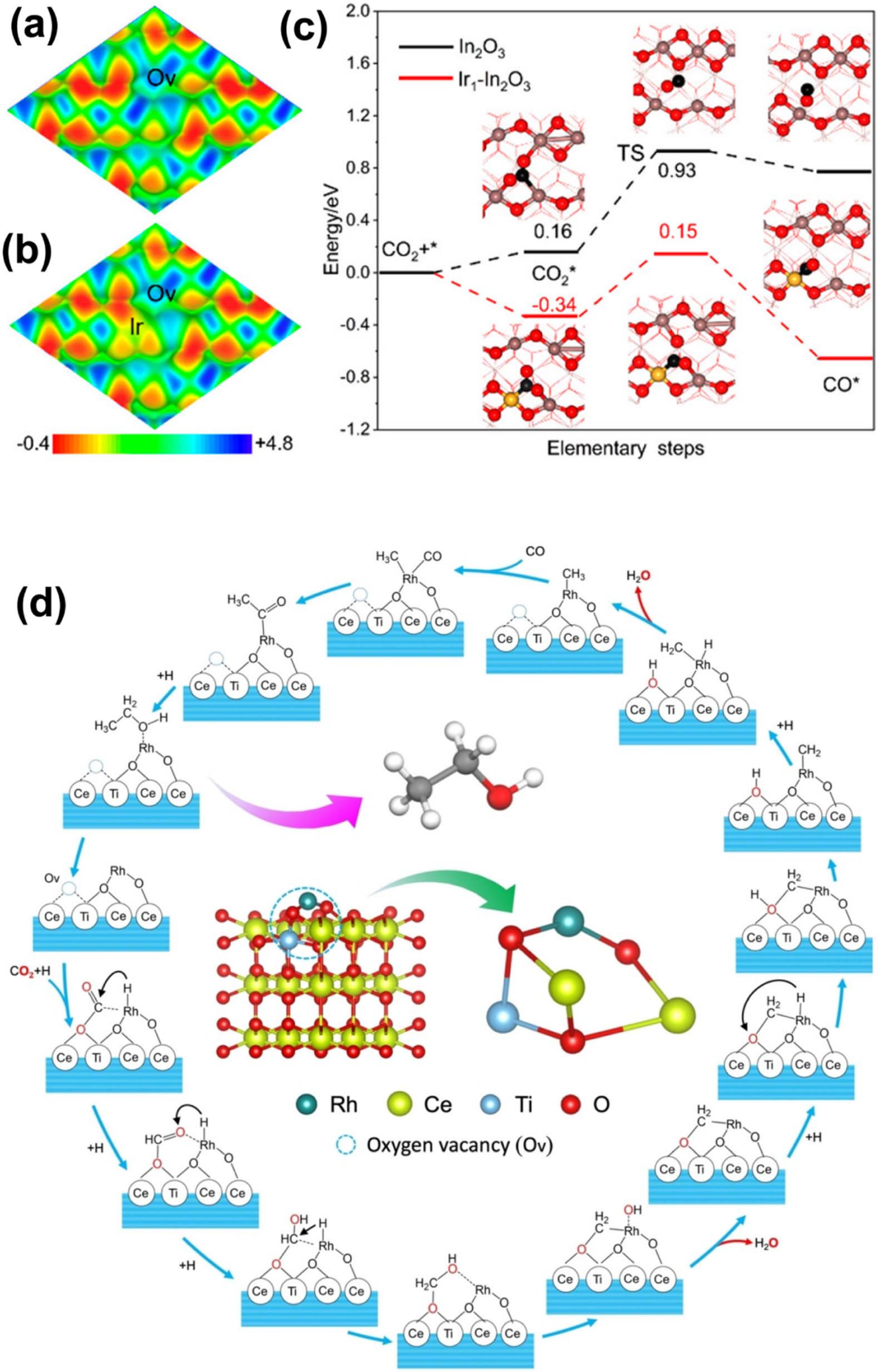

Fig. 30 Electrostatic potential diagrams of the In_2O_3 (a) and $Ir_1–In_2O_3$ catalyst surface (b). Free energy diagram for CO_2 dissociation over the In_2O_3 and $Ir_1–In_2O_3$ catalyst (c).[59] (d) The illustrated catalytic cycle of ethanol formation from CO_2 hydrogenation over the $Rh_1/CeTiO_x$ catalyst. The inset figure displays the structure of the $Rh_1/CeTiO_x$ catalyst.[284] Reproduced from ref. 59 and 284 with permission from American Chemical Society and Wiley, copyright 2020 and 2022.

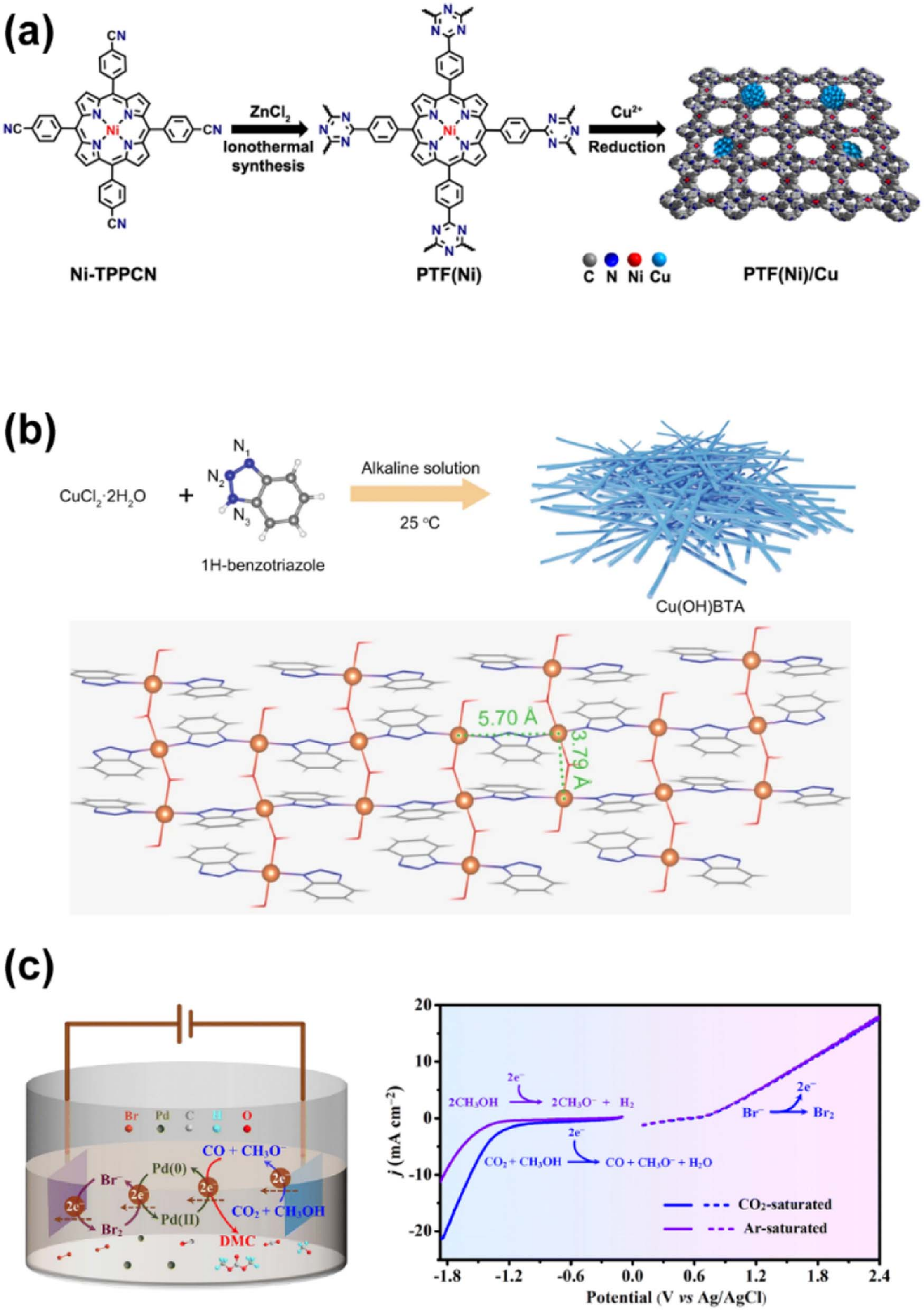

Fig. 31 (a) Schematic illustration of the synthesis procedure and the wireframe model of Cu(OH)BTA.[164] (b) Fabrication of PTF(Ni)/Cu with well dispersed copper sites from Ni-TPPCN. (c) Schematic for the convergent paired electrosynthesis of DMC from CO$_2$.[159] (b) LSV of Ni SAs/OMMNC for electrocatalytic CO$_2$RRs in CO$_2$-saturated 0.1 M KBr–CH$_3$OH in H-type cells.[291] Reproduced from ref. 159, 164 and 291 with permission from Wiley, Springer Nature and Royal Society of Chemistry, copyright 2021, 2023.

balanced performance of the two active centers and a further improved ethanol selectivity. Coincidentally, a similar SAC system containing such bifunctional components with Lewis acid–base pairs was reported by Zheng *et al.* They established a Rh-based SAC by embedding monoatomic Rh onto a Ti-doped CeO_2 support ($Rh_1/CeTiO_x$).[284] The formation of oxygen vacancies on the surface of reducible CeO_2 was promoted with the introduction of Rh SAs and Ti. Meanwhile, the Rh SAs coupled with neighboring oxygen vacancies, existing in the form of Rh_1–O_v Lewis acid–base pairs, played a vital role in the enhanced CO_2 adsorption and activation. Different from the reaction pathway over Ir_1–In_2O_3, CO_2 was converted into CH_3^* species *via* the HCOO* intermediate over Rh_1–O_v active sites, and subsequently CO* generated from RWGS was inserted into Rh–CH_3, leading to the formation of C–C bonds. Ethanol was formed and desorbed through the following hydrogenation eventually, completing a catalytic cycle (Fig. 30). In particular, the SAs ensured the high selectivity of ethanol by regulating the CO adsorption over metal sites, while NPs and NCs provided methanol-dominated products.

3.2.2 Electrochemical CO_2 reduction to C_{2+} chemicals. Generally, the synthesis of products with more than two carbon atoms needs not only the transfer of multiple electrons and protons, but also activity for C–C coupling. The complex nature of these reaction processes suggests that catalysts with multifunctional sites are always necessary to modulate and match different key steps.[285] In this case, SACs with isolated and relatively uniform sites might not be able to afford such an obligation, while bulk catalysts and integrated catalysts have accounted for these systems.[160–163] However, it is still possible that SA sites play a critical role in the synthesis of C_{2+} products by cooperating with other functionalities. For example, it was found that the products could be shifted from dominant methane over the catalyst with Cu NPs dispersed on a porphyrinic triazine framework (PTF/Cu) toward ethene over the catalyst with isolated Ni atoms (PTF(Ni)/Cu) (Fig. 31a).[164] The Ni SA sites were identified to provide a CO-enriched local environment for neighboring Cu sites. Since the coverage and local concentration of CO have been always considered as the key factors for C–C coupling reactions,[158] the probability of ethene formation was expected to increase through CO dimerization. By controlling the properties of metal centers and tuning the coordination environments, Zhao *et al.* realized the direct synthesis of CH_3COCH_3 by single atom copper encapsulated on N-doped porous carbon with a FE of 36.7%.[286] The coordination of Cu with four pyrrole-N atoms was believed to be responsible for the effective activation of CO_2 and subsequent C–C coupling. In some cases, accurately controlling the distance between two identical SA sites could also contribute to effective C–C couplings. Liang *et al.* reported such a Cu SAC with periodic copper SA sites in a coordination polymer (Cu(OH)BTA) for ethene production from CO_2 reduction[159] (Fig. 31b). By means of structural and *operando* characterization studies as well as computational calculations, they found that Cu(OH)BTA with a suitable distance (∼5.7 Å) between two adjacent Cu sites might require minimized conformational energy needs for structure reconstruction. Generally, such a reconstruction was inevitable due to the necessary match between the steric configurations of active sites and the transition state. Given that the distance between Cu sites during the adsorption of *CO, *CHO, and *OCCHO intermediates was in the range of 5.68–5.83 Å, very close to that in its original state (∼5.7 Å), such a specific structure hence favored the formation of *OCCHO energetically, which was one of the vital intermediates for C–C couplings between *CO and *CHO, thereby propelling the preferential production of ethene. Such cases where the distance and configuration take control of product distribution were also reported by Guan *et al.*[287] They found the preferential production of C_2H_4 by binding of two CO intermediates on two adjacent Cu–N_2 sites, whereas the isolated Cu–N_4, the neighboring Cu–N_4, and the isolated Cu–N_2 sites resulted in CH_4. These cases all suggest that two adjacent and similar active sites might favor the production of C_{2+} chemicals, and copper might be the best choice because of the moderate adsorption of intermediate species.[288,289] Recently, however, a tin-based tandem catalyst featuring Sn single atoms and SnS_2 nanosheets was developed for electroreduction of CO_2 to ethanol with a selectivity of 82.5%. A mechanistic pathway promoting C–C bond formation *via* a formyl-bicarbonate coupling intermediate was proposed by identifying the dual active centers of Sn and O atoms that could adsorb *CHO and *CO(OH) intermediates, respectively.[290]

Apart from the synthesis of C_{2+} products *via* C–C couplings, Li *et al.* reported a novel process for the production of dimethyl carbonate (DMC) through a so-called convergent paired electrosynthesis from CO_2 by integrating the anodic Br_2 evolution reaction and cathodic CO_2 reduction reaction in a membrane-free single cell (Fig. 31c).[291] Initially, they implemented a dual-channel SAC with Ni SAs asymmetrically coordinated with four planar nitrogen and one axial oxygen, which exhibited a lower energy barrier for CO_2 activation to *COOH in comparison with the common Ni SAC featuring a symmetric structure with only planar four-nitrogen coordination. By virtue of this SAC, they obtained an exclusively high CO FE of 99% and a partial current density of 325 mA cm^{-2} at −0.6 V *versus* RHE. This reduction process ($CO_2 + 2e^- + 2H^+ \rightarrow CO + H_2O$) was innovatively integrated with a Br_2 evolution reaction ($2Br^- \rightarrow Br_2 + 2e^-$) in CO_2-saturated 0.1 M KBr–CH_3OH electrolyte, accompanied by a subsequent chemical oxidation of Pd^0 to Pd^{2+} ($Pd^0 + Br_2 \rightarrow Pd^{2+} + 2Br^-$). Eventually, DMC was produced by the chemical oxidation of the formed CO and CH_3O^- with the synchronous reduction of Pd^{2+} to Pd^0 ($CO + 2CH_3O^- + Pd^{2+} \rightarrow (CH_3O)_2CO + Pd^0$). As a result, a high FE of DMC of up to 80% could be achieved at room temperature.

3.2.3 Photochemical CO_2 reduction to C_{2+} products. Acquiring valuable products with more than one carbon atom is an appealing but challenging task in photochemical CO_2 reduction, although many efforts have been devoted for this issue.[292–294] The formation of C_{2+} products should always afford much more electrons and protons engaging in the whole reaction process, and accordingly much higher energy barriers for the generation and stabilization of intermediates. This indicates a need for more efficient photocatalysts with optimized active sites for electron transfer and transformation. Intuitively, complicated reaction pathways involving multiple procedures especially C–C coupling steps need close cooperation between different sites with a suitable spatial distance and matched kinetics, suggesting that SACs with relatively isolated active sites might not be appropriate platforms for the synthesis of C_{2+} products. However, SACs have been still applied in the highly selective production of C_{2+} by employing other inspiring strategies. Shen *et al.* reported such a surprising process where propane with a high electron-based selectivity of 64.8% (product-based selectivity of 32.4%) was photosynthesized from CO_2 reduction with Cu SAs on vacancy-rich TiO_2 monolayer nanosheets (Fig. 32).[295] Owing to the presence of O_v, Cu SAs exhibited a coupling effect with neighboring Ti verified by the matched d-band centers, forming a unique Cu–Ti–V_O unit. In this unit, a certain number of electrons were transferred to Cu SAs from Ti atoms, resulting in remarkable electron accumulation at Cu sites and a corresponding electron depletion at Ti sites. Such a unit with asymmetric electron distribution could serve as a favorable active center for CO_2 activation, reducing the energy level of both *CHOCO (primary C–C coupling) and $^*CH_2OCOCO$ (secondary C–C coupling) intermediates. Thus, the production of propane was propelled through a tandem reaction route. In addition, by enhancing the formation of *CO from *COOH and CHO* from *CO and the corresponding coupling between them, an appreciable yield of ethanol could be achieved from CO_2 photoreduction over another Cu SAC based on a MOF material (Cu/UiO-66-NH_2).[271] Similarly, by promoting the CO formation and adsorption over Mo SA sites, the production of ethene could be reinforced to some extent over a Mo COF (Mo-TpBpy).[269] Preferential synthesis of acetaldehyde could be achieved with a rubidium (Rb) SAC supported by potassium (K) co-doped carbon nitride. The introduction of Rb could contribute to the inhibited formation of *CO and further protonation to *CHO. The facile C–C coupling occurring between two *CHO led to the formation of acetaldehyde through a successive protonation. Notably, an ethanol oxidation process was incorporated in the system, which not only depleted the holes and generated protons to engage in the reduction reaction, but also produced acetaldehyde as well.

Indeed, the above studies and other related research studies have addressed an effective strategy for the construction of superior SACs to realize preferential synthesis of complex products, that is, focusing on the intermediate steps, matching the electronic and geometric properties of SACs with key intermediates by accurately controlling microenvironments adjoining SAs and relying on the synergy between metal SAs and substrates with special properties. Certainly, a sufficient supply of electrons and protons should be ensured in the meantime. This strategy is quite consistent with that proposed in the thermal and electric process,[59,159,284] further suggesting the universality of SAC design in CO_2 reduction.

3.3 CO_2 conversion toward other organic products

The above CO_2 reduction reactions, no matter what the source of energy input is, show that nearly all carbon atoms of the products stem from CO_2 conversion and these carbon atoms constitute the main frame of product molecules. Massive production of valuable carbon-based platform chemicals and fuels, as well as alleviation of carbon emission is expected to be

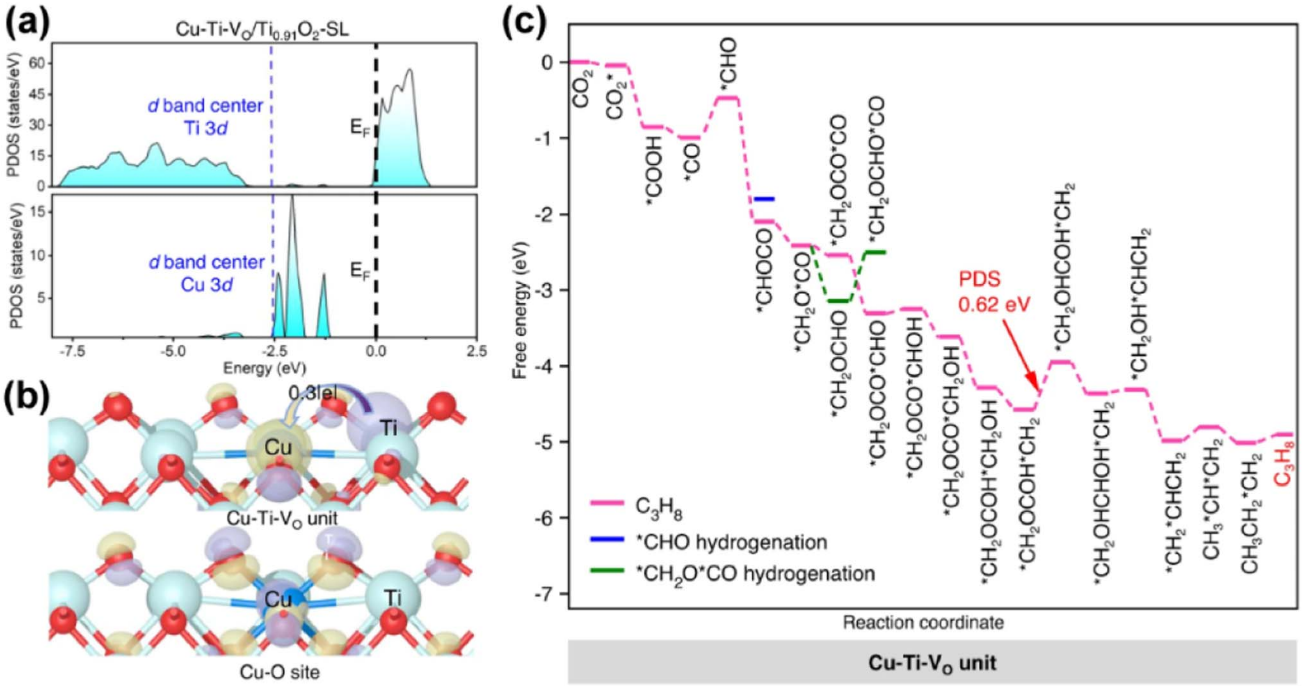

Fig. 32 (a) PDOS and d-band centres of Cu 3d and Ti 3d orbitals. (b) Charge density differences of the Cu–O site and Cu–Ti–V_O unit. (c) Gibbs free energy diagrams of CO_2 reduction on the Cu-Ti-V_O unit.[295] Reproduced from ref. 295 with permission from Springer Nature, copyright 2023.

achieved to some extent with the practical exploitation of these reactions, providing a viable opportunity for a sustainable industry. Besides, there have been also quite a few synthetic reactions encompassing not only CO_2 conversion but also the transformation of other compounds (not including H_2 or H_2O) towards the production of various chemicals with skeletal structures not based on CO_2-derived carbon atoms exclusively. A case in point is dry reforming reactions, which produces CO and H_2 *via* co-conversion of CO_2 and CH_4. Carbon atoms in CO are from both CO_2 and CH_4, as distinguished from other reactions of CO synthesis from CO_2 reduction mentioned above, although the CO_2 molecules also go through the procedures of reduction. Not just CH_4, but other reactants such as alkenes, alkynes, arenes, and heteroatom-containing compounds can be incorporated in the CO_2 conversion reactions as well, in which CO_2 might be transformed into carbonyl, carboxyl, and alkyl with different degrees of protonation.[9,10,14–16,296–303] On the basis of these reactions, the production of fine chemicals, drugs and some advanced organic materials might receive a good opportunity towards more environment-friendly operations with such a nontoxic carbon source. These processes are also expected to provide an opportunity for comprehensive utilization of CO_2.

Due to the increased complexity of feed reactants compared with that of CO_2 reduction reactions, the thermodynamics and kinetics involved in these systems are more complicated correspondingly, which indicates that design of efficient catalysts and exploration into the mechanism are in great demand. Given that homogeneous catalysts have been extensively used in certain reactions,[296,301] the applications of SACs possessing combined advantages of homogeneous and heterogeneous catalysts have been also reported for enhancing both activity and selectivity, as well as long-term stability under harsh conditions. Herein, we will focus on these synthetic reactions regarding the design strategies of SACs and relevant mechanism analysis for a more comprehensive understanding of SAC application in a broader spectrum of CO_2 conversion.

As a C_1 synthon, ubiquitous CO_2 provides a green, non-toxic carbon source for the synthesis of a large variety of chemicals by pharmaceutical and organic engineering in terms of the functionalization of C–H and the formation of C–C and C–X (X denotes heteroatoms).[14,296,300,304] For instance, in organic synthesis, CO_2 has been extensively used for the carboxylation of alkenes, alkynes, and arenes.[296] CO_2 plus H_2 could be also applied in carbonylation and alkylation reactions based on different reduction levels.[14] Generally, homogeneous catalysts are commonly chosen to realize effective conversion with appreciable activity in these reactions. As heterogeneous systems with the applications of SACs have been burgeoning in formylation and carbonylation reactions with CO,[305–307] the SACs are also expected to provide a glimmer of hope to the corresponding utilization of CO_2, as CO can be selectively generated *in situ* from CO_2 conversion *via* various routes. Fu *et al.* integrated cobalt SAs and CuPd NCs into a porphyrin-based MOF to construct composite photocatalysts $(Cu_1Pd_2)_z$@PCN-222(Co) for coupling the CO_2-to-CO photoconversion and Suzuki coupling reactions.[308] Under visible light irradiation, excited porphyrin could concurrently transfer electrons to Co SAs and CuPd NCs. CO could be formed over Co SA sites, and then participate in the subsequent Suzuki reactions with various substrate molecules (Fig. 33a–c). The synergy effect between SA sites and NCs led to the photosynthesis of benzophenone with over 97% selectivity and 90% yield. Fenofibrate, a well-known blood cholesterol lowering drug, could also be obtained with a yield of 67.3% under mild conditions. Similar coupling strategies could be also carried out in separated reactors combining different inputs of energy, in which CO was a bridge to link the primary and secondary reactions.[309,310] CO_2 fixation to cyclic carbonates could be also realized over SACs.[311,312] Jiang and his co-workers fabricated a class of novel hollow porous carbons (HPC) containing well dispersed dopants of nitrogen and Zn SAs through pyrolysis of template-directed hollow ZIF-8 spheres.[312] The optimized SAC featuring an ultrahigh loading of (11.3 wt%) Zn and surrounding N active sites achieved efficient catalytic CO_2 cycloaddition with epoxides *via* high-efficient photothermal conversion under light irradiation at ambient temperature. The enhanced photothermal effect was mainly contributed by the abundant ZnN_4 sites with a specific coordination structure derived from the parent ZIF-8 precursor plus the hollow structure of the carbon support which could harvest light in a broad spectrum by using the multiple reflections within the cavity (Fig. 33e). Coincidentally, Wang *et al.* also reported a Zn SAC achieving a cycloaddition reaction of epoxides and CO_2 with high yield (99%) and selectivity (98%) of propylene carbonate with a TOF of 2889 h^{-1}.[311] They anchored Zn on a nitrogen-doped graphene support (NG) with atomically dispersed $[ZnN_{3.76\pm0.2}]$ as active sites, as verified by XANES, EXAFS and XPS characterization studies. The active sites functioned by interacting with epoxide to polarize the C–O bond, followed by a ring-opening step *via* nucleophilic attack by the bromide anion. The subsequent nucleophilic attack of the intermediate at the CO_2 molecule led to the formation of an alkyl carbonate anion and final cyclic carbonate *via* ring closing (Fig. 33f). During the whole process, the Zn SA sites were considered to have facilitated the activation of epoxides and stabilization of the intermediate significantly. Xu *et al.*, on the other hand, exploited the strong electronic metal-support interaction between iridium single atoms and a WO_3 support, promoting the CO_2 cycloaddition of styrene oxide to styrene carbonate with 100% efficiency and high durability.[313] This is another validation of SACs used for an effective cycloaddition reaction involving CO_2 conversion and the synthesis of complex organic chemicals. Besides these mentioned reactions, more types of reactions were predicted to be realized promisingly over SACs based on the DFT calculations, such as conversion of methane and carbon dioxide to acetic acid.[314]

The production of urea, one of the most important nitrogen fertilizers, involving C–N formation between CO_2 and NH_3, has been operated at high pressure and temperature with large energy consumption conventionally (*e.g.*, Haber–Bosch process). Electrocatalytic urea synthesis, on the other hand, could be conducted under mild conditions, and is expected to be a promising alternative to current industrial protocols. Wang and his co-workers reported a diatomic catalyst (DA) with bonded Fe–Ni pairs for electrochemical urea synthesis.[315] As the capture and activation of CO_2 were both suppressed over sole-metal SACs, the subsequent C–N coupling was hindered with a much higher formation free energy of the key intermediate *COOH. On introducing a second metal into the system, the transfer of CO to engage in subsequent coupling became another obstacle with a high energy barrier due to the large distance, although the problems in CO formation were assuaged. The bonded Fe–Ni pairs, in contrast, could serve as efficient sites for coordinated adsorption and activation of multiple reactants, thereby enhancing the crucial C–N coupling thermodynamically and kinetically (Fig. 33d). In a later report, they further investigated the application of a Cu-based SAC with Cu SAs decorated on a CeO_2 support (denoted as Cu_1–CeO_2) in electrochemical urea synthesis from carbon dioxide and nitrate.[316] They found a reconstitution of copper SAs (Cu_1) to NCs (Cu_4) during electrolysis through *operando* X-ray absorption spectra. These electrochemically reconstituted Cu_4 clusters were identified as real active sites for electrocatalytic urea synthesis, since the favorable C–N coupling reactions and urea formation on Cu_4 were validated by *operando* synchrotron-radiation Fourier transform infrared spectroscopy and theoretical calculations. Such transformations between NCs and SAs were even reversible by switching the applied potential to an open-circuit potential. A similar formation of C–N bonds by SACs was also reported in organic synthesis. Zhao *et al.* prepared a stabilized Pt SAC over ultrathin two-dimensional $Ti_{3-x}C_2T_y$ MXene nanosheets (metal carbide with titanium vacancies; T: O, OH, F).[317] The Pt precursor ions went through a simultaneous self-reduction stabilization process at room temperature when adsorbing on a support treated by HCl/LiF. With the simultaneous formation of Ti vacancies, the SAs hence exhibited strong metal–carbon bonds with the $Ti_{3-x}C_2T_y$ support and were anchored onto the vacancy sites. $Pt_1/Ti_{3-x}C_2T_y$ afforded the efficient incorporation of CO_2 in the formylation of amines. More importantly, compared to Pt NPs, the SAs possessing partial positive charges significantly favored the

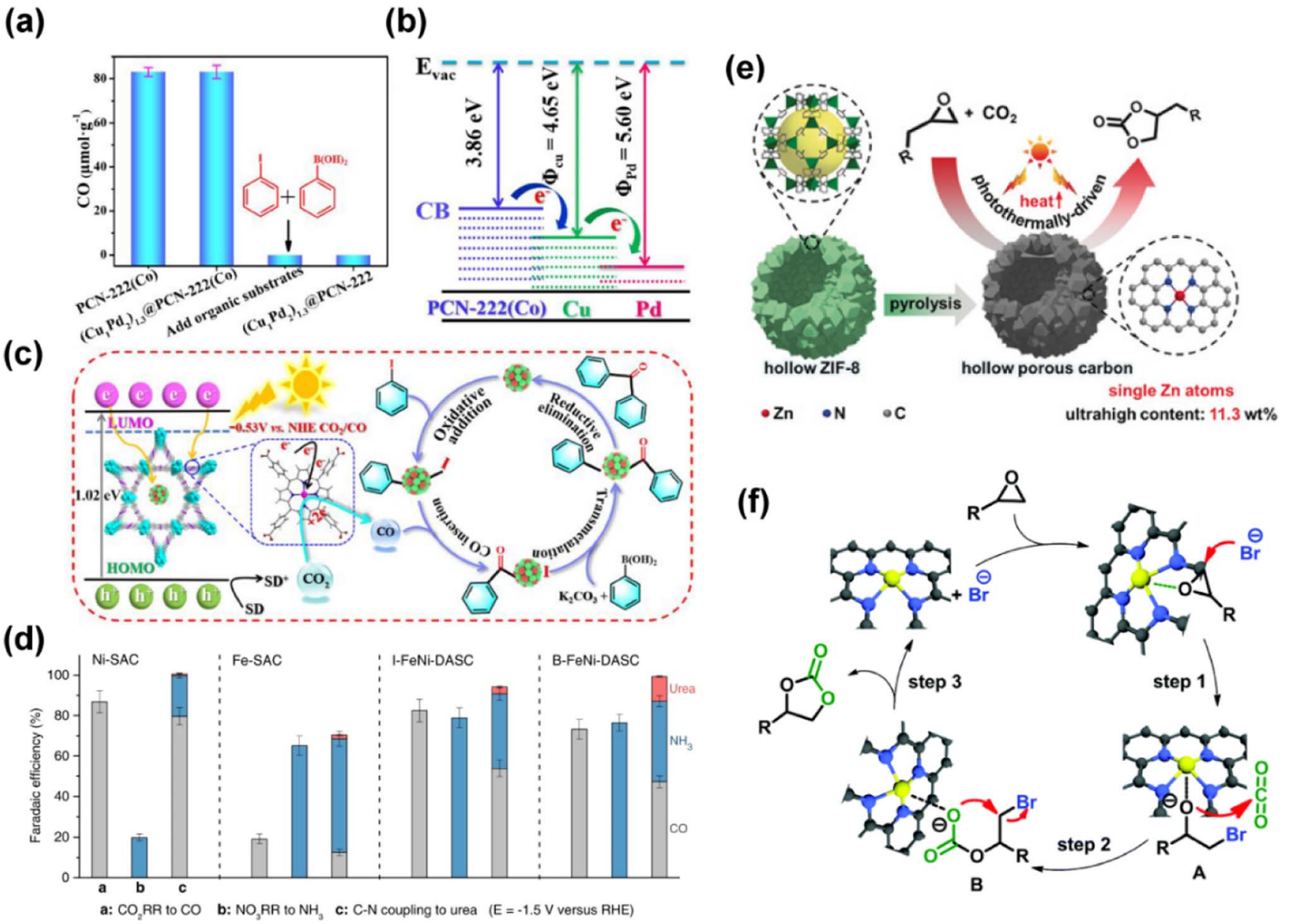

Fig. 33 (a) Photocatalytic evolution of CO under irradiation with a 300 W xenon lamp (λ >420 nm) in a CO_2-saturated solution of DMF/H_2O (1 : 1, v/v, 5 mL). (b) Cu-mediated electron transfer process over $(Cu_1Pd_2)_{1.3}$@PCN-222(Co). (c) Proposed mechanism for $(Cu_1Pd_2)_{1.3}$@PCN-222(Co)-catalyzed carbonylation Suzuki coupling CO_2 photoreduction.[308] Reproduced from ref. 308 with permission from American Chemical Society, copyright 2021. (d) The product distributions of the CO_2RR, the NO_3RR and urea synthesis on Ni-SAC, Fe-SAC, I-FeNi-DASC, and B-FeNi-DASC at −1.4 V *versus* RHE.[315] Reproduced from ref. 315 with permission from Springer Nature, copyright 2022. (e) Fabrication of the Zn SAC and its use in photothermal-driven CO_2 cycloaddition.[312] Reproduced from ref. 312 with permission from Wiley, copyright 2019. (f) Plausible atomic [ZnN] based reaction mechanism.[311] Reproduced from ref. 311 with permission from Royal Society of Chemistry, copyright 2019.

Table 1 A summary of some representative cases of SAC application in different systems

			Performances		
Catalysts	Systems[a]	Target products	Selectivity (%)	Activity[b]	Ref.
Rh_1–ZrO_2	T	CH_4	∼100	—	85
Na–Rh_1–ZrO_2		CO	∼99	9.4 mol CO per g_{Rh} per h	
Pd_1-FeO_x	T	CO	∼98	42.0 mmol CO·per g_{cat}·per h	86
Co/SBA-15	T	CO	∼99	304.6 mol CO per mol_{Co} per·h	88
Mo/NC	T	CH_4	∼100	Yield ∼46.3%	91
Ru/pBN	T	CH_4	∼93.5	1.86 $mmol_{CO_2}$ $g_{cat}{}^{-1}$ s^{-1}	94
Ir/AP-POP	T	HCOOH	—	TON 25135	101
Ru/LDH	T	HCOOH	—	TON 698	108
Ru@MCM	T	HCOOH	—	TON ∼2000	109
Pd/2,6-DCP-CTF	T	HCOOH	—	TOF 13.46 h^{-1}	110
Pt/MoS_2	T	CH_3OH	∼95	TOF 162.5 h^{-1} at 150 °C	112
Cu/ZrO_2	T	CH_3OH	∼100	TOF 1.37 h^{-1}	123
Cu/ZnO	T	CH_3OH	99.1	Yield ∼4.9%	124
Pt_1@MIL	T	CH_3OH	90.3	TOF 117 h^{-1}	126
A-Ni-NG	E	CO	97	TOF 14800 h^{-1}	140
Ni-NC	E	CO	92	—	150
NiSA/PCFM	E	CO	88	Current density 308.4 mA cm^{-2}	151
Fe^{3+}–N–C	E	CO	∼90	Current density 94 mA cm^{-2}	139
Fe-SAC/NPC	E	CO	∼97	—	155
Fe–N_4/CF	E	CO	94.9	Current density ∼10 mA cm^{-2}	156
Cu–APC on $Pd_{10}Te_3$ nanowires	E	CO	92	Current density 18.74 mA cm^{-2}	166
Cu–S_1N_3/Cu_x	E	CO	> 90	—	167
$Zn^{\delta+}$-NC	E	CO	95	Current density 1 A cm^{-2} in flow cell	169
Zn–NS–C	E	CO	99	TOF 11419 h^{-1}	173
Co–N_5/HNPCSs	E	CO	99	Current density 6.2 mA cm^{-2}	176
Cd-NC-t SAC	E	CO	91.4	Current density ∼5 mA cm^{-2}	180
Mn-MCs-(N,O)	E	CO	94.5	Current density 13.7 mA cm^{-2}	181
Ag_{SA}/MnO_2	E	CO	95.7	—	183
Mg–C_3N_4	E	CO	>90	TOF ∼18 000 h^{-1}	191
Ca–N_3O	E	CO	>90	TOF ∼15 000 h^{-1}	192
Ga-N_3S-PC	E	CO	∼92	—	193
InN_4/C	E	CO	97.2	TOF ∼40 000 h^{-1}	194
Bi-SAs-NS/C	E	CO	98.3	Current density 10.24 mA cm^{-2}	197
Sn(IV)–N_4/CNT–OH	E	HCOOH	89.4	Current density 74.8 mA cm^{-2}	210
$Sb^{\delta+}$–N_4 ($0 < \delta < 3$)	E	HCOOH	94	—	207
Cu SAs/GDY	E	CH_4	81	—	213
Cu SAs/TCNFs	E	CH_3OH	44	Current density 93 mA cm^{-2}	221
CoPc/CNT	E	CH_3OH	40	—	223
Cu_2NCN	E	CH_3OH	70	Current density 92.3 mA cm^{-2}	222
Cu_1/TiO_2	P	CH_4 (C_2H_6)	—	1416.9 (64.2) ppm g^{-1} h^{-1}	231
Bi/TiO_2	P	CH_4	—	4.1 μmol g^{-1} h^{-1}	230
$Cu_{0.8}Au_{0.2}$/TiO_2	P	CH_4 (C_2H_4)	—	3578.9 (369.8) μmol g^{-1} h^{-1}	234
Ag-HMO	P	CH_4	—	0.61 mol mol^{-1}	236
Pt–V_2O_5	P	CH_4	—	247.6 μmol g^{-1} h^{-1}	237
$CoSi_2$	P	CO	—	4.7 mol $g_{(Co)}{}^{-1}$	239
Co-2,3-DHTA-COF	P	CO	95.7	18 000 μmol g^{-1} h^{-1}	270
Ni-TpBpy	P	CO	96	∼4057 μmol g^{-1} (5 h)	267
Cu SAs/UiO-66-NH2	P	CH_3OH (CH_3CH_2OH)	—	5.33 (4.22) μmol g^{-1} h^{-1}	271
RuSA-mC_3N_4	P	CH_3OH	—	1500 μmol g^{-1} (6 h)	250
Co/g-C_3N_4	P	CH_3OH	—	941.9 μmol g^{-1} (4 h)	255
Co_1–C_3N_4@α-Fe_2O_3	P	CO	> 99	14.9 μmol g^{-1} h^{-1}	261
InCu/PCN	P	CH_3CH_2OH	92	28.5 μmol g^{-1} h^{-1}	318
Cu-Ti-V_O/$Ti_{0.91}O_2$-SL	P	C_3H_8 (C_{2+})	32.4 (50.2)	13.8 μmol g^{-1} h^{-1}	295
SnS_2/Sn_1–O3G	E	CH_3CH_2OH	82.5	Current density 17.8 mA cm^{-2}	290
PTF(Ni)/Cu	E	C_2H_4	57.3	—	164
0.1Pd/Fe_3O_4	T	CH_3CH_2OH	97.5	413 $mmol_{EtOH}$ $g_{Pd}{}^{-1}$ h^{-1}	282
Ir_1–In_2O_3	T	CH_3CH_2OH	> 99	TOF 481 h^{-1}	59
Rh_1/$CeTiO_x$	T	CH_3CH_2OH	99.1	TOF 493.1 h^{-1}	284
$K_{0.2}Rh_{0.2}$/β-Mo_2C	T	CH_3CH_2OH	72.1	33.7 μmol $g^{-1}h^{-1}$	283

[a] T: thermochemical reduction; E: electrochemical reduction; P: photochemical reduction. [b] TON: Abbreviation of the turnover number; TOF: abbreviation of the turnover frequency.

adsorption and activation of silane, CO_2, and aniline energetically, leading to boosted catalytic performance.

3.4 Summary

Actually, SACs have been exploited in all kinds of systems involving CO_2 conversion so far, suggesting their unparalleled potential and vitality. We provide a systematic summary of some representative cases of SAC application in different systems, especially various CO_2 reduction reactions in Table 1.

4. A molecular understanding of SACs in CO_2 conversion

In the above sections, we have provided a comprehensive summary of different reaction routes for CO_2 transformation and the outstanding performances of SACs in highly selective synthesis of various valuable products. However, the current stage of research mainly depends on case-by-case evaluation and empirical design. We must avoid pointless scientific research input on tediously screening catalysts and repetitively investigating mechanisms, or otherwise use excessive resources for future research studies. We truly expect a prospect that the construction and exploitation of optimized catalysts could be driven by rational design and get rid of the limitation of human resources.[319] Nowadays, we could catch a glimpse of such a promising prospect thanks to the findings on SACs, of which well-arranged and well-defined structures regarding both electronic and geometric aspects shed light on the systematic analysis and study (Fig. 34). Furthermore, the transformation of CO_2, a simple but important C_1 molecule, should offer an excellent opportunity to dive into the molecular understanding into all levels of SACs in specific catalytic reactions. As such, the discussion in this section might guide the establishment of potential research paradigms with unambiguous structure–activity relationships and inspire in-depth exploration into the intrinsic reaction mechanisms.

4.1 Central atoms

Generally, central atoms endow the SACs with fundamental catalytic properties at the core and top level, especially for those CO_2 reduction reactions, which just involve electron transfer and protonation procedures (Fig. 35). The intrinsic features of different types of central metal atoms have an effect on not only the primary interaction with neighboring atoms on the substrate but also the chemical adsorption of guest molecules including reactants and intermediates.[320] The former effect partially affords the specific localized structures of active moieties, the dynamic evolution and even the durability of

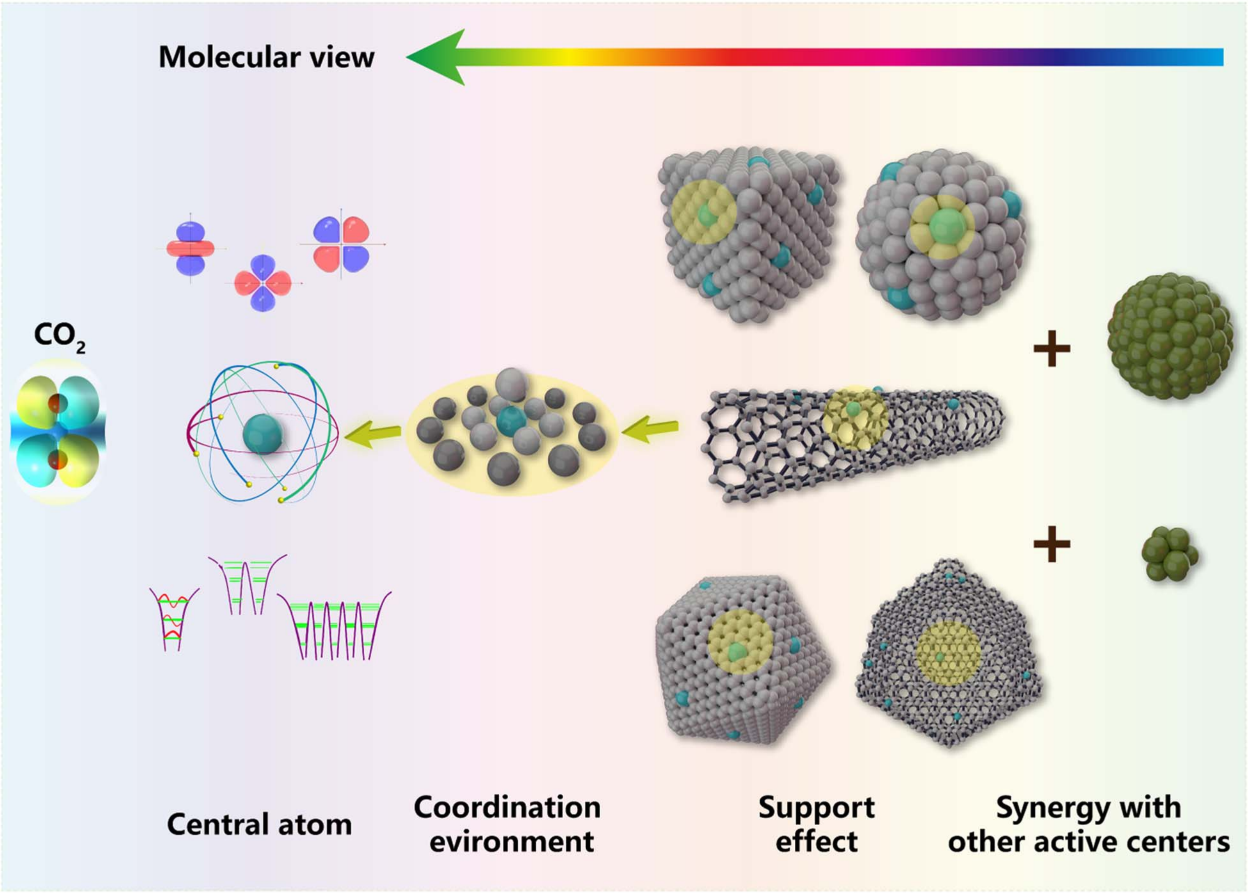

Fig. 34 Schematic of multi-level understanding of SACs for CO_2 transformation from a molecular point of view.

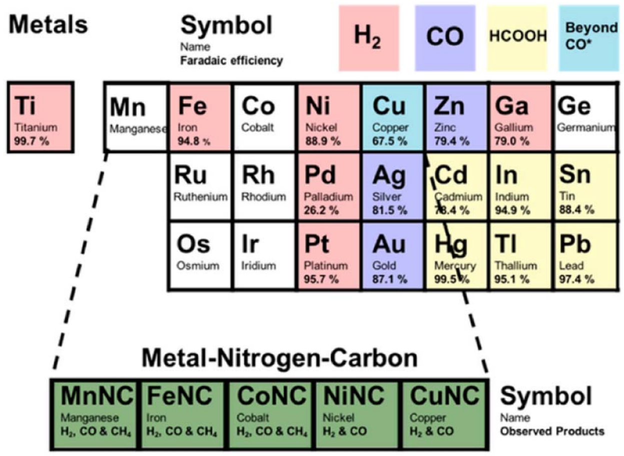

Fig. 35 A colored periodic table with metal catalyst performance obtained in the CO_2 electrochemical reduction reaction. Reproduced from ref. 326 with the permission from American Chemical Society, copyright 2019.

active sites under certain redox conditions. The latter effect consists of even more abundant connotations and drives the proposal of strategies for regulating the reaction pathway.[321] It has influence on the practical reaction kinetics following the Sabatier principle, which has qualitatively pointed that there should be an optimum "bond strength" of reactants and transition states on the active centers, defining the best catalyst for a given reaction.[322] Researchers further try hard to develop specific descriptors closely correlated with the intrinsic activity by mapping various parameters for quantitative implementation to open a path for predictable catalytic performance.[323,324] d-band and other d-electron related models have been proposed as a popular theoretical basis for offering comprehension of the scaling relations and variations in catalytic performance with regard to the electronic structure of transition-metal sites.[325] In addition, more specific descriptors might be more effective, which is decided by the catalytic systems.

For some electrochemical reactions over SACs, there has been primary progress recently.[327,328] Taking commonly used nitrogen-doped carbon as an identical substrate, SACs based on various transition metals, such as Fe, Co, Ni, Cu, and Mn, have been applied in electrochemical CO_2 reduction under consistent conditions (Fig. 36).[326,329] Strasser *et al.*[326] correlated the apparent performance of these M–N–C catalysts with specific energy descriptors *via* combined experimental and theoretical approaches. The catalytic reactivity trends and reaction pathway are divided into three potential regions deliberately with distinct kinetic features. By simply calculating the binding energy of possible intermediates *COOH and *CO, the potential onset could be correlated with the binding energy of *COOH in the low overpotential region, as the formation rate of CO correlates with the free energy of *CO in the medium overpotential region. Based on these relationships, the authors could infer that the rate-determining steps change from the first proton-coupled electron transfer into *COOH ($CO_2 + H^+ + e^- \rightarrow$ *COOH) to the subsequent proton-coupled electron transfer into *CO (*COOH + $H^+ + e^- \rightarrow$ *CO + H_2O). Even the higher CO FE of Ni at a certain current density at technologically relevant levels could be rationalized by using the gaps between the energy barriers of different types of metals regarding the HER. Adopting different substrates as platforms might lead to distinctly different descriptors.

Chang *et al.* studied and compared the isolated transition metals (Fe, Co, Ni, Cu, and Zn) using a series of crystalline molecular catalysts, namely metal-coordinated phthalocyanines, to investigate the intrinsic role of the central metals with identical local coordination environments in the performance of CO_2 electrochemical reduction.[330] In their discussion, they found that the free energy difference of *HOCO and *CO adsorption, rather than any single energy parameter for different metals, was well-correlated with the partial current density of CO production, and exhibited linear scaling relations over a wide range of potentials (Fig. 37). Their findings not only unveil that the optimal binding mode of *HOCO and *CO controls the CO production for various metal-coordinated phthalocyanines, but also manifest again that the electronic nature of central atoms have a great effect on the intrinsic kinetics by regulating the evolution of key intermediates. And the descriptors for correlating the microscopic structure and energy parameters with apparent activity might highly depend on the specific catalytic systems. Such conclusions are not limited to conventional transition metals. As mentioned in Section 3.1, plenty of main group elements, such as Ga,[193] In,[194] Sn,[198,210] Sb,[207] Mg,[191] Bi,[196,197] *etc.*, could also take advantage in CO_2 reduction reactions in the form of single atoms, although classical d band theory is not responsible for the explanation of their specific activity. The distinct variation in binding energy of key intermediates over SACs based on them stems from their inimitable electronic features, offering opportunities for designing innovative catalysts for efficient CO_2 transformation. Furthermore, such research strategies on the basis of the investigation into the molecular-scale interaction between central atoms and specific intermediate species could be also generalized to other SAC systems with different substrates and coordination environments, which are operated under thermochemical and photochemical conditions.[46,227,331]

The above discussion of central atoms regards atomically dispersed active sites as 'insular islands' in the sea of substrates or 'scattered stars' in the night sky of supports. They seem to function in an independent and equivalent way. However, the variation of catalytic properties might be potentially caused by the interplay between the central atoms, particularly when they are within close proximity. This implies that the spatial distance of the central atoms might be one of the critical factors, which is decided by using the distribution diagrams of single atoms, resulting from the loading amount and fabrication strategies. The distance of central atoms could be shortened continuously by applying specific precursors and preparation methods, until two or several atoms bond with each other or locate at adjacent sites.[332] The double-atom systems, so-called dual-atom or diatomic catalysts (DACs), have been burgeoning research subjects in recent years.[35,333–335] Strictly speaking, the DACs do not belong to the SACs, as the metal dimers might function as

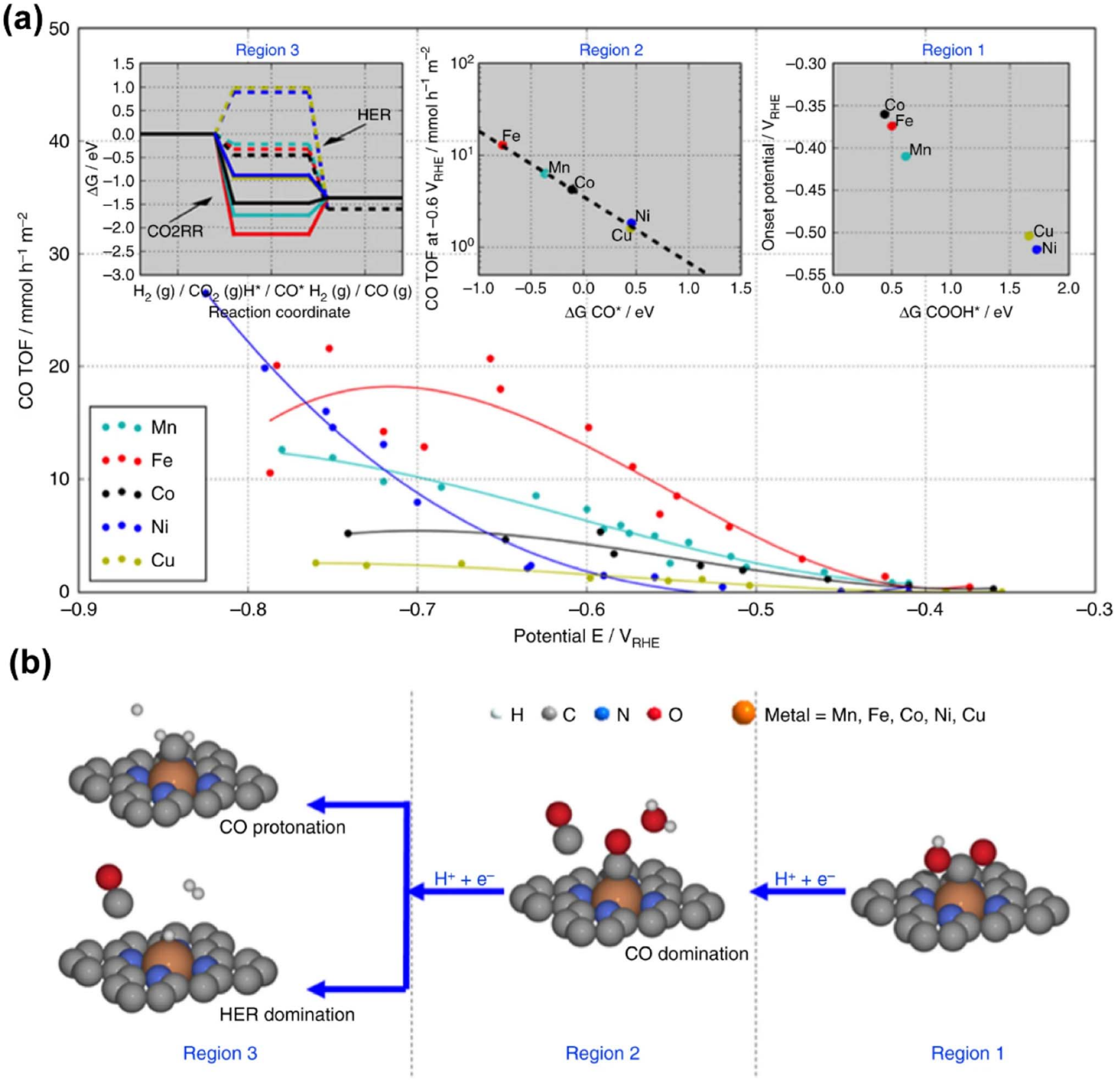

Fig. 36 Experimental correlation with simulations. The catalytic reactivity trends (a) and reaction pathway (b) are divided into 3 potential regions with distinctly different rate-determining mechanistic features. Reproduced from ref. 329 with the permission from Springer Nature, copyright 2017.

single sites but show distinctly different properties in comparison with ordinary single atoms, *i.e.*, they are 'single' dual atoms rather than 'double' single atoms. Such aggregations might further develop and comprise even more than two atoms until reaching the category of NCs. Generally, DACs also exhibit well-defined structures and have research methods similar to SACs. Therefore, we include the DACs in the discussion of SACs in this review and view them as the ultimate situation of shortening the distance between central atoms. Apart from the effect of spatial distance, different assemblies of single-atom sites (more than one type of central atom) might also remarkably affect the reaction kinetics and be exploited for enhanced performance of specific catalytic systems.

As mentioned in Section 3.1, neighboring Pt monomers not only render synergy to vary the reaction barrier, but also steer the reaction to go through a distinct pathway compared with isolated Pt atoms.[112] In this way, the catalyst based on neighboring sites exhibits much higher low-temperature performance due to the reduced activation energy in a stepwise process of CO_2 hydrogenation into formic acid and methanol. For the reforming reaction of methane with CO_2, two sets of single-atom sites, Ru and Ni, are anchored on the same surface

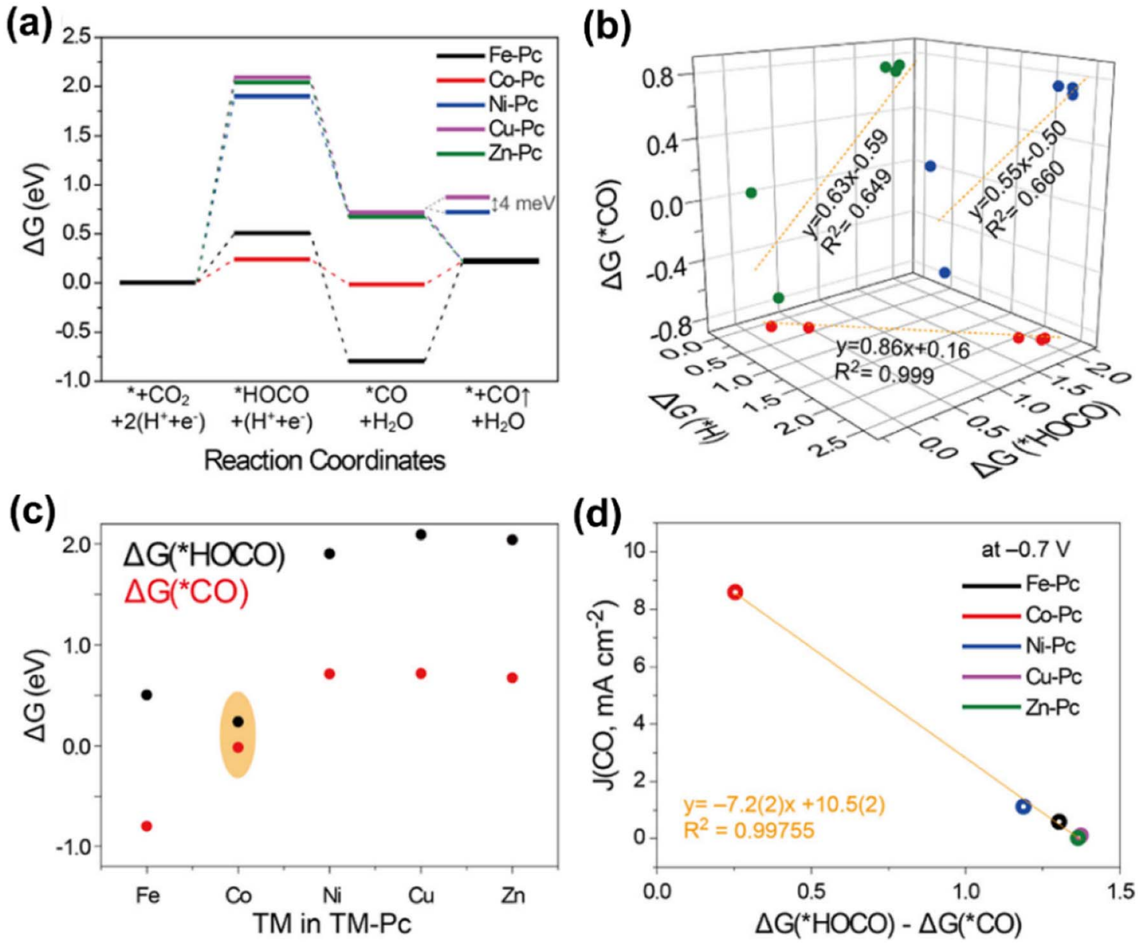

Fig. 37 Correlation between experimental results and theoretical calculations. (a) Free energy diagram for CO_2 reduction at $E = 0$ V. (b) Linear fitting between the free energy of reaction intermediates over different transition metals. (c) Free energy of *HOCO and *CO with different transition metals. (d) Plot of the free energy difference of *HOCO and *CO adsorption *versus* current density of CO production at −0.7 V. Reproduced from ref. 330 with the permission of American Chemical Society, copyright 2022.

of the CeO_2 support.[273] On the one hand, they play different roles in the whole reaction: Ni is responsible for the CH_4 conversion to CO and Ru is in charge of the dissociation of CO_2 into CO. On the other hand, however, they also contribute to the sequential formation of H atoms and generation of H_2 molecules in synergy: CH_4 is activated on Ni to form H atoms and then H atoms are coupled to H_2 over Ru sites.

There are more achievements emerging in electrochemical and photochemical circumstances,[337,338] such as Co dual-atom,[339] Ni–Cu,[340] Mn–Co,[341] Ni–Co,[342] and those mentioned in Section 3.1, and Ni dual-atom,[199] Pd dual-atom,[200] Ni–Fe,[203] Ni–Zn,[201] and Ni–Sn,[343] in which the central atoms could either be directly bonded, or bridged *via* non-metal atoms, or not be chemical bonded, yet remain close to each other. Relying on these catalysts featuring multiple-atom active sites, the production of a single C_1 product is promoted to different extents. To overcome the intrinsic restriction of the competition between molecular CO_2 activation and CO_2 reduction product release, a heteronuclear Fe_1–Mo_1 dual-metal catalytic pair on ordered porous carbon has been designed and achieved a high catalytic performance for driving electrochemical CO_2 reduction to CO[336] (Fig. 38). Chemical adsorption of CO_2 is proved on the Fe_1–Mo_1 catalytic pair through a bridge configuration, which prompts the bending of the CO_2 molecule for activation of the subsequent protonation. The dynamic change from the bridge configuration of adsorbed CO_2 species on hetero-diatomic Fe_1–Mo_1 centers to the linear configuration of CO on the Fe_1 center disentangles the scaling relationship between the CO_2 activation and the CO release, offering opportunities for regulating the reaction kinetics at the molecular scale in a promoted reaction pathway.

Besides improving the activity toward C_1 products, adjacent central atoms are always considered as desired active centers for the synthesis of C_{2+} products by enhancing specific C–C coupling processes, which are believed to be difficult on conventional SACs.[345,346] As mentioned in Section 3.1, the production of ethanol from CO_2 hydrogenation could be realized by the dimers of Pd with nearly 100% selectivity.[347] The Pd dual-atom structures not only promote the cleavage of C–O species in $*CH_xOH$ to form $*CH_x$, but also favor the C–C coupling between $*CH_x$ and *CO. Such a synergistic effect could contribute to superior ethanol selectivity with an appreciable

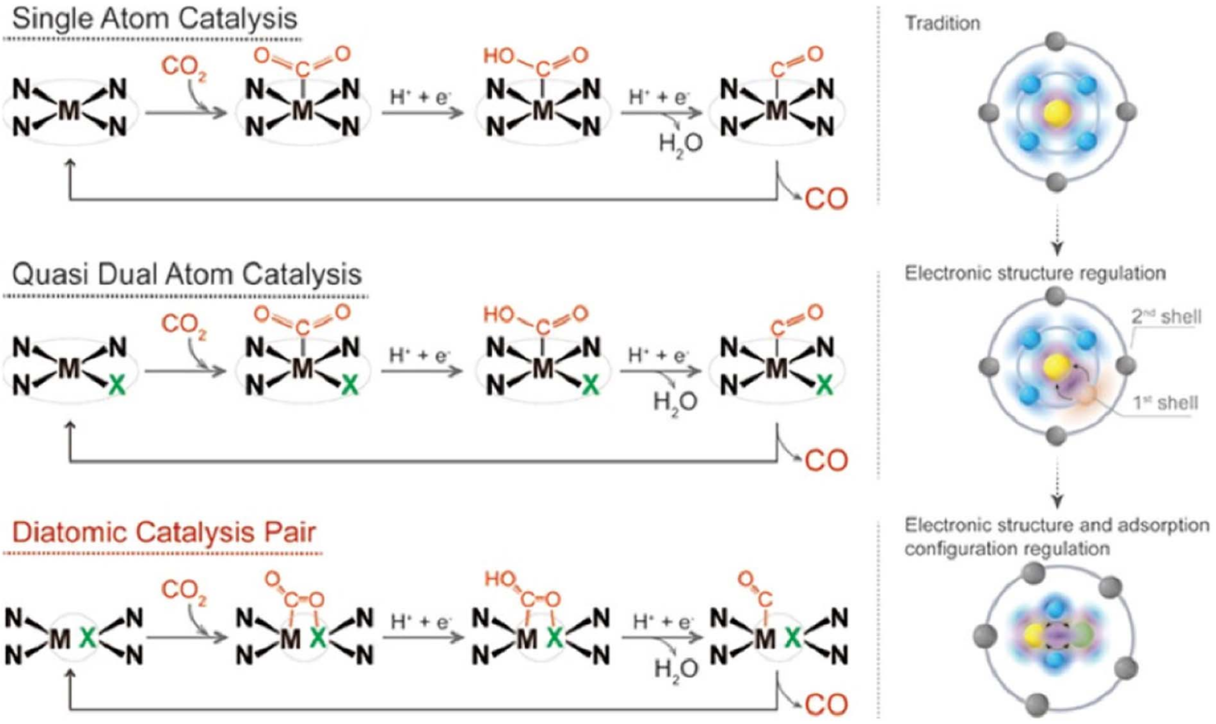

Fig. 38 The design of a heteronuclear Fe_1–Mo_1 DAC and proposed mechanisms for CO_2 electrochemical reduction. Reproduced from ref. 336 with the permission of American Chemical Society, copyright 2023.

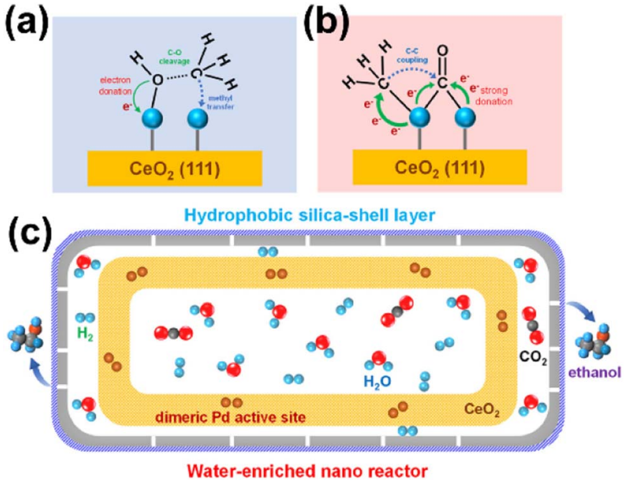

Fig. 39 Proposed mechanism for C–O bond cleavage (a) and C–C coupling (b) over the dual-atom Pd sites. (c) Model presenting the *in situ* generated water enriched in a nanoreactor with a hydrophobic silica shell layer. Reproduced from ref. 344 with the permission of American Chemical Society, copyright 2023.

persistence in a continuous-flow fixed-bed reactor, as the formed H_2O product could be enriched by a constructed hydrophobic SiO_2-shell layer, which creates a quasi-H_2O-solvent condition (Fig. 39).[344] As for electrochemical reduction of CO_2 toward ethanol, adjacent Cu single atom sites have been reported to promote C–C coupling with a higher efficiency compared with that of isolated sites (Fig. 40).[348] Such structures are established by increasing the loading amount and corresponding density of Cu atoms anchored on the thin-walled nanotube-shaped nitrogen-doped carbon support. The well-defined Cu–N_3 sites are maintained regardless of the extremely high loading, and create synergy between neighboring sites. As a result, the key intermediate species *CO, which are readily generated over single Cu–N_3 sites, go through a coupling step in a much more thermodynamically favorable path with ΔG <0 according to the theoretical simulations. In contrast, the isolated sites afford a much higher ΔG value of *CO conversion to *COCO, suggesting the huge thermodynamic barrier for the coupling step, leading to impossible formation of the ethanol product.

In photochemical reduction, on the other hand, hetero-diatomic sites have been believed to be more efficient for the C–C coupling reactions.[318,349] An In–Cu based photocatalyst could endow the CO_2 photochemical conversion toward ethanol with a superior selectivity of 92%. The In–Cu heteroatomic sites are found to promote the adsorption of *CO intermediates and lower the energy barrier of C–C coupling.[339] More specific discussion is provided by using a heteronuclear RuCu DAC, by which over 95% selectivity of acetate is achieved through CO_2 photochemical reduction (Fig. 41).[349] Intuitively, the intermediate atoms absorbed on the symmetrical homonuclear DAC sites (such as Cu dual-atom or Ru dual-atom active sites) would show identical electron scattering readily, which might lead to a strong repulsion between them and thus impede the subsequent C–C couplings. In contrast, possibly benefitting from the distinct electronegativity and gradient orbital coupling of the

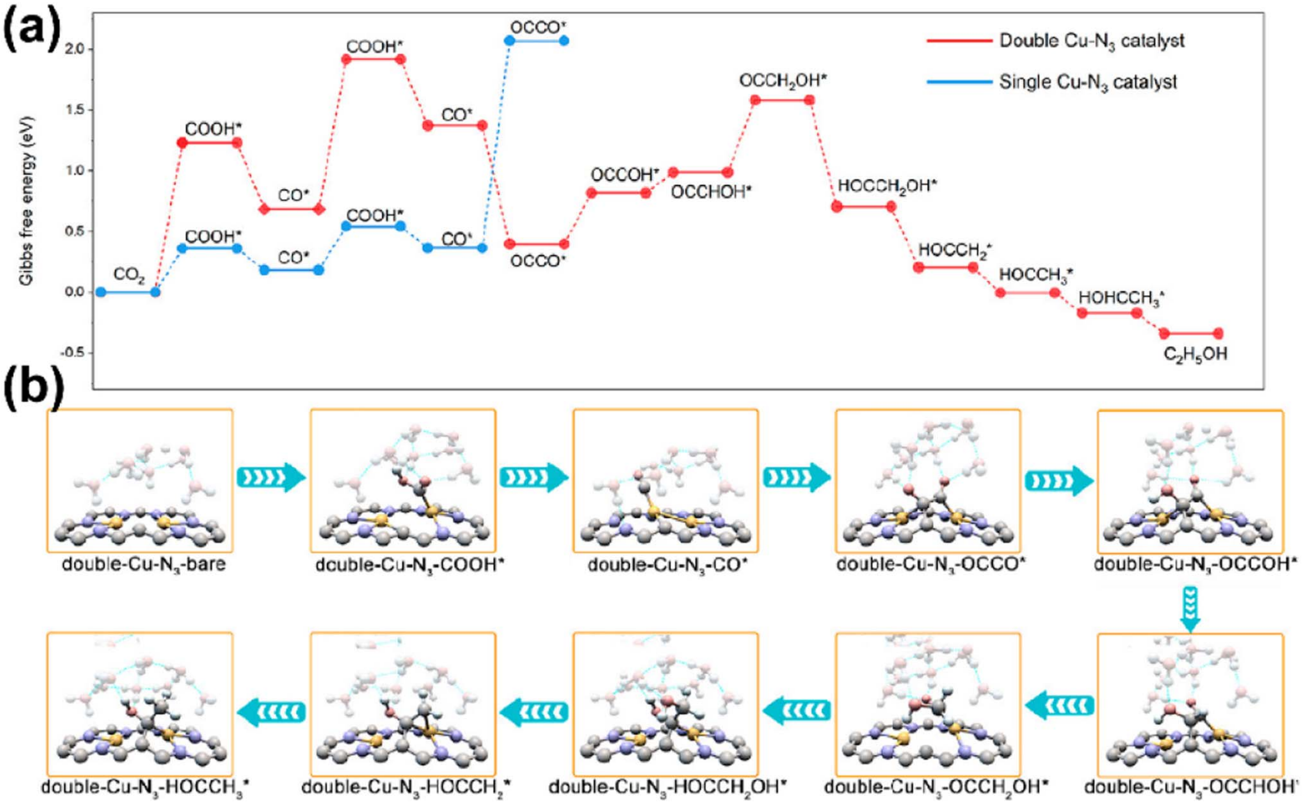

Fig. 40 (a) Free energy diagrams calculated for the reduction of CO_2 to CH_3CH_2OH on double Cu–N_3 sites and single Cu–N_3 sites. (b) Optimized structures in the pathways of CO_2 reduction on the double Cu–N_3 sites (gray: C of the catalyst; black: C of the adsorbate; red: O; orange: Cu; blue: N; white: H). Reproduced from ref. 348 with the permission of American Chemical Society, copyright 2022.

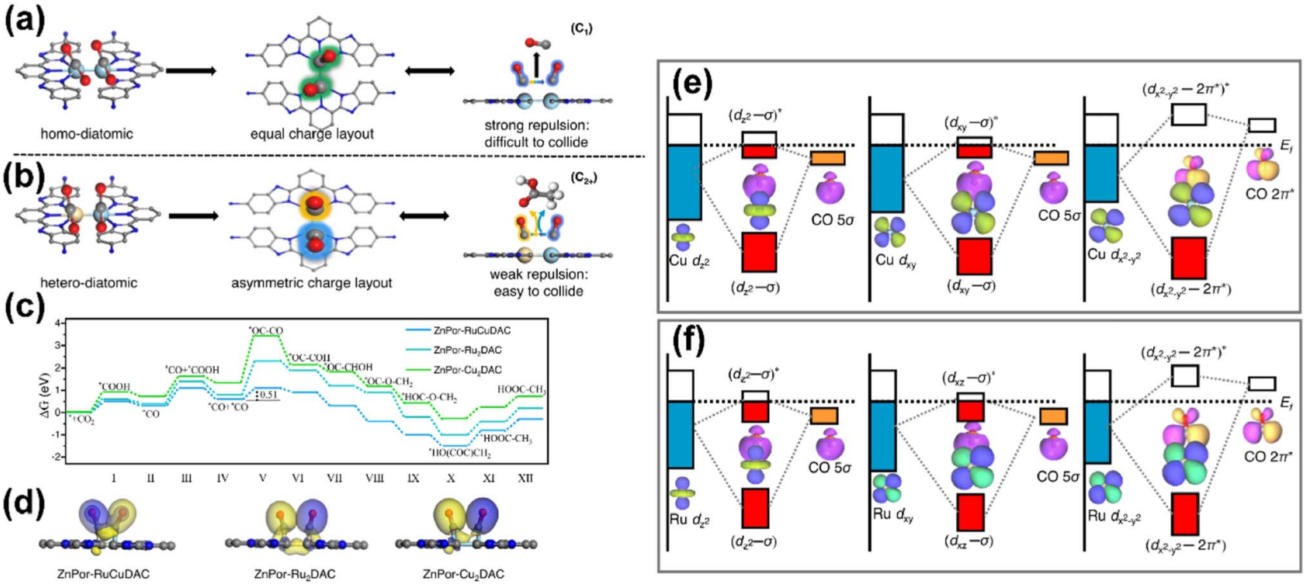

Fig. 41 (a) and (b) Assumed photocatalytic CO_2 reduction mechanism of C_1 and C_{2+} product formation using homo- and hetero-diatomic catalytic sites, respectively. (c) Gibbs free energy diagrams of CO_2 photoreduction to acetate of DACs based on RuCu, Ru_2 and Cu_2 active sites. (d) Differential charge density maps. Schematic illustration of the adsorbed CO (5σ, 2π*) orbital interactions with the (e) Cu 3d and (f) Ru 4d orbitals in a RuCu hetero-diatomic catalyst. Reproduced from ref. 349 with the permission from Springer Nature, copyright 2023.

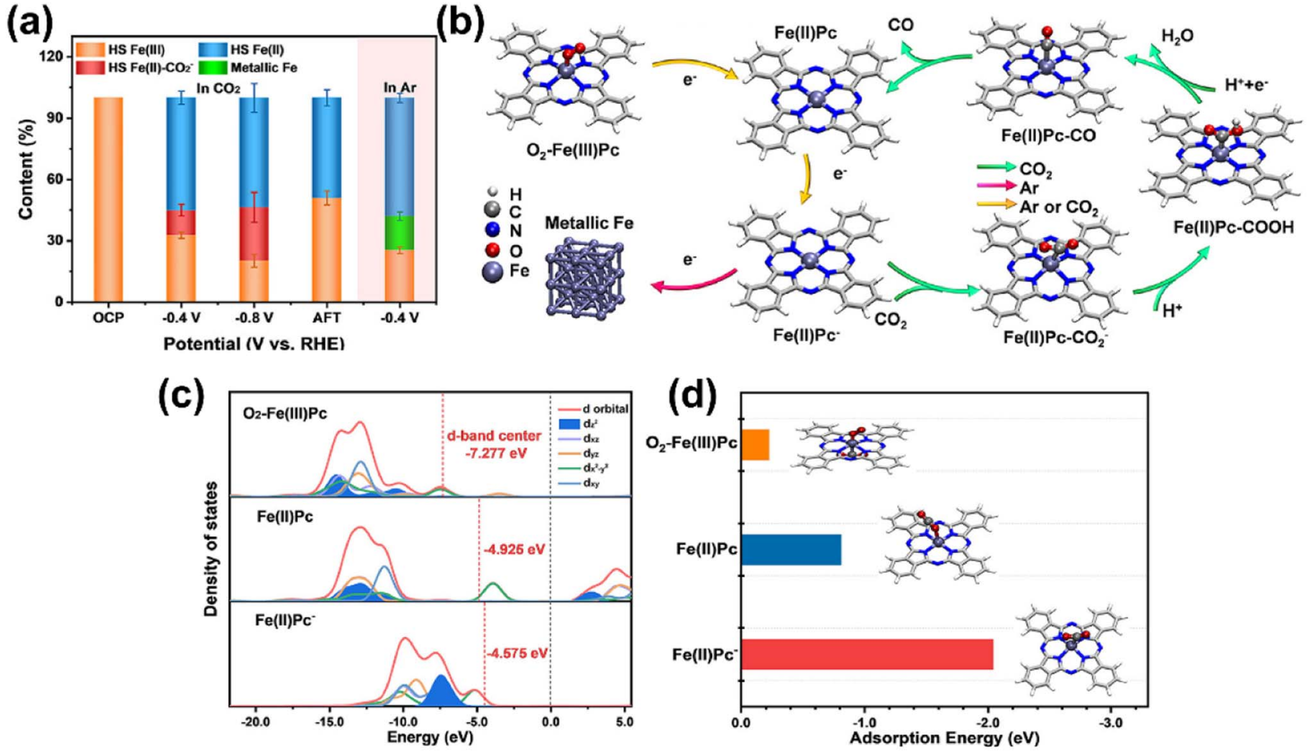

Fig. 42 (a) Relative signal intensity of different Fe species obtained from the fitting of ^{57}Fe Mössbauer measurements. (b) Proposed dynamic evolution routes of single-Fe-atom species during catalysis under CO_2- and Ar-saturated conditions. (c) Density of states (DOS) for Fe-3d orbitals in O_2–Fe(III)Pc, Fe(II)Pc, and Fe(II)Pc^-. (d) CO_2 adsorption energy over O_2–Fe(III)Pc, Fe(II)Pc, and Fe(II)Pc^-. (c) dz^2 orbital of Fe(II)Pc and Fe(II)Pc^- and the Kohn–Sham molecular orbital (MO) contours of the dz^2–π^* bonding orbital (BD) of Fe(II)Pc–CO_2^-, where the red and blue regions are positive and negative orbital phases whose isovalue is 0.05. Reproduced from ref. 357 with the permission of American Chemical Society, copyright 2023.

heteroatoms, the intermediates on heteronuclear DACs might exhibit an asymmetric charge distribution, which would deliver a mitigated repulsive effect and promote the molecular interactions of the formed intermediates, resulting in an augmentation of the collision probability of adjacent intermediates and the subsequent formation of the C_{2+} intermediates and products. This assumption has been manifested by the followed experimental results and theoretical simulations. Thorough investigations confirm that the strong gradient orbital coupling of Ru 4d–Cu 3d resonance leads to a remarkably weaker electrostatic repulsion of the two formed *CO intermediates on the Ru–Cu heteroatom with an asymmetric charge distribution. The adsorbed CO species are stabilized due to a decreasing energy splitting level, which stems from the strongly overlapped Ru/Cu-d and CO molecular orbitals and their facile split into bonding and antibonding orbitals. All these distinct features of electronic structures and chemical interaction contribute to a more favorable path toward C_{2+} products in terms of both thermodynamics and kinetics, especially the step of coupling between two side-to-side adsorbed CO.

In summary, regarding central atoms, two critical factors should be taken into account: the element type that determines the fundamental electronic properties of active sites and the peer effect of identical or different atomically dispersed active sites, which is influenced by both the spatial distance and element type. On the basis of the binding of key intermediate species with the central atom, various descriptors have been proposed for clarifying the molecular-scale structure–activity relationship and gaining in-depth understanding of the intrinsic mechanisms. Either for the enhancement of C_1 production or for the realization of C_{2+} synthesis, the cooperation between single atom sites, especially those in the neighboring location, has been exploited to break through the thermodynamic and kinetic obstacles on the reaction pathways, especially in terms of the stabilization of key intermediate species, subsequent C–C couplings and further transformation. In a word, the selection and engineering of central atoms will be continued for the rational design of SACs used for highly efficient CO_2 transformation.

4.2 Coordination environments

The effects of coordination have been fully discussed in homogeneous catalytic systems, as the catalytic properties of central atoms could be readily adjusted by manipulating the properties of ligands, such as steric hindrance effects, pH values and some other electronic features.[350–352] SACs, which can combine the merits of both heterogeneous and homogeneous catalysts, should benefit from not only the scaling relationship on the well-defined active sites, but also the adjustable performance by tailoring the local coordination environments,[353] as many concepts of coordination chemistry in homogeneous systems could also be extended to SAC systems.[354] Intuitively, we could envision a similarity between metal–ligand coordination in homogeneous catalysts and metal–support coordination in heterogeneous catalysts. The adsorption and activation of reactants and intermediates might either competitively or cooperatively co-exist with the interaction between central atoms and ligands, rendering distinctly controllable reaction pathways toward specific target products. The differences might be in the defect sites and standby sites of the support, where the dynamic evolution and the optimization of the coordination structure might take place for the metal-support and the metal–adsorbate interactions under redox conditions, as observed in some realistic catalytic systems.[80,81,316,354–356] On the other hand, distinguished from the cases involving metal–metal interplay in the DACs and the cases involving the metal–support interaction in a much longer range, we just discuss the coordination environment in terms of the interplay between metal and non-metal atoms/groups in a relatively near-range level in this section.

The effect of ligand atoms in the first coordination shell, which are nearest to the central atoms, has been studied in thermochemical CO_2 hydrogenation reactions. As mentioned in section 3.1, Pt_1@MIL provides an active center comprising a single Pt atom and its coordinated O atoms for CO_2 hydrogenation.[126] The metal–ligand cooperativity contributes to the dissociation of H_2 and leads to the formation of hydroxyl groups, in which the hydroxy H atoms are added to CO_2 to produce HCOO*. Subsequently, the HCOO* species could function as intermediates and go through stepwise hydrogenation, resulting in the preferential production of methanol. For the RWGS reaction, Co–N_4 (ref. 89) and Mo–N_3 (ref. 91) moieties have been found to afford excellent selectivity to CO. These distinct active centers efficiently steer the reaction pathway by modulating specific kinetic steps, which is *COOH conversion to *CO and the desorption of CO for Co–N_4, and direct dissociation of CO_2 to *CO. The valence and durability of certain metals could be also sustained with the assistance of coordination groups. Atomically dispersed Co^{2+}, which is stabilized by the –O–Si–ligand, has exhibited nearly 100% selectivity of CO in RWGS.[88] With the unique shift between the tetrahedral and the octahedral coordination structure, Co^{2+}–O–Si bonded on an SBA-15 support drives the adsorption of CO_2, the dissociation of H_2, and the formation and desorption of CO.

For electroreduction of CO_2 operated at a moderate temperature, a series of molecular catalysts which are fabricated by fixing metal complexes onto solid supports have been widely applied.[357,358] Such molecular catalysts could be viewed either as a transition between homogeneous and heterogeneous catalysts, or as roughly defined SACs that have to combine with ligands to have an effect on the catalytic reactions.[359,360] The well-defined isolated central metal atoms and corresponding ligand molecules are collectively responsible for the activation of reactants and the regulation of reaction pathways. For instance, phthalocyanine (Pc) ligands, commonly used in transition-metal-based SACs, are subjected to a one-electron reduction when coordinated to an iron single atom in a FePc SAC (Fig. 42). The environmental ligand functionalities, together with the adsorption and activation of the CO_2 molecule, prevent the over-reduction of Fe species from bivalent to univalent and even the metallic state. The Pc-coordinated bivalent iron species in the high-spin state (HS Fe(II)Pc^-), which are generated from *in situ* reduction of trivalent iron, are identified as efficient active centers with a modified d-band center and correspondingly stronger binding with CO_2 molecules. In such a SAC, the ligand molecule has two types of effects on the ultimate reaction performance: (i) modify and maintain the electronic configuration of the central atoms; (ii) help in the formation of intermediate species as an efficient charge transfer channel. These effects have been also reported in other SACs for CO_2 reduction, such as Cu–C,[213] Ni–N,[175,361] Fe–N,[175] Fe–B,[218] Zn–N,[173] Co–N,[362] In–N,[206] Fe–P,[363] *etc.*

Further doping of heteroatoms, such as O, S, P, Cl, *etc.*, into pristine SACs, or changing the coordination number might also have potentially positive influences on the reaction kinetics and apparent performances. For instance, main-group metals, which could intrinsically overcome the too strong adsorption of *H and *CO usually occurring over traditional d-block metals, have attracted more and more attention in the construction of SACs for CO_2 electrochemical reduction. Nevertheless, they always suffer from the delocalized p-orbitals and accordingly insufficient capability of CO_2 activation, as the localization of electrons is widely accepted as an effective strategy for promoted CO_2 activation.[190] Wang *et al.* developed a Ca-based SAC featuring localized electrons on p-orbitals through an asymmetric coordination by O (Ca–N_3O) doping (Fig. 43).[192] According to the theoretical analysis, such an asymmetric coordination creates a larger charge shift from active centers toward *COOH and a larger shift of the p-band center in the projected density of states (PDOS) in comparison with that of Ca–N_4. This always suggests the increasing ability for stabilizing the *COOH and a lower energy barrier from *CO_2 to *COOH. In addition, Ca–N_3O still retains an intrinsically higher energy barrier for the HER and easier desorption of *CO compared with the representative transition metal site Fe–N_4. Therefore, a reinforced performance of CO_2 conversion to CO could be achieved by Ca–N_3O. A similar result has also be reported in a Cu-based SAC, in which the asymmetric atomic interface of Cu single atoms (Cu–N_3O) affords enhanced performance of CO_2 electrochemical reduction toward CO.[364]

To realize localization of electrons, Zhang *et al.* fabricated a low-coordinate Ni SAC featuring Ni–N_3 sites[365] (Fig. 44). The change in the coordination number from the traditionally reported four to three in this work is carried out by retrofitting a Zn-based MOF derived material with Zn–N_3 sites. Such a Ni–N_3 active center delivers a much higher ability to stabilize the *COOH intermediate and thus contributes to a lower energy barrier for *CO_2 conversion to *COOH, which is the rate-determining step of the whole reaction. We should notice that the strategy of constructing an asymmetric configuration of the coordination environment of central atoms might be universal for the activation and transformation of such a symmetric nonpolar molecule CO_2, through either heteroatom doping[198,366–369] or coordination number changing.[146,176,370–373] Although possibly following different mechanisms, this strategy

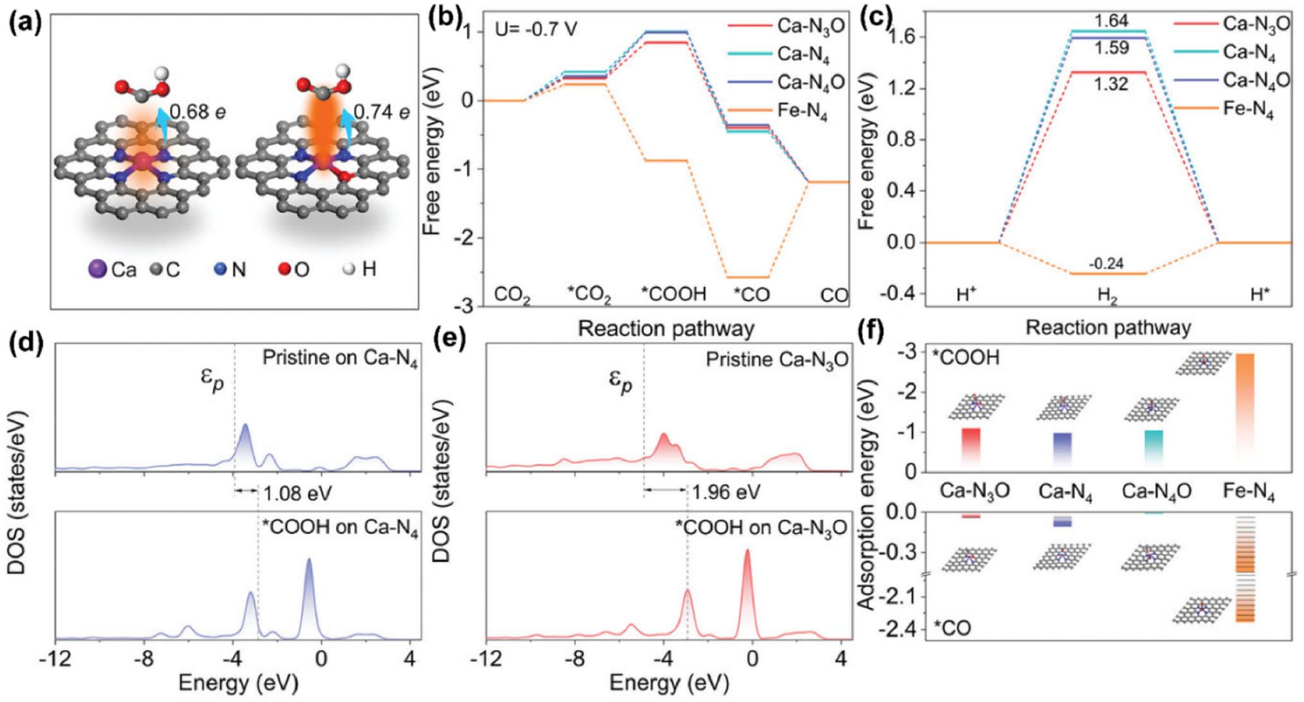

Fig. 43 (a) Comparison of the schematic diagram and Mulliken charge analysis for *COOH adsorbed on Ca–N$_3$O and Ca–N$_4$ orbitals. Free energy diagram for (b) CO$_2$-to-CO conversion and (c) hydrogen evolution. PDOS and p-band center (ε_p) before and after *COOH adsorption on (d) Ca–N$_4$ and (e) Ca–N$_3$O. (f) Adsorption energy of *COOH and *CO on catalysts. Reproduced from ref. 192 with the permission of Wiley, copyright 2023.

has also been reported in more generalized CO$_2$ reaction systems,[349,374] and might be extended to the activation of other nonpolar molecules.[375]

As for photochemical transformation of CO$_2$, metal–ligand assemblages might also play a vital role in the charge transfer process, which is possibly the rate-controlling step in a stepwise evolution from light to electron then to chemicals. In these catalysts, single atom sites with their adjacent ligand atoms or groups could function as not only an electron bridge for the promoted charge transfer, but also the active centers for CO$_2$ activation. As mentioned in Section 3.1, the rare-earth metal single atoms La,[248] Er[247,257] and Dy[244] in different coordination environments all exhibit dual functions of CO$_2$ molecular activation and charge transfer, in which the 4f levels of these metals and the interplay between their orbitals and the orbitals of neighboring coordination atoms both make a critical difference. Wang *et al.* developed a Cu single-atom-based electron bridge, N–Cu–S, in a Z-scheme photocatalyst for the production of CO and O$_2$ from CO$_2$ reduction.[376] Such an atomic structure achieves a great enhancement of the interfacial charge-transport process, thereby favoring the efficient catalytic transformation of CO$_2$ even in the absence of sacrificial agents. In contrast, impeded charge transfer is exhibited over the heterojunction material without any Cu species, and inferior promotion effect is presented by Cu NPs (Fig. 45).

Nowadays, the effect of the first coordination shell, which comprises non-metal atoms directly bonded to the central atoms, has been substantially learned. In fact, chemical interaction, which is a specific electrostatic force by nature, could also have a long-range influence. This implies that the atoms or groups in the second coordination shell, which are not directly bonded to central metal atoms, might also play an important role in the modulation of the performance of the central atoms, as already reported in some SAC systems for CO$_2$ transformation and other catalytic reactions.[377–382] We should emphasize that the non-metal species beyond the first coordination shell might also have an effect by acting as isolated active centers or adsorption sites,[383] which would not be discussed in this section but introduced in Section 4.4 when reviewing the synergy between single-atom sites and other active centers.

As mentioned in Section 3.1, simultaneously regulating the near- and long-range coordination environment has been reported to effectively modulate the electronic structure of single-atom Zn sites. ZnN$_4$ sites are decorated with an axial thiophene-S ligand in the first coordination shell, as the surrounding phosphorus atoms are constructed in the carbon matrix of a hollow carbon support (denoted as ZnN$_4$S$_1$/P-HC).[174] Such a dual manipulation of the microenvironment at different levels is able to synergistically contribute to the increase in electron localization around the Zn sites. Thus, the adsorption of the *COOH intermediate is strengthened, while the energy barrier for the formation of H$_2$ is still kept high enough to eliminate the competitive HER during an electrochemical CO$_2$ reduction reaction in H$_2$O solvent, resulting in an enhanced performance (Fig. 46). This successful example should be attributed to the remote electron induction effect, which might be an important and efficient strategy for supplementary modulation of the electronic structures of central atoms. In the

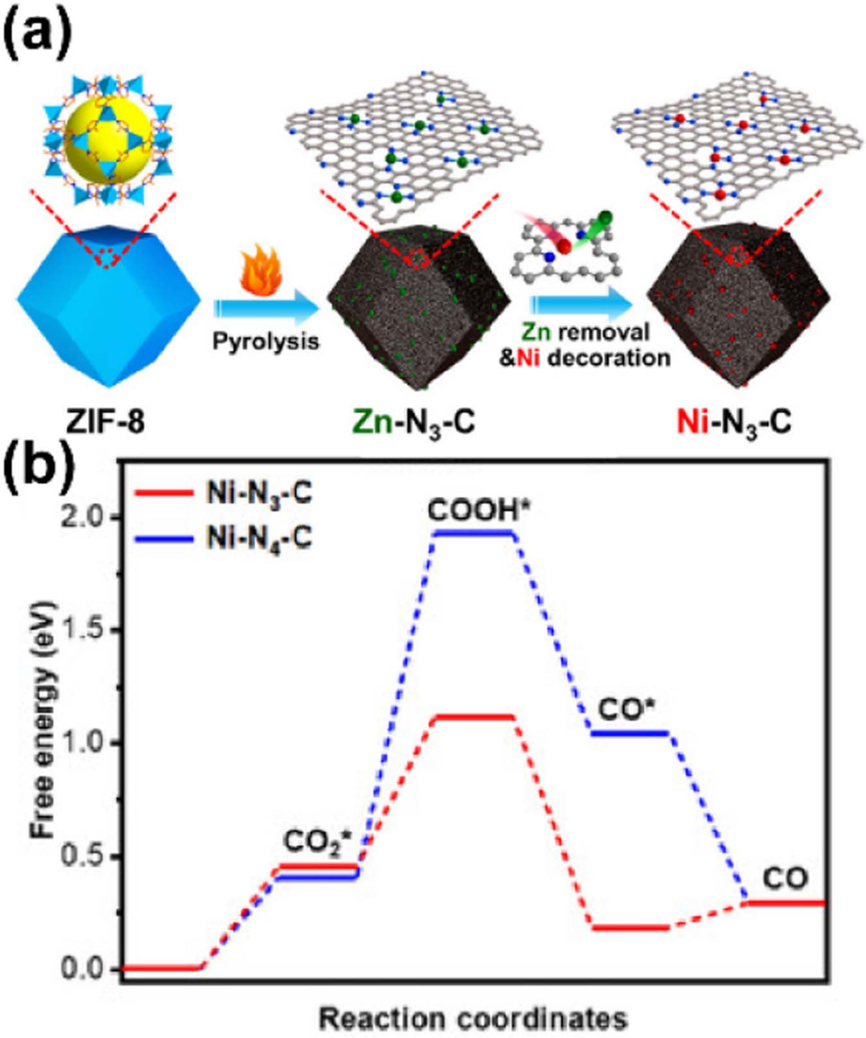

Fig. 44 (a) Fabrication of low-coordination single-atom Ni electrocatalysts. (b) Reaction paths and free energy diagrams of CO_2 reduction to CO for Ni–N_4–C and Ni–N_3–C. Reproduced from ref. 365 with the permission of Wiley, copyright 2021.

cases of sulfur-doping into the outer coordination shell of Zn–N_4 (ref. 173) and Fe–N_4,[384] a proton-feeding effect has been proposed as a more important contribution to the reinforced electroreduction of CO_2 compared to that of only the electronic effect on the central atoms, although the latter is also making a difference. As for S-doped Zn–N_4 sites, the dissociation of bicarbonate ($HCO_3^- \rightarrow H^+ + CO_3^{2-}$) is believed to be enhanced with the introduction of S atoms, leading to the accelerating formation of protons, which then participate in the activation of CO_2 toward *COOH. In contrast, the S-doped effect on Fe–N_4 is considered to promote the activation of H_2O, which offers protons for the continuous formation of the *COOH intermediate.

In this section, we provide a critical discussion about the effect of the coordination environment and its regulation for tuning the catalytic performance of SACs in CO_2 transformation processes. Different coordination endows central single atoms with distinctly varied electronic and geometric structures and accordingly reinforces the charge transfer and modulates specific reaction kinetics. By engineering the coordination microenvironment at different levels, including changing the coordination number, constructing axial coordination, and doping heteroatoms other than carbon and nitrogen, the intrinsic catalytic properties of central atoms could be well regulated with optimized energy bands, electron orbitals and correspondingly modulated intermediate adsorption and transformation. Furthermore, the non-metal atoms beyond the first shell might also have an effect on the central atoms through either remote electronic induction or other kinetic reinforcements to specific reaction procedures. As a result, all these efforts to regulate the coordination environment contribute to the highly controllable properties and performances of SACs, offering excellent opportunities for their widespread use in various reactions under different conditions.

4.3 Support effect

The most significant difference between homogeneous metal-based molecular catalysts and heterogeneous SACs is the application of supports. Supports, basically speaking, are

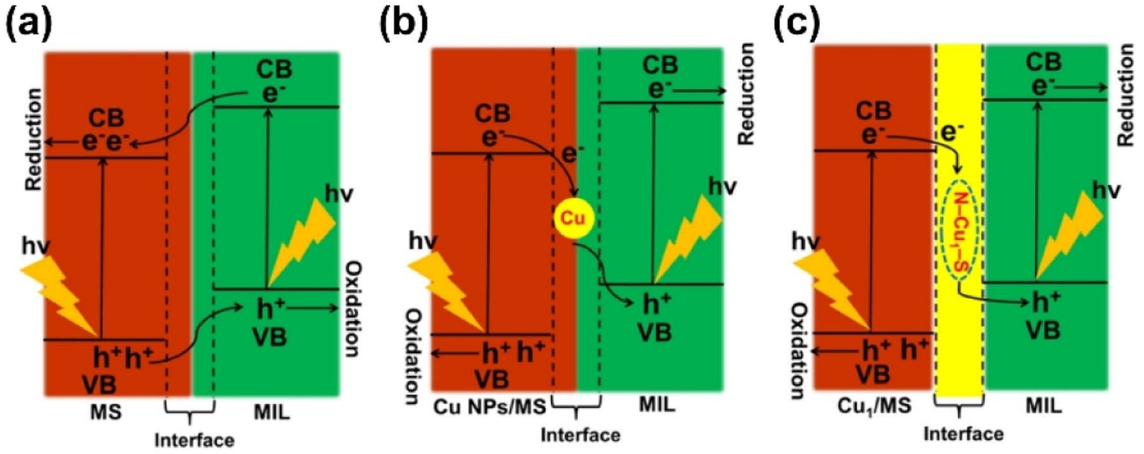

Fig. 45 Electron-transfer process models of (a) MS (MoS_2)/MIL (MIL-125-NH_2), (b) Cu NPs as the electron bridge, and (c) Cu SA as the electron bridge. Reproduced from ref. 376 with the permission of Wiley, copyright 2023.

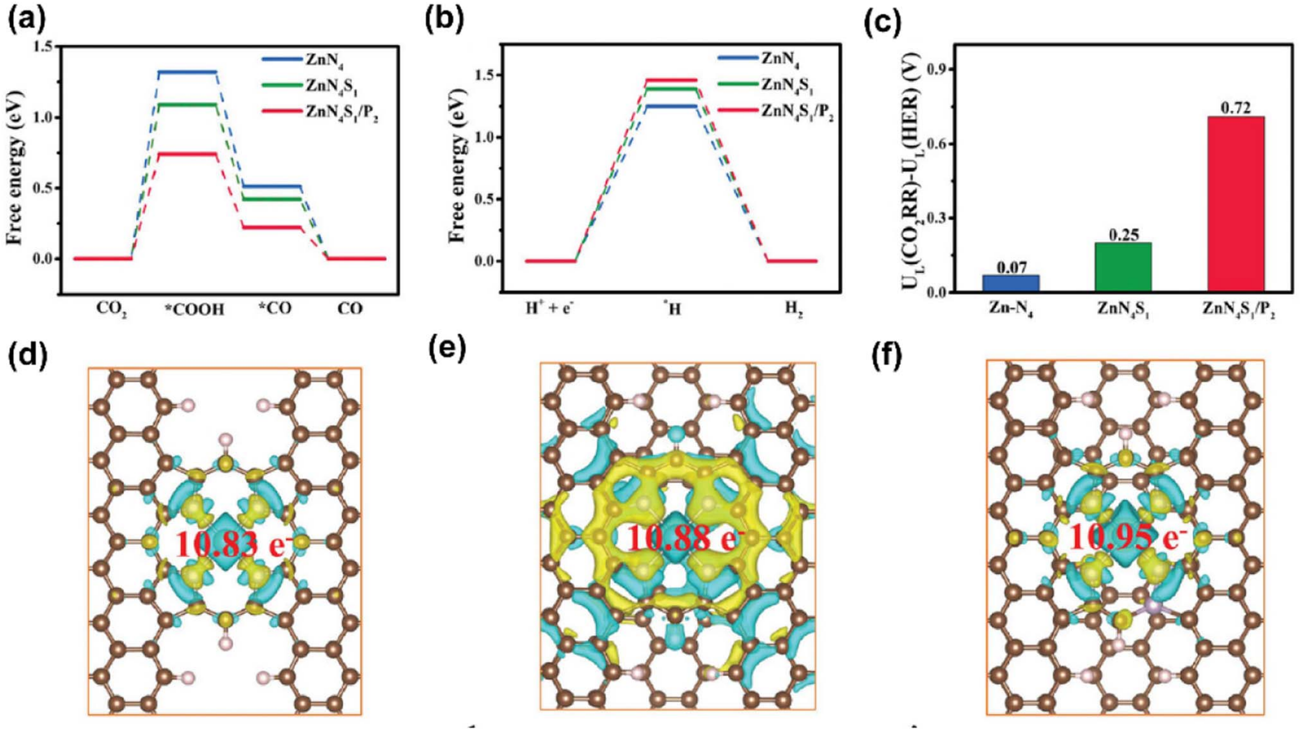

Fig. 46 Calculated free energy diagrams for (a) CO_2 reduction and (b) the HER. (c) Limiting potential differences for different active moieties at $U = 0$ V *versus* RHE. The charge density difference of (d) ZnN_4, (e) ZnN_4S_1, and (f) ZnN_4S_1/P_2 models. The iso-surfaces in yellow and cyan represent electron accumulation and repulsion, respectively. The iso-surfaces were set to be 0.04 e $Å^{-3}$. Reproduced from ref. 174 with the permission of Wiley, copyright 2023.

designed and prepared for fixing the central atoms onto specific locations of solid surfaces, thus preventing the loss of active sites during heterogeneous reactions under harsh conditions. Beyond the original intention of support construction, the chemical properties and catalytic performances could be also modulated by controlling the features of supports and the synergistic effects between supports and active centers. In particular, the supports used in electrochemical and photochemical processes are always responsible for charge transfer[385] and light-induced charge separation,[51,54] respectively. In some cases, the supports could also play a vital role in the adsorption, activation and transfer of certain reactive moieties, such as the most common hydrogen and oxygen species.[77,120,226] We should emphasis that the supports discussed in this section would be limited to their intrinsic topological and electronic properties, aiming at their effect on the single-atom sites but not involving active centers other than single atom sites grafted onto them. The synergy between single atom sites and other active centers would be elaborated in the next section.

Generally, the effect of supports might be able to be interpreted based on three aspects:[17] (i) the dispersion and location of central atoms for the optimal stability and activity of active centers; (ii) the chemical interaction between the substrate and central atoms leading to the structure change of active interfaces; (iii) porous structures and channels for the transportation of reactants and products.[132] These aspects could either exert influence independently or co-exist and convolute in a given catalyst. Thus, it might not be an easy task to design a suitable support for SACs without comprehensive understanding of the complex physicochemical factors.

First, the selection and engineering of supports should take the loading and stabilization of single atoms into consideration. As mentioned in Section 3.1, a porous organic polymer affords an excellent support for the anchoring of single atom iridium and provides a suitable chemical environment for quasi-homogeneous reduction of CO_2 into formate.[101] The much higher performance of this support in comparison with that of traditional activated carbon and popular C_3N_4 might be attributed to the abundant functional groups, which could be readily introduced during the preparation processes. Relatively high loading of Ir single atoms thus could be chelated onto the support with a satisfying durability. On the other hand, vacancy or defect sites have been extensively reported to be used to seize the single atoms and tune the intrinsic activity of SACs.[235,386,387] Single-atom Ir sites could be anchored on the In_2O_3 substrate, as In_2O_3 is partially reduced with H_2 with the formation of oxygen vacancies prior to being subjected to wet-chemical impregnation.[59] Beyond the effect on the fixing of single atoms, the oxygen vacancies even present a synergy with single-atom sites during the activation of CO_2 and C–C coupling. In this way, such an Ir SAC realizes effective ethanol production from liquid-phase CO_2 hydrogenation, as mentioned in Section 3.1. To tailor the local nitrogen coordination environment of the central single atom Ni for the construction of an efficient Ni–N moiety, Chen *et al.* adopted a preparation strategy of treating precursors by using low-pressure plasma induced in a microwave oven.[388] In this way, the coordination environment of Ni-SACs could be facilely tuned by varying the treatment duration. A longer treatment prompts the reconstruction of the coordinative nitrogen species around Ni atoms, forming a Ni–N_2 configuration with neighboring nitrogen vacancies. The resulting active centers with a highly defective local pyridinic N environment afford abundant spare sites for bonding CO_2 and thus reduce the energy barrier for the formation of intermediate COOH* and CO*, delivering an enhanced performance in CO_2 electroreduction. The formation of defect sites could be also realized by the chemical interaction between metal species and substrates rather than the preparation processes. For instance, on certain crystal facets of CeO_2, the presence of Pd could highly promote the formation of oxygen vacancies by providing dissociated H species under a H_2 atmosphere, which then facilitate the removal of surface oxygen atoms.[121] The oxygen vacancies could serve as adsorption sites for CO_2, where CO_2 is further activated and goes through stepwise hydrogenation into methanol. A similar effect of chemical interaction between metals and substrates has been also reported in a Cu–TiO_2 system for photochemical reduction of CO_2.[231] Besides inducing the spontaneous formation of oxygen vacancies, such an interaction even affects the spatial distribution of Cu single atoms, which form a configuration featuring neighboring sites engaging in the catalytic transformation of intermediate species.

Recently, with the assistance of the well-defined metal-coordinated phthalocyanines (Pc) as platform molecules supported on carbon-based substrates, the regulation of isolated metal sites based on the effect of chemical interaction between metal species and substrates has been extensively studied in the electrochemical reduction of CO_2.[330,389–399] As reported in many cases, the metal-Pc sites are loaded on carbon-based substrates, which feature high specific area and provide remarkable electrical conductivity and stability due to the inherent π-conjugated systems in them. However, a promoted strong d–π conjugation between the d orbitals of the metal centers and the π orbitals of the substrate always causes electron transfer from the metal center toward the substrate, *i.e.*, the strong delocalization of electrons introduced by the support. This turns out to be detrimental for the activation of CO_2 molecules on metal sites of SACs and vastly hampers the catalytic transformation. To solve this problem, Wang *et al.* introduced cyano groups (–CN) onto the C_3N_4 substrate for attenuating the d–π conjugation of single-atom Ni sites.[394] As a consequence of the rupture of an aromatic heterocycle near the Ni atoms, the CN groups break the integrity of the conjugated plane between Ni and substrates, therefore confining the electrons to the vicinity of the central metal. The increased localization of electrons in Ni not only favors the adsorption of CO_2, but also lowers the free energy barrier for the formation of the intermediate *COOH in the electroreduction of CO_2, as predicted by the theoretical calculations and proved by the experimental results (Fig. 47). Interestingly, in an earlier report, the decoration on the Pc ligands by molecular engineering of the pendant groups into –OCH_3 and –CN instead of the substrates gives a different result, in which the methoxy-decorated single-atom NiPc sites exhibit much higher performance than that of –CN due to the lower energy barrier for the formation of *COOH.[395]

The geometric structure of supports, such as the morphology of crystals[121,283] and the curvature of supports,[170,171,400] has been also considered as critical factors affecting the electronic structure of single-atom sites *via* changing the metal-support interaction. The former has been substantially studied in various catalytic systems, and could be rationalized with the distinct properties of different facets, *e.g.*, interatomic spacing, symmetry, lattice-matching, internal strain, defect sites, *etc.*[37,73,385] And the latter has been also more and more recognized in catalytic reactions recently, especially those with carbon-based substrates in electrochemical systems.[401,402] Based on the regulation of curvature, the optimization of performance in CO_2 reduction has been realized over Zn single-atom sites supported on carbon nanofibers and nano-onions.[170,171] By using carbon nanotubes (CNTs), an ideal substrate with an

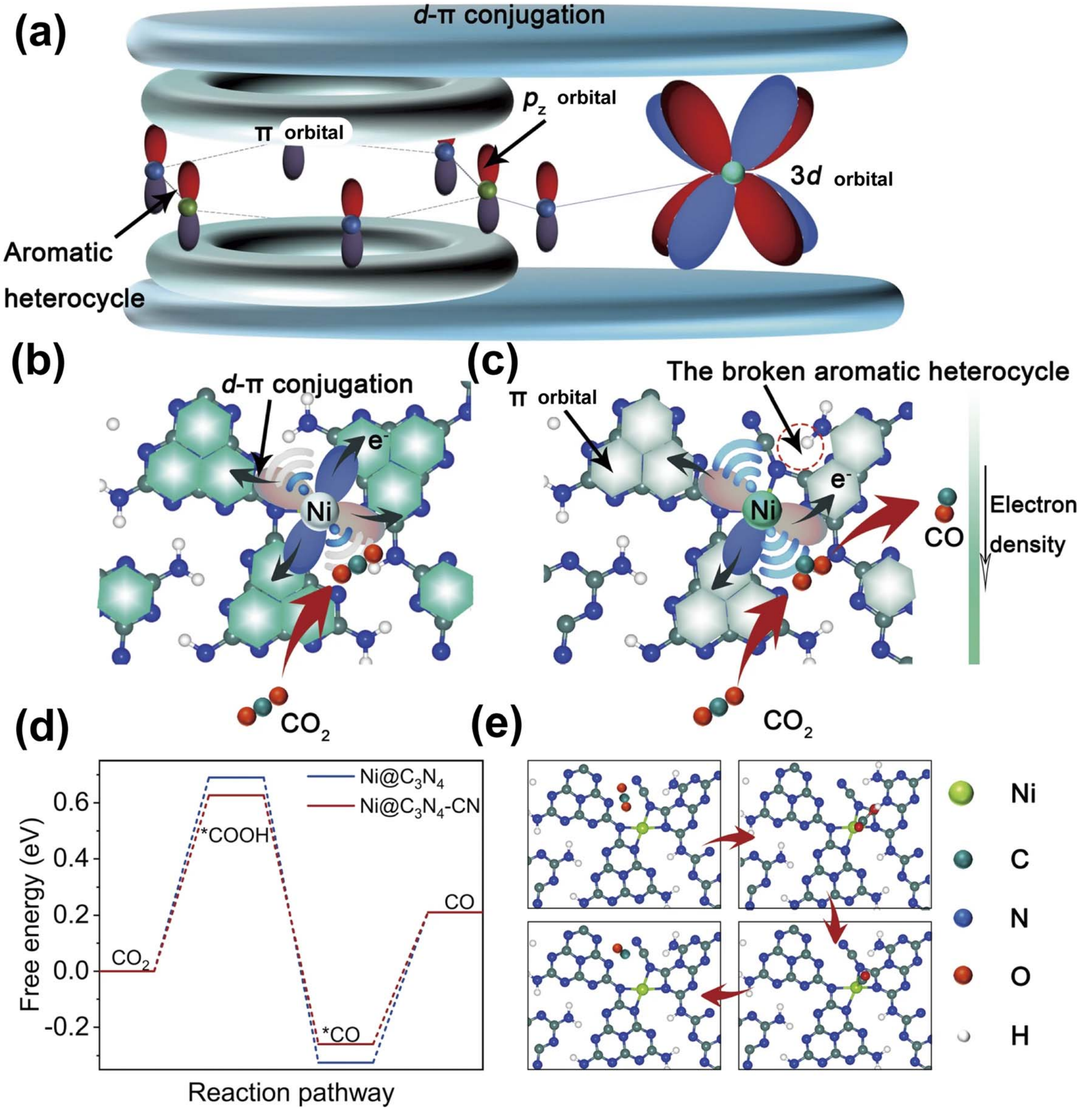

Fig. 47 (a) Schematic of d–π conjugation. The effect of d-π conjugation on CO_2 activation over (b) Ni–C_3N_4 and (c) Ni–C_3N_4–CN. (d) Free energy diagram of CO_2 conversion to CO. (e) Structure and adsorption configurations of key intermediates on Ni–C_3N_4–CN. Reproduced from ref. 394 with the permission of Nature Springer, copyright 2022.

adjustable surface curvature, for supporting molecular centers of single atoms, like CoPc, Su *et al.* studied the enhancement effect of the strain change on CO_2 reduction[396] (Fig. 48). The strain change of molecular sites, which is induced by the variation of local curvature, could be implemented by selecting CNTs with different diameters, *i.e.*, the longer the diameter, the smaller the curvature. The largest curvature occurs in a single-wall CNT (SWCNT), where the best performance of methanol production is also shown, as the CoPc has been supported beforehand. The better performance could be attributed to the significantly stronger adsorption of CO and promoted activation of the C═O bond in adsorption sites, which both facilitate the deep protonation toward methanol. More intrinsically, the strain induced by the curvature of substrates brings about the distortion of geometry of the adduct $CoPcH_4(CO)$, leading to a lower free energy than that of the flat analogue. Inspiringly, such an effect on the basis of strain modulation could even be extended to FePc and NiPc for the oxygen reduction reaction and CO_2 reduction reaction, respectively.

Apart from the effect on fixing single-atom species and modulating the properties and behaviors of active sites *via* metal-support interaction, the texture features of supports, like pores and channels, have also shown significant influence on the performance of SACs, such as controlling the diffusion for enhanced mass transfer. Such regulation of diffusion kinetics could not only accelerate reactions by enriching the reactants to a higher local concentration and increasing the probability of contact with active centers, but also shift the reaction

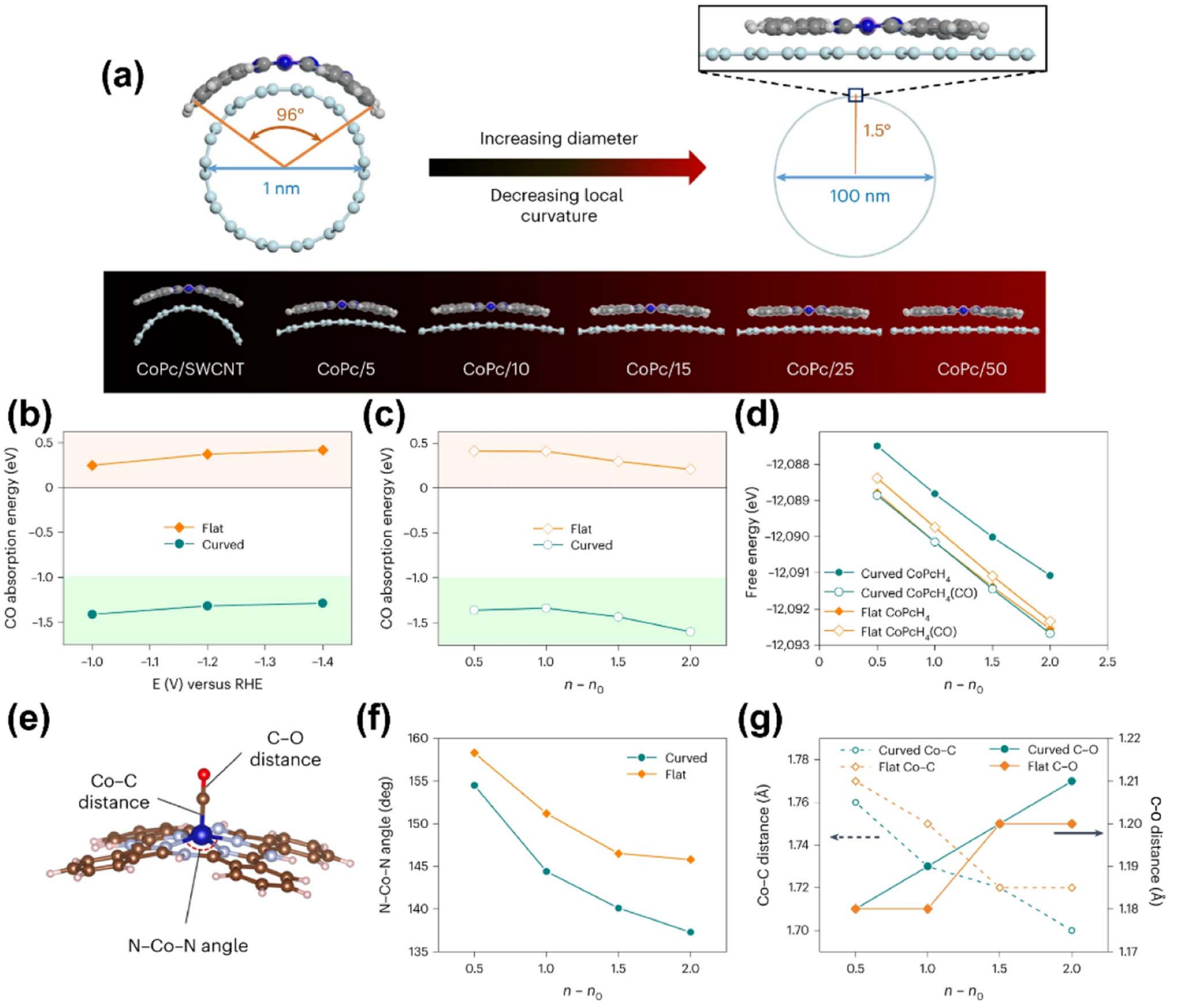

Fig. 48 (a) Illustration of the structural distortion of CoPc on different-diameter CNTs. Absorption energy *versus* potential (U_{RHE}, V) (b) and $n - n_0$ (c), where n is the number of electrons added ($n - n_0 = 1$ indicates that 1 electron has been added to the neutral system). (d) Free energies of curved and flat $CoPcH_4$ with and without CO adsorption *versus* $n - n_0$. (e) Representative N–Co–N angle and Co–C and C–O distances of $CoPcH_4$. (f) N–Co–N angle (degrees) *versus* $n - n_0$ for the curved and flat structures. (g) Co–C and C–O distances (Å) *versus* $n - n_0$. Reproduced from ref. 396 with the permission of Nature Springer, copyright 2023.

equilibrium to a positive orientation and prevent secondary side reactions by evacuating the products in time. Reticular materials, MOFs and COFs, and other porous carbon-based materials have been extensively used for this purpose,[403] either as precursors that go through subsequent pyrolysis and other post-treatment,[145,404] or directly as substrates for encapsulating or anchoring single-atom metal species.[103,107,266–270] Rather than their role in the photochemical catalytic reactions for light harvesting and charge dynamics as mentioned in Section 3.1,[226,242] the exploitation of their rigid, robust and multifunctional porous framework is more universal and widely realized in non-photochemical CO_2 transformation processes.[405] By using polystyrene spheres (PS) as a hard template during the synthesis of iron-doped ZIF-8, highly ordered hierarchical porous single-atom Fe catalysts are fabricated as an excellent platform to investigate the pore size effect on electrochemical CO_2 reduction in detail (Fig. 49).[404] The pore size could be facilely modulated by changing the size of PS, and a delicately designed porous structure with larger mesopores and macropores significantly creates an advantageous environment with a high local CO_2 concentration around the Fe single-atom active centers, which might be attributed to the intrinsically tuned mass transfer for enrichment of CO_2 inside the catalyst. Such a porous structure together with the single-atom sites helps to achieve higher performance, especially in the limited mass transfer region. In fact, whether in the thermochemical or the electrochemical or the photochemical processes, increasing the contact between reactants and active centers by enhancing mass transfer yet without affecting the intrinsic features of single-atom sites is always an efficient strategy for improving the apparent performance. The effect of mass transfer could be altered by using the operation conditions, and thus it might be not so significant for those cases that aim at studying the reaction kinetics of SACs rather than diffusion kinetics. However, it would still be an important subject to optimize the diffusion properties of SACs for their practical application in a realistic scenario. Besides the influence on the regulation of the concentration of guest molecules *via* controlling diffusion, the porous structures might also make a difference in modulating the density of active sites, as reported in a Cu SAC with single Cu atoms embedded onto two-dimensional carbon nitride[406] (Fig. 49). The nitrogen-appended nanometric pores afford high loading of single-atom Cu species and confine multiple Cu sites in adjacent locations through a metal ion exchange process between Li^+ or Na^+ and Cu^{2+}. These Cu sites are kept insulated from each other with a spatial distance beyond that of conventional Cu–Cu, and homogeneously coordinated with two nitrogen atoms within the nanopores of supports. It is manifested that these single-atom Cu sites cooperatively alter the reaction energy profiles into having a much lower barrier for the stepwise formation of CO* and CH* intermediates, resulting in a higher yield of CH_4 in the electrochemical CO_2 reduction reaction. In the design and fabrication of such a SAC, the porous structure plays a vital role in the confinement of active sites for cooperative catalysis.

In summary, besides the fundamental use in surface adsorption, as well as the specific use for charge generation and transfer in electrochemical and photochemical cases, the delicate regulation of supports provides extra opportunities for the optimization of SACs based on their effect on the central single-atom sites. The functional groups, defective sites and other chemical moieties help the dispersion and stabilization of single-atom active centers for durable application in various CO_2 transformation reactions under varied operating conditions and redox atmospheres. The chemical interaction between single-atom sites and substrates, which could be tuned by certain modifications in terms of both geometry and electrons, plays a critical role in regulating the local structure of central atoms, thereby leading to varied energy features for the adsorption and transformation of reactant and intermediate species. Furthermore, thanks to the porosity engineering of substrates, the local concentration of reactants could be well-regulated near the single-atom active centers, creating a specific microenvironment for the positive reactions. The confinement effect on the active sites derived from the porous structure, on the other hand, might contribute to synergistic and cooperative catalysis by controlling the density and location of active centers.

4.4 Synergy with other types of active centers

Despite their unique performance in some specific reactions, SACs are not panacea in all cases, especially those which need the cooperation between multiple active sites. Although the arrangement of peer single-atom sites, the regulation of the coordination environment and the modification of supports

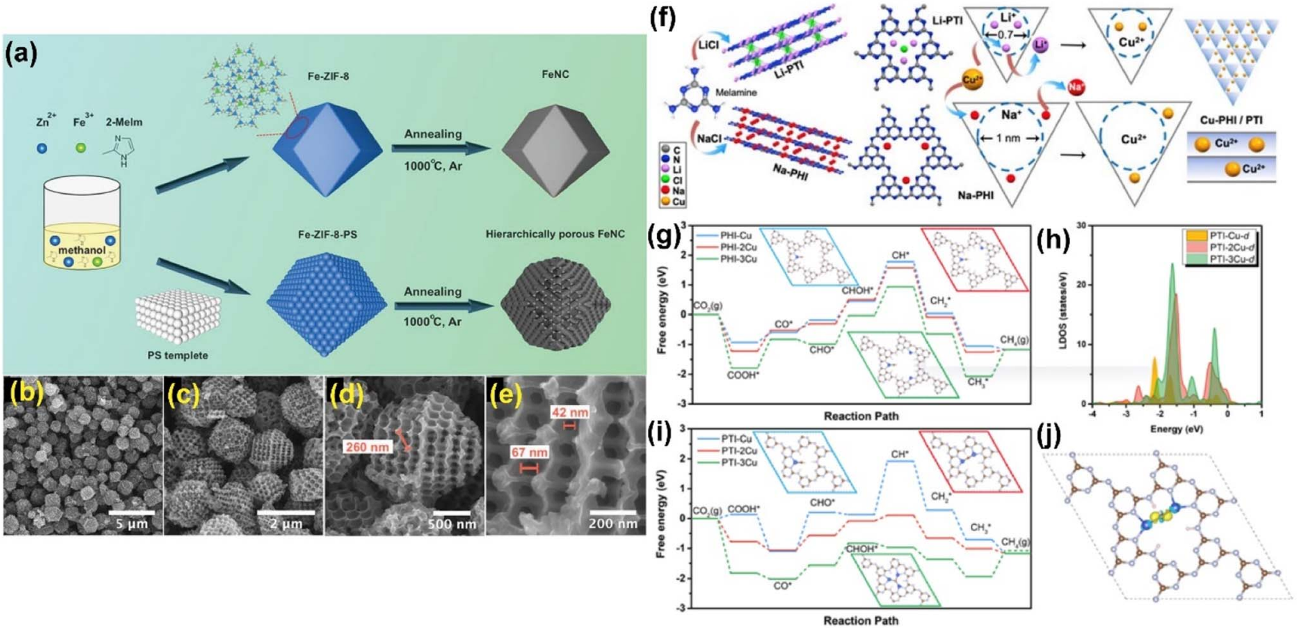

Fig. 49 (a) Illustration of the synthesis route of FeNC and hierarchical porous (HP)-FeNC; (b–e) SEM images of HP-FeNC. Reproduced from ref. 404 with the permission of Wiley, copyright 2023. (f) Synthetic scheme of various Cu-CN SACs (poly (heptazine imide) and poly (triazine imide) are denoted as PHI and PTI, respectively) samples through metal ion exchange with Li^+ and Na^+, respectively. (g) Reaction process of the CO_2 reduction reaction on PHI-*n*Cu ($n = 1, 2, 3$). (h) Local density of states of Cu-d orbitals on PTI-*n*Cu ($n = 1, 2, 3$). (i) Reaction process of the CO_2 reduction reaction on PTI-*n*Cu ($n = 1, 2, 3$). (j) Charge density difference of CH* absorbed on PTI-2Cu. The yellow and azure areas indicate electron accumulation and loss, respectively. The white, gray, silver, and blue balls represent H, C, N, and Cu atoms, respectively. Reproduced from ref. 406 with the permission of Wiley, copyright 2023.

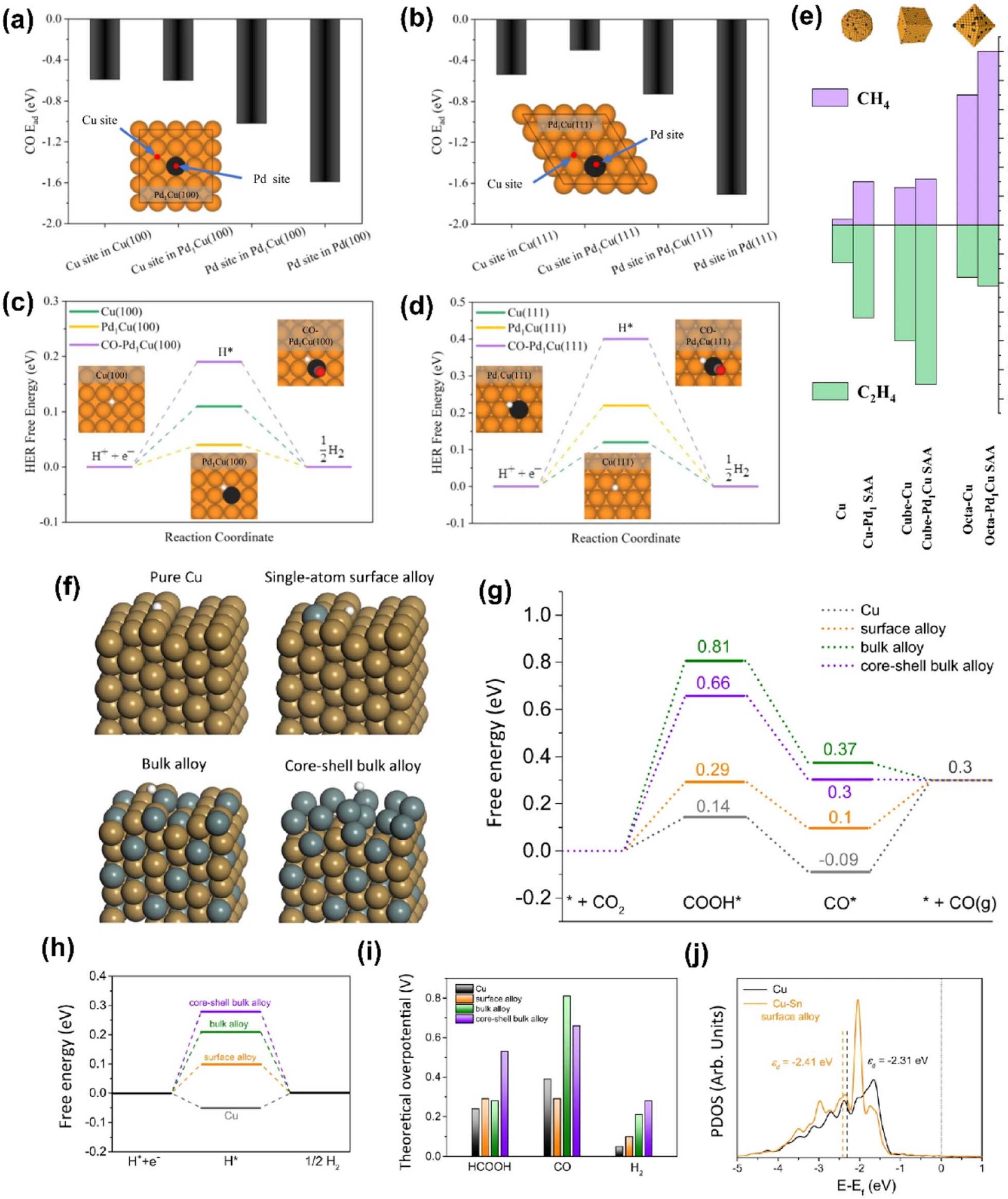

Fig. 50 The adsorption energy of *CO over the (a) (100) and (b) (111) facets of bare Cu, Pd$_1$Cu, and bare Pd, respectively. The free energy diagram of the HER over the (c) (100) and (d) (111) facets of bare Cu, Pd$_1$Cu, and Pd$_1$Cu in the presence of CO molecule adsorption over the Pd site (CO–Pd$_1$Cu). Color code: Cu (orange), Pd (black), C (gray), O (red) and H (white). (e) The FE distribution of CH$_4$ and C$_2$H$_4$ obtained using Cu and Pd$_1$Cu SAAs (at −1.1 V *vs.* RHE). Reproduced from ref. 411 with the permission of Nature Springer, copyright 2023. (f) The theoretical model structures on stepped facets of pure Cu, the Cu–Sn surface alloy, the bulk alloy and the core–shell bulk alloy with adsorbed H*. The dark goldenrod and slate gray balls represent Cu and Sn atoms, respectively. (g) The calculated free energy diagrams of CO$_2$-to-CO conversion. (h) The calculated free energy diagrams of the HER. (i) The theoretical overpotentials of HCOOH, CO, and H$_2$ production. (j) The projected density of states of d orbitals of active Cu atoms at the step edges on pure Cu and the Cu–Sn surface alloy. The dotted gray line indicates the Fermi level. The d-band centers (ε_d) are denoted by dashed lines. Reproduced from ref. 412 with the permission of Nature Springer, copyright 2023.

could make a difference, it still seems that the "Lone Ranger" should find its companies, as the old saying goes, "Many hands make light work". To date, for more extensive use of SACs in CO_2 transformation reactions, many other types of active centers have been introduced in the SAC systems to not only reinforce the reactions the SACs have already realized, but also break through the limitation of the current SACs into more complicated reactions. In these cases, the synergy between single-atom sites and other types of active centers should be the focus of study and design. We should emphasis that some components function as both active centers and substrates anchoring single-atom metal species, which might have an obscure boundary sometimes. In this section, we will try to focus more on their role as active components, while we could not deny the support effect in some cases as well.

The combinations of single-atom sites and other metal-containing species grafted on the single-atom catalysts, such as metal nanoparticles, nanoclusters, and metal-based compounds (oxides, carbides, nitrides, sulfides, phosphides, *etc.*) in three/two/one-dimensional morphology, have been reported for the application in various reactions[407,408] including CO_2 transformation reactions. As already mentioned in Section 3.1, single-atom Sb with Cu NPs,[205] isolated Ni–N with Cu NPs,[164] single-atom Pb with Cu NPs,[211] single-atom Cu doped SnO_2,[212] single-atom M doped gold and silver NPs (M = Cu, Ni, Pd, Pt, Co, Rh, and Ir),[409] single-atom Co with $Ti_3C_2T_x$-MXene,[272] single-atom Cu with a Au–Cu alloy,[234] single-atom Ag chains with MnO_2,[236] *etc.*, have already manifested their advantages in the electrochemical and photochemical reduction of CO_2 with respect to the experimental and theoretical results. There is a well-known term to define the cases where single atoms form an interface with metal NPs, a single-atom alloy (SAA), in which the NPs function as both primary supports and active components.[410] In fact, metal alloying is a broadly adopted strategy to improve the performance of a single metal, but is always limited by the side reactions induced by the introduced second metals, such as the HER promoted by platinum-group metals in CO_2 electroreduction. Thus, Chhetri *et al.* developed a series of dual-site catalysts featuring Pd and Pt single-atoms alloyed with Cu crystals, by which they promote the hydrocarbon production without prompting the HER[411] (Fig. 50). Owing to the suitable binding energy of both *CO and H*, metallic Cu species are responsible for the primary formation of CH intermediates and C–C coupling for the production of C_{2+} hydrocarbons, as Pd single-atom sites, instead of promoting the HER, theoretically afford a more stable adsorption of CO* and even suppressed the HER when CO* pre-exists on the top site of Pd. The experimental results further confirm the advantages of such a dual-site catalyst with an optimized configuration of single atoms and metal nanoparticles, where CH_4 and C_2H_4 are preferentially produced over varied morphologies of Cu crystals. Regarding the different interfaces between two metal species in the alloys, there has also been thorough investigation of the mechanisms. Depending on the loading amount of Sn, the Cu–Sn alloy could form distinct interfaces, *i.e.*, a single-atom surface alloy in $Cu_{99}Sn_1$ and $Cu_{97}Sn_3$ and core–shell bulk alloy in $Cu_{70}Sn_{30}$ (ref. 412) (Fig. 50). Such a configuration of interfaces has a great effect on the electronic structures of Cu atoms. As for the surface alloy with a left shift of the d-band center away from the Fermi energy level, the binding energy of intermediate species is thus weakened for more favored CO production, as the desorption of *CO is enhanced with a lower energy barrier. In contrast, the bulk alloy offers a much higher energy barrier for the formation of *COOH, thus making CO_2 through the dominant OCHO* intermediated route for HCOOH production. In a word, delicate design and fabrication of SAA catalysts have been believed to be an efficient method to break the linear scaling relationships shown in single metals, enhance specific procedures and adjust the reaction kinetics, in which the single-atom sites might function as not only the active centers but also the modifiers of metal NPs.[413]

In some cases, on the other hand, the single-atom sites do not directly come into contact with the other metal active centers, but afford a tandem process by solely catalyzing certain reactions.[414] For instance, Cu NPs and isolated Cu–N_4 sites co-exist on a carbon-based substrate for the CO_2 electroreduction to C_{2+} products[415] (Fig. 51). The single-atom sites seem to not be responsible for the formation of *CO from CO_2 due to the much higher energy barrier than that of Cu NPs according to the theoretical calculations. In contrast, the atomic Cu site could efficiently promote H_2O dissociation to provide *H, as verified by the high HER performance of the intact Cu–N–C catalysts. Since the reaction energy for protonation of *CO to *CHO is closely correlated with the *H coverage on the Cu NP surface and properly increased coverage leads to a lower energy barrier for the formation of *CHO, the key to the optimized catalytic performance might be the facilitated generation of *H from atomic Cu sites, which is then transferred to Cu NPs through the carbon matrix. The *H coverage on Cu NPs is accordingly increased, resulting in accelerated protonation and higher activity for C_{2+} production. Coincidentally, by regulating the preparation conditions, Fe NPs and pyrrole-type Fe–N_4 sites could be co-anchored on the less-oxygenated carbon supports for electrochemical CO_2 reduction[416] (Fig. 51). But the difference is that the isolated Fe–N_4 sites are in charge of the adsorption and initial activation of the CO_2 molecule, while Fe NPs reinforce the proton transfer from dissociation of water to the active centers for the formation of *COOH, as proved by the kinetic isotope effect in H_2O and D_2O. The theoretical simulation based on an Fe_{13}-cluster-containing model also implies that the introduction of Fe NPs possibly further favors the stabilization of the *COOH intermediate, thereby boosting the formation of CO. Inspired from these two examples, we should find out if the synergy between such insular active centers might not have on effect by changing their own properties like in the cases of the above mentioned SAA catalysts, but playing to their strengths for the best reaction coupling.

Besides cooperating with metal species, single-atom active sites could be also combined with non-metal active centers. We have demonstrated the synergy between the single atoms and vacancy sites of the substrates in the above sections.[59,121,152,215,231,235,295] Indeed, the formation of vacancies could not only change the coordination environment of central atoms but also afford the adsorption and activation of

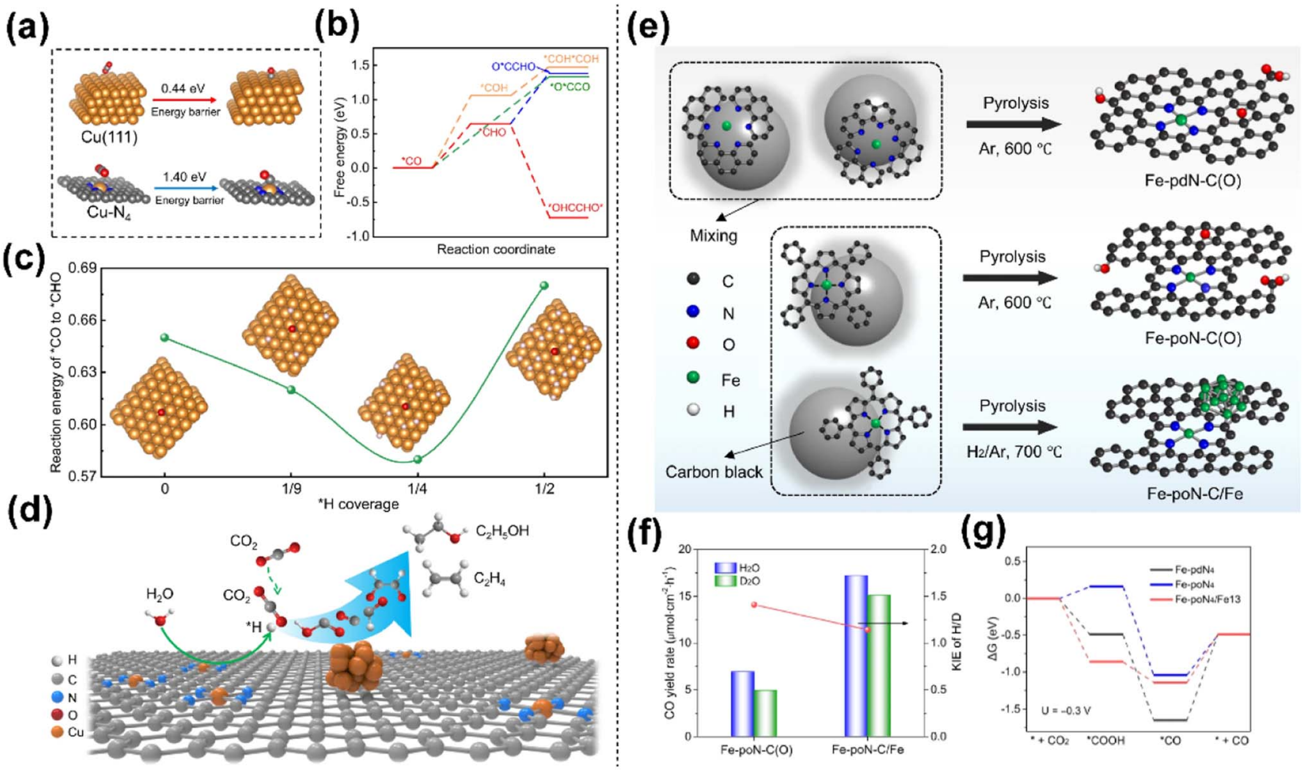

Fig. 51 (a) The energy barrier of CO_2 conversion to *CO over Cu(111) and Cu–N_4. (b) The free energy diagram for the CO_2RR to describe the possible C–C coupling step from *CO over Cu(111). (c) Reaction energy of *CO hydrogenation to *CHO on Cu(111) as a function of *H coverage. (d) Proposed reaction mechanism for CO_2 reduction to C_2 products on Cu_1/Cu_{NP}. Reproduced from ref. 415 with the permission of Nature Springer, copyright 2023. (e) Schematic illustration for the synthesis of Fe_{SA}-pdN-C(O), Fe_{SA}-poN-C(O) and Fe_{SA}-poN-C/Fe_{NP}. (f) Kinetic isotope effect (KIE) values and CO yield rates of Fe_{SA}-poN-C(O), and Fe_{SA}-poN-C/Fe_{NP}. (g) Free energy diagrams at −0.3 V. Reproduced from ref. 416 with the permission of Nature Springer, copyright 2023.

reactants, thus promoting specific reaction kinetics. Non-metal species, in addition to their role in coordination as ligands, could function as active sites as well. For instance, a photocatalyst comprising P and Cu dual sites anchored on graphitic carbon nitride (P/Cu SAs@CN) has been employed in CO_2 reduction with a high C_2H_6 evolution rate of up to 616.6 μmol g^{-1} h^{-1}.[417] The single-atom Cu sites are in a charge-enrichment stage for the adsorption and activation of CO_2 molecules, while the isolated P atoms serve as hole capture sites for the accelerated light-driven formation and transfer of charge. In this way, such a catalyst realizes kinetically enhanced C–C coupling between *CO and *COH intermediates and thus achieve a higher C_2H_6 production. We should notice that, in this process, P atoms do not coordinate with or modify Cu sites, but function as independent active centers. In fact, non-metal elements applied in photocatalytic CO_2 transformation are not rare at all, as non-metal semiconductors have exhibited significant light-to-electron activity intrinsically.[54,242] Future investigations into the activity of non-metal species in more reactions might require greater efforts for the analysis of local structures, as it would be difficult to distinguish the activity from the coordination and support effects and reach an unambiguous conclusion.

In this section, we demonstrate the cooperation between the single-atom sites and other types of active centers and show how the synergy has an effect. By closely contacting and forming an alloy with well-regulated interfaces, the cooperative sites could break the scaling relationship in a single metal, retrofitting the reaction kinetics. In a separate position, the cooperative sites could afford their own activity for coupling into a tandem process with enhanced procedures. In particular, the non-metal sites have been proved to be able to serve as independent active centers in some light-driven reactions. The introduction of other active centers remarkably breaks through the limitation of SACs in more complicated reactions and is expected to fully exploit the unique advantages of SACs in terms of both structures and performances.

5. Research methods

In the above sections, we have reviewed significant progress on the SACs for chemical conversion of CO_2 from the perspective of reaction types, focusing on the distinctive effect that SACs have on the catalytic performance. In fact, the synthetic methods, the characterization techniques and the computational approaches for modelling for structure analysis and mechanism investigation, which are just as important as the catalytic performance, should be also paid great attention. There should be a positive feedback loop in an ideal research process, that is, reasonable design and ingenious synthesis offering preliminary SACs, then accurate evaluation and advanced characterization studies giving a fundamental structure–performance relationship, followed by in-depth investigations into mechanisms providing explanations regarding internal logic and modeling theory, and eventually the obtained insights in turn propelling reasonable design and synthesis (Fig. 52). As the loops are executed over and over again, the catalysts are correspondingly getting closer to the optimum. In comparison with other types of heterogeneous catalysts, SACs possess more potential to realize such desired loops due to their commonly well-defined active sites. Furthermore, as a simple linear triatomic molecule, the conversion of CO_2 embraces mazy pathways involving multiple key intermediate species and rate-determining steps. Hence, the incorporation of SACs into CO_2 conversion systems, despite bringing greater challenges to penetrating into the inherent understanding, provides more opportunities for accessing the rewarding experience of catalysis studies. Herein, we will concentrate on the crucial issues in terms of material synthesis, characterization, and mechanisms in the systems of CO_2 conversion with SACs as catalysts, and very general research studies that are not related to CO_2 conversion will be circumvented as possible.

5.1 Material synthesis

From the perspective of methodology, the synthetic routes of SACs can be divided into two categories: one is the bottom-up strategy, *i.e.*, establishing a substrate initially followed by loading SAs or the corresponding metal precursors onto it, such as precipitation, impregnation, deposition, and adsorption; another is the top-down strategy, *i.e.*, fabricating a metal-substrate mosaic preliminarily followed by transformation into SAC structures, such as pyrolysis, etching, and redispersion. Generally, the choice of synthetic method is highly dependent on not only the features of metal elements and supports, but also the reaction conditions and desired performance. For instance, for the synthesis of a SAC operated at a relatively higher temperature and in a complex redox atmosphere in a thermochemical catalytic system, oxides always more suitably serve as a support rather than carbonitride, since the stronger electronegativity of oxygen atoms favors the enhanced bonding between SAs and supports. Commonly, reducible oxides with the potential of creating vacancies by removing partial oxygen atoms have been applied in these cases. This is rather important for the application of SACs in thermal catalytic CO_2 hydrogenation involving C–C coupling that a second type of active sites other than metal SAs, such as O_v, is highly required. In this case, defect engineering is supposed to take into account the synthesis of SACs, so that the synergy effect derived from the collaboration between SAs and O_v could be feasibly cast on both the activation of CO_2 and the formation of C–C bonds.[59,284] In the meantime, the SA sites always present distinct valence states and electronic structures from that of their NP and NC counterparts *via* coordinating with neighboring atoms, in which the inherence of supports (*e.g.*, crystal faces and acidity/basicity) contribute to a great extent through the metal-support interactions.[49,353,418] For accurately controlling such interactions, meticulous selection of synthetic temperature, solvent, precursors and other relevant parameters should be the focus during the whole preparation procedure.

As for typical electrochemical reduction reactions, moderate reaction conditions as well as flexible carbon supports featuring high specific surface area and electricity/heat conductivity endows the synthesis of SACs with more chances for modulating the electronic structure of metal sites. A number of strategies such as defect engineering,[152,215] heteroatom doping,[173] structural modification,[170,171] and functional group attachment[210] have be applied in the synthesis process for the regulation of microenvironments. Such variations of chemical microenvironments not only change the electronic states and hybridized orbitals of active sites, but also impose appreciable effects on the mass transfer of reactants, intermediates and products, leading to the corresponding tuned performances

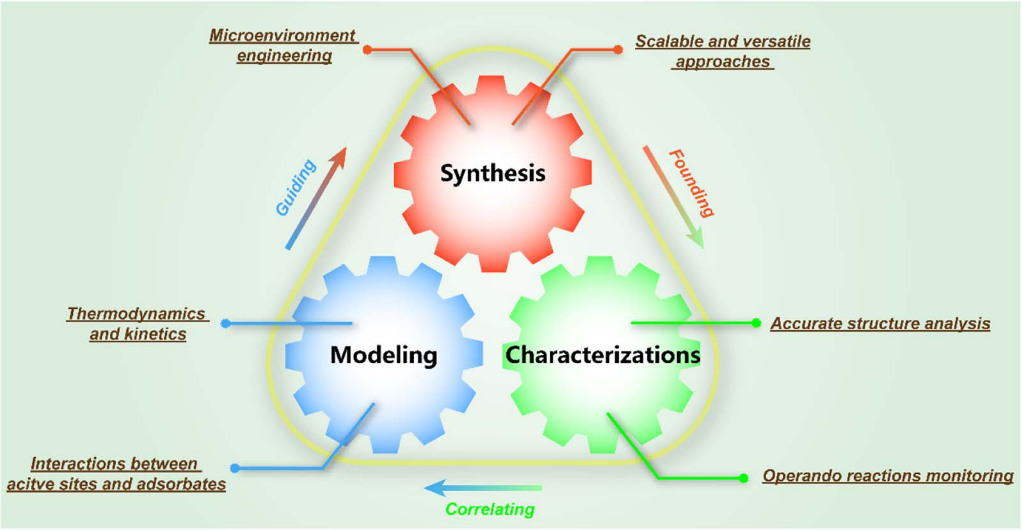

Fig. 52 Crucial issues of SAC research for CO_2 conversion and a positive loop encompassing them.

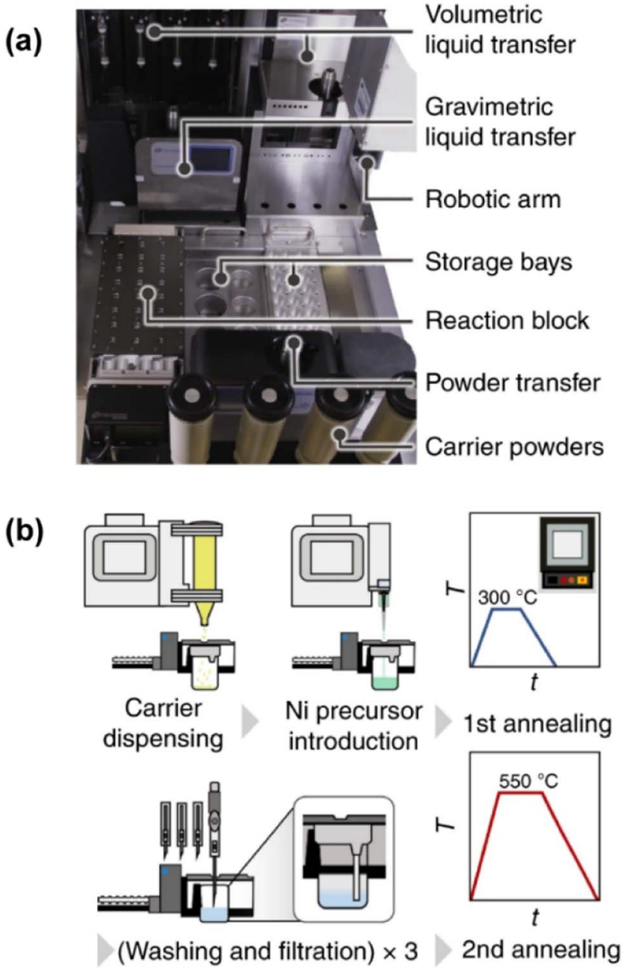

Fig. 53 (a) Photograph of the robotic synthesis platform and assignment of tools to unit operations. (b) Flowsheet of the synthesis protocol.[421] Reproduced from ref. 421 with permission from Springer Nature, copyright 2022.

thermodynamically and kinetically.[132,378,379,385,419] To realize these goals, superior carbon supports such as graphene and CNTs with abundant functional groups have been applied in the bottom-up routes, in which metal SAs could be immobilized *via* either electrostatic interaction with metal ions as precursors, or π–π interaction with certain metal–organic complex precursors. Furthermore, one-step or multi-step pyrolysis processes with MOFs or certain other metal–organic assemblages as precursors offer opportunities for the construction of more types of SACs, such as various M–N–C (M = metal) materials.

Light-driven reduction reactions involve the generation and transfer of photoexcited electrons, in which the introduced SACs can function as not only active sites for the adsorption and activation of CO_2, but also promoters for the modulation of the energy bands of semiconductors. Given that both oxides (*e.g.*, TiO_2) and carbon-based[240,241] (*e.g.*, g-C_3N_4) materials can serve as substrates for embedding metal SAs, plus that the MOFs and COFs can be also used when extra photosensitizers and sacrificed hole scavengers exist,[226] the synthesis of SACs for photochemical reduction is just like the combination of electro- and thermo-catalysis, although the targets are not completely identical. For instance, silver SAs featuring a chain-like arrangement on the surface of manganese oxides, form a unique structure just like a Z-scheme heterojunction with the combination of neighboring oxide species, resulting in an enhanced performance due to the well-matched energy bands for electron transfer.[236]

Indeed, no matter which system the SACs are applied in, there are some common goals for propelling the practical application of SACs in CO_2 conversion towards an industrial scale: to extend the range of loadings and types,[332,420,421] to lower the cost of preparation,[43] and to expand the scale of production.[43,421] It was reported that a versatile strategy combining impregnation and secondary step annealing could be used for synthesizing ultra-high-density SACs with metal contents up to 23 wt% for 15 metals on chemically distinct carriers.[421] This method could be even translated into a standardized, automated protocol executed by a robotic platform, enabling the reproducible preparation (Fig. 53), which further indicated the feasibility and scalability of this strategy. In addition, a straightforward and cost-effective three-dimensional (3D) printing approach has been reported for fabricating a library of SACs in a simple and economic way.[43] It is also expected that this 3D-printing technique to make a difference in large-scale commercial production of SACs, thereby steering the use of these materials to a broader spectrum of industrial applications. Notably, aside from the retrofitted conventional synthetic methods, burgeoning machine learning (ML) and artificial intelligence (AI) techniques have been also providing new paradigms for the highly efficient approaches for massive production of SACs.[422] Once a large and high-quality database is established, the explosion of efficiency would be brought about by high throughput screening and automated optimization based on reliable prediction of the structure–performance relationship.

5.2 Characterization

The rapid development of atom-scale characterization has propelled the identification of SA species and deepened the proposition of the SAC concept, which was simultaneously inspired by a number of experimental observations. Aberration-corrected scanning transmission electron microscopy (STEM)[21] and scanning tunneling microscopy (STM)[423] offer opportunities for directly observing the dispersion and arrangement as well as certain surficial properties regarding electronic behaviors. The XAS technique exhibits advantages in obtaining the information about the refined structure including the spatial distance and coordination state between the central atom and neighboring atoms, the electronic states of specific orbitals, the disorder degree of materials, and the geometric configuration with regard to symmetry, thereby being widely applied in most of the recent studies on SACs and could be well combined with theoretical modeling and calculations. The solid state nuclear magnetic resonance (ssNMR) technique specializes in the investigation of SACs based on isotropic chemical shift, chemical shift anisotropy, dipole–dipole coupling, J-coupling, and quadrupole interaction of certain metals and supports, exhibiting unparalleled advantages for the identification of specific metal SAs and understanding of certain interactions between active centers and intermediate species. The infrared (IR) technique, on the other hand, can be used in the studies on SACs *via* a more indirect approach, *e.g.*, CO-adsorption spectra are commonly acquired to reflect the form of metal species, since metal sites with different geometric and electronic properties possess a characteristic CO-adsorption configuration (on-top, bridged, geminal, *etc.*) thereby displaying varied absorbance band positions.[37] In particular, Mössbauer spectroscopy has been developed to track the dynamic changes in the electronic and coordination structures of iron and tin SACs recently,[157,210,424] which are both commonly used as active components for CO_2 reduction. This could be attributed to its high energy resolution and feasible acquirement of quantitative information and chemical states, spin state, and coordination symmetry of "selected" elements (Fe, Sn, Ni, Au, *etc.*).

Nowadays, the advancement of various characterization studies is no longer limited to discrimination of SA species from their nano-counterparts (NCs or NPs), but steps forward to in-depth explorations in terms of dynamic evolution, electronic state and host–guest interactions, all of which are of great concerns about the practical application of SACs in CO_2 conversion. In order to achieve these goals, higher temporal and spatial resolution under harsh conditions is in great demand, which might be afforded by the incorporation of state-of-the-art devices and upgraded research strategies.[425] On the other hand, the innovative exploitation of computational science and big data has promisingly ignited the revolutionary development of characterization techniques by not only predicting the most probable structure of SACs referring to the existing experimental data[426,427] but also assisting the collection and analysis of data and accordingly increasing the efficiency and accuracy.[428,429] Martini *et al.* provided an example of tracking the evolution of SACs for the CO_2 electrocatalytic reduction using operando XAS and machine learning, while addressing the nature, stability, and evolution of the Ni active sites during the reaction.[430] The combination of unsupervised and supervised machine learning (SML) approaches is shown to be able to decipher the X-ray absorption near edge structure (XANES) of the transition-metal based single-atom sites, decoupling the roles of diversified metal sites coexisting in the working catalyst with quantitative structural information about the local environment of active species and the interplay between metal species and adsorbates, such as CO (Fig. 54). Overall, it is plausible to suppose that the intersection between advanced characterization techniques and modern computational science could shed light on the precise analysis of sophisticated SACs.

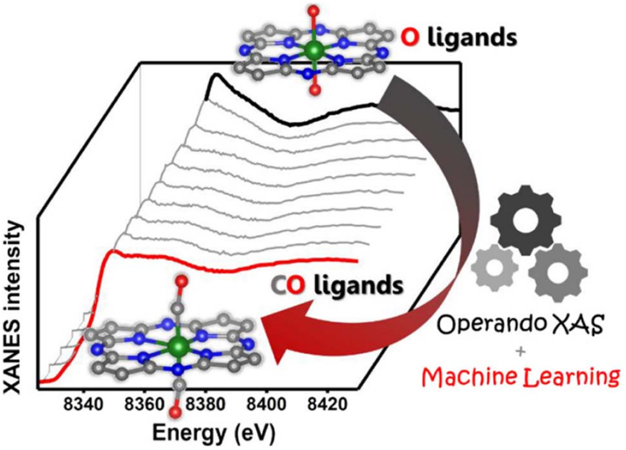

Fig. 54 Schematic of tracking the evolution of SACs for CO_2 electrocatalytic reduction with a combination of operando XAS and machine learning. Reproduced from ref. 430 with permission from American Chemical Society, copyright 2023.

5.3 Computation and modeling

SACs integrating the merits of homogeneous and heterogeneous catalysis endow the catalytic research studies with more chances to dive into inherent and microscopic perspectives. As for CO_2 conversion, just CO_2 activation and protonation have involved a complex reaction network, especially in the cases where the formation of main products encompasses multi-step electron and proton transfer. During the reaction process, the active sites can even evolve with the change in redox atmospheres, leading to perceptible variation of reaction pathways. To this end, a complementary approach aside from the experimental observation has been expected to bring a potential solution, which is theoretical simulation based on computational technology.

In general, most recent studies show that the initial adsorption and activation of CO_2 molecules that break the C═O bonds are the potential limited steps of CO_2 reduction to $2e^-$ products (*e.g.*, CO and HCOOH), no matter what type of energy input it is. The ambiguities are whether the intermediate binds *via* a carbon atom (*e.g.*, *COOH) or oxygen atoms (HCOO*) or both carbon and oxygen atoms in a bridged form, and whether the intermediate is formed through coupled proton-electron transfer or a charged state.[158] Key descriptors such as the band structure (d-band center for transition metals amd s- and p-bands for main group metals), electronic density and state of (s-, p-, d-, f-) orbitals and charge transfer, are commonly used for predicting and explaining the structure–performance relationships due to their decisive role in intramolecular bond breaking and regeneration, and adsorption and desorption at active interfaces.[186,188] The situations are even more complicated for CO_2 reduction towards more than $2e^-$ products, particularly those involving C–C coupling. CO or *CO is always considered as the key intermediate, while either the consecutive protonation step *via* intermediate species such as *CHO and *COH or the dimerization step between CO is probably the limited step.[158] Besides, the CO insertion mechanism is also proposed in the thermo-catalytic C–C coupling process in the presence of multifunctional components,[59,284] as C–C couplings between other types of intermediates (*e.g.*, CHO) have been also reported for some electro- and photo-catalytic processes.[163,295] A common circumstance is that isolate metal sites in SACs cannot be in

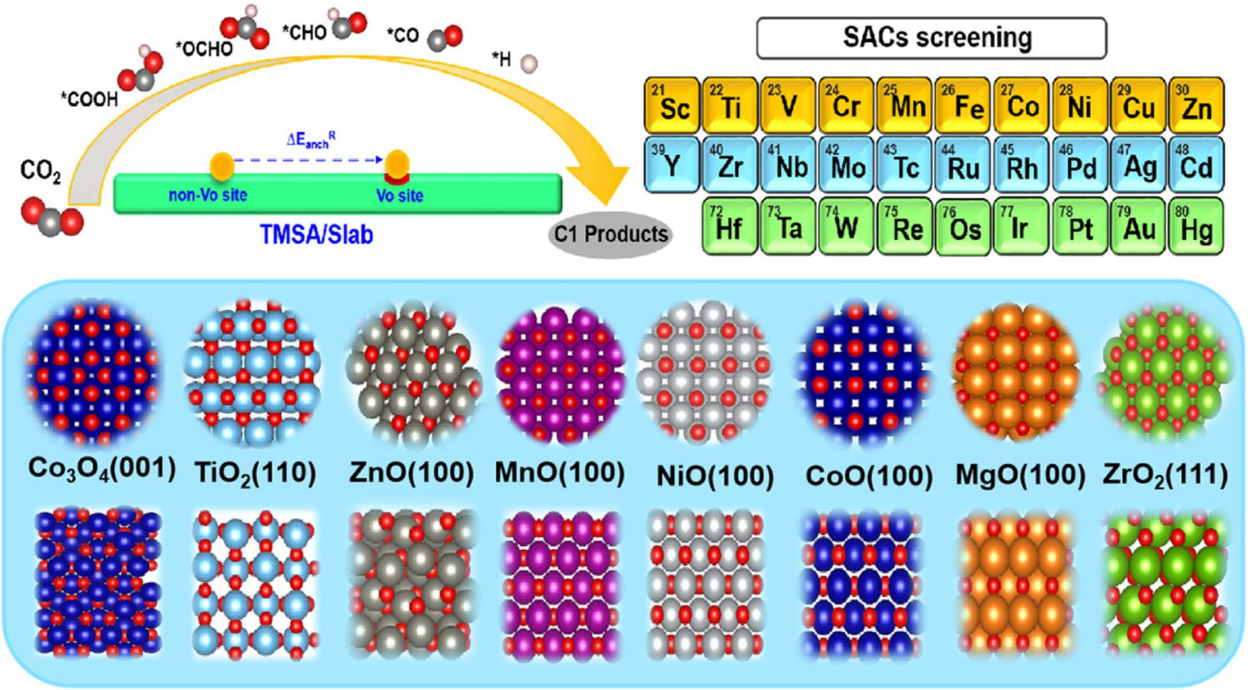

Fig. 55 Schematic diagram of structures for 29 kinds of transition-metal SACs with eight different types of oxide supports. Reproduced from ref. 431 with the permission of Nature Springer, copyright 2022.

charge of all these reactions alone, but have an effect with the incorporation of neighboring active sites (*e.g.*, second type of metal and vacancy).[59,295] Indeed, multi-electron processes are more likely to be influenced by factors other than only kinetics and thermodynamics, such as coverage of the intermediate, mass transfer, and pH,[158] which could be attributed to the inherent complexity. All these mechanism studies have been subjected to a long-term restriction in traditional heterogeneous catalysts because of the difficulty in clarifying the realistic structures and discriminating the role of uneven active centers. Although the computational chemistry has ignited buzz among the scholars hammering at reaction kinetics with the development of computer science, it was not until the concept of SACs that computational chemistry really breaks through the shackles of complex systems and shows great strength in the study of carbon dioxide conversion. On the basis of the principles of quantum chemistry, the Schrodinger equation and various computational methods with specific approximations, researchers might be able to provide valuable information about electron orbitals, density of states, energy profiles of transition states and other intrinsic parameters on a molecular or even atomic scale. Such parameters further push forward the understanding of the interplay between the active centers and guest molecules, contributing to the insight of inherent kinetics, which are always hazed due to the limited experimental approaches. More importantly, in comparison to heterogeneous catalysts with uneven structures, the theoretical studies on SACs could be more easily generalized, providing opportunities for modelling and accordingly developing new catalysts. For instance, Qi *et al.* combined the first-principles calculations and an artificial intelligence approach to high-throughput screen the stability and activity of 3d, 4d, and 5d transition metal SAs on eight defective metal oxide surfaces during the CO_2 reduction reaction (Fig. 55).[431] By evaluating the energies of 232 catalytic systems, only 28 of them remain stable with the adsorption of intermediates (*COOH, *OCHO, *CO, *CHO, and *H), although 100 kinds of SACs could be stably anchored in a vacuum. The stability during adsorption could further be reasonably attributed to the electronegativity and number of outer electrons of the SA, the d-band center of metal oxides, and the relative coordination number of the adsorbed species together. As the free energy diagram could be given for various CO_2 reduction reactions, the catalytic performance should be also predicted in such modelling systems. Similarly, SACs based on different metals embedded on different substrates can also be modelled and mapped based on the theoretical parameters from computation.[432] Such modelling strategies, in turn, have been extensively used for screening efficient SACs, potentially paving the way for wide-spread application of SACs in CO_2 transformation and even other specific reactions.

6. Conclusions and future outlook

Given that we all look forward to an earth suitable for human habitation for a long time, the solution to excessive carbon emission is in an urgent demand for assuaging climate change and environment deterioration. Chemical CO_2 conversion not only offers a potential approach to partially replace the fossil routes by transforming CO_2 into valuable products, but also renders enhanced carbon recycling as combined with efficient carbon capture in the future. Burgeoning SACs featuring extremely high atom utilization efficiency as well as unique electronic and geometric properties integrate the merits of homogeneous and heterogeneous catalysts, providing a powerful tool to tackle the critical problems regarding efficiency and economy of CO_2 conversion. In the above sections, we have reviewed some critical progress and provided a comprehensive summary of SAC application in the widely adopted CO_2 reduction reaction *via* thermochemical, electrochemical, and photochemical routes, as well as some miscellaneous synthetic reactions involving CO_2 conversion. We further offer a multilevel understanding of SACs from a molecular point of view in terms of the central atom, coordination environment, support effect and synergy with other active centers. The ingenious design of materials with regard to the reasonable regulation of the chemical microenvironment and rational explanations toward reaction mechanisms in charge of the specific structure–performance relationships of SACs were highlighted. We also addressed some general issues of research methods for SACs from the perspective of material synthesis, characterization techniques and computation-assisted theoretical modelling in chemical conversion of CO_2 based on the summaries of current research results, expecting to inspire further advances in this field.

To date, the 'young and vigorous' SAC research studies are still in the prime of their lives, and their rapid growth has made great difference in the studies on quite a number of catalysis systems, especially chemical CO_2 conversion. Despite holding significant promise, there is still much work to be accomplished before the SACs stepping into a more in-depth stage for both scientific explorations and industrial targets. Herein, we will briefly present our outlook on several important orientations for future research studies of SACs in CO_2 conversion.

6.1 From an empirical paradigm to rational design

Over a long time, studies on catalysis have been more likely to follow an empirical paradigm, given that achieving thorough understanding of energy and mass transfer processes is limited due to the complicated nature of chemical reactions and the scarcity of advanced technical approaches. A lot of depletion of temporal and financial resources therefore emerged inevitably. Thanks to the development of characterization studies, the assistance of computational science, and the relatively well-defined active sites of SACs, more general theories are expected to be proposed to guide the rational design of new catalytic materials and reaction processes. Such a 'rationale' indicates accurate control and constructing SACs on the basis of abstract descriptors derived from the inherence of reactions rather than only concrete performances. In order to achieve this, we not only urge the further advancement of *in situ* and *operando* techniques combined with theoretical calculations but also of a large open-access database including structural information, and kinetic and thermodynamic factors of CO_2 conversion according to existing research studies. A milestone is supposed to be providing multiscale modeling of SACs with certain uniformity and quantifiable parameters. Once the model was established, the design of SACs would become simple screening *via* machine learning or other reasonable analysis methods based on big data. The underlying challenges are data mining in the catalytic science of SACs and a way to guarantee the consistency of predictions and actuality.

6.2 From scattered studies to integrated systems

Currently, most studies on SACs for CO_2 conversion are still restrained in several specific fields, *i.e.*, thermo-, photo-, and electro-catalysis, and the corresponding up- and down-stream processes (*e.g.*, up: capture and down: separation) are separated and conducted alone. That favors the research studies to some extent due to their specialty concentrating on one target, whereas quite a few potentials of integrated systems are neglected despite also making sense in the meantime. Fortunately, there have been plenty of studies dedicated to combine catalytic systems *via* various routes featuring different forms of energy inputs,[50,433,434] although most of them are still in the preliminary or developmental stages. Furthermore, miscellaneous disciplines such as engineering issues, materials science, and automation technologies could be also involved in highly efficient integrated systems, *e.g.*, electrolytes might play a vital role in an electro-catalytic process; enhanced mass transfer could be realized either by engineering or with the innovation of the material; the extensive exploitation of embodied artificial intelligence like robots and disembodied artificial intelligence like ChatGPT might greatly liberate the manpower from the burdensome and endangered tasks in labs and render a balance between efficiency and safety. In general, harmony is the core of such an integrated system, which can be depicted with a 'barrel effect', *i.e.*, highly effective SACs might function as a longer slab, but the volume of a 'barrel' is more likely to be determined by the possibly inconspicuous short slabs. Thus, it would be an explicit goal to construct 'a barrel with slabs of nearly equal length' from a global perspective. In this regard, the necessary interdisciplinarity should make a great difference.

6.3 From laboratory research to commercial application

An ultimate goal of the studies on SACs for CO_2 conversion is stepping out of labs one day, toward massive production and sustainable processes by making profits. However, as more is different,[435] there is still a long way to go for the practical use of SACs for CO_2 conversion. Economic analysis should be the first step. We must know what the market really needs, how much the cost is, and the potential income over a period. Then, we should consider how to cutdown the cost and increase the production by both scientific and engineering methods, *e.g.*, *via* upgrading the device, improving energy efficiency, and optimizing operation conditions. Another common concern is how to realize the scalability of production, which not only needs massive preparation of SACs but is also associated with a complex scaling effect. Such a scalable process might create new demands for the SAC design and application in turn. Moreover, it could be with more essential factors that the durability and reliability of SACs become successful in some practical cases, especially when operated under harsh conditions. We should pay more attention to the long-term running status of SACs, particularly the dynamic evolution of both electronic and geometric structures, so that we could ensure the stability of SACs and pave a promising way to their feasible commercial application.

Author contributions

X. Shang performed the literature search, analyzed the published results, and wrote the manuscript. X. Yang, G. Liu, T. Zhang and X. Su provided key advice and supervised the preparation of the text.

Conflicts of interest

The authors declare no competing financial interests.

Acknowledgements

We gratefully acknowledge the financial support from the National Key R&D Program of China (2022YFA1506200), the Strategic Priority Research Program of the Chinese Academy of Sciences (No. XDB36030200 and No. XDA29040600), the CAS Project for Young Scientists in Basic Research (YSBR-022), the National Natural Science Foundation of China (21978286, 22208021, and U19A2015), the Youth Innovation Promotion Association CAS, and the Young Top-notch Talents of Liaoning Province (XLYC2007082).

References

1 M. R. Allen, D. J. Frame, C. Huntingford, C. D. Jones, J. A. Lowe, M. Meinshausen and N. Meinshausen, *Nature*, 2009, **458**, 1163–1166.
2 S. I. Seneviratne, M. G. Donat, A. J. Pitman, R. Knutti and R. L. Wilby, *Nature*, 2016, **529**, 477–483.
3 S. Fuss, J. G. Canadell, G. P. Peters, M. Tavoni, R. M. Andrew, P. Ciais, R. B. Jackson, C. D. Jones, F. Kraxner, N. Nakicenovic, C. Le Quéré, M. R. Raupach, A. Sharifi, P. Smith and Y. Yamagata, *Nat. Clim. Change*, 2014, **4**, 850–853.
4 S. Ding, M. J. Hülsey, J. Pérez-Ramírez and N. Yan, *Joule*, 2019, **3**, 2897–2929.
5 P. Markewitz, W. Kuckshinrichs, W. Leitner, J. Linssen, P. Zapp, R. Bongartz, A. Schreiber and T. E. Müller, *Energy Environ. Sci.*, 2012, **5**, 7281–7305.
6 Y. Li, J. Wang, S. Fan, F. Wang, Z. Shen, H. Duan, J. Xu and Y. Huang, *J. Energy Chem.*, 2021, **53**, 168–174.
7 O. S. Bushuyev, P. De Luna, C. T. Dinh, L. Tao, G. Saur, J. van de Lagemaat, S. O. Kelley and E. H. Sargent, *Joule*, 2018, **2**, 825–832.
8 C. Ampelli, S. Perathoner and G. Centi, *Philos. Trans. R. Soc., A*, 2015, **373**, 20140177.
9 M. Aresta, A. Dibenedetto and A. Angelini, *Chem. Rev.*, 2014, **114**, 1709–1742.
10 Y. Li, X. Cui, K. Dong, K. Junge and M. Beller, *ACS Catal.*, 2017, **7**, 1077–1086.
11 N. Mac Dowell, P. S. Fennell, N. Shah and G. C. Maitland, *Nat. Clim. Change*, 2017, **7**, 243–249.
12 C. Hepburn, E. Adlen, J. Beddington, E. A. Carter, S. Fuss, N. Mac Dowell, J. C. Minx, P. Smith and C. K. Williams, *Nature*, 2019, **575**, 87–97.
13 C. Martín, G. Fiorani and A. W. Kleij, *ACS Catal.*, 2015, **5**, 1353–1370.
14 J. Klankermayer, S. Wesselbaum, K. Beydoun and W. Leitner, *Angew. Chem., Int. Ed.*, 2016, **55**, 7296–7343.
15 A. S. Lindsey and H. Jeskey, *Chem. Rev.*, 1957, **57**, 583–620.
16 A. Otto, T. Grube, S. Schiebahn and D. Stolten, *Energy Environ. Sci.*, 2015, **8**, 3283–3297.
17 T. W. van Deelen, C. Hernández Mejía and K. P. de Jong, *Nat. Catal.*, 2019, **2**, 955–970.
18 A. Wang, J. Li and T. Zhang, *Nat. Rev. Chem*, 2018, **2**, 65–81.
19 X. Li, X. Yang, Y. Huang, T. Zhang and B. Liu, *Adv. Mater.*, 2019, **31**, 1902031.
20 X. Li, Y. Huang and B. Liu, *Chem*, 2019, **5**, 2733–2735.
21 B. Qiao, A. Wang, X. Yang, L. F. Allard, Z. Jiang, Y. Cui, J. Liu, J. Li and T. Zhang, *Nat. Chem.*, 2011, **3**, 634–641.
22 J. J. Rooney and G. Webb, *J. Catal.*, 1964, **3**, 488–501.
23 H. S. Taylor and E. F. Armstrong, *Proc. R. Soc. London, Ser. A*, 1925, **108**, 105–111.
24 W. R. Patterson and J. J. Rooney, *Catal. Today*, 1992, **12**, 113–129.
25 K. Asakura, H. Nagahiro, N. Ichikuni and Y. Iwasawa, *Appl. Catal., A*, 1999, **188**, 313–324.
26 Q. Fu, H. Saltsburg and M. Flytzani-Stephanopoulos, *Science*, 2003, **301**, 935–938.
27 S. F. J. Hackett, R. M. Brydson, M. H. Gass, I. Harvey, A. D. Newman, K. Wilson and A. F. Lee, *Angew. Chem., Int. Ed.*, 2007, **46**, 8593–8596.
28 T. Maschmeyer, F. Rey, G. Sankar and J. M. Thomas, *Nature*, 1995, **378**, 159–162.
29 J. T. Yates, S. D. Worley, T. M. Duncan and R. W. Vaughan, *J. Chem. Phys.*, 1979, **70**, 1225–1230.
30 W. Jing, H. Shen, R. Qin, Q. Wu, K. Liu and N. Zheng, *Chem. Rev.*, 2022, **123**, 5948–6002.
31 J. Yang, W. Li, D. Wang and Y. Li, *Adv. Mater.*, 2020, **32**, 2003300.
32 J. Kim, H.-E. Kim and H. Lee, *ChemSusChem*, 2018, **11**, 104–113.
33 C. Zhu, S. Fu, Q. Shi, D. Du and Y. Lin, *Angew. Chem., Int. Ed.*, 2017, **56**, 13944–13960.
34 X. He, Q. He, Y. Deng, M. Peng, H. Chen, Y. Zhang, S. Yao, M. Zhang, D. Xiao, D. Ma, B. Ge and H. Ji, *Nat. Commun.*, 2019, **10**, 3663.
35 Y. Chen, J. Lin, B. Jia, X. Wang, S. Jiang and T. Ma, *Adv. Mater.*, 2022, **34**, 2201796.
36 T. Zhang, *Nano Lett.*, 2021, **21**, 9835–9837.
37 R. Lang, X. Du, Y. Huang, X. Jiang, Q. Zhang, Y. Guo, K. Liu, B. Qiao, A. Wang and T. Zhang, *Chem. Rev.*, 2020, **120**, 11986–12043.
38 X.-F. Yang, A. Wang, B. Qiao, J. Li, J. Liu and T. Zhang, *Acc. Chem. Res.*, 2013, **46**, 1740–1748.

39 L. Wang, D. Wang and Y. Li, *Carbon Energy*, 2022, **4**, 1021–1079.

40 H. B. Zhang, G. G. Liu, L. Shi and J. H. Ye, *Adv. Energy Mater.*, 2018, **8**, 1701343.

41 J. Zhang, C. Liu and B. Zhang, *Small Methods*, 2019, **3**, 1800481.

42 L. Zhang, Y. Wang, Z. Niu and J. Chen, *Small Methods*, 2019, **3**, 1800443.

43 F. Xie, X. Cui, X. Zhi, D. Yao, B. Johannessen, T. Lin, J. Tang, T. B. F. Woodfield, L. Gu and S.-Z. Qiao, *Nat. Synth.*, 2023, **2**, 129–139.

44 Z. Li, B. Li and C. Yu, *Adv. Mater.*, 2023, 2211221.

45 C. B. Hiragond, N. S. Powar, J. Lee and S.-I. In, *Small*, 2022, **18**, 2201428.

46 Y. Wang, L. R. Winter, J. G. Chen and B. Yan, *Green Chem.*, 2021, **23**, 249–267.

47 C. Xu, A. Vasileff, Y. Zheng and S.-Z. Qiao, *Adv. Mater. Interfaces*, 2021, **8**, 2001904.

48 X. Su, X.-F. Yang, Y. Huang, B. Liu and T. Zhang, *Acc. Chem. Res.*, 2019, **52**, 656–664.

49 L. Liu and A. Corma, *Chem. Rev.*, 2018, **118**, 4981–5079.

50 Y. Song, X. Zhang, K. Xie, G. Wang and X. Bao, *Adv. Mater.*, 2019, **31**, 1902033.

51 J. Ran, M. Jaroniec and S.-Z. Qiao, *Adv. Mater.*, 2018, **30**, 1704649.

52 E. Gong, S. Ali, C. B. Hiragond, H. S. Kim, N. S. Powar, D. Kim, H. Kim and S.-I. In, *Energy Environ. Sci.*, 2022, **15**, 880–937.

53 Ž. Kovačič, B. Likozar and M. Huš, *ACS Catal.*, 2020, **10**, 14984–15007.

54 X. Li, J. Yu, M. Jaroniec and X. Chen, *Chem. Rev.*, 2019, **119**, 3962–4179.

55 C. Wang, E. Guan, L. Wang, X. Chu, Z. Wu, J. Zhang, Z. Yang, Y. Jiang, L. Zhang, X. Meng, B. C. Gates and F.-S. Xiao, *J. Am. Chem. Soc.*, 2019, **141**, 8482–8488.

56 X. Yang, X. Su, X. Chen, H. Duan, B. Liang, Q. Liu, X. Liu, Y. Ren, Y. Huang and T. Zhang, *Appl. Catal., B*, 2017, **216**, 95–105.

57 J. Zhong, X. Yang, Z. Wu, B. Liang, Y. Huang and T. Zhang, *Chem. Soc. Rev.*, 2020, **49**, 1385–1413.

58 L. P. Ding, T. T. Shi, J. Gu, Y. Cui, Z. Y. Zhang, C. J. Yang, T. Chen, M. Lin, P. Wang, N. H. Xue, L. M. Peng, X. F. Guo, Y. Zhu, Z. X. Chen and W. P. Ding, *Chem*, 2020, **6**, 2673–2689.

59 X. Ye, C. Yang, X. Pan, J. Ma, Y. Zhang, Y. Ren, X. Liu, L. Li and Y. Huang, *J. Am. Chem. Soc.*, 2020, **142**, 19001–19005.

60 M. Yang, J. Yu, A. Zimina, B. B. Sarma, L. Pandit, J. D. Grunwaldt, L. Zhang, H. Xu and J. Sun, *Angew. Chem., Int. Ed.*, 2023, **62**, e202216803.

61 X. Zhang, G. Zhang, W. Liu, F. Yuan, J. Wang, J. Zhu, X. Jiang, A. Zhang, F. Ding, C. Song and X. Guo, *Appl. Catal., B*, 2021, **284**, 119700.

62 S. Kattel, B. Yan, Y. Yang, J. G. Chen and P. Liu, *J. Am. Chem. Soc.*, 2016, **138**, 12440–12450.

63 J. Wang, G. Li, Z. Li, C. Tang, Z. Feng, H. An, H. Liu, T. Liu and C. Li, *Sci. Adv.*, 2017, **3**, e1701290.

64 B. Liang, J. Ma, X. Su, C. Yang, H. Duan, H. Zhou, S. Deng, L. Li and Y. Huang, *Ind. Eng. Chem. Res.*, 2019, **58**, 9030–9037.

65 X. L. Liu, M. H. Wang, H. R. Yin, J. T. Hu, K. Cheng, J. C. Kang, Q. H. Zhang and Y. Wang, *ACS Catal.*, 2020, **10**, 8303–8314.

66 C. Zhou, J. Shi, W. Zhou, K. Cheng, Q. Zhang, J. Kang and Y. Wang, *ACS Catal.*, 2019, **10**, 302–310.

67 Z. Li, Y. Qu, J. Wang, H. Liu, M. Li, S. Miao and C. Li, *Joule*, 2019, **3**, 570–583.

68 Y. Ni, Z. Chen, Y. Fu, Y. Liu, W. Zhu and Z. Liu, *Nat. Commun.*, 2018, **9**, 3457.

69 Y. Zhang, Z. Zhang, X. Yang, R. Wang, H. Duan, Z. Shen, L. Li, Y. Su, R. Yang, Y. Zhang, X. Su, Y. Huang and T. Zhang, *Green Chem.*, 2020, **22**, 6855–6861.

70 M. T. Arslan, G. Tian, B. Ali, C. Zhang, H. Xiong, Z. Li, L. Luo, X. Chen and F. Wei, *ACS Catal.*, 2022, **12**, 2023–2033.

71 P. Gao, S. Li, X. Bu, S. Dang, Z. Liu, H. Wang, L. Zhong, M. Qiu, C. Yang, J. Cai, W. Wei and Y. Sun, *Nat. Chem.*, 2017, **9**, 1019.

72 J. Wei, Q. Ge, R. Yao, Z. Wen, C. Fang, L. Guo, H. Xu and J. Sun, *Nat. Commun.*, 2017, **8**, 15174.

73 S. Kattel, P. Liu and J. G. Chen, *J. Am. Chem. Soc.*, 2017, **139**, 9739–9754.

74 M. Mikkelsen, M. Jørgensen and F. C. Krebs, *Energy Environ. Sci.*, 2010, **3**, 43–81.

75 V. Dieterich, A. Buttler, A. Hanel, H. Spliethoff and S. Fendt, *Energy Environ. Sci.*, 2020, **13**, 3207–3252.

76 S. Overa, T. G. Feric, A.-H. A. Park and F. Jiao, *Joule*, 2021, **5**, 8–13.

77 J. H. Kwak, L. Kovarik and J. Szanyi, *ACS Catal.*, 2013, **3**, 2094–2100.

78 J. H. Kwak, L. Kovarik and J. Szanyi, *ACS Catal.*, 2013, **3**, 2449–2455.

79 J. C. Matsubu, V. N. Yang and P. Christopher, *J. Am. Chem. Soc.*, 2015, **137**, 3076–3084.

80 Y. Tang, C. Asokan, M. Xu, G. W. Graham, X. Pan, P. Christopher, J. Li and P. Sautet, *Nat. Commun.*, 2019, **10**, 4488.

81 L. DeRita, J. Resasco, S. Dai, A. Boubnov, H. V. Thang, A. S. Hoffman, I. Ro, G. W. Graham, S. R. Bare, G. Pacchioni, X. Pan and P. Christopher, *Nat. Mater.*, 2019, **18**, 746–751.

82 M. Moliner, J. E. Gabay, C. E. Kliewer, R. T. Carr, J. Guzman, G. L. Casty, P. Serna and A. Corma, *J. Am. Chem. Soc.*, 2016, **138**, 15743–15750.

83 G. S. Parkinson, Z. Novotny, G. Argentero, M. Schmid, J. Pavelec, R. Kosak, P. Blaha and U. Diebold, *Nat. Mater.*, 2013, **12**, 724–728.

84 S. Wei, A. Li, J.-C. Liu, Z. Li, W. Chen, Y. Gong, Q. Zhang, W.-C. Cheong, Y. Wang, L. Zheng, H. Xiao, C. Chen, D. Wang, Q. Peng, L. Gu, X. Han, J. Li and Y. Li, *Nat. Nanotechnol.*, 2018, **13**, 856–861.

85 S. Li, Y. Xu, H. Wang, B. Teng, Q. Liu, Q. Li, L. Xu, X. Liu and J. Lu, *Angew. Chem., Int. Ed.*, 2023, **62**, e202218167.

86 P. Du, R. Qi, Y. Zhang, Q. Gu, X. Xu, Y. Tan, X. Liu, A. Wang, B. Zhu, B. Yang and T. Zhang, *Chem*, 2022, **8**, 3252–3262.

87 M.-M. Millet, G. Algara-Siller, S. Wrabetz, A. Mazheika, F. Girgsdies, D. Teschner, F. Seitz, A. Tarasov, S. V. Levchenko, R. Schlögl and E. Frei, *J. Am. Chem. Soc.*, 2019, **141**, 2451–2461.

88 H. Liang, B. Zhang, P. Gao, X. Yu, X. Liu, X. Yang, H. Wu, L. Zhai, S. Zhao, G. Wang, A. P. van Bavel and Y. Qin, *Chem Catal.*, 2022, **2**, 610–621.

89 Y. Li, Z. Zhao, W. Lu, H. Zhu, F. Sun, B. Mei, Z. Jiang, Y. Lyu, X. Chen, L. Guo, T. Wu, X. Ma, Y. Meng and Y. Ding, *Appl. Catal., B*, 2023, **324**, 122298.

90 N. H. M. D. Dostagir, R. Rattanawan, M. Gao, J. Ota, J.-y. Hasegawa, K. Asakura, A. Fukouka and A. Shrotri, *ACS Catal.*, 2021, **11**, 9450–9461.

91 Y. Jiang, Y. Sung, C. Choi, G. Joo Bang, S. Hong, X. Tan, T.-S. Wu, Y.-L. Soo, P. Xiong, M. Meng-Jung Li, L. Hao, Y. Jung and Z. Sun, *Angew. Chem., Int. Ed.*, 2022, **61**, e202203836.

92 H. Xin, L. Lin, R. Li, D. Li, T. Song, R. Mu, Q. Fu and X. Bao, *J. Am. Chem. Soc.*, 2022, **144**, 4874–4882.

93 X. Chen, X. Su, H.-Y. Su, X. Liu, S. Miao, Y. Zhao, K. Sun, Y. Huang and T. Zhang, *ACS Catal.*, 2017, **7**, 4613–4620.

94 M. Fan, J. D. Jimenez, S. N. Shirodkar, J. Wu, S. Chen, L. Song, M. M. Royko, J. Zhang, H. Guo, J. Cui, K. Zuo, W. Wang, C. Zhang, F. Yuan, R. Vajtai, J. Qian, J. Yang, B. I. Yakobson, J. M. Tour, J. Lauterbach, D. Sun and P. M. Ajayan, *ACS Catal.*, 2019, **9**, 10077–10086.

95 D. Kim and J. Han, *Appl. Energy*, 2020, **264**, 114711.

96 M. Liu, Y. Xu, Y. Meng, L. Wang, H. Wang, Y. Huang, N. Onishi, L. Wang, Z. Fan and Y. Himeda, *Adv. Energy Mater.*, 2022, **12**, 2200817.

97 D. Mellmann, P. Sponholz, H. Junge and M. Beller, *Chem. Soc. Rev.*, 2016, **45**, 3954–3988.

98 S. Enthaler, J. von Langermann and T. Schmidt, *Energy Environ. Sci.*, 2010, **3**, 1207–1217.

99 W.-H. Wang, Y. Himeda, J. T. Muckerman, G. F. Manbeck and E. Fujita, *Chem. Rev.*, 2015, **115**, 12936–12973.

100 R. Sun, Y. Liao, S.-T. Bai, M. Zheng, C. Zhou, T. Zhang and B. F. Sels, *Energy Environ. Sci.*, 2021, **14**, 1247–1285.

101 X. Shao, X. Yang, J. Xu, S. Liu, S. Miao, X. Liu, X. Su, H. Duan, Y. Huang and T. Zhang, *Chem*, 2019, **5**, 693–705.

102 G. H. Gunasekar, J. Shin, K.-D. Jung, K. Park and S. Yoon, *ACS Catal.*, 2018, **8**, 4346–4353.

103 Z. Li, T. M. Rayder, L. Luo, J. A. Byers and C.-K. Tsung, *J. Am. Chem. Soc.*, 2018, **140**, 8082–8085.

104 K. Park, G. H. Gunasekar, S.-H. Kim, H. Park, S. Kim, K. Park, K.-D. Jung and S. Yoon, *Green Chem.*, 2020, **22**, 1639–1649.

105 G. M. Eder, D. A. Pyles, E. R. Wolfson and P. L. McGrier, *Chem. Commun.*, 2019, **55**, 7195–7198.

106 Z.-Z. Yang, H. Zhang, B. Yu, Y. Zhao, G. Ji and Z. Liu, *Chem. Commun.*, 2015, **51**, 1271–1274.

107 B. An, L. Zeng, M. Jia, Z. Li, Z. Lin, Y. Song, Y. Zhou, J. Cheng, C. Wang and W. Lin, *J. Am. Chem. Soc.*, 2017, **139**, 17747–17750.

108 K. Mori, T. Taga and H. Yamashita, *ACS Catal.*, 2017, **7**, 3147–3151.

109 Q. Wang, S. Santos, C. A. Urbina-Blanco, W. Y. Hernández, M. Impéror-Clerc, E. I. Vovk, M. Marinova, O. Ersen, W. Baaziz, O. V. Safonova, A. Y. Khodakov, M. Saeys and V. V. Ordomsky, *Appl. Catal., B*, 2021, **290**, 120036.

110 G. Ren, J. Sun, S. Zhai, L. Yang, T. Yu, L. Sun and W. Deng, *Cell Rep. Phys. Sci.*, 2022, **3**, 100705.

111 S. Zhai, L. Zhang, J. Sun, L. Sun, S. Jiang, T. Yu, D. Zhai, C. Liu, Z. Li and G. Ren, *Front. Chem.*, 2022, **10**, 957412.

112 H. Li, L. Wang, Y. Dai, Z. Pu, Z. Lao, Y. Chen, M. Wang, X. Zheng, J. Zhu, W. Zhang, R. Si, C. Ma and J. Zeng, *Nat. Nanotechnol.*, 2018, **13**, 411–417.

113 T. J. Deka, A. I. Osman, D. C. Baruah and D. W. Rooney, *Environ. Chem. Lett.*, 2022, **20**, 3525–3554.

114 J. Nyári, M. Magdeldin, M. Larmi, M. Järvinen and A. Santasalo-Aarnio, *J. CO2 Util.*, 2020, **39**, 101166.

115 S. Sollai, A. Porcu, V. Tola, F. Ferrara and A. Pettinau, *J. CO2 Util.*, 2023, **68**, 102345.

116 G. A. Olah, *Angew. Chem., Int. Ed.*, 2005, **44**, 2636–2639.

117 S. T. Bai, G. De Smet, Y. Liao, R. Sun, C. Zhou, M. Beller, B. U. W. Maes and B. F. Sels, *Chem. Soc. Rev.*, 2021, **50**, 4259–4298.

118 A. Goeppert, M. Czaun, J.-P. Jones, G. K. Surya Prakash and G. A. Olah, *Chem. Soc. Rev.*, 2014, **43**, 7995–8048.

119 O. Martin, A. J. Martín, C. Mondelli, S. Mitchell, T. F. Segawa, R. Hauert, C. Drouilly, D. Curulla-Ferré and J. Pérez-Ramírez, *Angew. Chem., Int. Ed.*, 2016, **55**, 6261–6265.

120 N. H. M. D. Dostagir, C. Thompson, H. Kobayashi, A. M. Karim, A. Fukuoka and A. Shrotri, *Catal. Sci. Technol.*, 2020, **10**, 8196–8202.

121 F. Jiang, S. Wang, B. Liu, J. Liu, L. Wang, Y. Xiao, Y. Xu and X. Liu, *ACS Catal.*, 2020, **10**, 11493–11509.

122 R. Sen, A. Goeppert and G. K. Surya Prakash, *Angew. Chem., Int. Ed.*, 2022, **61**, e202207278.

123 H. Zhao, R. Yu, S. Ma, K. Xu, Y. Chen, K. Jiang, Y. Fang, C. Zhu, X. Liu, Y. Tang, L. Wu, Y. Wu, Q. Jiang, P. He, Z. Liu and L. Tan, *Nat. Catal.*, 2022, **5**, 818–831.

124 W. Wu, Y. Wang, L. Luo, M. Wang, Z. Li, Y. Chen, Z. Wang, J. Chai, Z. Cen, Y. Shi, J. Zhao, J. Zeng and H. Li, *Angew. Chem., Int. Ed.*, 2022, **61**, e202213024.

125 X.-K. Wu, H.-M. Yan, W. Zhang, J. Zhang, G.-J. Xia and Y.-G. Wang, *J. Energy Chem.*, 2021, **61**, 582–593.

126 Y. Chen, H. Li, W. Zhao, W. Zhang, J. Li, W. Li, X. Zheng, W. Yan, W. Zhang, J. Zhu, R. Si and J. Zeng, *Nat. Commun.*, 2019, **10**, 1885.

127 S. J. Davis, N. S. Lewis, M. Shaner, S. Aggarwal, D. Arent, I. L. Azevedo, S. M. Benson, T. Bradley, J. Brouwer, Y.-M. Chiang, C. T. M. Clack, A. Cohen, S. Doig, J. Edmonds, P. Fennell, C. B. Field, B. Hannegan, B.-M. Hodge, M. I. Hoffert, E. Ingersoll, P. Jaramillo, K. S. Lackner, K. J. Mach, M. Mastrandrea, J. Ogden, P. F. Peterson, D. L. Sanchez, D. Sperling, J. Stagner, J. E. Trancik, C.-J. Yang and K. Caldeira, *Science*, 2018, **360**, eaas9793.

128 X. Tan, X. Sun and B. Han, *Natl. Sci. Rev.*, 2022, **9**, nwab022.

129 S. Jin, Z. Hao, K. Zhang, Z. Yan and J. Chen, *Angew. Chem., Int. Ed.*, 2021, **60**, 20627–20648.

130 S. Liang, L. Huang, Y. Gao, Q. Wang and B. Liu, *Adv. Sci.*, 2021, **8**, 2102886.
131 Y. Cheng, S. Yang, S. P. Jiang and S. Wang, *Small Methods*, 2019, **3**, 1800440.
132 C. Jia, Z. Shi and C. Zhao, *Curr. Opin. Green Sustainable Chem.*, 2022, **37**, 100651.
133 T. Tang, Z. Wang and J. Guan, *Adv. Funct. Mater.*, 2022, **32**, 2111504.
134 L. Wang, L. Wang, L. Zhang, H. Liu and J. Yang, *Trends Chem.*, 2022, **4**, 1135–1148.
135 J. Zhang, W. Cai, F. X. Hu, H. Yang and B. Liu, *Chem. Sci.*, 2021, **12**, 6800–6819.
136 L. Wang, W. Chen, D. Zhang, Y. Du, R. Amal, S. Qiao, J. Wu and Z. Yin, *Chem. Soc. Rev.*, 2019, **48**, 5310–5349.
137 T. Zheng, K. Jiang and H. Wang, *Adv. Mater.*, 2018, **30**, 1802066.
138 K. P. Kuhl, T. Hatsukade, E. R. Cave, D. N. Abram, J. Kibsgaard and T. F. Jaramillo, *J. Am. Chem. Soc.*, 2014, **136**, 14107–14113.
139 J. Gu, C.-S. Hsu, L. Bai, H. M. Chen and X. Hu, *Science*, 2019, **364**, 1091–1094.
140 H. B. Yang, S.-F. Hung, S. Liu, K. Yuan, S. Miao, L. Zhang, X. Huang, H.-Y. Wang, W. Cai, R. Chen, J. Gao, X. Yang, W. Chen, Y. Huang, H. M. Chen, C. M. Li, T. Zhang and B. Liu, *Nat. Energy*, 2018, **3**, 140–147.
141 Z. Zhao, Z. Chen and G. Lu, *J. Phys. Chem. C*, 2017, **121**, 20865–20870.
142 M. Beley, J.-P. Collin, R. Ruppert and J.-P. Sauvage, *J. Chem. Soc., Chem. Commun.*, 1984, 1315–1316, DOI: 10.1039/C39840001315.
143 M. Beley, J. P. Collin, R. Ruppert and J. P. Sauvage, *J. Am. Chem. Soc.*, 1986, **108**, 7461–7467.
144 J. Schneider, H. Jia, K. Kobiro, D. E. Cabelli, J. T. Muckerman and E. Fujita, *Energy Environ. Sci.*, 2012, **5**, 9502–9510.
145 C. Zhao, X. Dai, T. Yao, W. Chen, X. Wang, J. Wang, J. Yang, S. Wei, Y. Wu and Y. Li, *J. Am. Chem. Soc.*, 2017, **139**, 8078–8081.
146 C. Yan, H. Li, Y. Ye, H. Wu, F. Cai, R. Si, J. Xiao, S. Miao, S. Xie, F. Yang, Y. Li, G. Wang and X. Bao, *Energy Environ. Sci.*, 2018, **11**, 1204–1210.
147 K. Jiang, S. Siahrostami, T. Zheng, Y. Hu, S. Hwang, E. Stavitski, Y. Peng, J. Dynes, M. Gangisetty, D. Su, K. Attenkofer and H. Wang, *Energy Environ. Sci.*, 2018, **11**, 893–903.
148 P. Su, K. Iwase, S. Nakanishi, K. Hashimoto and K. Kamiya, *Small*, 2016, **12**, 6083–6089.
149 S. Liu, H. B. Yang, S.-F. Hung, J. Ding, W. Cai, L. Liu, J. Gao, X. Li, X. Ren, Z. Kuang, Y. Huang, T. Zhang and B. Liu, *Angew. Chem., Int. Ed.*, 2020, **59**, 798–803.
150 D. Xi, J. Li, J. Low, K. Mao, R. Long, J. Li, Z. Dai, T. Shao, Y. Zhong, Y. Li, Z. Li, X. J. Loh, L. Song, E. Ye and Y. Xiong, *Adv. Mater.*, 2022, **34**, 2104090.
151 H. Yang, Q. Lin, C. Zhang, X. Yu, Z. Cheng, G. Li, Q. Hu, X. Ren, Q. Zhang, J. Liu and C. He, *Nat. Commun.*, 2020, **11**, 593.
152 R. Boppella, M. Austeria P, Y. Kim, E. Kim, I. Song, Y. Eom, D. P. Kumar, M. Balamurugan, E. Sim, D. H. Kim and T. K. Kim, *Adv. Funct. Mater.*, 2022, **32**, 2202351.
153 M. D. Hossain, Y. Huang, T. H. Yu, W. A. Goddard Iii and Z. Luo, *Nat. Commun.*, 2020, **11**, 2256.
154 H. Li, H. Li, P. Wei, Y. Wang, Y. Zang, D. Gao, G. Wang and X. Bao, *Energy Environ. Sci.*, 2023, **16**, 1502–1510.
155 X. Sun, Y. Tuo, C. Ye, C. Chen, Q. Lu, G. Li, P. Jiang, S. Chen, P. Zhu, M. Ma, J. Zhang, J. H. Bitter, D. Wang and Y. Li, *Angew. Chem., Int. Ed.*, 2021, **60**, 23614–23618.
156 Z. Zhang, C. Ma, Y. Tu, R. Si, J. Wei, S. Zhang, Z. Wang, J.-F. Li, Y. Wang and D. Deng, *Nano Res.*, 2019, **12**, 2313–2317.
157 X. Li, Y. Zeng, C.-W. Tung, Y.-R. Lu, S. Baskaran, S.-F. Hung, S. Wang, C.-Q. Xu, J. Wang, T.-S. Chan, H. M. Chen, J. Jiang, Q. Yu, Y. Huang, J. Li, T. Zhang and B. Liu, *ACS Catal.*, 2021, **11**, 7292–7301.
158 S. Nitopi, E. Bertheussen, S. B. Scott, X. Liu, A. K. Engstfeld, S. Horch, B. Seger, I. E. L. Stephens, K. Chan, C. Hahn, J. K. Nørskov, T. F. Jaramillo and I. Chorkendorff, *Chem. Rev.*, 2019, **119**, 7610–7672.
159 Y. Liang, J. Zhao, Y. Yang, S.-F. Hung, J. Li, S. Zhang, Y. Zhao, A. Zhang, C. Wang, D. Appadoo, L. Zhang, Z. Geng, F. Li and J. Zeng, *Nat. Commun.*, 2023, **14**, 474.
160 H. Xu, D. Rebollar, H. He, L. Chong, Y. Liu, C. Liu, C.-J. Sun, T. Li, J. V. Muntean, R. E. Winans, D.-J. Liu and T. Xu, *Nat. Energy*, 2020, **5**, 623–632.
161 R. Qiu, J. Jia, L. Peng, R. Li, S. Yan, J. Li, J. Zhang, D. T. Sun, Z. Lan, T. Xue, G. Xu, L. Cui, Z. Lv, C. Li, Y. Hong, Y. Guo, B. Ren, S. Yang, J. Li and B. Han, *Green Chem.*, 2023, **25**, 684–691.
162 L. Ding, N. Zhu, Y. Hu, Z. Chen, P. Song, T. Sheng, Z. Wu and Y. Xiong, *Angew. Chem., Int. Ed.*, 2022, **61**, e202209268.
163 W. Ma, S. Xie, T. Liu, Q. Fan, J. Ye, F. Sun, Z. Jiang, Q. Zhang, J. Cheng and Y. Wang, *Nat. Catal.*, 2020, **3**, 478–487.
164 D.-L. Meng, M.-D. Zhang, D.-H. Si, M.-J. Mao, Y. Hou, Y.-B. Huang and R. Cao, *Angew. Chem., Int. Ed.*, 2021, **60**, 25485–25492.
165 L. Yan, X.-D. Liang, Y. Sun, L.-P. Xiao, B.-A. Lu, G. Li, Y.-Y. Li, Y.-H. Hong, L.-Y. Wan, C. Chen, J. Yang, Z.-Y. Zhou, N. Tian and S.-G. Sun, *Chem. Commun.*, 2022, **58**, 2488–2491.
166 J. Jiao, R. Lin, S. Liu, W.-C. Cheong, C. Zhang, Z. Chen, Y. Pan, J. Tang, K. Wu, S.-F. Hung, H. M. Chen, L. Zheng, Q. Lu, X. Yang, B. Xu, H. Xiao, J. Li, D. Wang, Q. Peng, C. Chen and Y. Li, *Nat. Chem.*, 2019, **11**, 222–228.
167 D. Chen, L.-H. Zhang, J. Du, H. Wang, J. Guo, J. Zhan, F. Li and F. Yu, *Angew. Chem., Int. Ed.*, 2021, **60**, 24022–24027.
168 J. Rosen, G. S. Hutchings, Q. Lu, R. V. Forest, A. Moore and F. Jiao, *ACS Catal.*, 2015, **5**, 4586–4591.
169 S. Li, S. Zhao, X. Lu, M. Ceccato, X.-M. Hu, A. Roldan, J. Catalano, M. Liu, T. Skrydstrup and K. Daasbjerg, *Angew. Chem., Int. Ed.*, 2021, **60**, 22826–22832.
170 Z. Hao, J. Chen, D. Zhang, L. Zheng, Y. Li, Z. Yin, G. He, L. Jiao, Z. Wen and X.-J. Lv, *Sci. Bull.*, 2021, **66**, 1649–1658.

171 M. Fang, X. Wang, X. Li, Y. Zhu, G. Xiao, J. Feng, X. Jiang, K. Lv, Y. Zhu and W.-F. Lin, *ChemCatChem*, 2021, **13**, 603–609.

172 N. Wang, Z. Liu, J. Ma, J. Liu, P. Zhou, Y. Chao, C. Ma, X. Bo, J. Liu, Y. Hei, Y. Bi, M. Sun, M. Cao, H. Zhang, F. Chang, H.-L. Wang, P. Xu, Z. Hu, J. Bai, H. Sun, G. Hu and M. Zhou, *ACS Sustainable Chem. Eng.*, 2020, **8**, 13813–13822.

173 W. Zheng, D. Wang, W. Cui, X. Sang, X. Qin, Z. Zhao, Z. Li, B. Yang, M. Zhong, L. Lei, Q. Zheng, S. Yao, G. Wu and Y. Hou, *Energy Environ. Sci.*, 2023, **16**, 1007–1015.

174 C. Hu, Y. Zhang, A. Hu, Y. Wang, X. Wei, K. Shen, L. Chen and Y. Li, *Adv. Mater.*, 2023, **35**, e2209298.

175 M. Ma and Q. Tang, *J. Mater. Chem. C*, 2022, **10**, 15948–15956.

176 Y. Pan, R. Lin, Y. Chen, S. Liu, W. Zhu, X. Cao, W. Chen, K. Wu, W.-C. Cheong, Y. Wang, L. Zheng, J. Luo, Y. Lin, Y. Liu, C. Liu, J. Li, Q. Lu, X. Chen, D. Wang, Q. Peng, C. Chen and Y. Li, *J. Am. Chem. Soc.*, 2018, **140**, 4218–4221.

177 S. Lin, C. S. Diercks, Y.-B. Zhang, N. Kornienko, E. M. Nichols, Y. Zhao, A. R. Paris, D. Kim, P. Yang, O. M. Yaghi and C. J. Chang, *Science*, 2015, **349**, 1208–1213.

178 J. Han, P. An, S. Liu, X. Zhang, D. Wang, Y. Yuan, J. Guo, X. Qiu, K. Hou, L. Shi, Y. Zhang, S. Zhao, C. Long and Z. Tang, *Angew. Chem., Int. Ed.*, 2019, **58**, 12711–12716.

179 J. Shen, R. Kortlever, R. Kas, Y. Y. Birdja, O. Diaz-Morales, Y. Kwon, I. Ledezma-Yanez, K. J. P. Schouten, G. Mul and M. T. M. Koper, *Nat. Commun.*, 2015, **6**, 8177.

180 S. Wang, P. Zhou, L. Zhou, F. Lv, Y. Sun, Q. Zhang, L. Gu, H. Yang and S. Guo, *Nano Lett.*, 2021, **21**, 4262–4269.

181 M. Wang, Y. Yao, Y. Tian, Y. Yuan, L. Wang, F. Yang, J. Ren, X. Hu, F. Wu, S. Zhang, J. Wu and J. Lu, *Adv. Mater.*, 2023, **35**, e2210658.

182 B. Zhang, J. Zhang, J. Shi, D. Tan, L. Liu, F. Zhang, C. Lu, Z. Su, X. Tan, X. Cheng, B. Han, L. Zheng and J. Zhang, *Nat. Commun.*, 2019, **10**, 2980.

183 N. Zhang, X. Zhang, L. Tao, P. Jiang, C. Ye, R. Lin, Z. Huang, A. Li, D. Pang, H. Yan, Y. Wang, P. Xu, S. An, Q. Zhang, L. Liu, S. Du, X. Han, D. Wang and Y. Li, *Angew. Chem., Int. Ed.*, 2021, **60**, 6170–6176.

184 J. Liu, X. Kong, L. Zheng, X. Guo, X. Liu and J. Shui, *ACS Nano*, 2020, **14**, 1093–1101.

185 B. Hammer and J. K. Nørskov, *Adv. Catal.*, 2000, **45**, 71–129.

186 Y. Wang, W. Qiu, E. Song, F. Gu, Z. Zheng, X. Zhao, Y. Zhao, J. Liu and W. Zhang, *Natl. Sci. Rev.*, 2018, **5**, 327–341.

187 B. I. Lundqvist, O. Gunnarsson, H. Hjelmberg and J. K. Nørskov, *Surf. Sci.*, 1979, **89**, 196–225.

188 H. Xu, D. Cheng, D. Cao and X. C. Zeng, *Nat. Catal.*, 2018, **1**, 339–348.

189 S. Liu, Z. Li, C. Wang, W. Tao, M. Huang, M. Zuo, Y. Yang, K. Yang, L. Zhang, S. Chen, P. Xu and Q. Chen, *Nat. Commun.*, 2020, **11**, 938.

190 N. Han, P. Ding, L. He, Y. Li and Y. Li, *Adv. Energy Mater.*, 2020, **10**, 1902338.

191 Q. Wang, K. Liu, J. Fu, C. Cai, H. Li, Y. Long, S. Chen, B. Liu, H. Li, W. Li, X. Qiu, N. Zhang, J. Hu, H. Pan and M. Liu, *Angew. Chem., Int. Ed.*, 2021, **60**, 25241–25245.

192 Q. Wang, M. Dai, H. Li, Y. R. Lu, T. S. Chan, C. Ma, K. Liu, J. Fu, W. Liao, S. Chen, E. Pensa, Y. Wang, S. Zhang, Y. Sun, E. Cortes and M. Liu, *Adv. Mater.*, 2023, e2300695.

193 Z. Zhang, J. Zhu, S. Chen, W. Sun and D. Wang, *Angew. Chem., Int. Ed.*, 2022, e202215136.

194 W. Guo, X. Tan, J. Bi, L. Xu, D. Yang, C. Chen, Q. Zhu, J. Ma, A. Tayal, J. Ma, Y. Huang, X. Sun, S. Liu and B. Han, *J. Am. Chem. Soc.*, 2021, **143**, 6877–6885.

195 M. Jia, S. Hong, T.-S. Wu, X. Li, Y.-L. Soo and Z. Sun, *Chem. Commun.*, 2019, **55**, 12024–12027.

196 E. Zhang, T. Wang, K. Yu, J. Liu, W. Chen, A. Li, H. Rong, R. Lin, S. Ji, X. Zheng, Y. Wang, L. Zheng, C. Chen, D. Wang, J. Zhang and Y. Li, *J. Am. Chem. Soc.*, 2019, **141**, 16569–16573.

197 Z. Wang, C. Wang, Y. Hu, S. Yang, J. Yang, W. Chen, H. Zhou, F. Zhou, L. Wang, J. Du, Y. Li and Y. Wu, *Nano Res.*, 2021, **14**, 2790–2796.

198 J. Guo, W. Zhang, L.-H. Zhang, D. Chen, J. Zhan, X. Wang, N. R. Shiju and F. Yu, *Adv. Sci.*, 2021, **8**, 2102884.

199 Q. Hao, H.-X. Zhong, J. Z. Wang, K.-H. Liu, J.-M. Yan, Z.-H. Ren, N. Zhou, X. Zhao, H. Zhang, D.-X. Liu, X. Liu, L.-W. Chen, J. Luo and X.-B. Zhang, *Nat. Synth.*, 2022, **1**, 719–728.

200 N. Zhang, X. Zhang, Y. Kang, C. Ye, R. Jin, H. Yan, R. Lin, J. Yang, Q. Xu, Y. Wang, Q. Zhang, L. Gu, L. Liu, W. Song, J. Liu, D. Wang and Y. Li, *Angew. Chem., Int. Ed.*, 2021, **60**, 13388–13393.

201 Y. Li, B. Wei, M. Zhu, J. Chen, Q. Jiang, B. Yang, Y. Hou, L. Lei, Z. Li, R. Zhang and Y. Lu, *Adv. Mater.*, 2021, **33**, 2102212.

202 L. Zhang, J. Feng, S. Liu, X. Tan, L. Wu, S. Jia, L. Xu, X. Ma, X. Song, J. Ma, X. Sun and B. Han, *Adv. Mater.*, 2023, **35**, e2209590.

203 Z. Zeng, L. Y. Gan, H. Bin Yang, X. Su, J. Gao, W. Liu, H. Matsumoto, J. Gong, J. Zhang, W. Cai, Z. Zhang, Y. Yan, B. Liu and P. Chen, *Nat. Commun.*, 2021, **12**, 4088.

204 X. Wang, N. Fu, J. C. Liu, K. Yu, Z. Li, Z. Xu, X. Liang, P. Zhu, C. Ye, A. Zhou, A. Li, L. Zheng, L. M. Liu, C. Chen, D. Wang, Q. Peng and Y. Li, *J. Am. Chem. Soc.*, 2022, **144**, 23223–23229.

205 J. Li, H. Zeng, X. Dong, Y. Ding, S. Hu, R. Zhang, Y. Dai, P. Cui, Z. Xiao, D. Zhao, L. Zhou, T. Zheng, J. Xiao, J. Zeng and C. Xia, *Nat. Commun.*, 2023, **14**, 340.

206 H. Shang, T. Wang, J. Pei, Z. Jiang, D. Zhou, Y. Wang, H. Li, J. Dong, Z. Zhuang, W. Chen, D. Wang, J. Zhang and Y. Li, *Angew. Chem., Int. Ed.*, 2020, **59**, 22465–22469.

207 Z. Jiang, T. Wang, J. Pei, H. Shang, D. Zhou, H. Li, J. Dong, Y. Wang, R. Cao, Z. Zhuang, W. Chen, D. Wang, J. Zhang and Y. Li, *Energy Environ. Sci.*, 2020, **13**, 2856–2863.

208 P. Huang, M. Cheng, H. Zhang, M. Zuo, C. Xiao and Y. Xie, *Nano Energy*, 2019, **61**, 428–434.

209 X. Zu, X. Li, W. Liu, Y. Sun, J. Xu, T. Yao, W. Yan, S. Gao, C. Wang, S. Wei and Y. Xie, *Adv. Mater.*, 2019, **31**, 1808135.

210 Y. Deng, J. Zhao, S. Wang, R. Chen, J. Ding, H.-J. Tsai, W.-J. Zeng, S.-F. Hung, W. Xu, J. Wang, F. Jaouen, X. Li, Y. Huang and B. Liu, *J. Am. Chem. Soc.*, 2023, **145**, 7242–7251.

211 T. Zheng, C. Liu, C. Guo, M. Zhang, X. Li, Q. Jiang, W. Xue, H. Li, A. Li, C.-W. Pao, J. Xiao, C. Xia and J. Zeng, *Nat. Nanotechnol.*, 2021, **16**, 1386–1393.

212 Y. Jiang, J. Shan, P. Wang, L. Huang, Y. Zheng and S.-Z. Qiao, *ACS Catal.*, 2023, **13**, 3101–3108.

213 G. Shi, Y. Xie, L. Du, X. Fu, X. Chen, W. Xie, T.-B. Lu, M. Yuan and M. Wang, *Angew. Chem., Int. Ed.*, 2022, **61**, e202203569.

214 H. Zou, G. Zhao, H. Dai, H. Dong, W. Luo, L. Wang, Z. Lu, Y. Luo, G. Zhang and L. Duan, *Angew. Chem., Int. Ed.*, 2022, **62**, e202217220.

215 Y. Wang, Z. Chen, P. Han, Y. Du, Z. Gu, X. Xu and G. Zheng, *ACS Catal.*, 2018, **8**, 7113–7119.

216 S. Chen, B. Wang, J. Zhu, L. Wang, H. Ou, Z. Zhang, X. Liang, L. Zheng, L. Zhou, Y.-Q. Su, D. Wang and Y. Li, *Nano Lett.*, 2021, **21**, 7325–7331.

217 L. Han, S. Song, M. Liu, S. Yao, Z. Liang, H. Cheng, Z. Ren, W. Liu, R. Lin, G. Qi, X. Liu, Q. Wu, J. Luo and H. L. Xin, *J. Am. Chem. Soc.*, 2020, **142**, 12563–12567.

218 M. Ren, X. Guo and S. Huang, *Chem. Eng. J.*, 2022, **433**, 134270.

219 S. Back and Y. Jung, *ACS Energy Lett.*, 2017, **2**, 969–975.

220 A. A. Peterson, F. Abild-Pedersen, F. Studt, J. Rossmeisl and J. K. Nørskov, *Energy Environ. Sci.*, 2010, **3**, 1311–1315.

221 H. Yang, Y. Wu, G. Li, Q. Lin, Q. Hu, Q. Zhang, J. Liu and C. He, *J. Am. Chem. Soc.*, 2019, **141**, 12717–12723.

222 S. Kong, X. Lv, X. Wang, Z. Liu, Z. Li, B. Jia, D. Sun, C. Yang, L. Liu, A. Guan, J. Wang, G. Zheng and F. Huang, *Nat. Catal.*, 2022, **6**, 6–15.

223 Y. Wu, Z. Jiang, X. Lu, Y. Liang and H. Wang, *Nature*, 2019, **575**, 639–642.

224 L. Ju, X. Tan, X. Mao, Y. Gu, S. Smith, A. Du, Z. Chen, C. Chen and L. Kou, *Nat. Commun.*, 2021, **12**, 5128.

225 H. Lin, S. Luo, H. Zhang and J. Ye, *Joule*, 2022, **6**, 294–314.

226 V. N. Gopalakrishnan, J. Becerra, E. F. Pena, M. Sakar, F. Béland and T.-O. Do, *Green Chem.*, 2021, **23**, 8332–8360.

227 H. Zhang, W. Tian, X. Duan, H. Sun, Y. Huang, Y. Fang and S. Wang, *Chin. J. Catal.*, 2022, **43**, 2301–2315.

228 A. Khandelwal, D. Maarisetty and S. S. Baral, *Renewable Sustainable Energy Rev.*, 2022, **167**, 112693.

229 Y. Wang, E. Chen and J. Tang, *ACS Catal.*, 2022, **12**, 7300–7316.

230 X. Li, W. Bi, Z. Wang, W. Zhu, W. Chu, C. Wu and Y. Xie, *Nano Res.*, 2018, **11**, 3362–3370.

231 B.-H. Lee, E. Gong, M. Kim, S. Park, H. R. Kim, J. Lee, E. Jung, C. W. Lee, J. Bok, Y. Jung, Y. S. Kim, K.-S. Lee, S.-P. Cho, J.-W. Jung, C.-H. Cho, S. Lebègue, K. T. Nam, H. Kim, S.-I. In and T. Hyeon, *Energy Environ. Sci.*, 2022, **15**, 601–609.

232 Z. Jiang, W. Sun, W. Miao, Z. Yuan, G. Yang, F. Kong, T. Yan, J. Chen, B. Huang, C. An and G. A. Ozin, *Adv. Sci.*, 2019, **6**, 1900289.

233 L. Yuan, S.-F. Hung, Z.-R. Tang, H. M. Chen, Y. Xiong and Y.-J. Xu, *ACS Catal.*, 2019, **9**, 4824–4833.

234 Y. Yu, X. a. Dong, P. Chen, Q. Geng, H. Wang, J. Li, Y. Zhou and F. Dong, *ACS Nano*, 2021, **15**, 14453–14464.

235 X. Xiong, C. Mao, Z. Yang, Q. Zhang, G. I. N. Waterhouse, L. Gu and T. Zhang, *Adv. Energy Mater.*, 2020, **10**, 2002928.

236 J. Ding, X. Liu, M. Shi, T. Li, M. Xia, X. Du, R. Shang, H. Gu and Q. Zhong, *Sol. Energy Mater. Sol. Cells*, 2019, **195**, 34–42.

237 Y. J. Wang, G. L. Zhuang, J. W. Zhang, F. Luo, X. Cheng, F. L. Sun, S. S. Fu, T. B. Lu and Z. M. Zhang, *Angew. Chem., Int. Ed.*, 2022, **62**, e202216592.

238 Y. Cao, L. Guo, M. Dan, D. E. Doronkin, C. Han, Z. Rao, Y. Liu, J. Meng, Z. Huang, K. Zheng, P. Chen, F. Dong and Y. Zhou, *Nat. Commun.*, 2021, **12**, 1675.

239 H. Chen, Y. Xiong, J. Li, J. Abed, D. Wang, A. Pedrazo-Tardajos, Y. Cao, Y. Zhang, Y. Wang, M. Shakouri, Q. Xiao, Y. Hu, S. Bals, E. H. Sargent, C.-Y. Su and Z. Yang, *Nat. Commun.*, 2023, **14**, 1719.

240 S. Cao and J. Yu, *J. Photochem. Photobiol., C*, 2016, **27**, 72–99.

241 P. Kumar, R. Boukherroub and K. Shankar, *J. Mater. Chem. A*, 2018, **6**, 12876–12931.

242 W.-J. Ong, L.-L. Tan, Y. H. Ng, S.-T. Yong and S.-P. Chai, *Chem. Rev.*, 2016, **116**, 7159–7329.

243 J. Luo, H. Han, X. Wang, X. Qiu, B. Liu, Y. Lai, X. Chen, R. Zhong, L. Wang and C. Wang, *Appl. Catal., B*, 2023, **328**, 122495.

244 Y. Zhao, Z. Han, G. Gao, W. Zhang, Y. Qu, H. Zhu, P. Zhu and G. Wang, *Adv. Funct. Mater.*, 2021, **31**, 2104976.

245 P. Huang, J. Huang, S. A. Pantovich, A. D. Carl, T. G. Fenton, C. A. Caputo, R. L. Grimm, A. I. Frenkel and G. Li, *J. Am. Chem. Soc.*, 2018, **140**, 16042–16047.

246 Y. Yang, F. Li, J. Chen, J. Fan and Q. Xiang, *ChemSusChem*, 2020, **13**, 1979–1985.

247 Z. Han, Y. Zhao, G. Gao, W. Zhang, Y. Qu, H. Zhu, P. Zhu and G. Wang, *Small*, 2021, **17**, 2102089.

248 P. Chen, B. Lei, X. a. Dong, H. Wang, J. Sheng, W. Cui, J. Li, Y. Sun, Z. Wang and F. Dong, *ACS Nano*, 2020, **14**, 15841–15852.

249 H. Cao, J. Wang, J.-H. Kim, Z. Guo, J. Xiao, J. Yang, J. Chang, Y. Shi and Y. Xie, *Appl. Catal., B*, 2021, **296**, 120362.

250 P. Sharma, S. Kumar, O. Tomanec, M. Petr, J. Zhu Chen, J. T. Miller, R. S. Varma, M. B. Gawande and R. Zbořil, *Small*, 2021, **17**, 2006478.

251 T. Tong, B. Zhu, C. Jiang, B. Cheng and J. Yu, *Appl. Surf. Sci.*, 2018, **433**, 1175–1183.

252 G. Gao, Y. Jiao, E. R. Waclawik and A. Du, *J. Am. Chem. Soc.*, 2016, **138**, 6292–6297.

253 L. Cheng, H. Yin, C. Cai, J. Fan and Q. Xiang, *Small*, 2020, **16**, 2002411.

254 Y. Li, B. Li, D. Zhang, L. Cheng and Q. Xiang, *ACS Nano*, 2020, **14**, 10552–10561.

255 M. Ma, Z. Huang, D. E. Doronkin, W. Fa, Z. Rao, Y. Zou, R. Wang, Y. Zhong, Y. Cao, R. Zhang and Y. Zhou, *Appl. Catal., B*, 2022, **300**, 120695.

256 S. Hu, P. Qiao, X. Yi, Y. Lei, H. Hu, J. Ye and D. Wang, *Angew. Chem., Int. Ed.*, 2023, **62**, e202304585.

257 Q. Chen, G. Gao, Y. Zhang, Y. li, H. Zhu, P. Zhu, Y. Qu, G. Wang and W. Qin, *J. Mater. Chem. A*, 2021, **9**, 15820–15826.

258 A. J. Bard, *J. Photochem.*, 1979, **10**, 59–75.

259 J. Low, J. Yu, M. Jaroniec, S. Wageh and A. A. Al-Ghamdi, *Adv. Mater.*, 2017, **29**, 1601694.

260 Q. Xu, L. Zhang, B. Cheng, J. Fan and J. Yu, *Chem*, 2020, **6**, 1543–1559.

261 B.-C. He, C. Zhang, P.-P. Luo, Y. Li and T.-B. Lu, *Green Chem.*, 2020, **22**, 7552–7559.

262 S. Ji, Y. Qu, T. Wang, Y. Chen, G. Wang, X. Li, J. Dong, Q. Chen, W. Zhang, Z. Zhang, S. Liang, R. Yu, Y. Wang, D. Wang and Y. Li, *Angew. Chem., Int. Ed.*, 2020, **59**, 10651–10657.

263 C. Gao, S. Chen, Y. Wang, J. Wang, X. Zheng, J. Zhu, L. Song, W. Zhang and Y. Xiong, *Adv. Mater.*, 2018, **30**, 1704624.

264 Z. Wang, J. Yang, J. Cao, W. Chen, G. Wang, F. Liao, X. Zhou, F. Zhou, R. Li, Z.-Q. Yu, G. Zhang, X. Duan and Y. Wu, *ACS Nano*, 2020, **14**, 6164–6172.

265 J. Yang, Z. Wang, J. Jiang, W. Chen, F. Liao, X. Ge, X. Zhou, M. Chen, R. Li, Z. Xue, G. Wang, X. Duan, G. Zhang, Y.-G. Wang and Y. Wu, *Nano Energy*, 2020, **76**, 105059.

266 H. Zhang, J. Wei, J. Dong, G. Liu, L. Shi, P. An, G. Zhao, J. Kong, X. Wang, X. Meng, J. Zhang and J. Ye, *Angew. Chem., Int. Ed.*, 2016, **55**, 14310–14314.

267 W. Zhong, R. Sa, L. Li, Y. He, L. Li, J. Bi, Z. Zhuang, Y. Yu and Z. Zou, *J. Am. Chem. Soc.*, 2019, **141**, 7615–7621.

268 J. Li, H. Huang, W. Xue, K. Sun, X. Song, C. Wu, L. Nie, Y. Li, C. Liu, Y. Pan, H.-L. Jiang, D. Mei and C. Zhong, *Nat. Catal.*, 2021, **4**, 719–729.

269 M. Kou, W. Liu, Y. Wang, J. Huang, Y. Chen, Y. Zhou, Y. Chen, M. Ma, K. Lei, H. Xie, P. K. Wong and L. Ye, *Appl. Catal., B*, 2021, **291**, 120146.

270 Q. Zhang, S. Gao, Y. Guo, H. Wang, J. Wei, X. Su, H. Zhang, Z. Liu and J. Wang, *Nat. Commun.*, 2023, **14**, 1147.

271 G. Wang, C.-T. He, R. Huang, J. Mao, D. Wang and Y. Li, *J. Am. Chem. Soc.*, 2020, **142**, 19339–19345.

272 Y.-H. Chen, M.-Y. Qi, Y.-H. Li, Z.-R. Tang, T. Wang, J. Gong and Y.-J. Xu, *Cell Rep. Phys. Sci.*, 2021, **2**, 100371.

273 Y. Tang, Y. Wei, Z. Wang, S. Zhang, Y. Li, L. Nguyen, Y. Li, Y. Zhou, W. Shen, F. F. Tao and P. Hu, *J. Am. Chem. Soc.*, 2019, **141**, 7283–7293.

274 A. V. Tavasoli, M. Preston and G. Ozin, *Energy Environ. Sci.*, 2021, **14**, 3098–3109.

275 W. L. Luyben, *Ind. Eng. Chem. Res.*, 2014, **53**, 14423–14439.

276 M. Akri, S. Zhao, X. Li, K. Zang, A. F. Lee, M. A. Isaacs, W. Xi, Y. Gangarajula, J. Luo, Y. Ren, Y.-T. Cui, L. Li, Y. Su, X. Pan, W. Wen, Y. Pan, K. Wilson, L. Li, B. Qiao, H. Ishii, Y.-F. Liao, A. Wang, X. Wang and T. Zhang, *Nat. Commun.*, 2019, **10**, 5181.

277 J. Wu, J. Gao, S. Lian, J. Li, K. Sun, S. Zhao, Y. D. Kim, Y. Ren, M. Zhang, Q. Liu, Z. Liu and Z. Peng, *Appl. Catal., B*, 2022, **314**, 121516.

278 D. Shen, Z. Li, J. Shan, G. Yu, X. Wang, Y. Zhang, C. Liu, S. Lyu, J. Li and L. Li, *Appl. Catal., B*, 2022, **318**, 121809.

279 S. Kim, J. Lauterbach and E. Sasmaz, *ACS Catal.*, 2021, **11**, 8247–8260.

280 L. Zhou, J. M. P. Martirez, J. Finzel, C. Zhang, D. F. Swearer, S. Tian, H. Robatjazi, M. Lou, L. Dong, L. Henderson, P. Christopher, E. A. Carter, P. Nordlander and N. J. Halas, *Nat. Energy*, 2020, **5**, 61–70.

281 J. Goldemberg, *Science*, 2007, **315**, 808–810.

282 F. J. Caparrós, L. Soler, M. D. Rossell, I. Angurell, L. Piccolo, O. Rossell and J. Llorca, *ChemCatChem*, 2018, **10**, 2365–2369.

283 X. Ye, J. Ma, W. Yu, X. Pan, C. Yang, C. Wang, Q. Liu and Y. Huang, *J. Energy Chem.*, 2022, **67**, 184–192.

284 K. Zheng, Y. Li, B. Liu, F. Jiang, Y. Xu and X. Liu, *Angew. Chem., Int. Ed.*, 2022, **61**, e202210991.

285 X. Shang, G. Liu, X. Su, Y. Huang and T. Zhang, *EES Catal.*, 2023, **1**, 353–368.

286 K. Zhao, X. Nie, H. Wang, S. Chen, X. Quan, H. Yu, W. Choi, G. Zhang, B. Kim and J. G. Chen, *Nat. Commun.*, 2020, **11**, 2455.

287 A. Guan, Z. Chen, Y. Quan, C. Peng, Z. Wang, T.-K. Sham, C. Yang, Y. Ji, L. Qian, X. Xu and G. Zheng, *ACS Energy Lett.*, 2020, **5**, 1044–1053.

288 G. Sun, Y. Cao, D. Li, M. Hu, X. Liang, Z. Wang, Z. Cai, F. Shen, B. Chen and K. Zhou, *Appl. Catal., A*, 2023, **651**, 119025.

289 J. Wang, D. Deng, Q. Wu, M. Liu, Y. Wang, J. Jiang, X. Zheng, H. Zheng, Y. Bai, Y. Chen, X. Xiong and Y. Lei, *ACS Nano*, 2023, **17**, 18688–18705.

290 J. Ding, H. Bin Yang, X.-L. Ma, S. Liu, W. Liu, Q. Mao, Y. Huang, J. Li, T. Zhang and B. Liu, *Nat. Energy*, 2023, **8**, 1386–1394.

291 X. Li, S.-G. Han, W. Wu, K. Zhang, B. Chen, S.-H. Zhou, D.-D. Ma, W. Wei, X.-T. Wu, R. Zou and Q.-L. Zhu, *Energy Environ. Sci.*, 2023, **16**, 502–512.

292 J. Albero, Y. Peng and H. García, *ACS Catal.*, 2020, **10**, 5734–5749.

293 N. Li, B. Wang, Y. Si, F. Xue, J. Zhou, Y. Lu and M. Liu, *ACS Catal.*, 2019, **9**, 5590–5602.

294 S. Yu and P. K. Jain, *Nat. Commun.*, 2019, **10**, 2022.

295 Y. Shen, C. Ren, L. Zheng, X. Xu, R. Long, W. Zhang, Y. Yang, Y. Zhang, Y. Yao, H. Chi, J. Wang, Q. Shen, Y. Xiong, Z. Zou and Y. Zhou, *Nat. Commun.*, 2023, **14**, 1117.

296 J. Hong, M. Li, J. Zhang, B. Sun and F. Mo, *ChemSusChem*, 2019, **12**, 6–39.

297 Y. Quan, R. Yu, J. Zhu, A. Guan, X. Lv, C. Yang, S. Li, J. Wu and G. Zheng, *J. Colloid Interface Sci.*, 2021, **601**, 378–384.

298 X. Shang, G. Liu, X. Su, Y. Huang and T. Zhang, *ACS Catal.*, 2022, **12**, 13741–13754.

299 J. Zuo, W. Chen, J. Liu, X. Duan, L. Ye and Y. Yuan, *Sci. Adv.*, 2020, **6**, eaba5433.

300 X. Peng, L. Zeng, D. Wang, Z. Liu, Y. Li, Z. Li, B. Yang, L. Lei, L. Dai and Y. Hou, *Chem. Soc. Rev.*, 2023, **52**, 2193–2237.

301 S. Saini, P. K. Prajapati and S. L. Jain, *Catal. Rev.*, 2022, **64**, 631–677.

302 X. Shang, H. Zhuo, Q. Han, X. Yang, G. Hou, G. Liu, X. Su, Y. Huang and T. Zhang, *Angew. Chem., Int. Ed.*, 2023, **62**, e202309377.

303 Q.-W. Song, R. Ma, P. Liu, K. Zhang and L.-N. He, *Green Chem.*, 2023, **25**, 6538–6560.

304 Y. Yang and J.-W. Lee, *Chem. Sci.*, 2019, **10**, 3905–3926.

305 T. Li, F. Chen, R. Lang, H. Wang, Y. Su, B. Qiao, A. Wang and T. Zhang, *Angew. Chem., Int. Ed.*, 2020, **59**, 7430–7434.

306 I. Ro, J. Qi, S. Lee, M. Xu, X. Yan, Z. Xie, G. Zakem, A. Morales, J. G. Chen, X. Pan, D. G. Vlachos, S. Caratzoulas and P. Christopher, *Nature*, 2022, **609**, 287–292.

307 S. Feng, X. Lin, X. Song, B. Mei, J. Mu, J. Li, Y. Liu, Z. Jiang and Y. Ding, *ACS Catal.*, 2021, **11**, 682–690.

308 S. Fu, S. Yao, S. Guo, G.-C. Guo, W. Yuan, T.-B. Lu and Z.-M. Zhang, *J. Am. Chem. Soc.*, 2021, **143**, 20792–20801.

309 M. T. Jensen, M. H. Rønne, A. K. Ravn, R. W. Juhl, D. U. Nielsen, X.-M. Hu, S. U. Pedersen, K. Daasbjerg and T. Skrydstrup, *Nat. Commun.*, 2017, **8**, 489.

310 R. Sang, Y. Hu, R. Razzaq, G. Mollaert, H. Atia, U. Bentrup, M. Sharif, H. Neumann, H. Junge, R. Jackstell, B. U. W. Maes and M. Beller, *Nat. Commun.*, 2022, **13**, 4432.

311 C. Wang, Q. Song, K. Zhang, P. Liu, J. Wang, J. Wang, H. Zhang and J. Wang, *Chem. Commun.*, 2019, **55**, 1299–1302.

312 Q. Yang, C.-C. Yang, C.-H. Lin and H.-L. Jiang, *Angew. Chem., Int. Ed.*, 2019, **58**, 3511–3515.

313 J. Xu, H. Xu, A. Q. Dong, H. Zhang, Y. T. Zhou, H. Dong, B. Tang, Y. F. Liu, L. X. Zhang, X. J. Liu, J. Luo, L. J. Bie, S. Dai, Y. H. Wang, X. H. Sun and Y. G. Li, *Adv. Mater.*, 2022, **34**, 2206991.

314 J. Sittiwong, O. Opasmongkolchai, P. Srifa, B. Boekfa, P. Treesukol, W. Sangthong, T. Maihom and J. Limtrakul, *Mol. Catal.*, 2023, **535**, 112855.

315 X. Zhang, X. Zhu, S. Bo, C. Chen, M. Qiu, X. Wei, N. He, C. Xie, W. Chen, J. Zheng, P. Chen, S. P. Jiang, Y. Li, Q. Liu and S. Wang, *Nat. Commun.*, 2022, **13**, 5337.

316 X. Wei, Y. Liu, X. Zhu, S. Bo, L. Xiao, C. Chen, T. T. T. Nga, Y. He, M. Qiu, C. Xie, D. Wang, Q. Liu, F. Dong, C. L. Dong, X. Z. Fu and S. Wang, *Adv. Mater.*, 2023, **35**, e2300020.

317 D. Zhao, Z. Chen, W. Yang, S. Liu, X. Zhang, Y. Yu, W.-C. Cheong, L. Zheng, F. Ren, G. Ying, X. Cao, D. Wang, Q. Peng, G. Wang and C. Chen, *J. Am. Chem. Soc.*, 2019, **141**, 4086–4093.

318 H. Shi, H. Wang, Y. Zhou, J. Li, P. Zhai, X. Li, G. G. Gurzadyan, J. Hou, H. Yang and X. Guo, *Angew. Chem., Int. Ed.*, 2022, **61**, e202208904.

319 B. Peng, H. Liu, Z. Liu, X. Duan and Y. Huang, *J. Phys. Chem. Lett.*, 2021, **12**, 2837–2847.

320 Y. Hori, H. Wakebe, T. Tsukamoto and O. Koga, *Electrochim. Acta*, 1994, **39**, 1833–1839.

321 G. A. Somorjai and J. Y. Park, *Angew. Chem., Int. Ed.*, 2008, **47**, 9212–9228.

322 A. J. Medford, A. Vojvodic, J. S. Hummelshøj, J. Voss, F. Abild-Pedersen, F. Studt, T. Bligaard, A. Nilsson and J. K. Nørskov, *J. Catal.*, 2015, **328**, 36–42.

323 X. Chang, Z.-J. Zhao, Z. Lu, S. Chen, R. Luo, S. Zha, L. Li, G. Sun, C. Pei and J. Gong, *Nat. Nanotechnol.*, 2023, **18**, 611–616.

324 Z.-J. Zhao, S. Liu, S. Zha, D. Cheng, F. Studt, G. Henkelman and J. Gong, *Nat. Rev. Mater.*, 2019, **4**, 792–804.

325 S. Jiao, X. Fu and H. Huang, *Adv. Funct. Mater.*, 2022, **32**, 2107651.

326 A. S. Varela, W. Ju, A. Bagger, P. Franco, J. Rossmeisl and P. Strasser, *ACS Catal.*, 2019, **9**, 7270–7284.

327 T. Dai, Z. Wang, X. Lang and Q. Jiang, *J. Mater. Chem. A*, 2022, **10**, 16900–16907.

328 H. Jin, R. Zhao, P. Cui, X. Liu, J. Yan, X. Yu, D. Ma, W. Song and C. Cao, *J. Am. Chem. Soc.*, 2023, **145**, 12023–12032.

329 W. Ju, A. Bagger, G.-P. Hao, A. S. Varela, I. Sinev, V. Bon, B. Roldan Cuenya, S. Kaskel, J. Rossmeisl and P. Strasser, *Nat. Commun.*, 2017, **8**, 944.

330 Q. Chang, Y. Liu, J.-H. Lee, D. Ologunagba, S. Hwang, Z. Xie, S. Kattel, J. H. Lee and J. G. Chen, *J. Am. Chem. Soc.*, 2022, **144**, 16131–16138.

331 P. Brimley, H. Almajed, Y. Alsunni, A. W. Alherz, Z. J. L. Bare, W. A. Smith and C. B. Musgrave, *ACS Catal.*, 2022, **12**, 10161–10171.

332 Y.-X. Zhang, S. Zhang, H. Huang, X. Liu, B. Li, Y. Lee, X. Wang, Y. Bai, M. Sun, Y. Wu, S. Gong, X. Liu, Z. Zhuang, T. Tan and Z. Niu, *J. Am. Chem. Soc.*, 2023, **145**, 4819–4827.

333 L. Li, K. Yuan and Y. Chen, *Acc. Mater. Res.*, 2022, **3**, 584–596.

334 H. Li, R. Li, G. Liu, M. Zhai and J. Yu, *Adv. Mater.*, 2023, 2301307.

335 T. Pu, J. Ding, F. Zhang, K. Wang, N. Cao, E. J. M. Hensen and P. Xie, *Angew. Chem., Int. Ed.*, 2023, e202305964.

336 J. Ding, F. Li, J. Zhang, Q. Zhang, Y. Liu, W. Wang, W. Liu, B. Wang, J. Cai, X. Su, H. B. Yang, X. Yang, Y. Huang, Y. Zhai and B. Liu, *J. Am. Chem. Soc.*, 2023, **145**, 11829–11836.

337 T. Ding, X. Liu, Z. Tao, T. Liu, T. Chen, W. Zhang, X. Shen, D. Liu, S. Wang, B. Pang, D. Wu, L. Cao, L. Wang, T. Liu, Y. Li, H. Sheng, M. Zhu and T. Yao, *J. Am. Chem. Soc.*, 2021, **143**, 11317–11324.

338 J. Pei, T. Wang, R. Sui, X. Zhang, D. Zhou, F. Qin, X. Zhao, Q. Liu, W. Yan, J. Dong, L. Zheng, A. Li, J. Mao, W. Zhu, W. Chen and Z. Zhuang, *Energy Environ. Sci.*, 2021, **14**, 3019–3028.

339 J. Wang, E. Kim, D. P. Kumar, A. P. Rangappa, Y. Kim, Y. Zhang and T. K. Kim, *Angew. Chem., Int. Ed.*, 2022, **61**, e202113044.

340 J. Zhu, M. Xiao, D. Ren, R. Gao, X. Liu, Z. Zhang, D. Luo, W. Xing, D. Su, A. Yu and Z. Chen, *J. Am. Chem. Soc.*, 2022, **144**, 9661–9671.

341 H. Ou, S. Ning, P. Zhu, S. Chen, A. Han, Q. Kang, Z. Hu, J. Ye, D. Wang and Y. Li, *Angew. Chem., Int. Ed.*, 2022, **61**, e202206579.

342 Q. Zhang, D. Liu, Y. Zhang, Z. Guo, M. Chen, Y. Chen, B. Jin, Y. Song and H. Pan, *J. Energy Chem.*, 2023, **87**, 509–517.

343 W. Xie, H. Li, G. Cui, J. Li, Y. Song, S. Li, X. Zhang, J. Y. Lee, M. Shao and M. Wei, *Angew. Chem., Int. Ed.*, 2021, **60**, 7382–7388.

344 J. Chen, Y. Zha, B. Liu, Y. Li, Y. Xu and X. Liu, *ACS Catal.*, 2023, 7110–7121, DOI: 10.1021/acscatal.3c00586.

345 H. Wang, X. Bi, Y. Yan, Y. Zhao, Z. Yang, H. Ning and M. Wu, *Adv. Funct. Mater.*, 2023, **33**, 2214946.

346 W. Yang, Z. Jia, B. Zhou, L. Chen, X. Ding, L. Jiao, H. Zheng, Z. Gao, Q. Wang and H. Li, *ACS Catal.*, 2023, **13**, 9695–9705.

347 Y. Lou, F. jiang, W. Zhu, L. Wang, T. Yao, S. Wang, B. Yang, B. Yang, Y. Zhu and X. Liu, *Appl. Catal., B*, 2021, **291**, 120122.

348 W. Xia, Y. Xie, S. Jia, S. Han, R. Qi, T. Chen, X. Xing, T. Yao, D. Zhou, X. Dong, J. Zhai, J. Li, J. He, D. Jiang, Y. Yamauchi, M. He, H. Wu and B. Han, *J. Am. Chem. Soc.*, 2023, **145**, 17253–17264.

349 J. M. Wang, Q. Y. Zhu, J. H. Lee, T. G. Woo, Y. X. Zhang, W.-D. Jang and T. K. Kim, *Nat. Commun.*, 2023, **14**, 3808.

350 P. Braunstein and F. Naud, *Angew. Chem., Int. Ed.*, 2001, **40**, 680–699.

351 A. F. Littke and G. C. Fu, *Angew. Chem., Int. Ed.*, 1998, **37**, 3387–3388.

352 M. Huser, M.-T. Youinou and J. A. Osborn, *Angew. Chem., Int. Ed.*, 1989, **28**, 1386–1388.

353 Y. Ren, Y. Tang, L. Zhang, X. Liu, L. Li, S. Miao, D. Sheng Su, A. Wang, J. Li and T. Zhang, *Nat. Commun.*, 2019, **10**, 4500.

354 Z. Chen, Z. Liu and X. Xu, *Nat. Commun.*, 2023, **14**, 2512.

355 L. Chen, R. R. Unocic, A. S. Hoffman, J. Hong, A. H. Braga, Z. Bao, S. R. Bare and J. Szanyi, *JACS Au*, 2021, **1**, 977–986.

356 C.-S. Hsu, J. Wang, Y.-C. Chu, J.-H. Chen, C.-Y. Chien, K.-H. Lin, L. D. Tsai, H.-C. Chen, Y.-F. Liao, N. Hiraoka, Y.-C. Cheng and H. M. Chen, *Nat. Commun.*, 2023, **14**, 5245.

357 Y. Zeng, J. Zhao, S. Wang, X. Ren, Y. Tan, Y.-R. Lu, S. Xi, J. Wang, F. Jaouen, X. Li, Y. Huang, T. Zhang and B. Liu, *J. Am. Chem. Soc.*, 2023, **145**, 15600–15610.

358 X. Ren, J. Zhao, X. Li, J. Shao, B. Pan, A. Salamé, E. Boutin, T. Groizard, S. Wang, J. Ding, X. Zhang, W.-Y. Huang, W.-J. Zeng, C. Liu, Y. Li, S.-F. Hung, Y. Huang, M. Robert and B. Liu, *Nat. Commun.*, 2023, **14**, 3401.

359 S. Ren, D. Joulié, D. Salvatore, K. Torbensen, M. Wang, M. Robert and C. P. Berlinguette, *Science*, 2019, **365**, 367–369.

360 L. Sévery, J. Szczerbiński, M. Taskin, I. Tuncay, F. Brandalise Nunes, C. Cignarella, G. Tocci, O. Blacque, J. Osterwalder, R. Zenobi, M. Iannuzzi and S. D. Tilley, *Nat. Chem.*, 2021, **13**, 523–529.

361 X. Cao, L. Zhao, B. Wulan, D. Tan, Q. Chen, J. Ma and J. Zhang, *Angew. Chem., Int. Ed.*, 2022, **61**, e202113918.

362 X. Ren, S. Liu, H. Li, J. Ding, L. Liu, Z. Kuang, L. Li, H. Yang, F. Bai, Y. Huang, T. Zhang and B. Liu, *Sci. China: Chem.*, 2020, **63**, 1727–1733.

363 Q. Zhang, H. J. Tsai, F. Li, Z. Wei, Q. He, J. Ding, Y. Liu, Z.-Y. Lin, X. Yang, Z. Chen, F. Hu, X. Yang, Q. Tang, H. B. Yang, S.-F. Hung and Y. Zhai, *Angew. Chem., Int. Ed.*, 2023, **n/a**, e202311550.

364 P. Song, B. Hu, D. Zhao, J. Fu, X. Su, W. Feng, K. Yu, S. Liu, J. Zhang and C. Chen, *ACS Nano*, 2023, **17**, 4619–4628.

365 Y. Zhang, L. Jiao, W. Yang, C. Xie and H.-L. Jiang, *Angew. Chem., Int. Ed.*, 2021, **60**, 7607–7611.

366 X. Zhao, S. Huang, Z. Chen, C. Lu, S. Han, C. Ke, J. Zhu, J. Zhang, D. Tranca and X. Zhuang, *Carbon*, 2021, **178**, 488–496.

367 Z. Li, R. Wu, S. Xiao, Y. Yang, L. Lai, J. S. Chen and Y. Chen, *Chem. Eng. J.*, 2022, **430**, 132882.

368 X. Wang, Y. Wang, X. Sang, W. Zheng, S. Zhang, L. Shuai, B. Yang, Z. Li, J. Chen, L. Lei, N. M. Adli, M. K. H. Leung, M. Qiu, G. Wu and Y. Hou, *Angew. Chem., Int. Ed.*, 2021, **60**, 4192–4198.

369 Z. Chen, C. Wang, X. Zhong, H. Lei, J. Li, Y. Ji, C. Liu, M. Ding, Y. Dai, X. Li, T. Zheng, Q. Jiang, H.-J. Peng and C. Xia, *Nano Lett.*, 2023, **23**, 7046–7053.

370 W. Zhang, D. Liu, T. Liu, C. Ding, T. Chen, Y. Li, X. Liu, L. Wang, C. Li, J. He, T. Ding and T. Yao, *Nano Res.*, 2023, **16**, 10873–10880.

371 W. Zheng, J. Yang, H. Chen, Y. Hou, Q. Wang, M. Gu, F. He, Y. Xia, Z. Xia, Z. Li, B. Yang, L. Lei, C. Yuan, Q. He, M. Qiu and X. Feng, *Adv. Funct. Mater.*, 2020, **30**, 1907658.

372 Y. Zhou, Q. Zhou, H. Liu, W. Xu, Z. Wang, S. Qiao, H. Ding, D. Chen, J. Zhu, Z. Qi, X. Wu, Q. He and L. Song, *Nat. Commun.*, 2023, **14**, 3776.

373 Y.-N. Gong, L. Jiao, Y. Qian, C.-Y. Pan, L. Zheng, X. Cai, B. Liu, S.-H. Yu and H.-L. Jiang, *Angew. Chem., Int. Ed.*, 2020, **59**, 2705–2709.

374 Z. Feng, C. Tang, P. Zhang, K. Li, G. Li, J. Wang, Z. Feng and C. Li, *J. Am. Chem. Soc.*, 2023, **145**, 12663–12672.

375 J. Ding, Z. Teng, X. Su, K. Kato, Y. Liu, T. Xiao, W. Liu, L. Liu, Q. Zhang, X. Ren, J. Zhang, Z. Chen, O. Teruhisa, A. Yamakata, H. Yang, Y. Huang, B. Liu and Y. Zhai, *Chem*, 2023, **9**, 1017–1035.

376 G. Wang, Y. Wu, Z. Li, Z. Lou, Q. Chen, Y. Li, D. Wang and J. Mao, *Angew. Chem., Int. Ed.*, 2023, **62**, e202218460.

377 Y. Zhou, F. Wei, H. Qi, Y. Chai, L. Cao, J. Lin, Q. Wan, X. Liu, Y. Xing, S. Lin, A. Wang, X. Wang and T. Zhang, *Nat. Catal.*, 2022, **5**, 1145–1156.

378 Y. Gao, B. Liu and D. Wang, *Adv. Mater.*, 2023, **35**, e2209654.

379 P. Song, P. Zhu, X. Su, M. Hou, D. Zhao and J. Zhang, *Chem. - Asian J.*, 2022, **17**, e202200716.

380 J. Zhao, S. Ji, C. Guo, H. Li, J. Dong, P. Guo, D. Wang, Y. Li and F. D. Toste, *Nat. Catal.*, 2021, **4**, 523–531.

381 Y. Chen, R. Gao, S. Ji, H. Li, K. Tang, P. Jiang, H. Hu, Z. Zhang, H. Hao, Q. Qu, X. Liang, W. Chen, J. Dong, D. Wang and Y. Li, *Angew. Chem., Int. Ed.*, 2021, **60**, 3212–3221.

382 H. Liu, Q. Lei, R. Miao, M. Sun, C. Qin, L. Zhang, G. Ye, Y. Yao, B. Huang and Z. Ma, *Adv. Funct. Mater.*, 2022, **32**, 2207408.

383 W. Ni, H. Chen, J. Zeng, Y. Zhang, H. A. Younus, Z. Zeng, M. Dai, W. Zhang and S. Zhang, *Energy Environ. Sci.*, 2023, **16**, 3679–3710.

384 S. Chen, X. Li, C.-W. Kao, T. Luo, K. Chen, J. Fu, C. Ma, H. Li, M. Li, T.-S. Chan and M. Liu, *Angew. Chem., Int. Ed.*, 2022, **61**, e202206233.

385 D. Liu, Q. He, S. Ding and L. Song, *Adv. Energy Mater.*, 2020, **10**, 2001482.

386 N. Zhang, C. Gao and Y. Xiong, *J. Energy Chem.*, 2019, **37**, 43–57.

387 Y. Li, Z. He, F. Wu, S. Wang, Y. Cheng and S. Jiang, *Mater. Rep.: Energy*, 2023, **3**, 100197.

388 C. Jia, S. Li, Y. Zhao, R. K. Hocking, W. Ren, X. Chen, Z. Su, W. Yang, Y. Wang, S. Zheng, F. Pan and C. Zhao, *Adv. Funct. Mater.*, 2021, **31**, 2107072.

389 E. Boutin, M. Wang, J. C. Lin, M. Mesnage, D. Mendoza, B. Lassalle-Kaiser, C. Hahn, T. F. Jaramillo and M. Robert, *Angew. Chem., Int. Ed.*, 2019, **58**, 16172–16176.

390 Y. Song, J.-J. Zhang, Z. Zhu, X. Chen, L. Huang, J. Su, Z. Xu, T. H. Ly, C.-S. Lee, B. I. Yakobson, B. Z. Tang and R. Ye, *Appl. Catal., B*, 2021, **284**, 119750.

391 M. Zhu, R. Ye, K. Jin, N. Lazouski and K. Manthiram, *ACS Energy Lett.*, 2018, **3**, 1381–1386.

392 N. Han, Y. Wang, L. Ma, J. Wen, J. Li, H. Zheng, K. Nie, X. Wang, F. Zhao, Y. Li, J. Fan, J. Zhong, T. Wu, D. J. Miller, J. Lu, S.-T. Lee and Y. Li, *Chem*, 2017, **3**, 652–664.

393 X. Zhang, Z. Wu, X. Zhang, L. Li, Y. Li, H. Xu, X. Li, X. Yu, Z. Zhang, Y. Liang and H. Wang, *Nat. Commun.*, 2017, **8**, 14675.

394 Q. Wang, K. Liu, K. Hu, C. Cai, H. Li, H. Li, M. Herran, Y.-R. Lu, T.-S. Chan, C. Ma, J. Fu, S. Zhang, Y. Liang, E. Cortés and M. Liu, *Nat. Commun.*, 2022, **13**, 6082.

395 X. Zhang, Y. Wang, M. Gu, M. Wang, Z. Zhang, W. Pan, Z. Jiang, H. Zheng, M. Lucero, H. Wang, G. E. Sterbinsky, Q. Ma, Y.-G. Wang, Z. Feng, J. Li, H. Dai and Y. Liang, *Nat. Energy*, 2020, **5**, 684–692.

396 J. Su, C. B. Musgrave, Y. Song, L. Huang, Y. Liu, G. Li, Y. Xin, P. Xiong, M. M.-J. Li, H. Wu, M. Zhu, H. M. Chen, J. Zhang, H. Shen, B. Z. Tang, M. Robert, W. A. Goddard and R. Ye, *Nat. Catal.*, 2023, **6**, 818–828.

397 K. Chen, M. Cao, G. Ni, S. Chen, H. Liao, L. Zhu, H. Li, J. Fu, J. Hu, E. Cortés and M. Liu, *Appl. Catal., B*, 2022, **306**, 121093.

398 K. Chen, M. Cao, Y. Lin, J. Fu, H. Liao, Y. Zhou, H. Li, X. Qiu, J. Hu, X. Zheng, M. Shakouri, Q. Xiao, Y. Hu, J. Li, J. Liu, E. Cortés and M. Liu, *Adv. Funct. Mater.*, 2022, **32**, 2111322.

399 W. Zhu, S. Liu, K. Zhao, G. Ye, K. Huang and Z. He, *Small*, 2023, 2306144.

400 T. Wang, J. Wang, C. Lu, K. Jiang, S. Yang, Z. Ren, J. Zhang, X. Liu, L. Chen, X. Zhuang and J. Fu, *Adv. Mater.*, 2023, **35**, 2205553.

401 D. Liu, X. Li, S. Chen, H. Yan, C. Wang, C. Wu, Y. A. Haleem, S. Duan, J. Lu, B. Ge, P. M. Ajayan, Y. Luo, J. Jiang and L. Song, *Nat. Energy*, 2019, **4**, 512–518.

402 Y. Wang, Z. Bao, M. Shi, Z. Liang, R. Cao and H. Zheng, *Chem. - Eur. J.*, 2022, **28**, e202102915.

403 H. Li, F. Pan, C. Qin, T. Wang and K.-J. Chen, *Adv. Energy Mater.*, 2023, **13**, 2301378.

404 C. Jia, Y. Zhao, S. Song, Q. Sun, Q. Meyer, S. Liu, Y. Shen and C. Zhao, *Adv. Energy Mater.*, 2023, 2302007.

405 C. Wang, Y. Chen, D. Su, W.-L. Man, K.-C. Lau, L. Han, L. Zhao, D. Zhan and X. Zhu, *Adv. Mater.*, 2023, 2303179.

406 S. Roy, Z. Li, Z. Chen, A. C. Mata, P. Kumar, S. C. Sarma, I. F. Teixeira, I. F. Silva, G. Gao, N. V. Tarakina, M. G. Kibria, C. V. Singh, J. Wu and P. M. Ajayan, *Adv. Mater.*, 2023, 2300713.

407 X. Zhang, M. Zhang, Y. Deng, M. Xu, L. Artiglia, W. Wen, R. Gao, B. Chen, S. Yao, X. Zhang, M. Peng, J. Yan, A. Li, Z. Jiang, X. Gao, S. Cao, C. Yang, A. J. Kropf, J. Shi, J. Xie, M. Bi, J. A. van Bokhoven, Y.-W. Li, X. Wen, M. Flytzani-Stephanopoulos, C. Shi, W. Zhou and D. Ma, *Nature*, 2021, **589**, 396–401.

408 Y. Guo, M. Wang, Q. Zhu, D. Xiao and D. Ma, *Nat. Catal.*, 2022, **5**, 766–776.

409 M.-J. Cheng, E. L. Clark, H. H. Pham, A. T. Bell and M. Head-Gordon, *ACS Catal.*, 2016, **6**, 7769–7777.

410 B. Kim, Y. C. Tan, Y. Ryu, K. Jang, H. G. Abbas, T. Kang, H. Choi, K.-S. Lee, S. Park, W. Kim, P.-P. Choi, S. Ringe and J. Oh, *ACS Energy Lett.*, 2023, **8**, 3356–3364.

411 M. Chhetri, M. Wan, Z. Jin, J. Yeager, C. Sandor, C. Rapp, H. Wang, S. Lee, C. J. Bodenschatz, M. J. Zachman, F. Che and M. Yang, *Nat. Commun.*, 2023, **14**, 3075.

412 W. Ren, X. Tan, J. Qu, S. Li, J. Li, X. Liu, S. P. Ringer, J. M. Cairney, K. Wang, S. C. Smith and C. Zhao, *Nat. Commun.*, 2021, **12**, 1449.

413 Y. Cao, S. Chen, S. Bo, W. Fan, J. Li, C. Jia, Z. Zhou, Q. Liu, L. Zheng and F. Zhang, *Angew. Chem., Int. Ed.*, 2023, **62**, e202303048.

414 R. Xia, J. Cheng, Z. Chen, Z. Zhang, X. Zhou, J. Zhou and M. Zhang, *Adv. Mater.*, 2023, 2304920.

415 J. Feng, L. Zhang, S. Liu, L. Xu, X. Ma, X. Tan, L. Wu, Q. Qian, T. Wu, J. Zhang, X. Sun and B. Han, *Nat. Commun.*, 2023, **14**, 4615.

416 C. Wang, X. Wang, H. Ren, Y. Zhang, X. Zhou, J. Wang, Q. Guan, Y. Liu and W. Li, *Nat. Commun.*, 2023, **14**, 5108.

417 G. Wang, Z. Chen, T. Wang, D. Wang and J. Mao, *Angew. Chem., Int. Ed.*, 2022, **61**, e202210789.

418 Y. Guo, S. Mei, K. Yuan, D.-J. Wang, H.-C. Liu, C.-H. Yan and Y.-W. Zhang, *ACS Catal.*, 2018, **8**, 6203–6215.

419 X. Li, L. Liu, X. Ren, J. Gao, Y. Huang and B. Liu, *Sci. Adv.*, 2020, **6**, eabb6833.

420 J. Zheng, K. Lebedev, S. Wu, C. Huang, T. Ayvalı, T.-S. Wu, Y. Li, P.-L. Ho, Y.-L. Soo, A. Kirkland and S. C. E. Tsang, *J. Am. Chem. Soc.*, 2021, **143**, 7979–7990.

421 X. Hai, S. Xi, S. Mitchell, K. Harrath, H. Xu, D. F. Akl, D. Kong, J. Li, Z. Li, T. Sun, H. Yang, Y. Cui, C. Su, X. Zhao, J. Li, J. Pérez-Ramírez and J. Lu, *Nat. Nanotechnol.*, 2022, **17**, 174–181.

422 M. Tamtaji, H. Gao, M. D. Hossain, P. R. Galligan, H. Wong, Z. Liu, H. Liu, Y. Cai, W. A. Goddard and Z. Luo, *J. Mater. Chem. A*, 2022, **10**, 15309–15331.

423 G. Kyriakou, M. B. Boucher, A. D. Jewell, E. A. Lewis, T. J. Lawton, A. E. Baber, H. L. Tierney, M. Flytzani-Stephanopoulos and E. C. H. Sykes, *Science*, 2012, **335**, 1209–1212.

424 R. Chen, J. Zhao, Y. Li, Y. Cui, Y.-R. Lu, S.-F. Hung, S. Wang, W. Wang, G. Huo, Y. Zhao, W. Liu, J. Wang, H. Xiao, X. Li, Y. Huang and B. Liu, *J. Am. Chem. Soc.*, 2023, **145**, 20683–20691.

425 Y. Hu, F. Zhan, Q. Wang, Y. Sun, C. Yu, X. Zhao, H. Wang, R. Long, G. Zhang, C. Gao, W. Zhang, J. Jiang, Y. Tao and Y. Xiong, *J. Am. Chem. Soc.*, 2020, **142**, 5618–5626.

426 Y. Chai, X. Han, W. Li, S. Liu, S. Yao, C. Wang, W. Shi, I. da-Silva, P. Manuel, Y. Cheng, L. D. Daemen, A. J. Ramirez-Cuesta, C. C. Tang, L. Jiang, S. Yang, N. Guan and L. Li, *Science*, 2020, **368**, 1002–1006.

427 Y. Liu, Z. Li, Q. Yu, Y. Chen, Z. Chai, G. Zhao, S. Liu, W.-C. Cheong, Y. Pan, Q. Zhang, L. Gu, L. Zheng, Y. Wang, Y. Lu, D. Wang, C. Chen, Q. Peng, Y. Liu, L. Liu, J. Chen and Y. Li, *J. Am. Chem. Soc.*, 2019, **141**, 9305–9311.

428 Z. Ji, M. Hu and H. L. Xin, *Sci. Rep.*, 2023, **13**, 14132.

429 A. Annys, D. Jannis and J. Verbeeck, *Sci. Rep.*, 2023, **13**, 13724.

430 A. Martini, D. Hursán, J. Timoshenko, M. Rüscher, F. Haase, C. Rettenmaier, E. Ortega, A. Etxebarria and B. Roldan Cuenya, *J. Am. Chem. Soc.*, 2023, **145**, 17351–17366.

431 R. Qi, B. Zhu, Z. Han and Y. Gao, *ACS Catal.*, 2022, **12**, 8269–8278.

432 M. Sun, T. Wu, Y. Xue, A. W. Dougherty, B. Huang, Y. Li and C.-H. Yan, *Nano Energy*, 2019, **62**, 754–763.

433 C. Song, Z. Wang, Z. Yin, D. Xiao and D. Ma, *Chem Catal.*, 2022, **2**, 52–83.

434 T. Inoue, A. Fujishima, S. Konishi and K. Honda, *Nature*, 1979, **277**, 637–638.

435 P. W. Anderson, *Science*, 1972, **177**, 393–396.